Interfacial Behaviors of

Polymer and Metal-Polymer Thin Films

under Contact and Solvent Stimuli

by

Fan Zhao

A thesis

presented to the University of Waterloo

in fulfillment of the

thesis requirement for the degree of

Doctor of Philosophy

in

Chemical Engineering (Nanotechnology)

Waterloo, Ontario, Canada, 2025

© Fan Zhao 2025

Examining Committee Membership

The following served on the Examining Committee for this thesis. The decision of the Examining committee is by majority vote.

External Examiner:	**Prof. Jeffery A. Wood** Faculty of Science and Technology, University of Twente
Supervisor(s):	**Prof. Boxin Zhao** Department of Chemical Engineering, University of Waterloo
Supervisor(s):	**Prof. Sushanta K. Mitra** Department of Mechanical & Mechatronics Engineering, University of Waterloo
Internal Member:	**Prof. Tizazu Mekonnen** Department of Chemical Engineering, University of Waterloo
Internal Member:	**Prof. Hamed Shahsavan** Department of Chemical Engineering, University of Waterloo
Internal-External Member:	**Prof. Yimin Wu** Department of Mechanical & Mechatronics Engineering, University of Waterloo

Author's Declaration

This thesis consists of material all of which I authored or co-authored: see Statement of Contributions included in the thesis. This is a true copy of the thesis, including any required final revisions, as accepted by my examiners.

I understand that my thesis may be made electronically available to the public.

Statement of Contributions

This dissertation incorporates content from 4 journal articles, all of which have been published or ready to submit for publication during my PhD studies. As the first author of these works, I made major contributions to conceptualization, experimental design, data acquisition, analysis, and manuscript preparation.

Chapter 3 of this dissertation is presented from

1. **Fan Zhao**, Surjyasish Mitra, Zhao Qi, Minmin Xu, Yaxian Yuan, Jianlin Yao, Sushanta K Mitra, and Boxin Zhao. "In-situ Raman Spectroscopy of Soft Contact." *Journal of Colloid and Interface Science* (2025): 138084-.
(DOI: 10.1016/j.jcis.2025.138084)

Chapter 4 of this dissertation is presented from

2. **Fan Zhao**, Surjyasish Mitra, A-Reum Kim, Minmin Xu, Jianlin Yao, Sushanta K Mitra, and Boxin Zhao. "Determining Effective Refractive Index and Elasticity of Nanoscale Metal - Thin, Soft Polymer Bilayers Using Interference Signatures of a Glass Probe." *Colloids and Surfaces. A, Physicochemical and Engineering Aspects* 674 (2023): 131861-.
(DOI: 10.1016/j.colsurfa.2023.131861)

Chapter 5 of this dissertation is presented from

3. **Fan Zhao**, Surjyasish Mitra, A-Reum Kim, Minmin Xu, Jianlin Yao, Sushanta K Mitra, and Boxin Zhao. "Profiling Contact Ridge of Soft Substrates with Metallic Thin Films Using a Novel Interference Technique." *Surfaces and Interfaces* 49 (2024): 104458-.
(DOI: 10.1016/j.surfin.2024.104458)

Chapter 6 of this dissertation is presented from

4. **Fan Zhao**, Surjyasish Mitra, Minmin Xu, Jianlin Yao, Sushanta K Mitra, and Boxin Zhao. "Solvent-induced Triradial Pattern Formation on Solid-supported Viscoelastic Thin Films and Gel". (Under Review)

Abstract

Polymeric thin films and metal-polymer bilayers are foundational components in flexible electronics, adaptive surfaces, and emerging interface technologies, valued for their mechanical compliance, ease of processing, and tunable functionality. Unlike homogeneous rigid or bulk elastic materials, polymer thin films exhibit inherently display scale-dependent mechanical and optical properties, particularly at interfaces, where deformation behavior is governed by factors such as film thickness, cross-link density, and free liquid content, often resulting in nonlinear and time-dependent viscoelastic phenomena. The integration of nanoscale metallic coatings introduces an additional layer of complexity: the rigid-soft coupling further alters both mechanical and optical properties, giving rise to hybrid contact behaviors that go beyond the assumptions of classical contact theories developed for either purely stiff or bulk soft materials. Moreover, the interfacial deformations are typically confined to micro- or even nanometer scales, where stress localization, modulus gradients, and geometric confinement jointly govern the contact behaviors and its evolution. This multiscale, multiphysics coupling presents significant challenges for experimental characterization. Most conventional techniques isolate mechanical and optical measurements, rely on model-specific assumptions, and involve multi-step or complicated procedures. Thus, these techniques present certain challenges in precisely characterizing the real micro-scale structural properties and deformation behavior under actual loading or environmental conditions. Despite growing interest in these bilayer systems, a clear, experimentally accessible framework for quantitatively probing their contact behaviors and underlying properties remains lacking. Addressing this gap is essential not only for advancing the fundamental understanding of thin film mechanics, but also for enabling the rational design of high performance, multifunctional soft interfaces for next generation technologies.

To address this gap, this dissertation applies spectroscopy and microscopy techniques: confocal Raman spectroscopy and dual-wavelength reflection interference contrast

microscopy (DW-RICM), to systematically investigate the interfacial behaviors of polymeric and metal-polymer bilayer thin films under contact and solvent stimuli. The resulting insights aim to inform the rational design of multifunctional soft interfaces with enhanced performance and broader applicability in next generation surface and device technologies.

The dissertation first highlights a parameter independent framework for characterizing soft contact deformation using in-situ confocal Raman spectroscopy. To achieve this, a calibration platform was constructed using a five-glass sphere probe assembly, with a glass slide placed on top to establish a reliable measurement protocol. This setup was then adapted for soft contact analysis by replacing the upper glass slide with a PDMS coated glass slide (P_{10}), enabling localized deformation under controlled spherical contact. Raman mapping was performed in three spatial dimensions by tracking the intensity distribution of the 2905 cm^{-1} Raman peak, which serves as the -CH_3 stretching of PDMS. The resulting contour maps enabled imaging of the deformation region across multiple planes, allowing the extraction of physical parameters such as contact radius and indentation depth. The obtained results were broadly consistent with Hertz predictions, while revealing local deviations indicative of non-conformal contact behavior. The proposed technique and framework offers a unique method to observe the formation and change of contact deformation, leading to a deeper insight into the soft contact system.

Building upon this molecular insight, a methodology was developed to simultaneously extract the optical and mechanical properties of polymer and metal-polymer bilayer thin films using dual-wavelength reflection interference contrast microscopy (DW-RICM). Nanoscale gold (Au) and silver (Ag) layers were deposited on PDMS substrates with varying elasticity and coating thickness. By analyzing interference patterns obtained at two wavelengths (488 nm and 561 nm) during contact with a glass probe of known geometry, the effective refractive indices and elastic modulus of the bilayer system were quantitatively determined. The refractive index was found to decrease with increasing metal deposition time, decreasing PDMS elasticity and increasing coating thickness, consistent with UV/Vis spectroscopy

measurement. Elastic moduli were derived using Hertz theory based on the measured contact radii. This integrated optical-mechanical approach simplifies current multi-step characterization procedures, offering insights into fundamental properties of the metal-polymer bilayers.

To further investigate the metal thin layer coating on the contact behavior of metal-polymer bilayers, a black-ink-coated probe was incorporated with DW-RICM to suppress unwanted reflections at the probe-air interface. This modified configuration enabled visualization of deformation features including contact deformation region and contact ridge formation with nanoscale resolution. Experimental results show that increasing the metal deposition time (i.e., metal coating thickness) leads to a reduction in both contact radius and contact ridge height. Moreover, long-term contact analysis of the gold coated bilayers showed a steady increase in ridge height over time, unlike the gradual decrease observed in the bare counterparts until reaching a steady state, suggesting altered interfacial viscoelastic behavior driven by the presence of the metal coating layer.

Building on insights into the role of free liquids in thin film contact behavior, the final phase of this dissertation investigates out-of-equilibrium interfacial mechanic of solvent-induced surface instabilities on solid supported soft substrates using DW-RICM. The morphological evolution of PDMS and silicone gel substrates were monitored over prolonged hexane extraction and drying. A consistent transition was observed from shallow circular depressions to highly ordered triradial (Y-shaped) surface patterns driven by internal stress accumulation and elastic modulus gradients between the surface and bulk. Comparative analysis across formulations with varying crosslinking densities revealed that while the pattern formation mechanism is broadly conserved, it remains sensitive to material properties such as free liquid content and elasticity. These findings shed light on the mechanisms of solvent-mediated patterning and underscore solvent processing as a promising strategy for engineering programmable surface architectures in soft materials.

Overall, this dissertation constructs a framework for soft interface characterization, integrating mechanical deformation under contact and surface morphological transformation under solvent extraction. The findings highlight how vibrational spectroscopy and optical interferometry can be used in tandem to probe complex contact phenomena, offering new tools and insights for the design of adaptive, compliant surfaces in applications such as soft robotics, flexible electronics, and interfacial patterning.

Acknowledgements

First, I would like to express my deepest gratitude to my research supervisors, Prof. Jianlin Yao, Prof. Sushanta K. Mitra, and Prof. Boxin Zhao, for giving me the invaluable opportunity to pursue my doctoral studies under their mentorship. It has been a true honor and a great blessing to be guided by three outstanding professors. I am deeply thankful for your trust, encouragement, and generous support throughout this journey. Your guidance has not only shaped my research but also inspired me to grow as an independent thinker. I am especially grateful for the freedom you gave me to explore my own ideas, and for the valuable opportunity to work across two universities and three laboratories, an experience that has profoundly enriched my academic and personal life.

Second, I would like to thank the external examiner, Prof. Jeffery A. Wood, and members of my supervisory committee, Prof. Tizazu Mekonnen, Prof. Yimin Wu and Prof. Hamed Shahsavan, for their valuable suggestions during my thesis evaluation and Ph.D. defense. I am especially grateful to Prof. Wood for his detailed comments and shared papers, especially that paper which offered valuable guidance on a problem I have been interested in for a long time.

I also thank Waterloo Institute for Nanotechnology (WIN) and Soochow University for the funding support via the Doctoral Program Scholarship.

I would like to thank Prof. Qinmin Pan for her kind recommendation and for providing experimental instruments during my exchange period at Soochow University, and Prof. Minmin Xu for his academic guidance and support. I am also grateful to Prof. Yaxian Yuan for her academic guidance and kind assistance during my exchange period at Soochow University. In addition, I sincerely thank Dr. Mei Wang at the Testing Center of Soochow University for Raman spectroscopy training and providing access to the instrumentation.

Finally, I am thankful to all lab members in Waterloo and Suzhou for their help, co-operation, useful discussion and suggestions, work time and cheer-up time when I was with them. Particularly, I appreciate help from Dr. Surjyasish Mitra during my PhD period.

Lastly, thanks to Dr. Chao-hui Kuo, a mentor, senior, and friend, for leading by example and guiding me forward with wisdom and support.

Super lastly, thanks to my parents for their endless love and support.

Table of Contents

Author's Declaration iii

Statement of Contributions iv

Abstract v

Acknowledgements ix

List of Figures xvi

List of Tables xxxvii

List of Abbreviations xxxviii

List of Symbols xxxix

Chapter 1 Introduction 1

1.1 Motivation 1

1.2 Methodological Framework 4

1.3 Structure of the Dissertation 6

Chapter 2 Literature Review 8

2.1 Introduction 8

2.2 Contact theories and existing findings in soft contact 8

2.3 Existing characterization techniques and findings for Soft Contact 13

2.4 Confocal Raman Spectroscopy: Principle and Applications in soft contact 17

2.5 DW-RICM: Principle and Applications in soft contact 20

Chapter 3 In-situ Raman Spectroscopy for Soft Contacts 24

3.1 Introduction 25

3.2 Experimental 30
3.2.1 Preparation of soft substrates 30
3.2.2 Raman measurements 31
3.3 Results and discussion 32
3.3.1 Calibration experiments: glass-glass contact 33
3.3.2 PDMS-glass experiments 38
3.3.3 Confocal Raman mapping of contact deformation 41
3.3.4 Limitations of the study 45
3.3.5 Assessment of robustness and broader applicability 47
3.4 Conclusion 48
Chapter 4 Determining effective refractive index and elasticity of nanoscale metal - thin, soft polymer bilayers using interference signatures of a glass probe 50
4.1 Introduction 50
4.2 Experimental 53
4.2.1 Fabrication of soft substrates 53
4.2.2 Deposition of metal film 54
4.2.3 RICM measurements 55
4.3 Results and discussion 58
4.3.1 Pristine PDMS coating 59
4.3.2 Ag film on PDMS coating 66
4.3.3 Au film on PDMS coating 71
4.3.4 Comparison with UV/Vis measurements 74

4.4 Conclusion 76

4.5 Outlook 77

Chapter 5 Profiling contact ridge of soft substrates with metallic thin films using a novel interference technique 79

5.1 Introduction 80

5.2 Experimental 82

5.2.1 Preparation of black ink-coated probe 82

5.2.2 Optical loss measurement of black ink 83

5.2.3 Preparation of soft coatings 84

5.2.4 Preparation of Au-coated soft substrates 84

5.2.5 Measurements of RICM 84

5.2.6 Refractive indices of soft substrates and Au-coated soft substrates 87

5.2.7 Measurements using Raman spectroscopy 88

5.3 Results and discussion 88

5.3.1 Deformation profiles of pristine polymer substrates 91

5.3.2 Deformation profiles of metal-polymer bilayer substrates 94

5.3.3 Evolution of contact deformation 97

5.4 Conclusion 103

Chapter 6 Solvent-induced triradial pattern formation on solid-supported viscoelastic thin films and gel 105

6.1 Introduction 105

6.2 Materials and experiments 107

6.2.1 Materials 107
6.2.2 Fabrication of silicone elastomer thin films 108
6.2.3 Fabrication of silicone gel thin films 108
6.2.4 Hexane-induced pattern formation 108
6.2.5 DW-RICM measurement 109
6.2.6 Optical Microscopic measurement 109
6.2.7 AFM measurement 109
6.2.8 SEM measurement 110
6.2.9 Rheological measurement 110
6.2.10 Raman spectroscopy measurement 110
6.3 Results and discussion 111
6.3.1 Formation and characterization of solvent-induced patterns on silicone elastomer thin films. 111
6.3.2 Formation and characterization of solvent-induced patterns on silicone gel thin films 122
6.3.3 Mechanism of solvent-induced soft thin film surface patterning 133
6.4 Conclusion 136
Chapter 7 Conclusions and Future Outlook 138
7.1 Conclusions of present research 138
7.2 Suggestions for future research 140
References 143
Appendix A Supporting Information for Chapter 3 173

Appendix B Supporting Information for Chapter 4 181

Appendix C Supporting Information for Chapter 5 198

Appendix D Supporting Information for Chapter 6 210

List of Figures

Figure 1-1 The methodological framework of the research objective. P_{10}, P_{35}, P_{60}, P_{64}, and P_{80} represent PDMS formulations with differing base-to-curing-agent ratios of 10:1, 35:1, 60:1, 64:1, and 80:1, respectively. DW-RICM: Dual-wavelength reflection interference contrast microscopy. n_{eff}: effective refractive index. E: Young's modulus. 4

Figure 2-1 Schematic of representative contact of elastic solids with the contact radius a under the preload F. (a) Solid sphere on solid sphere with different radius, R_1 and R_2, respectively. (b) Solid sphere on solid semi-infinite substrate. The underlying substrate has a thickness H larger than the radius R_1. 9

Figure 2-2 Characterization Techniques for soft contacts. (a) An SEM image of a polystyrene particle on a soft polyurethane substrate. The particle embed into the soft substrate, thereby creating a contact zone of radius. (Adapted from ref.[50] with permission. © 1989 AIP Publishing.) (b) Surface indentation profiles of soft solids under a spherical silica particles of radii 15 mm. Surface stiffness is 3 kPa (blue), 85 kPa (magenta), and 500 kPa (cyan) (Adapted from ref. [18] © 2013 Springer Nature Limited.) (c) Schematic of a colloidal probe in contact with a soft solid surface labeled with parameters of force F, contact radius a, indentation δ, and the particle radius R. A representative force-indentation curve measured by AFM indentation on PDMS with E_{bulk} = 5 kPa and a maximum indentation depth $\delta \approx 2.8$ μm and corresponding cross-sectional confocal images obtained by confocal microscopy of the labeled points on the force-indentation curve. The green dashed line represents the interface between solid and air, which is determined by measuring reflection at the surface. The gray circle represents the spherical probe as a guide to the eye. The particle radius is R = 6.5 μm. Scale bars: 5 μm. (Adapted from ref.[53] with permission. © 2017 American Physical Society.) (d) Confocal images of indentation of a glass microsphere into soft substrates (yellow) with a thin oil layer (green), a thick oil layer, and no oil layer. Both the soft substrates and the oil were mixed with different fluorescent dye (Adapted from ref.[53] with permission. © 2017 American Physical

Society.) (e) Schematic view of the compression device installed in the tomograph (left) and the segmentation process for extracting the contact area from an X-ray computed tomography image (right). The two bodies in contact are installed inside the compression device where a displacement can be imposed through a motorized vertical translating stage (not visible in the current image). While the materials are exposed to X-rays, the entire device rotates 360° to acquire projections (called radiographs) of the specimens at different angles. The inset on the right shows one of the radiographs collected during a scan at low resolution to visualize the two materials in contact with the upper and lower rods of the compression device. Here, the PMMA disk is fixed while the displacement is imposed on the PDMS specimen. (Adapted from ref. [63] with permission. © 2023 Elsevier Masson SAS.) (f) Schematic of the optical sensing system, the relation between surface deformation angle and reflected light. (g) Schematic of the sphere vertical contact PDMS with different depths and the corresponding distribution of irradiance of reflected light along the x-axis with different contact depths. ((f) and (g) adapted from ref.[61] with permission. © 2024 Wiley-VCH GmbH.) 16

Figure 2-3 Schematic diagram for Rayleigh, Stokes and Anti-Stokes scattering. E_0: ground state. E_1: vibrational state..... 18

Figure 2-4 Representative applications of Raman spectroscopy in soft contact systems and thin film analysis. (a) Schematic of confocal Raman microscopy integrated with a surface forces apparatus (SFA) for in-situ analysis of confined PDMS films. (b) Corresponding Raman intensity map (2907 cm^{-1}) in the *x*-*y* plane at a confinement thickness of 3.5 nm. ((a) and (b) Adapted from ref.[70] with permission. © 2005 American Chemical Society.) (c) In-situ Raman spectra and images recorded during friction cycles of a glass hemisphere sliding against a Pb–Mo–S coating. (Adapted from ref.[71] with permission. © 2003 AIP Publishing.) (d) Schematic of the Raman-tribology setup (not to scale), showing side and front views of a rotating ball in contact. (e) Lubricant thickness profile along the *z*-axis, derived from normalized Raman intensity of the 1053 cm^{-1} glycerol peak. ((d) and (e) Adapted from Ref.[72] with permission . © 2008 AIP Publishing). (f) (g) and (h) Raman analysis of patterned a-Si:H on c-Si substrate shows spectral contrast, sample structure, and c-Si intensity mapping (505–535 cm^{-1}) for

optical profilometry, respectively. (Adapted from ref.[73] with permission. © 2016 Springer Nature.) 19
Figure 2-5 Representative applications of DW-RICM in soft contact systems and thin film analysis. (a) Schematics of the RICM model of an immersed object close to a substrate. The interfaces are assumed to be locally parallel. Optical multilayer model used for (b) a spherical polystyrene bead and (c) a vesicle settled on a glass substrate. ((a) (b) and (c) Adapted from ref. [79] with permission. © 2009 American Chemical Society.) (d) A water drop on a soft gel coated glass surface. (b) The extracted wetting ridge profile for the water drop on soft gel from the intensity distribution along the white line shown in the interference signature (inset), scale bar: 50 μm. Red and green circles represent height extracted from intensity distribution of red and green wavelength, respectively. ((d) and (e) Adapted from ref.[58] with permission. © 2022 American Chemical Society.) (f) Interferograms of glass-gel (thickness: 35 μm)-glass contact at 5 min, 1 hr, 20 hrs, 40 hrs, 85 hrs (steady state), 138 hrs (steady state), and 258 hrs (steady state), and the optical microscopic bottom view of the contact area. Scale bar: 200 μm. (g) Schematics of the contact zone. V_{ridge} includes the volume of the phase-separated liquids and elastic network. ((f) and (g) Adapted from ref. [44] with permission. © 2022 Elsevier Inc.) (h) The experimental snap showing a pinned acetone microdroplet. AB is a randomly chosen vertical slice across the microdroplet of interest. Red dots labeled A and B indicate the locations of the droplet contact line, while the cyan dot labeled C indicates the projected location of the droplet apex on the base plane. Scale bar: 20 μm. (i) Reconstructed height profile of the droplet along the line AB (as shown in part h). (j) Reconstructed 3D topography of the entire droplet. ((h) (i) and (j) Adapted from ref. [80] with permission. © 2021 American Chemical Society.) 22
Figure 3-1 (a) Schematic of Raman spectroscopy set-up highlighting the different components. Light source: laser with wavelength $\lambda = 638$ nm. CCD: Charged coupled device. (b) The typical Raman spectra of glass and P_{10} at a laser power of 3.77 mW. 32
Figure 3-2 Workflow illustration of Raman mapping measurement of the glass sphere - glass substrate contact system. (a) Snapshot of the set-up of the calibration experiment: five glass

spheres of 2.6 mm radius each fixed on a glass substrate with another cleaned glass substrate on top of the five glass spheres. The contact between the central glass sphere and the top glass slide is of interest here. (b) Schematic of the set-up of the calibration experiment (glass-glass system), where the origin $O(0,0,0)$ is located at the center of the contact area between the glass sphere and the top glass substrate. The x and y axis are located on the free surface of the top glass substrate, and the z-axis goes through the center of the contact interface and the top glass substrate. (c) The typical Raman spectra of glass obtained at a laser power of 3.77 mW with integration times of 1 s and 5 s. The peaks at 1111 cm^{-1} are highlighted. (d), (e), and (f) Optical snapshots of the mapping regions of interest at z locations of z = 4 μm, z = 0 μm and z = -4 μm, respectively. (g) The schematic of the laser spot focusing on the z layers of z = 4 μm, z = 0 μm and z = -4 μm. n_0, and n_1 are the refractive index of air (1.0) and glass (1.5), respectively and $n_0 < n_1$. θ_0 and θ_1 are the refraction angle of air and glass, respectively and obey the condition $\theta_0 > \theta_1$ (A3.8, Appendix A). δ_0 and δ_1 are the real penetration depth of laser in air and glass, respectively and obey the condition $\delta_0 < \delta_1$ (A3.8, Appendix A). Note that additional discussion on the penetration depth of the laser in air and glass is included in A3.8, Appendix A. (h), (i) and (j) The Raman mapped images (contour plots) based on the normalized Raman peak intensity of 1111 cm^{-1} (see text) at z layers of z = -4 μm, z = 0 μm and z = -4 μm, respectively. 35

Figure 3-3 (a) Schematic of the set-up of the PDMS-glass system, where the origin $O(0,0,0)$ is located inside the glass sphere, i.e., at the secant of the glass sphere at z = 0 μm. The x and y axis are located on the free surface (lower surface) of the PDMS/glass, and the z axis goes through the center of the contact interface and the upper PDMS/glass slide. (b) Single point Raman scans along z-direction from z = -4 μm to z = 10 μm in 2 μm steps focusing on the center of the glass sphere-PDMS contact configuration. 38

Figure 3-4 Raman mapped images (contour plots) based on the normalized Raman peak intensity (I_r) of 2905 cm^{-1} (see text) at (a) z = 0 μm, (c) z = 2 μm, and (e) z = 10 μm. (b) Raman spectra at the locations (-180, 120, 0) (reference point) and at the origin (0,0,0). The intensity

of the 2905 cm^{-1} peak at the location (-180, 120, 0) is used as the reference intensity and denoted as $I_{0,\,max}$ (2905 cm^{-1}). The intensity ratio, i.e., I_r (2905 cm^{-1}) = I_i (2905 cm^{-1})/ $I_{z=0,\,max}$ (2905 cm^{-1}) is highlighted. (d) Raman spectra at the locations (-180, 120, 0) (reference point) and (200, 200, 2), i.e., at a location on the $z = 2$ μm plane. The corresponding I_r is highlighted. (f) Raman spectra at the locations (-180, 120, 0) (reference point), (0, 0, 10), and (150, 140, 10) i.e., at two different locations on the z = 10 μm plane. The corresponding I_r's are highlighted. 40

Figure 3-5 (a) The Raman mapped images (contour plots) based on the normalized Raman peak intensity (I_r) of 2905 cm^{-1} (see text) at z = -4 μm, z = -2 μm, z = 0 μm, z = 2 μm, z = 4 μm, z = 5 μm, z = 6 μm, z = 8 μm, and z = 10 μm, respectively. (b) Top view optical imaging snapshot of the glass sphere-PDMS contact interface (dark region) where the green dot is the origin O(0,0,0) or its projection. Note that the central dark region remains unchanged at neighboring z-planes. (c) Schematic of the contact deformation of glass sphere-PDMS contact pair based on the Hertz theory and the Raman contour plots. 43

Figure 4-1 (a) Schematic of dual wavelength reflection interference contrast microscopy setup. The light sources are green (λ_g = 488 nm) and red (λ_r = 561 nm). SRM: Semi-refractive Mirror, GM: Galvanometric Mirror, HM: Half Mirror, DM: Dichroic Mirror, PMT: Photomultiplier Tube. (b) Schematic of the calibration experiment: a glass sphere atop a glass slide. n_1 and n_2 are the refractive indices of glass and air, respectively. (c) The curved glass profile represented as a series of three parallel dielectric layers with the air layer sandwiched between two glass layers. (d) Interference signature corresponding to green and red wavelengths for the system shown in (b). (e) Plot of raw (I (a.u.)) and normalized (I_0) intensity with radial location r for the slice shown in (d). (f) Plot of glass sphere profile for the interference signature shown in (d) and (e). The symbols represent the height extracted from experimentally obtained intensity profiles and the solid line represents the theoretical glass profile. 56

Figure 4-2 (a) Schematic of the glass sphere (R_0 = 2.6 mm) on soft PDMS (10:1) coating of finite coating thickness h_1 = 35 μm. n_1, n_2, and n_3 are the refractive indices of glass, air, and PDMS, respectively. (b) Optical multilayer model used for predicting the curved surface of the

glass sphere on the soft substrate shown in (a). (c) Unprocessed interference signature corresponding to the contact system shown in (a). (d) Plot of raw (I) and normalized (I_0) intensity with radial location r for the slice shown in (c). (e) Plot of glass sphere profile for the interference signature shown in (d) along the dashed line. The symbols represent the height extracted using $\Delta h_{g,r} = m\lambda_{g,r}/4\sqrt{n_{air}n_{PDMS}}$ and the solid lines represent the theoretical glass profile, i.e., $h = \sqrt{2600^2 - a^2} - \sqrt{2600^2 - r^2}$. Here, a is the contact radius. 61

Figure 4-3 (a) Interference signature of glass sphere contact with the soft substrate P_{20} (35 μm). (b) Plot of glass sphere profile for the interference signature shown in (a) along the dashed line. The symbols represent the height extracted using $\Delta h_{g,r} = m\lambda_{g,r}/4\sqrt{n_{air}n_{PDMS}}$ and the solid lines represent the theoretical glass profile. 63

Figure 4-4 (a) and (c) Interference signatures of glass spheres in contact with thick, soft substrates P_{10}(1 mm) and P_{20}(1 mm). (b) and (d) Plots of glass sphere profiles for the interference signature shown in (a) and (c) along the dashed lines. The symbols represent the height extracted using $\Delta h_{g,r} = m\lambda_{g,r}/4\sqrt{n_{air}n_{PDMS}}$ and the solid lines represent the theoretical glass profile. 64

Figure 4-5 (a) The refractive index of soft substrates predicted by fitting the profile of the glass sphere. (b) The contact radius of the spherical glass probe on the soft substrates surface and the calculated elastic (Young's) modulus based on the Hertz theory (Eq. 4-3). Error bars represent standard deviations calculated from three independent experiments. In some cases, they are smaller than the symbol size and thus not visible.. 65

Figure 4-6 (a) Schematic of a glass sphere atop a Ag coated PDMS film of finite thickness h_1. n_1, n_2, n_3, and n_4 are the refractive indices of glass, air, PDMS, and Ag, respectively. (b) Optical multilayer model used for predicting the curved surface of the glass sphere on the soft substrate shown in (a). (c) and (f) Interference signatures of glass sphere in contact with Ag coated PDMS films, P_{10} (35 μm) – Ag (10s) and P_{20} (35 μm) – Ag (10s). (d) and (g) Plots of raw (I (a.u.)) and normalized (I_0) intensity with radial location r for the slices shown in (c) and (f). (e) and (h) Plots of glass sphere profile for the interference signature shown in (c) and (f). The

symbols represent the heights extracted from experimentally obtained intensity profiles using $\Delta h_{g,r} = m\lambda_{g,r}/4\sqrt{n_{air}n_{Ag/PDMS}}$ and the solid lines represent the theoretical glass profile.. 68

Figure 4-7 (a) Variation of the refractive index corresponding to both green and red wavelengths with Ag sputtering time for 35 µm thin PDMS 10:1 substrate. (b) Variation of the refractive index corresponding to both green and red wavelengths with Ag sputtering time for 35 µm thin PDMS 20:1 substrate. (c) Variation of the refractive index corresponding to both green and red wavelengths with Ag sputtering time for 1mm thick PDMS 10:1 and PDMS 20:1 substrate. (d) Variation of experimentally obtained contact radius of glass probe and calculated Young's modulus (using Hertz theory) with Ag sputtering time for 35 µm thin PDMS 10:1 substrate. (e) Variation of experimentally obtained contact radius of glass probe and calculated Young's modulus (using Hertz theory) with Ag sputtering time for 35 µm thin PDMS 20:1 substrate. (f) Variation of experimentally obtained contact radius of glass probe and calculated Young's modulus (using Hertz theory) with Ag sputtering time for 1mm thick PDMS 10:1 and PDMS 20:1 substrate. Error bars represent standard deviations calculated from three independent experiments. In some cases, they are smaller than the symbol size and thus not visible. 70

Figure 4-8 (a) and (c) Interference signatures of glass spheres in contact with Au coated soft PDMS substrates P_{10} (35 µm) – Au (60s) and P_{20} (35 µm) – Au (60s). (b) and (d) Plots of glass sphere profiles for the interference signature shown in (a) and (c) along the dashed lines. The symbols represent the height extracted using $\Delta h_{g,r} = m\lambda_{g,r}/4\sqrt{n_{air}n_{Au/PDMS}}$ and the solid lines represent the theoretical glass profile. 71

Figure 4-9 (a) and (b) Variation of the refractive index corresponding to both green and red wavelengths with Au sputtering time for 35 µm thin PDMS 10:1 and PDMS 20:1 substrate. (c) and (d) Variation of experimentally obtained contact radius of glass probe and calculated Young's modulus (using Hertz theory) with Au sputtering time for 35 µm thin PDMS 10:1 and PDMS 20:1 substrate. Error bars represent standard deviations calculated from three

independent experiments. In some cases, they are smaller than the symbol size and thus not visible. 73

Figure 4-10 (a) Comparison of refractive index n_g values between RICM and UV/Vis spectroscopy measurements corresponding to wavelength, λ = 488 nm for Ag/PDMS bilayer films of varying deposition times for PDMS coating thickness of 35 μm. (b) Comparison of refractive index n_r values between RICM and UV/Vis spectroscopy measurements corresponding to wavelength, λ = 561 nm for Ag/PDMS bilayer films of varying deposition times for PDMS coating thickness of 35 μm. (c) Comparison of refractive index n_g values between RICM and UV/Vis spectroscopy measurements corresponding to wavelength, λ = 488 nm for Au/PDMS bilayer films of varying deposition times for PDMS coating thickness of 35 μm. (d) Comparison of refractive index n_r values between RICM and UV/Vis spectroscopy measurements corresponding to wavelength, λ = 561 nm for Au/PDMS bilayer films of varying deposition times for PDMS coating thickness of 35 μm. 76

Figure 5-1 (a) Schematic of Dual Wavelength - Reflectance Interference Contrast Microscopy (DW-RICM) set-up. Light sources: λ_g = 488 nm and λ_r = 561 nm. DM: Dichroic Mirror. GM: Galvanometric Mirror. SRM: Semi-refractive Mirror. PMT: Photomultiplier Tube. (b) Photo of a black ink-coated glass probe atop a glass slide used in the calibration experiment. Scale bar: 2 mm. (c) Schematic of optical configurations: the three parallel dielectric layers of black ink coated probe / air / glass slide represented the curved probe profile. n_1, n_2 and n_3 are the indices of refraction of glass, air, and black ink, respectively. (d) Images from DW-RICM at green and red wavelengths. 86

Figure 5-2 Calculated refractive indices. Au-coated soft substrates: (a) P_{35}, (b) P_{45}, and (c) P_{60} with different sputter coating times of 0 s, 10 s, 30 s, and 60 s under wavelengths of 488 nm and 561 nm. 87

Figure 5-3 (a) Schematics of a 2.6-mm-radius glass probe in contact with PDMS 10:1 (P_{10}) (left) and PDMS 60:1 (P_{60}) (right) coating of finite thickness of 35 μm and the laser path. n_1, n_2 and n_3 are the indexes of refraction of glass slice, air, and PDMS coating, respectively. The origin O is inside the glass probe. Point D is the lowest point of the glass probe that contacted

with soft coating. Point H_1 is located at the interface between the PDMS coating and the glass slide. Point A is located at the contact boundary between the glass probe and the PDMS coating. Point B is the crossing point of the free surface of soft coating with the *r*-axis. Point C is the base of the contact ridge. (b) RICM observation of a bare 2.6-mm-radius glass sphere sitting on a soft substrate with different elasticities: P_{10} (35 μm) and P_{60} (35 μm), and the corresponding reconstructed profile of glass probe (left: blue box) and partial contact deformation profile of P_{60} (35 μm) (right: blue box) based on the interference fringes. 90

Figure 5-4 (a) Schematic of the ink-coated probe (R = 2.615 mm) on a soft PDMS substrate of finite thickness ~ 35 μm. (b) Optical configurations of a four parallel dielectric layers model for simulating the curved surface of the black probe on the PDMS coating as illustrated in (a). n_1, n_2, n_3 and n_4 are the indexes of refraction of glass slice, air, PDMS coating, and ink, respectively. (c) and (e) The obtained interference signature generated by the ink-coated probe in contact with PDMS 45:1 (P_{45}) and PDMS 60:1 (P_{60}) with a thickness of 35 μm. (d) and (f) Reconstructed profiles of the ink-coated probe and contact deformation of the soft substrates based on the interference signature along the white, dotted lines drawn in (c) and (e). The green and red symbols indicate the extracted height using $h_{g,r} = m\lambda_{g,r}/4n_{PDMS}$. The dark solid line indicates the theoretical profile of the ink-coated probe using $h = \sqrt{R^2 - a^2} + h_0 - \sqrt{R^2 - r^2}$, h_0 and l_0 are the peak ridge height and width, respectively. 93

Figure 5-5 (a) Unprocessed interference signature corresponding to the contact of the ink-coated probe with the Au sputtered soft substrates P_{60} with varying sputtering times. Scale bars: 50 μm. (b) A plot of raw and normalized intensity distribution for the P_{60} - Au (30 s) substrate along the white dashed line in (a). (c) Profile of the ink-coated probe and contact deformation of the Au sputtered soft substrate based on the interference signature along the dashed line shown in (a). The green and red symbols indicate the height extracted using $h_{g,r} = m\lambda_{g,r}/4n_{PDMS}$ The dark solid line indicates the theoretical profile of the ink-coated probe using $h = \sqrt{R^2 - a^2} + h_0 - \sqrt{R^2 - r^2}$. 95

Figure 5-6 Reconstructed profiles of the ink-coated probe with a radius of 2.615 mm and the contact deformation of Au-coated (a) P_{35}, (b) P_{45}, and (c) P_{60} substrates at different Au deposition times of 10 s, 30 s, and 60 s based on the interferograms. The green and red symbols indicate the height extracted using $hg,r = m\lambda_{g,r}/4n_{Au/PDMS}$. The solid lines indicate the theoretical profile of ink-coated probes using $h = \sqrt{R^2 - a^2} + h_0 - \sqrt{R^2 - r^2}$. (d) Ridge height h_0 of different PDMS-Au bilayer substrates. Error bars represent standard deviations, though some are smaller than the size of the data point. 97

Figure 5-7 (a) Interferograms of a 2.615-mm-radius ink-coated probe on P_{60} soft substrate at 5 min, 11.5 hrs., and 35 hrs. after contact. (b) Interferograms of a 2.615-mm-radius ink-coated probe on P_{60} - Au (10 s) metal - polymer bilayer substrate at 5 min, 12 hrs., and 27.5 hrs. after contact. (c) Plots of the ink-coated probe and contact deformation profiles for the interferograms shown in (a) at the location of the white dashed lines. (d) Plots of the ink-coated probe and contact deformation profiles for the interferograms (shown in (b)) at the location of the white dashed lines. The green and red symbols indicate the height extracted using $h_{g,r} = m\lambda_{g,r}/4n_{PDMS,Au/PDMS}$. The solid lines indicate the theoretical profiles of the ink-coated probes using $h = \sqrt{R^2 - a^2} + h_0 - \sqrt{R^2 - r^2}$. 99

Figure 5-8 Evolution of ridge height h_0 (a) and maximum lateral deformation, i.e., ridge width l_0 (b) for bare P_{60} and P_{60} with Au sputtering for 10 s. Error bars represent the standard deviations of the reconstructed h_0 and l_0 obtained from measurements at the laser wavelengths (488 nm and 561 nm). In some cases, the error bars are smaller than the data symbols and are therefore not visible in the figure. 100

Figure 5-9 Raman spectra of P_{60} - Au (10s) in contact with the glass probe (hemispherical lens) and its variation over time. 102

Figure 6-1 (a) Schematic of the hexane-extraction experimental set-up. (b) Dual-Wavelength Reflection Interference Microscopy (DW-RICM) snapshots of the pattern formation. The green and the red channels reflect imaging using 488 nm and 561 nm wavelengths, respectively. The combined channel image is the overlay of the green and red channel images. l_a represents

the pattern arm length. (c) Optical microscopy snapshot of the pattern formation. (d) Atomic force microscopy scan and profile reconstruction of a pattern. (e) Profile of the ridge along the blue line highlighted in (d). The angles are shown for clarity. The dashed line is an approximate linear fit of the profile shown to highlight the angles. (f) Schematic of the ridge tip highlighting the opening angle. 113

Figure 6-2 (a) Raman spectra of pristine P_{60} and hexane-extracted P_{60} soft substrates. (b) Raman spectra of multiple selected positions around a pattern on the surface of the hexane-extracted P_{60} soft substrate. 115

Figure 6-3 Effect of drying conditions on the pattern formation: (a) In air for 10 mins, (b) In air for 12 hrs, (c) In a fume hood for 12 hrs, and (d) In an oven for 12 hrs at 80 °C. The green (first column) and the red channels (second column) reflect imaging using 488 nm and 561 nm wavelengths, respectively. The combined channel image (third column) is the overlay of the green and red channel images. The final column images are zoomed-in versions of the combined channel images, highlighting a single pattern. 117

Figure 6-4 Effect of hexane extraction time (t_E) on the pattern formation on P_{60} substrates of 35 μm thickness: (a) t_E = 8 min, (b) t_E = 1 hr, (c) t_E = 10 hrs and (d) t_E = 96 hr. Observations at two different drying times, t_O = 10 min and t_O = 90 min, are shown. The green and the red channels reflect imaging using 488 nm and 561 nm wavelengths, respectively. (e) Corresponding optical microscopy images of the patterns. (f) Variation of post-solvent extraction weight loss and arm length of the pattern l_a with different extraction times. Error bars for weight loss and length represent standard deviation from three independent experiments. 119

Figure 6-5 (a) Pattern formation on silicone gel substrates after 96 hrs of hexane immersion followed by drying in air. The green (first column) and the red channels (second column) reflect imaging using 488 nm and 561 nm wavelengths, respectively. The combined channel image (third column) is the overlay of the green and red channel images. The final column images are zoomed-in versions of the combined channel images, highlighting a single pattern. (b) Variation of normalized intensity I_0 corresponding to the green and red wavelengths along

the white dashed line shown in the last image of (A). (c) Height profile (h) extracted from the intensity distribution of (B). The green and the red symbols represent height extracted from 488 nm and 561 nm wavelengths, respectively (see methods). 123
Figure 6-6 Effect of hexane extraction time (t_E) on the pattern formation on silicone gel substrates of 35 μm thickness: (a) t_E = 8 min, (b) t_E = 1 hr, (c) t_E = 10 hrs, and (d) t_E = 96 hr. Observations at two different drying times, t_O = 10 min and t_O = 96 min, are shown. The overlay of the green and the red channels images are shown here. Individual channel images are shown in the Appendix D (Figure D6-11, Appendix D). (e) Corresponding optical microscopy images of the patterns. (f) Variation of post-solvent extraction weight loss and arm length of the pattern l_a with different extraction times. Error bars for weight loss and length represent standard deviation from three independent experiments. 126
Figure 6-7 Atomic force microscopy scans of the pattern formation on silicon gel substrates for swelling durations of (a) t_E = 1 hr and (b) t_E = 10 hrs. (c) DW-RICM images of a similar pattern formation for swelling duration of 1 hr. The green (first column) and the red channels (second column) reflect imaging using 488 nm and 561 wavelengths, respectively. (d) Height profile (h) extracted from RICM images along the white dashed line in (c). The green and the red symbols represent height extracted from 488 nm and 561 nm wavelengths, respectively (see methods). The patterns in (b) and (c) are not the exact same pattern. 129
Figure 6-8 Effect of drying conditions on the pattern formation: (a) In air for 10 min, (b) In air for 12 hrs, (c) In an oven for 12 hrs at 60 °C. The green (first column) and the red channels (second column) reflect imaging using 488 nm and 561 nm wavelengths, respectively. The combined channel image (third column) is the overlay of the green and red channel images. The final column images are zoomed-in versions of the combined channel images, highlighting a single pattern. 131
Figure 6-9 Pattern formation for PDMS substrates with different base-crosslinker ratios: (a) PDMS 64:1 and (b) PDMS 80:1. The green (first column) and the red channels (second column) reflect imaging using 488 nm and 561 nm wavelengths, respectively. The combined channel image (third column) is the overlay of the green and red channel images. The final image in

each row is the zoomed-in image of a pattern. Compared to PDMS 60:1, these surfaces have a higher fraction of free liquid chains and lower elasticity. (c) and (d) Height profiles (h) extracted from RICM images along the white dashed lines in (a) and (b). The green and the red symbols represent height extracted from 488 nm and 561 nm wavelengths, respectively (see methods). 133

Figure 6-10 Schematic of the solvent-induced surface pattern formation mechanism in confined soft elastomer films, highlighting the five distinct stages: (a) Pre-extraction and early solvent extraction (see step 1 in the main text), (b) Progressive swelling (see step 2 in the main text), (c) Solvent evaporation (see step 3 in the main text), (d) Mechanical instability, and pattern formation and stabilization (see steps 4 and 5 in the main text). 134

Figure A3-1 The cross sectional SEM image of the PDMS layer coated on a glass slide..... 173

Figure A3-2 (a) Plots of transmittance using UV/Vis spectroscopy measurements for glass slide and PDMS coated glass slide. (b) Plots of reflectance using UV/Vis spectroscopy measurements for glass slide and PDMS coated glass slide. 174

Figure A3-3 (a) Schematic of light transmitting through a glass slide. (b) Schematic of light transmitting through the PDMS coated glass slide. n_1, n_2, and n_3 are the refractive indices of air, glass, and PDMS, respectively. 175

Figure A3-4 The Raman spectra of (a) glass and (b) P_{10} (PDMS 10:1) at laser powers of 0.13 mW, 1.41 mW, and 3.77 mW between 400 cm^{-1} to 3200 cm^{-1} Raman shift. 175

Figure A3-5 Schematic of the laser spot focused on the interface of different materials (a) air, (b) glass, and (c) PDMS film. n_0, n_1 and n_2 are the refractive index of air (1.0), glass (1.5) and PDMS (1.4), respectively and $n_0 < n_2 < n_1$. θ_0, θ_1 and θ_2 are the maximum angle with respect to the optical axis in the observation medium (here is air) and in the analyzed material: glass and PDMS, respectively and $\theta_0 > \theta_2 > \theta_1$ see text. δ_0, δ_1 and δ_2 are the real penetration depth of laser in air, glass and PDMS, respectively. 177

Figure B4-1 (a) Tensile stress-strain curves for PDMS 10:1 (P_{10}) and 20:1 (P_{20}) substrates. (b, c) True tensile stress versus true strain for P_{10} and P_{20}, respectively, along with the fitted slopes corresponding to the Young's modulus (E (P_{10}): 1.88 MPa; E (P_{20}): 0.68 MPa). The linear regressions were performed in the low-strain regime, and the fitted slopes were confirmed to lie within the 95 % confidence interval.…….. 181

Figure B4-2 (a) and (c) Atomic force microscopy (AFM) scans of sputtered Ag layer on bare and PDMS 10:1 coated glass slides. (b) and (d) Plot of Ag layer thickness corresponding to the micrographs shown in (a) and (c) along the marked lines. 182

Figure B4-3 SEM micrographs of (a) bare PDMS (10:1), (b) PDMS (10:1) coated with Ag for 60 s, and (c) PDMS (10:1) coated with Ag for 120 s. 183

Figure B4-4 Plot of glass sphere profiles, i.e., variation of h over r on PDMS 10:1 substrates corresponding to interference signature using various expressions of n_{eff} in Eq. 4-2 (see main text): $n_{eff} = n_{air}$ (squares), $n_{eff} = n_{PDMS}$ (pentagram), $n_{eff} = \sqrt{n_{air} n_{PDMS}}$ (circles), $n_{eff} = n_{air} + n_{PDMS}$ (cross), $n_{eff} = (1/n_{air} + 1/n_{PDMS})^{-1}$ (crossed circles). The solid line shows the geometrical glass profile. 184

Figure B4-5 (a) and (c) Interference signatures of glass spheres on pristine, thin (35 μm) PDMS 10:1 and 20:1 substrates submerged under DI water. (b) and (d) Plots of the glass sphere profiles corresponding to the interference signatures shown in (a) and (c). The symbols represent the height extracted using $\Delta h_{g,r} = m\lambda_{g,r}/4\sqrt{n_{water} n_{PDMS}}$ and the solid lines represent the theoretical glass profile, i.e., $h = \sqrt{2600^2 - a^2} - \sqrt{2600^2 - r^2}$. Here, a is the contact radius. 189

Figure B4-6 Plot of refractive index measurement of bare Ag. 190

Figure B4-7 (a) and (b) Interference signatures of glass spheres on thin (35 μm) and thick (1 mm) PDMS 10:1 substrates with Ag layer of deposition time 10 s. (c) Plots of the glass sphere profiles corresponding to the interference signature shown in (a) and (b). The symbols

represent the height extracted using $\Delta h_{g,r} = m\lambda_{g,r}/4\sqrt{n_{air}n_{Ag/PDMS}}$ and the solid lines represent the theoretical glass profile, i.e.,$h = \sqrt{2600^2 - a^2} - \sqrt{2600^2 - r^2}$. Here, *a* is the contact radius. 190
Figure B4-8 (a) and (b) Interference signatures of glass spheres on thin (35 μm) and thick (1 mm) PDMS 10:1 substrates with Ag layer of deposition time 60 s. (c) Plots of the glass sphere profiles corresponding to the interference signature shown in (a) and (b). The symbols represent the height extracted using $\Delta h_{g,r} = m\lambda_{g,r}/4\sqrt{n_{air}n_{Ag/PDMS}}$ and the solid lines represent the theoretical glass profile, i.e.,$h = \sqrt{2600^2 - a^2} - \sqrt{2600^2 - r^2}$. Here, *a* is the contact radius. 191
Figure B4-9 (a) and (b) Interference signatures of glass spheres on thin (35 μm) and thick (1 mm) PDMS 10:1 substrates with Ag layer of deposition time 120 s. (c) Plots of the glass sphere profiles corresponding to the interference signature shown in (a) and (b). The symbols represent the height extracted using $\Delta h_{g,r} = m\lambda_{g,r}/4\sqrt{n_{air}n_{Ag/PDMS}}$ and the solid lines represent the theoretical glass profile, i.e.,$h = \sqrt{2600^2 - a^2} - \sqrt{2600^2 - r^2}$. Here, *a* is the contact radius. 192
Figure B4-10 (a) and (b) Interference signatures of glass spheres on thin (35 μm) and thick (1 mm) PDMS 20:1 substrates with Ag layer of deposition time 90 s. (c) Plots of the glass sphere profiles corresponding to the interference signature shown in (a) and (b). The symbols represent the height extracted using $\Delta h_{g,r} = m\lambda_{g,r}/4\sqrt{n_{air}n_{Ag/PDMS}}$ and the solid lines represent the theoretical glass profile, i.e.,$h = \sqrt{2600^2 - a^2} - \sqrt{2600^2 - r^2}$. Here, *a* is the contact radius. 193
Figure B4-11 (a) and (b) Interference signatures of glass spheres on thin (35 μm) and thick (1 mm) PDMS 20:1 substrates with Ag layer of deposition time 120 s. (c) Plots of the glass sphere profiles corresponding to the interference signature shown in (a) and (b). The symbols represent the height extracted using $\Delta h_{g,r} = m\lambda_{g,r}/4\sqrt{n_{air}n_{Ag/PDMS}}$ and the solid lines

represent the theoretical glass profile, i.e.,$h = \sqrt{2600^2 - a^2} - \sqrt{2600^2 - r^2}$. Here, a is the contact radius. 194

Figure B4-12 Comparison of predicted elastic (Young's) modulus values for Ag coated PDMS films using Hertz and JKR theories for (a) PDMS 20:1 substrates of film thickness 35 μm with varying Ag deposition times, (b) PDMS 20:1 substrates of film thickness 35 μm with varying Ag deposition times, and (c) PDMS 10:1 and 20:1 substrates of film thickness 1 mm with varying Ag deposition times. 194

Figure B4-13 Schematic of Ag sputtered PDMS film adhered to glass slide set-up. n_1, n_2 and n_3 are the refractive indices of air, glass, and Ag coated PDMS medium, respectively. 195

Figure B4-14 Plots of transmittance using UV/Vis spectroscopy measurements for PDMS 10:1 with Ag deposition (a) and PDMS 20:1 with Ag deposition (b). Plots of reflectance using UV/Vis spectroscopy measurements for PDMS 10:1 with Ag deposition (c) and PDMS 20:1 with Ag deposition (d). 196

Figure B4-15 Plots of transmittance using UV/Vis spectroscopy measurements for PDMS 10:1 with Au deposition (a) and PDMS 20:1 with Au deposition (b). Plots of reflectance using UV/Vis spectroscopy measurements for PDMS 10:1 with Au deposition (c) and PDMS 20:1 with Au deposition (d). 197

Figure C5-1 (a) Schematic of a glass sphere atop a glass slide. (b) Interference signature corresponding to green and red wavelengths for the system shown in (a). The scale bar represents 50 μm. (c) A plot of the glass sphere profile along the dashed white lines for the interference signature in (b). The symbols represent the height extracted corresponding to the green and red wavelengths using the relation $\Delta h_{g,r} = m\lambda_{g,r}/4n_{air}$ and the solid line represents the theoretical glass profile……...199

Figure C5-2 Optical images of the black ink-coated glass probe before and after sonication. 200

Figure C5-3 The roughness (1.29 μm) of the mixture black ink (with a thickness of 15 μm)-coated on glass slides using surface profiler measurements. 200

Figure C5-4 Plots of reflectance (a) and transmittance (b) using UV/Vis spectroscopy measurements for glass slide, black ink #1 (with a thickness of 15 μm) coated on a glass slide, and the mixture black ink with a weight ratio of black ink #1 and black ink #2 = 1:1 (thickness of 15 μm) coated on glass slide..... 201
Figure C5-5 Plots of optical loss using UV/Vis spectroscopy measurements for a glass slide, black ink #1 (with a thickness of 15 μm) coated on a glass slide, and the mixture black ink with a weight ratio of black ink #1 and black ink #2 = 1:1 (thickness of 15 μm) coated on a glass slide. 201
Figure C5-6 Atomic force microscopy (AFM) scans and thickness measurement of sputtered Au layer on a glass slide for 2 min. 202
Figure C5-7 The photograph of the experimental measurement set-up using DW-RICM. 202
Figure C5-8 Unprocessed interference signature corresponding to the glass sphere (R_0 = 2.6 mm) on (a) PDMS 10:1 (P_{10}) and (d) PDMS 20:1 (P_{20}) coatings of finite thickness at 35 μm. (b) and (e) Plots of raw (I(a,u)) and normalized (I_0) intensity with radial location r for the slice shown in (a) and (d), respectively. (c) and (f) Plots of glass sphere profile for the interference signature shown in (a) and (d) along the dashed lines. The symbols represent the height extracted using $\Delta h_{g,r} = m\lambda_{g,r}/4\sqrt{n_{air}n_{PDMS}}$ and the solid lines represent the theoretical glass profile, i.e., $h = \sqrt{2600^2 - a^2} - \sqrt{2600^2 - r^2}$. Here, a is the contact radius. 203
Figure C5-9 Unprocessed interference signature corresponding to the glass sphere (R_0 = 2.6 mm) on 35-μm-thickness (a) P_{35}, (c) P_{45}, and (e) P_{60} films deposited with Au for 60s, 60s and 30s, respectively. (b), (d) and (f) Plots of the glass sphere profile for the interference signature shown in (a), (c), and (e) along the dashed lines. The symbols represent the height extracted using $\Delta h_{g,r} = m\lambda_{g,r}/4\sqrt{n_{air}n_{Au/PDMS}}$ and the solid lines represent the theoretical glass profile, i.e., $h = \sqrt{2600^2 - a^2} - \sqrt{2600^2 - r^2}$. Here, a is the contact radius. 204
Figure C5-10 The photograph of the experimental measurement set-up using Raman Microscopy. 205

Figure C5-11 The photograph of the experimental measurement set-up of the Raman laser focused on (a) the sample surface without going through the hemispherical lens (left) and the glass probe (right); (c) the sample surface with going through the edge of the hemispherical lens (left) and the glass probe (right); (e) the sample surface with going through almost the center of the hemispherical lens (left) and the glass probe (right). The corresponding laser spot of the Raman laser focused on (b) the sample surface without going through the hemispherical lens (left) and the glass probe (right); (d) the sample surface with going through the edge of the hemispherical lens (left) and the glass probe (right); (f) the sample surface with going through almost the center of the hemispherical lens (left) and the glass probe (right)..... 206
Figure C5-12 Raman spectrum of the surface and inside of P_{10} and P_{60}..... 207
Figure C5-13 Raman spectrum of the surface of P_{60}-Au (10s) without placing the hemispherical lens..... 207
Figure C5-14 (a) and (c) Unprocessed interference signature corresponding to the black probe (R = 2.615 mm) on a 35-μm-thickness P_{60}. (b) and (d) Profiles of the probe and deformation of the soft substrate based on the interference signature shown in (a) and (c) along the marked line drawn. The green and red symbols represent the height extracted using $h_{g,r} = m\lambda_{g,r}/4n_{PDMS}$ and the dark solid line represents the theoretical profile of ink coated probe, i.e., $h = \sqrt{R^2 - a^2} + h_0 - \sqrt{R^2 - r^2}$..... 208
Figure C5-15 The contact radius of ink coated probe and bare glass probe contacting with different soft substrates. Error bars represent the standard deviation. 209
Figure C5-16 (a) Interference signature of a truncated ink-coated steel probe with a diameter of 19 mm on a 35-μm-thick soft PDMS film. The green and red interference signatures correspond to 488 nm and 561 nm wavelengths, respectively. (b) Profile of the contact ridge along the white line shown in (a). The green and red symbols represent the height extracted using $h_{g,r} = m\lambda_{g,r}/4n_{PDMS}$ and the dark solid line represents the theoretical profile of the ink-coated probe, i.e., $h = \sqrt{R^2 - a^2} + h_0 - \sqrt{R^2 - r^2}$ 209

Figure D6-1 (a) The cross sectional Scanning Electron Microscopy (SEM) image of the P_{60} (PDMS base and curing agent ratio: 60:1) layer coated on a glass slide. (b) Rheology measurements showing the variation of storage modulus, G' (closed symbols) and loss modulus, G'' (open symbols) with frequency, ω for the P_{60} soft substrate…… 210

Figure D6-2 Polarized optical microscopy images of a soft PDMS P_{60} substrate after immersion in hexane for 96 hrs and drying in air. 210

Figure D6-3 The cross sectional SEM image of a soft PDMS P_{60} substrate after immersion in hexane for 96 hrs and drying in air. 211

Figure D6-4 Dual-wavelength reflection interference contrast microscopy (DW-RICM) images of the soft PDMS P_{60} substrate after 96 hrs hexane extraction and 90 min air drying. The image shows the morphology of the surface pattern at a region mechanically cut by a blade to examine pattern change across the cut. 211

Figure D6-5 Atomic force microscopy (AFM) scan and profile of a pattern of the soft PDMS P_{60} substrate after 96 hrs hexane extraction and 12 hrs fume hood drying. 212

Figure D6-6 (a) Variation of pattern arm length with drying conditions for PDMS P_{60} substrate swollen in hexane for 96hrs. Error bars represent the standard deviation of measured pattern lengths. (b) Corresponding histograms showing the distribution of arm lengths for each drying condition, with fitted curves included to illustrate the overall spread of the data. 212

Figure D6-7 Dual-wavelength reflection interference contrasts with microscopy (DW-RICM) images and the corresponding zommed-in images of the pattern structure for soft PDMS P_{60} substrates with hexane extraction times of (a) 8 min and (b) 1 hr for air drying times of 10 min and 90 min. The green color corresponding to laser wavelength of 488 nm. 213

Figure D6-8 Atomic force microscopy (AFM) scan and profile of a pattern of the soft silicone gel substrate after 96 hrs hexane extraction and air drying. 213

Figure D6-9 The cross sectional SEM images of a soft PDMS P_{60} substrate before (a) and after immersion in hexane for 96 hrs and drying in air (b). 214

Figure D6-10 Dual-wavelength reflection interference contrast microscopy (DW-RICM) images of the soft silicone gel substrate after 96 hrs hexane extraction and 90 min air drying. The image shows the morphology of the surface pattern at a region mechanically cut by a blade to examine pattern change across the cut. 214
Figure D6-11 Dual-wavelength reflection interference contrast microscopy (DW-RICM) images of the silicone gel soft substrate with hexane extraction times of (a) 8 min, (b) 1 hr, (c) 10 hrs, and (d) 96 hrs for air drying times of 10 min and 90 min. The green and red color corresponding to laser wavelength of 488 nm and 561 nm, respectively. 215
Figure D6-12 Dual-wavelength reflection interference contrast microscopy (DW-RICM) images and the corresponding zommed-in images of the pattern structure for silicone gel soft substrates with hexane extraction times of (a) 8 min and (b) 1 hr for air drying times of 10 min and 90 min. The green color corresponding to laser wavelength of 488 nm. 216
Figure D6-13 (a) Dual-wavelength reflection interference contrast microscopy (DW-RICM) image of a single pattern on soft silicone gel substrate swollen in hexane for 96 hrs and then dried in an oven for 12 hrs at 60 °C. (b) and (c) Variation of the pattern height profile along the dashed lines representing the ridge slope (x) and the ridge side (x_0). 216
Figure D6-14 (a) Raman spectra of the gel soft substrates before and after hexane extraction of 96 hrs and drying in air more than 24 hrs. (b) Raman spectra of the pattern on the gel soft substrate surface. 217
Figure D6-15 (a) Variation of post-solvent extraction weight loss (%) and arm length of the pattern l_a of P_{60}, P_{64}, P_{80}, and silicon gel substrates with hexane extraction time of 96 hrs followed by drying in air. Error bars for weight loss and length represent standard deviation from three independent experiments. (b) The distribution of arm lengths l_a of P_{60} (52.54 ± 7.74 μm), P_{64} (60.97 ± 7.36 μm), P_{80} (62.67 ± 11.08 μm), and silicon gel (40.14 ± 5.50 μm) under the same extraction and drying conditions. 217
Figure D6-16 Dual-wavelength reflection interference contrast microscopy (DW-RICM) images of PDMS substrates with different base-crosslinker ratios: (a) PDMS 64:1 and (b) PDMS 80:1 with hexane extaction (t_E) for 10 hrs and then dry in air for 10 min. The green

(first column) and the red channels (second column) reflect imaging using 488 nm and 561 nm wavelengths, respectively. The combined channel image (third column) is the overlay of the green and red channel images. Compared to PDMS 60:1, these surfaces have a higher fraction of free liquid chains and lower elasticity. 218

List of Tables

Table 2-1 Classical and extended contact theories. (a: contact radius, H: thickness of the soft substrate, ϑ: Poisson's ratio.)..... 12
Table 3-1 Imaging techniques for visualizing soft contact deformation of elastomer film. (R: Radius of the probe; E: Elastic modulus of the soft substrate; H: thickness of the soft substrate. Resolution implies spatial resolution: instrument-defined (confocal microscopy, XRCT, Raman) or extracted (DW-RICM).)..... 28
Table 3-2 Mapping parameters of glass-glass system..... 36

List of Abbreviations

PDMS	Polydimethylsiloxane
DW-RICM	Dual-wavelength reflection interference contrast microscopy
GM	Galvanometric mirror
DM	Dichroic mirror
PMT	Photomultiplier tubes
SRM	Semi reflective mirror
DMA	Dynamic mechanical analyzer
XRCT	X-ray computed tomography
CCD	Charged coupled device
NA	Numerical aperture of the microscope objective
FWHM	The full width at half maximum criterion
RI	Refractive index
SPR	Surface plasmon resonance
OLED	Organic light-emitting diodes
AR	Anti-Reflection (Coating)
SERS	Surface-enhanced Raman spectroscopy
AFM	Atomic force microscopy
SEM	Scanning electron microscope
LSCM	Laser scanning confocal microscopy

List of Symbols

R_1, R_2	Curvatures of contact pairs
E_1, E_2	Young's modulus of contact pairs
$a_H, a_{JKR}, a_{DMT}, a(\alpha, F)$	Contact radius of Hertz, JKR, DMT, COS theory
$F, F_c(\alpha)$	Preload, Critical pull-off force
E^*, R^*	Reduced (or effective) elasticity and curvature
ϑ_1, ϑ_2	Poisson's ratio of contact pairs
H	Soft substrate thickness
w	Work of adhesion
Λ	Tabor's dimensionless parameter
z_0	The characteristic range of surface forces
a, $a_{F=0}(\alpha)$	Contact radius and contact radius of COS mode at zero load
ϖ	COS' dimensionless parameter
k	Effective modulus
G, G', G''	Shear modulus of elasticity, storage modulus and loss modulus
$q(x)$	Local pressure
$\omega(x)$	Vertical displacement
S	Contact area
δ, ${\delta_{JKR}}'$	Indentation depth and modified JKR indentation depth
$f_p\left(\frac{a}{H}\right), f_\delta\left(\frac{a}{H}\right), f_\delta\left(\frac{a}{H}\right)$	Correction factors for load, displacement, compliance
h	Planck constant
I_i, I_r	Raman peak intensity and normalized Raman peak intensity
$I_{z=0,max}$	The maximum Raman peak intensity at z = 0
$\lambda, \lambda_g, \lambda_r$	Laser wavelength, laser wavelength at 488 nm and 561 nm
n, n_g, n_r	Refractive index, refractive index at 488 nm and 561 nm

r	Radial location
I, I_1, I_2	Laser intensity of interference fringes, incident laser intensity, reflected laser intensity
$I_0, I_{(a,u)}$	Raw intensity and normalized intensity of interference fringes
$n_{eff}, \tilde{n}$	Effective refractive index, complex refractive index
T, R, A	Transmittance, Reflectance, Absorbance
T_{23}, T_{31}	Transmittance from medium 2 to medium 3, medium 3 to medium 2
R_{23}, R_{31}	Reflectance from medium 2 to medium 3, medium 3 to medium 2
φ	Phase difference
$\Delta h_{\mathrm{g,r}}$	Extracted height at laser wavelength of 488 nm and 561 nm
σ, σ^*	Tensile stress, true tensile stress
$\varepsilon, \varepsilon^*$	Strain, true strain
k	Imagery refractive index
m	Interference fringe's order
ϵ_0	Vacuum permittivity
ε_s	The relative permittivity
υ_0, υ_s	Frequency of incident photon, Frequency of scattered photon
l_0	Contact ridge width
$\Delta\upsilon$	Raman shift
γ	Surface tension
t_E, t_O	Extraction time, drying time
l_a	Pattern arm length
L_{EC}	Elastocapillary length
N_a	Avogadro number
M	Molecular weight

Chapter 1

Introduction

1.1 Motivation

Flexible smart wristbands for health monitoring, protective films in touchscreen devices, and tactile end-effectors in soft robots exemplify the pervasive integration of polymeric thin films and metal-polymer bilayer interfaces in modern technologies. These interfaces, characterized by their mechanical compliance, ease of fabrication, and multifunctional tunability [1,2], are indispensable across diverse fields, including flexible electronics [3], bio-integrated systems [4], soft robotics [5], artificial skin technologies [6], flexible sensing [7,8], wearable electronics [9], and micro-manipulation systems [10]. In practical scenarios, these interfaces frequently come into contact with other materials, undergoing periodic or sustained loading, making their deformation behaviors crucial at the micro- and nanoscales. The interfacial deformations significantly impact device reliability, signal integrity, adhesion stability, and overall operational efficiency. For instance, minor interfacial deformation greatly influences user comfort and signal fidelity in wearable biomedical devices [9], while precisely controlled contact mechanics are vital for soft robotic end-effectors to effectively execute delicate manipulation tasks [11–13]. Hence, understanding and controlling these deformations are critical for ensuring device robustness and reliability.

Despite extensive applications, precisely understanding and controlling interfacial behaviors of polymer-based soft interfaces remains challenging. The challenge arises primarily from the inherent complexity of polymer, including the nonlinear viscoelasticity, multiscale mechanical responses, and structural heterogeneity. Variations in internal polymer structure, such as crosslink density and free polymer chain content, fundamentally influence mechanical properties, including Young's modulus, energy dissipation, adhesion, and solvent sensitivity. Moreover, when metallic coatings are deposited onto polymer substrates, additional mechanical constraints are introduced, altering surface energy and modifying interfacial stress distributions, further complicating deformation behaviors. Consequently, a holistic

understanding of interfacial deformation behaviors in these bilayer systems demands integrated analyses of how internal polymer structure and external surface coatings collectively influence mechanical responses.

Theoretical contact modes and experimental characterization techniques are essential tools for investigating contact behaviors of soft polymer interfaces. Classical contact theories, including Hertz [14], Johnson-Kendall-Roberts (JKR) [15], Derjaguin-Muller-Toporov (DMT) [16], and Maugis-Dugdale (MD) [17] models, have been widely applied to polymer interface studies. However, these models typically rely on assumptions such as linear elasticity, isotropy, idealized geometry, and semi-infinite substrate thickness, significantly limiting their accuracy and applicability when film thickness is reduced to micro- or nanoscales, or when materials exhibit nonlinear viscoelasticity [18] and time-dependent responses [19]. Moreover, these theories usually depend on predefined material parameters (e.g., elastic modulus, surface energy), which can substantially vary upon surface modifications such as nanoscale metallic coatings. Therefore, a crucial research challenge is developing methods capable of capturing micro- or nanoscale deformation without extensive reliance on predefined material parameters.

While parameter-independent approach offers new avenues for interface research, the accurate measurement of material properties remains essential. Especially, polymer surfaces modified by nanoscale metallic coatings undergo significant changes in properties, including elastic modulus, surface energy, and effective refractive index. However, existing experimental methods often struggle to simultaneously measure these evolving properties within a single experimental framework. Conventional mechanical characterization methods, such as nanoindentation and atomic force microscopy (AFM), provide valuable insights on mechanical properties but face limitations probe-substrate interactions, especially for soft materials at reduced scales. Similarly, optical characterization methods, such as ellipsometry, although capable of precisely measuring refractive index, generally require complex experimental procedures and iterative parameter fitting. These limitations impede a comprehensive understanding of how fundamental interfacial properties evolve upon metallic

coatings, constraining deeper insights into interfacial deformation mechanisms. Besides, for ultra-soft polymeric materials, capillary interactions at interfaces increasingly dominate and significantly influence contact deformation behaviors [18]. Specifically, depositing metallic thin films onto softer polymer substrates leads to distinct, complex deformation responses compared to their stiffer counterparts. Currently, the underlying mechanisms driving these distinctly different deformation behaviors are not fully elucidated, necessitating systematic experimental and theoretical exploration.

Moreover, in polymer systems with larger amounts of free polymer chains, solvent treatment often induces spontaneous surface pattern formation. Upon swelling, soft films supported on rigid substrates develop spatial gradients in elastic modulus and compressive stress, decreasing from the surface towards the substrate, which can lead to buckling, wrinkling, or delamination [20–25]. Previous studies primarily focused on characterizing these final surface morphologies. Further studies are required to clarify how interactions between free polymer chains and solvents govern the evolution of interfacial morphology.

Therefore, this dissertation aims to investigate the interfacial behavior of polymer and metal-polymer thin films under two distinct conditions: mechanical contact and solvent-induced stimuli. The primary focus is on contact deformation behaviors under external loading, while the secondary theme, addressing solvent-induced morphological evolution, extends this study by investigating how the free polymer chains affect interfacial instability and pattern formation. These two complementary investigations provide a multiscale understanding of how internal structure and external stimuli collectively govern the mechanical response and morphological transformations in soft thin film system.

Guided by this objective, the dissertation addresses four interrelated scientific questions:

Q1: *How can we characterize the contact deformation of polymer thin films without relying heavily on predefined material parameters?*

Q2: *How does nanoscale metallic coating deposition (e.g., Au, Ag) influence the mechanical and optical properties of polymer thin films, and how can these changes be measured?*

Q3: *How does nanoscale metallic coating deposition influence the contact behavior of polymer thin films with less crosslink density or high free polymer chains fraction?*

Q4: *How does solvent-induced extraction of free polymer chains influence the mechanical response and surface morphology of polymer thin films?*

1.2 Methodological Framework

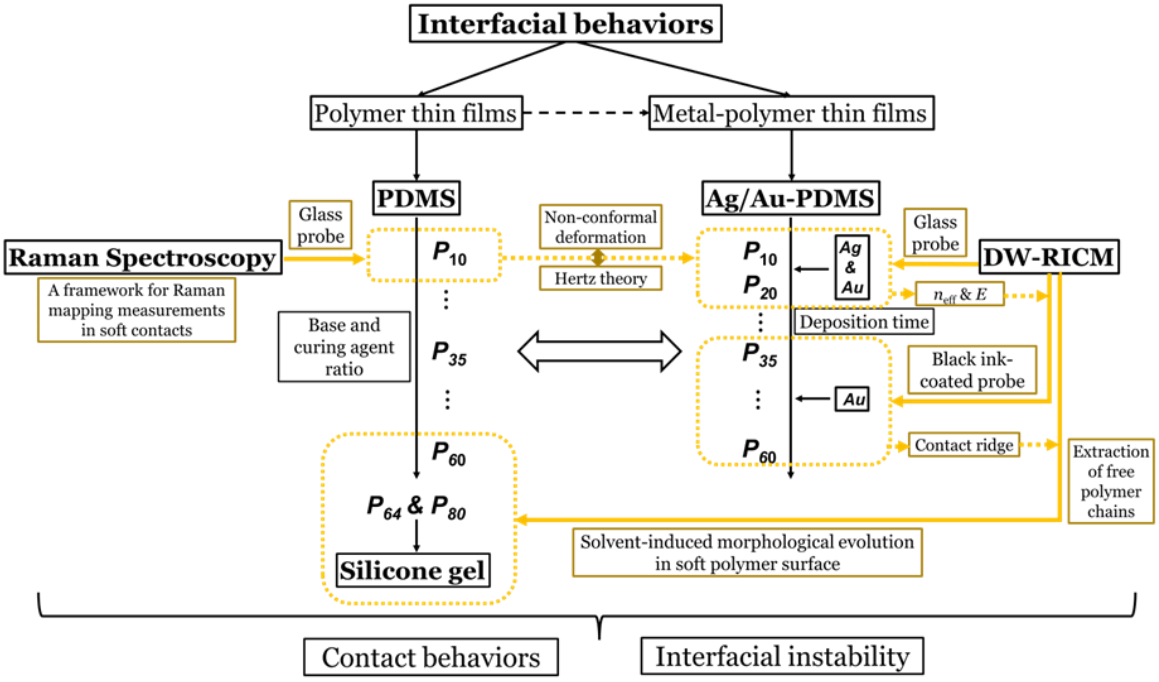


Figure 1-1 The methodological framework of the research objective. P_{10}, P_{35}, P_{60}, P_{64}, and P_{80} represent PDMS formulations with differing base-to-curing-agent ratios of 10:1, 35:1, 60:1, 64:1, and 80:1, respectively. DW-RICM: Dual-wavelength reflection interference contrast microscopy. n_{eff}: effective refractive index. E: Young's modulus.

To address the four questions outlined above, Polydimethylsiloxane (PDMS), a widely used silicone-based elastomer, was selected due to its high optical transparency in the visible

spectrum, strong infrared absorption, chemical inertness, solvent uptake capability, and excellent biocompatibility [26,27]. By varying the base-to-curing agent ratio, PDMS thin films with tunable elastic moduli and controllable fractions of free polymer chains were fabricated to represent different structural conditions. Additionally, gold (Au) and silver (Ag) thin film were deposited onto PDMS substrates via sputter coating, creating representative metal-polymer bilayers to investigate the effects of metallic surface modifications. Two advanced characterization techniques, confocal Raman spectroscopy and dual-wavelength reflection interference contrast microscopy (DW-RICM), were utilized to capture complementary aspects of interfacial behavior. Raman spectroscopy provided molecular-level insights into chemical and structural changes within the polymer thin films during deformation, while DW-RICM enabled real-time, high-resolution visualization of interfacial deformation and morphological evolution. Figure 1-1 illustrates the logic and methodological framework underlying the research objective. The experimental framework was structured into four sequential stages, each carefully designed to address one of the questions, progressively building complexity and depth:

Firstly, to establish a parameter independent methodology (Q1), fully crosslinked PDMS films (base-to-curing-agent ratio of 10:1, denoted as P_{10}) with minimal free chains were selected and brought into contact with a glass sphere as the simplest model system. The contact deformation behavior under external loading was characterized using confocal Raman spectroscopy. Changes in Raman peak intensities provided quantitative measures of localized deformation without relying on predefined mechanical parameters. Secondly, building upon this foundational understanding, metallic coatings of Au or Ag were deposited onto relatively stiff PDMS films (P_{10} and P_{20}) to systematically investigate how these coatings influence fundamental properties such as elasticity and effective refractive index (Q2). DW-RICM was employed to simultaneously capture mechanical deformation and optical changes under contact, revealing fundamental properties variations induced by metal coatings. Thirdly, the investigation extended to softer PDMS substrates with higher fractions of free polymer chain

(P_{35}, P_{45}, and P_{60}), exploring how substrate softness and metallic coatings collectively influence deformation behavior (Q3). By employing DW-RICM in conjunction with black ink-coated probe to eliminate unwanted reflections, subtle yet significant interfacial phenomena such as time-dependent contact ridge formation was characterized. Finally, advancing complexity further, PDMS films containing significant amounts of free polymer chains (P_{60}, P_{64}, P_{80}, and silicone gel) underwent solvent extraction and drying (Q4). This treatment induced complex morphological instabilities, and DW-RICM tracked the real-time evolution of these spontaneous patterns. Comparative analysis across different compositions provided new insights into the dynamic interplay between free polymer chains, solvent interactions, and morphological evolution.

1.3 Structure of the Dissertation

This dissertation is organized into seven chapters as follows:

Chapter 1 (the present chapter) outlines the general motivation, methodological framework and structure of this dissertation.

Chapter 2 reviews classical contact theories, current characterization techniques for soft contact, and briefly introduces the techniques used in this dissertation: confocal Raman spectroscopy and DW-RICM.

Chapter 3 addresses Q1 by developing a parameter-independent Raman mapping method using Raman spectroscopy to characterize contact deformation in polymer thin films.

Chapter 4 addresses Q2 by combining the DW-RICM with a glass probe of know profile to simultaneously measure the effective refractive index and elastic moduli of metal-polymer bilayer films.

Chapter 5 addresses Q3 by combining the DW-RICM with a black ink-coated glass probe to characterize the contact ridge and time-dependent deformation behaviors of metal-polymer bilayers.

Chapter 6 addresses Q4 by investigating the time-dependent evolution of patterns in solid-supported soft thin films subjected to solvent extraction using DW-RICM.

Chapter 7 concludes the dissertation by summarizing the key findings and proposing potential directions for future research in soft contact and solvent-induced patterning.

Chapter 2

Literature Review

2.1 Introduction

This chapter reviews the classical and extended contact theories, recent characterization techniques in soft contact, and introduces confocal Raman spectroscopy and DW-RICM, the primary techniques used in this dissertation.

2.2 Contact theories and existing findings in soft contact

Classical contact theory, first established by Heinrich Hertz in 1882 [14], was formulated under a set of idealized assumptions: linear elasticity, infinitesimal deformations, frictionless contact, and the absence of adhesion. It provides analytical solutions for elastic contact configurations, including sphere-on-sphere and sphere-on-flat (Figure 2-1). For a rigid sphere of radius R_1 and Young's modulus E_1 indenting a compliant elastic half-space of radius R_2 and Young's modulus E_2 under a normal load F, the contact radius a_H is given by:

$$a_H{}^3 = \frac{3FR^*}{4E^*} \tag{2-1}$$

where R^* is the effective radius ($1/R^* = 1/R_1 + 1/R_2$) and E^* is the reduced modulus ($1/E^* = (1-\vartheta_1^2)/E_1 + (1-\vartheta_2^2)/E_2$), ϑ_1 and ϑ_2 are the Poisson's ratio of the two contact bodies, respectively.

With the growing interest in soft, adhesive materials, Johnson, Kendall, and Roberts (1971) [15] formulated the JKR theory, extending Hertzian theory by incorporating the work of adhesion into the contact description. The contact radius a_{JKR} is given by:

$$a_{JKR}{}^3 = 3R^*\left(F + 3\pi wR^* + \sqrt{6\pi wR^*F + (3\pi wR^*)^2}\right)/4E^* \tag{2-2}$$

where w is work of adhesion per unit area, related to the surface energies of the two contacting bodies. Using monochromatic reflection interference microscopy, they quantitatively

measured the contact radius and indentation depth between a rubber sphere and a rigid substrate and reported a finite contact area even under zero applied load, attributable to surface energy. Hysteresis between the loading and unloading curves was also observed, indicating energy dissipation associated with adhesion. These findings validated the JKR model and demonstrated the value of optical interferometry in resolving contact deformation, a technique that remains essential in today.

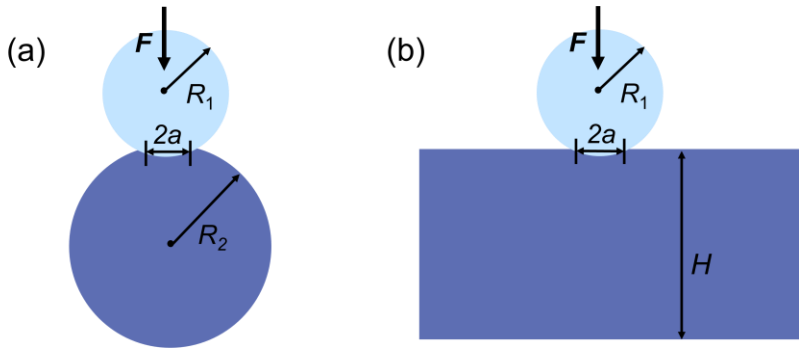


Figure 2-1 Schematic of representative contact of elastic solids with the contact radius a under the preload F. (a) Solid sphere on solid sphere with different radius, R_1 and R_2, respectively. (b) Solid sphere on solid semi-infinite substrate. The underlying substrate has a thickness H larger than the radius R_1.

However, the assumption that adhesion acts within the contact area and modifies the stress field does not hold in all material systems. In stiff or weakly adhesive contacts, adhesion is better described as acting outside the contact zone. The Derjaguin, Muller, and Toporov (i.e., DMT theory) (1975) [16] assumed that adhesion contributes only as an external surface force acting at the edge of contact and predicted the contact radius a_{DMT} as:

$$a_{DMT}{}^3 = 3R^* (F + 4\pi w R^*)/4E^* \qquad (2\text{-}3)$$

Notably, its practical relevance grew significantly with the advent of atomic force microscopy (AFM), where it proved valuable for interpreting nanoscale tip-sample adhesion in high stiffness, low adhesion systems [28]. Nevertheless, many real soft contact systems exhibit intermediate behavior between the JKR and DMT. To capture this transitional behavior, the Maugis-Dugdale cohesive zone model (i.e., MD model) (1992) [17] defined a finite adhesive

region, where adhesive stresses act over a finite range, and introduced the Tabor parameter $\Lambda = \left(R^* w^2/(E^{*2} z_0{}^3)\right)^{\frac{1}{3}}$, z_0 is the characteristic range of surface forces, i.e., the cohesive zone range. For van der Waals/Lennard-Jones–type interactions, z_0 is typically 0.157 nm [29–31]. The parameter Λ governs the transition between limiting cases: $\Lambda \gg 1$ approaches the JKR limit, while $\Lambda \ll 1$ corresponds to DMT behavior. It provides a physically consistent framework but often requires numerical computation. To address this limitation, Carpick, Ogletree, and Salmeron (1999) [32] proposed an empirical formulation (i.e., COS model), which allows a smooth transition between the two regimes using a dimensionless empirical parameter ϖ . The model expresses the contact radius as: $a(\varpi, F) = a_{F=0}(\varpi)\left[\alpha + \sqrt{1 - F(1+\varpi)/(F_c\,(\varpi)\,)}\right]^{\frac{2}{3}}$, where $a_{F=0}(\varpi)$ is the contact radius at zero load and $F_c(\varpi)$ is the critical pull-off force. The model recovers the JKR limit when $\alpha = 1$ and approximates the DMT limit $\varpi = 0$. Subsequent theoretical analysis by Schwarz (2003) [33] independently validated the model, demonstrating its consistency with classical contact mechanics. Owing to its computational simplicity, the COS model has become a practical tool for fitting force-displacement data in nanoscale contact scenarios, particularly in AFM tip-sample systems involving both soft and stiff materials [28,34].

While above classical and extended contact models provide the foundational framework for analyzing stress fields and adhesive interactions in soft contact systems, under the idealized assumptions of semi-infinite linear elastic substrates (i.e., the ratio of the contact radius and film thickness, $a/H \approx 0$), instantaneous mechanical response, and spatial homogeneity. However, real soft materials often exhibit finite thickness (i.e., $a/H > 0$), viscoelasticity, structural heterogeneity etc., thereby necessitating further extensions. A classical framework for thin elastic layers on rigid substrates is the Winkler model (1867) [35,36], which described the elastic response under external loading. It assumes that 1): the substrate behaves as an array of independent vertical springs, leading to localized normal deformation without lateral coupling. The local stiffness is characterized by an effective modulus $k \approx$

$G(1-\vartheta)/H(1-2\vartheta)$, where $G = E/2(1+\vartheta)$ is the shear modulus of the elastic substrate, relating local pressure $q(x)$ to vertical displacement $\omega(x)$ via $q(x) = k\omega(x)$. Under this assumption, the indentation force and displacement exhibit a linear relationship: $F \approx kS\delta$, where $S = \pi a^2$ is the contact area. Several studies have explored the transition from Hertzian to Winkler responses as the layer becomes thinner [37–40]. The model transition occurs as follows: for *a/H* < 1 (thick elastic layers, small contact radius): the substrate has negligible influence, and Hertzian contact mechanics applies. For *a/H* > 1 (thin elastic layers, large contact radius): the substrate imposes a dominant influence, and a Winkler-type foundation better describes the response [39,40]. However, it has also been shown that the Winkler model breaks down for nearly incompressible materials (i.e., $\vartheta \to 0.5$) [39,41], as it neglects lateral coupling. In chapter 3 of this dissertation, we further confirmed this point.

Besides, to account for finite thickness effects, Shull et al. (1998 & 2002) [42,43] developed a linear elastic fracture mechanics framework for axisymmetric adhesive contact on thin compliant films. They identified the ratio *a/H* as a critical parameter, with validity in the range $0 < a/H < 5$. By introducing correction factors for load $f_p(a/H) = (1 + 0.33(a/H)^3)$, displacement $f_\delta(a/H) = (0.4 + 0.6\exp((-1.8a)/H))$, and compliance $f_c(a/H) = (1 + (0.75/((a/H + (a/H)\text{^}3)) + 2.8(1-2\vartheta)/(a/H))^{-1})^{-1}$, the modified Hertz equation in confined geometries: $F = 4E^*a^3(1 + 0.33(a/H)^3)/3R^*$ and the modified JKR equation becomes: $\delta_{JKR}{}' = a^2 f_\delta(a/H)/R^* + f_c(a/H)\left(F - 4E^*(a)^3 f_p\left(\frac{a}{H}\right)/3R\right)/2E^*$. The key assumptions, characteristics and application of above models are summarized in Table 2-1. This comparison highlights both the versatility and the limitations of classical and extended contact theories when applied to soft, thin film systems.

Table 2-1 Classical and extended contact theories. (a: contact radius, H: thickness of the soft substrate, ϑ: Poisson's ratio.)

Theory	Assumptions	Adhesion	Applicability	Limitations
Hertzian (1882) [14]	Linear elastic, frictionless, small deformation (a/H~0)	No	Stiff, non-adhesion	Ignores adhesion and viscoelasticity
JKR (1971) [15]	Short-range adhesion	Within contact area region	Soft, high adhesion	Not valid for viscoelasticity
DMT (1975) [16]	Long-rang van der Waals force	Outside contact area region	The indenting sphere with smaller radii of curvature	Overestimates pull-off force in soft systems
MD (1992) [17]	Finite adhesive zone, cohesive stress	Cohesive zone	Transitional cases	Requires numerical solution
COS (1999 & 2003) [32,33]	Adjustable parameter	Empirical interpolation	Nanoscale system	Limited physical basis
Thin Film Corrections (1998 & 2002) [42,43]	Finite thickness effect	Optional	Thin soft film ($0 < a/H < 5$)	Linear elastic base
Winkler (1867) [36]	Localized normal deformation without lateral coupling	No	Thin films	Not valid for incompressible materials (i.e., $\vartheta \rightarrow 0.5$)

Recent work by Kim et al. (2022) [44] has shown that the Hertzian theory can extend beyond its classical assumption of $a/H \ll 0$ and still provides valid predictions for glass-elastomer systems even when the ratio of contact radius to film thickness is as large as $a/H \approx 3.5$. In contrast, when the system involves a glass-gel contact with much larger confinement ratios ($a/H \approx 14$ - 18), neither the Hertzian nor the JKR theory, nor even modified JKR theory incorporating confinement effects, were able to capture the observed contact mechanics. Using DW-RICM, the authors reconstructed the time-dependent evolution of the gel surface,

revealing two key features: (i) the formation of capillary-induced ridges at the contact boundary and (ii) the phase separation of liquid components from the gel network. These observations highlight the inadequacy of existing elastic and adhesive contact theories for describing gel-based systems and emphasize the crucial role of capillarity and liquid migration in governing long-term interfacial mechanics. Actually, the role of capillarity in soft contact was systematically investigated by Style et al. (2013) [18], who used confocal microscopy to study the adhesion of microspheres on soft silicone substrates. They demonstrated that when the contact radius falls below a critical elastocapillary length scale, the JKR theory break down, and surface tension dominates the contact behavior, leading to an interface geometry and force balance analogous to particle adsorption at fluid interfaces.

These observations not only highlight the limitations of classical and modified contact models in capturing complex deformation behaviors in soft materials but also underscore the indispensable role of advanced characterization techniques in revealing phenomena that lie beyond the predictive scope of existing theories. The synergy between advanced experimental methods and theoretical analysis proves essential for refining our understanding of soft contact mechanics.

2.3 Existing characterization techniques and findings for Soft Contact

The development of soft contact mechanics has been deeply integrated with the evolution of experimental characterization techniques. Early works using optical interference microscopy enabled direct visualization of the contact interface, providing key validation for the JKR theory [15]. Subsequently, AFM introduced nanoscale force-displacement measurements, crucially supporting validation of DMT and MD models [28,34].

Indentation-based methods remain central for investigating mechanical properties at interfaces, facilitating the measurement of elastic modulus, adhesion energy, and viscoelastic behavior [45–47]. AFM, popularized in the 1990s, offers exceptional spatial resolution; its accuracy heavily depends on parameters such as probe geometry, indentation depth, and

chosen theoretical models [48]. Despite its precision, AFM faces limitations from substrate effects, probe variability, and unresolved nanoscale interactions, particularly challenging when characterizing softer films and interfaces governed by capillary forces [28,34,48].

These limitations have prompted a shift toward imaging and visualization-based techniques that enable observation of interfacial deformation. For example, SEM was first used in 1989 to measure adhesion-induced contact radii of microspheres on polyurethane substrates (Figure 2-2(a)) [49]. Later, SEM facilitated studies of meniscus shapes and deformation mechanisms at elastomeric interfaces [50]. More recently, confocal microscopy emerged as a powerful tool for capturing detailed interfacial geometries [18,51]. Style et al. (2013) [18] utilized confocal microscopy to explore transitions from classical JKR-like adhesion mechanics to surface tension-driven behavior in soft substrates (Figure 2-2(b)). Additionally, Pham et al.[52] combined colloidal probe AFM with confocal microscopy, uncovering limitations of the traditional JKR theory in interpreting low-modulus interfaces dominated by capillary forces, leading to the proposal of modified theoretical frameworks (Figure 2-2(c)). Confocal fluorescence microscopy has also significantly advanced the field by enabling visualization of internal deformation and phase separation through embedded tracers [51–55]. For example, Glover and Pham [53] demonstrated how varying thicknesses of silicone oil layers affect indentation mechanics, transitioning from solid-like adhesion to capillarity-dominated interactions (Figures 2-2(d)). Similarly, high-resolution transmission X-ray microscopy provided insights into wetting ridge formations with nanoscale resolution, emphasizing the role of capillary phenomena over elastic responses in governing ridge tip mechanics [56] .

While these advanced visualization techniques effectively capture macroscopic and mesoscopic deformation phenomena such as contact ridges [44,52,57] or phase separation [54,58], they often fall short in resolving finer-scale, sub-surface deformations, particularly in thin films or stiffer soft materials. Such localized, micro- to nanoscale deformations characterized by sharp geometric transitions [59–61]. Therefore, specialized techniques have been developed. For instance, Acito et al. [62] developed an in situ X-ray computed tomography for volumetric, non-

destructive characterization of soft contact interfaces, overcoming transparency and resolution barriers inherent in optical methods (Figures 2-2(e)). Zou et al. [60] introduced an optical tactile sensing technique to quantitatively assess soft surface deformation under contact conditions (Figures 2-2(f)-(g)).

Despite numerous new characterization methods, many remain limited by insufficient resolution, penetration depth, or incompatibility with multilayer composite materials. The specific advantages and disadvantages have been detailed later on in the thesis, in Chapters 3 and 5. To fully understand soft contact phenomena, especially in thin-film systems involving elastic, capillary, and adhesive forces, advanced techniques capable of simultaneously capturing chemical signatures and physical deformation at the micro- and nanoscales are thus needed. This warrants the development of tools with high spatial sensitivity, multimodal contrast, and compatibility with soft heterogeneous systems. Addressing these challenges, the following sections introduce Raman spectroscopy and DW-RICM, as techniques capable of offering molecular-level insights and nanoscale topographic mapping. Thus, providing new perspectives on deformation, adhesion, and interfacial mechanics.

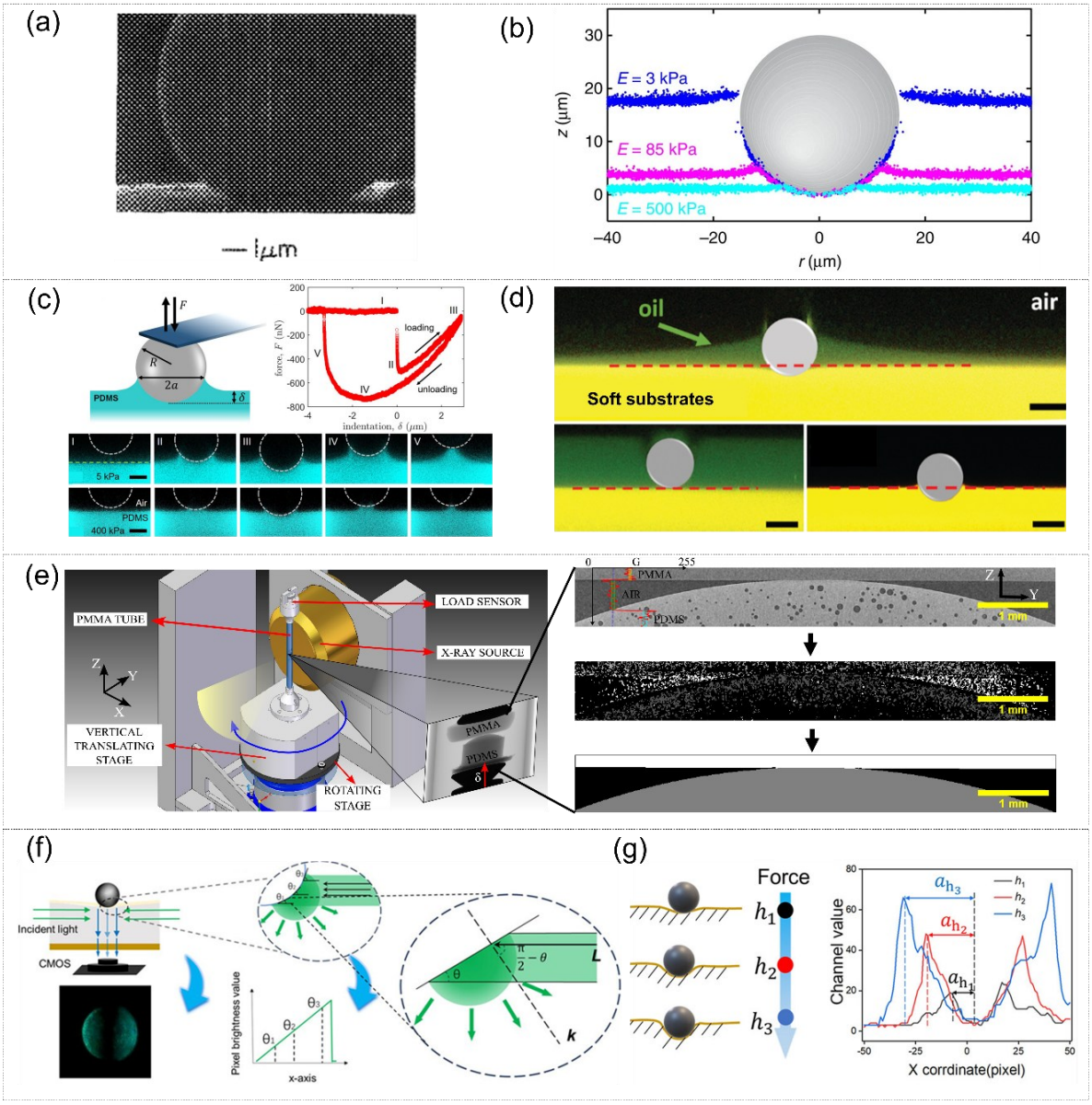


Figure 2-2 Characterization Techniques for soft contacts. (a) An SEM image of a polystyrene particle on a soft polyurethane substrate. The particle embed into the soft substrate, thereby creating a contact zone of radius. (Adapted from ref.[49] with permission. © 1989 AIP Publishing.) (b) Surface indentation profiles of soft solids under a spherical silica particles of radii 15 mm. Surface stiffness is 3 kPa (blue), 85 kPa (magenta), and 500 kPa (cyan) (Adapted from ref. [18] © 2013 Springer Nature Limited.) (c) Schematic of a colloidal probe in contact with a soft solid surface labeled with parameters of force *F*, contact radius a, indentation *δ*, and the particle radius *R*.

A representative force-indentation curve measured by AFM indentation on PDMS with E_{bulk} = 5 kPa and a maximum indentation depth $\delta \approx 2.8$ μm and corresponding cross-sectional confocal images obtained by confocal microscopy of the labeled points on the force-indentation curve. The green dashed line represents the interface between solid and air, which is determined by measuring reflection at the surface. The gray circle represents the spherical probe as a guide to the eye. The particle radius is R = 6.5 μm. Scale bars: 5 μm. (Adapted from ref.[52] with permission. © 2017 American Physical Society.) (d) Confocal images of indentation of a glass microsphere into soft substrates (yellow) with a thin oil layer (green), a thick oil layer, and no oil layer. Both the soft substrates and the oil were mixed with different fluorescent dye (Adapted from ref.[52] with permission. © 2017 American Physical Society.) (e) Schematic view of the compression device installed in the tomograph (left) and the segmentation process for extracting the contact area from an X-ray computed tomography image (right). The two bodies in contact are installed inside the compression device where a displacement can be imposed through a motorized vertical translating stage (not visible in the current image). While the materials are exposed to X-rays, the entire device rotates 360° to acquire projections (called radiographs) of the specimens at different angles. The inset on the right shows one of the radiographs collected during a scan at low resolution to visualize the two materials in contact with the upper and lower rods of the compression device. Here, the PMMA disk is fixed while the displacement is imposed on the PDMS specimen. (Adapted from ref. [62] with permission. © 2023 Elsevier Masson SAS.) (f) Schematic of the optical sensing system, the relation between surface deformation angle and reflected light. (g) Schematic of the sphere vertical contact PDMS with different depths and the corresponding distribution of irradiance of reflected light along the x-axis with different contact depths. ((f) and (g) adapted from ref.[60] with permission. © 2024 Wiley-VCH GmbH.)

2.4 Confocal Raman Spectroscopy: Principle and Applications in soft contact

The Raman effect was predicted by Smekal in 1923 [63] and experimentally observed by C.V. Raman in 1928 [64]. Using focused sunlight and later a filtered mercury-arc lamp (≈435 nm) to illuminate carbon tetrachloride (CCl_4), C.V. Raman observed shifted spectral lines indicative of inelastic scattering phenomena that earned him the 1930 Nobel Prize in Physics. It describes the inelastic scattering of photons due to interactions with molecular vibrations [65], as shown in Figure 2-3. When an incident photon of energy $h\upsilon_0$ (h: plank constant, 6.626×10^{-34} J · s; υ_0: frequency of incident photon) interacts with a molecule, it excites the molecule to a virtual energy state. If the molecule returns to its initial state, the scattered photon retains its energy ($h\upsilon_s = h\upsilon_0$, υ_s: frequency of scattered photon), resulting in Rayleigh scattering. However, if

the molecule gains energy, the scattered photon loses energy ($h\upsilon_s = h(\upsilon_0 - \Delta\upsilon)$), producing a Stokes line. Conversely, if the molecule loses energy to the photon ($h\upsilon_s = h(\upsilon_0 + \Delta\upsilon)$), an anti-Stokes line is observed. The shift in the energy of the scattered photon is called the Raman shift and is expressed in wavenumbers: $\Delta\upsilon = \nu_0 - \nu_s$ (cm^{-1}). Under ambient conditions, most molecules reside in the ground vibrational state, making Stokes scattering more probable than anti-Stokes scattering, following the Boltzmann distribution. As a result, Raman spectra typically show stronger Stokes lines symmetrically positioned alongside weaker anti-Stokes lines around the central Rayleigh peak. Therefore, Raman spectroscopy, provides a powerful, non-destructive method for probing vibrational energy levels and molecular structure by analyzing Raman shifts, characteristic peak positions, and relative peak intensities [66].

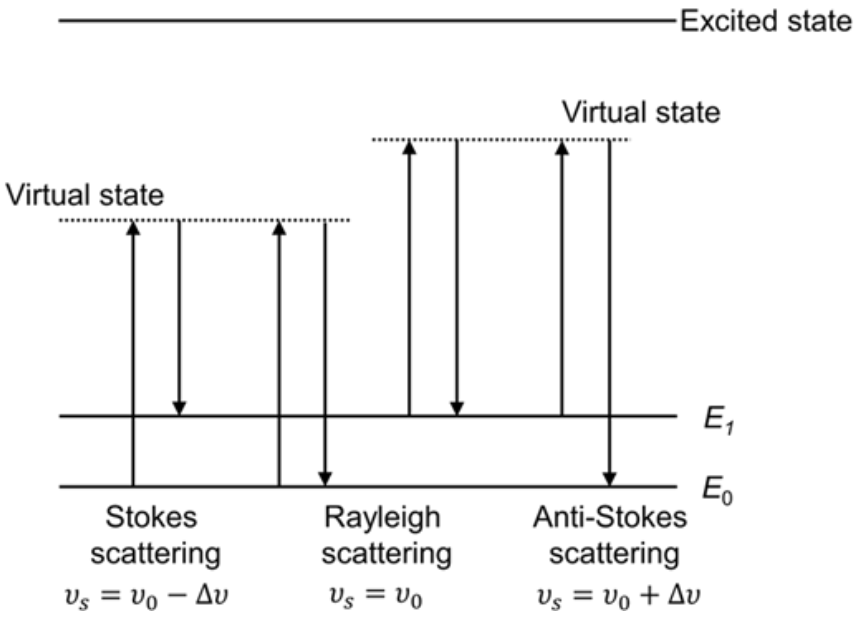


Figure 2-3 Schematic diagram for Rayleigh, Stokes and Anti-Stokes scattering. E_0: ground state. E_1: vibrational state.

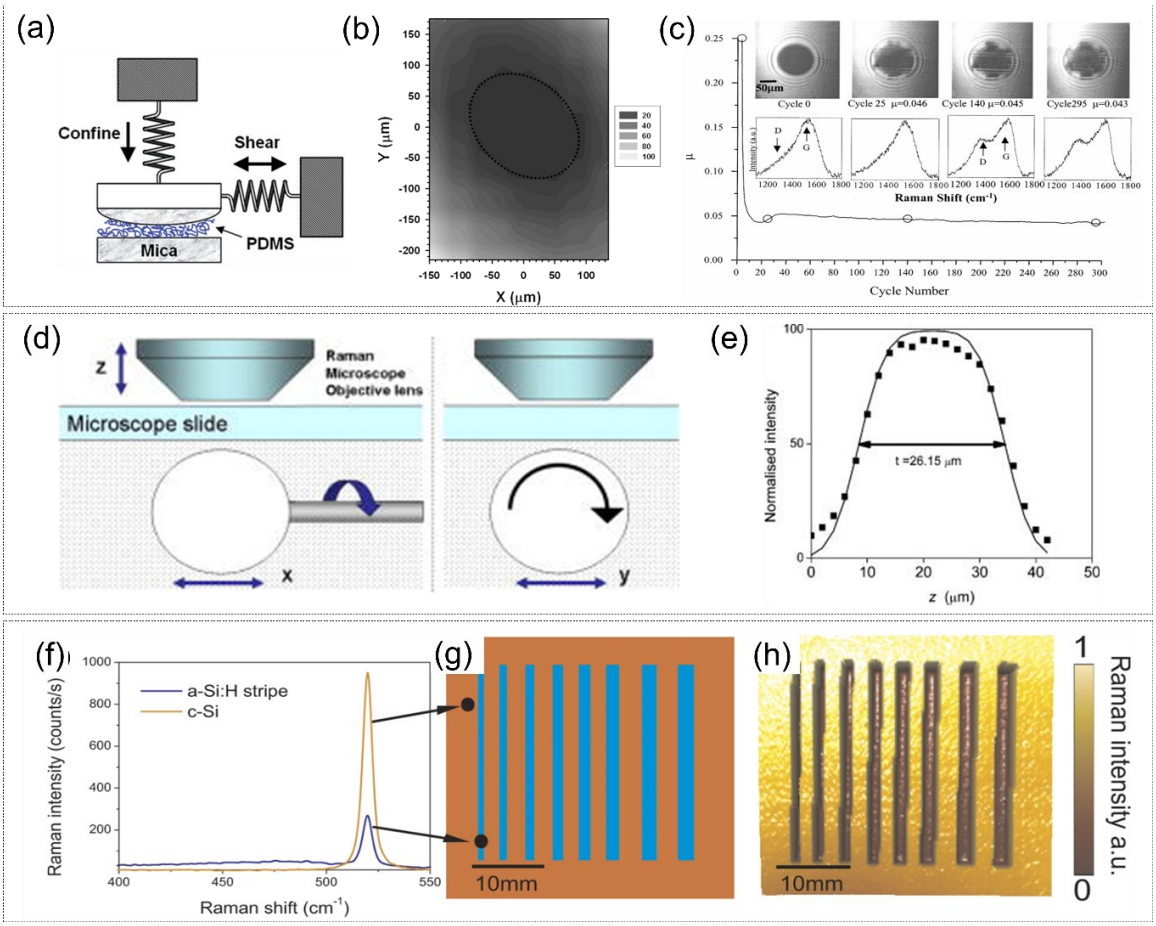


Figure 2-4 Representative applications of Raman spectroscopy in soft contact systems and thin film analysis. (a) Schematic of confocal Raman microscopy integrated with a surface forces apparatus (SFA) for in-situ analysis of confined PDMS films. (b) Corresponding Raman intensity map (2907 cm^{-1}) in the x–y plane at a confinement thickness of 3.5 nm. ((a) and (b) Adapted from ref.[67] with permission. © 2005 American Chemical Society.) (c) In-situ Raman spectra and images recorded during friction cycles of a glass hemisphere sliding against a Pb-Mo-S coating. (Adapted from ref.[68] with permission. © 2003 AIP Publishing.) (d) Schematic of the Raman-tribology setup (not to scale), showing side and front views of a rotating ball in contact. (e) Lubricant thickness profile along the z-axis, derived from normalized Raman intensity of the 1053 cm^{-1} glycerol peak. ((d) and (e) Adapted from Ref.[69] with permission . © 2008 AIP Publishing). (f) (g) and (h) Raman analysis of patterned a-Si:H on c-Si substrate shows spectral contrast, sample structure, and c-Si intensity mapping (505-535 cm^{-1}) for optical profilometry, respectively. (Adapted from ref.[70] with permission. © 2016 Springer Nature.)

Building on this principle, Raman spectroscopy has become an essential tool in materials science, chemistry, biology, and soft matter physics, owing to its non-invasive, label-free nature and molecular-level specificity. By scanning a laser systematically over the sample area, Raman mapping provides spatially resolved chemical imaging, revealing variations in local composition, molecular orientation, and structural dynamics with high spatial precision [71,72]. This capability is particularly useful in soft contact systems. For instance, Bae et al. [67] integrated confocal Raman spectroscopy with a surface forces apparatus (SFA) to image confined PDMS films (~3.5 nm thickness), demonstrating molecular alignment at interfaces (Figures 2-4(a) and (b)). Similarly, Singer et al. [68] used Raman spectroscopy to track friction-induced chemical transformations within glass/Pb-Mo-S interfaces (Figure 2-4(c)). While Bongaerts et al. [69] quantified lubricant film thickness in elastohydrodynamic lubrication through in-situ Raman imaging (Figures 2-4(d) and (e)). Additionally, Ledinský et al. [70] utilized Raman attenuation to measure amorphous silicon film thickness with submicron precision, even on optically rough substrates (Figure 2-4(f)-(h)). These studies highlight Raman spectroscopy's versatility as a powerful analytical and metrological tool, crucial for elucidating the coupled chemical and mechanical phenomena in soft interfaces under dynamic and confined conditions.

2.5 DW-RICM: Principle and Applications in soft contact

RICM was first introduced by Curtis in the 1960s [73] for observing the contact zone between living cells and substrates. Later, Ploen (1975) [74] enhanced it through the use of quarter-wave plates and central stops to improve contrast for biological specimens. It is a non-invasive optical technique that leverages interference between light beams reflected at interfaces with differing refractive indices. The resulting image intensity depends on the optical path difference, allowing visualization of the distance between the object and the reflective surface with nanoscale resolution. The detailed principles have been thoroughly described in Chapters 4 and 5.

Although conventional RICM achieves high axial resolution, it suffers from phase ambiguity due to monochromatic interference patterns, complicating quantitative height determination. Additionally, accurate interpretation typically requires prior knowledge of sample refractive indices and well-defined geometry, rendering quantitative measurements difficult in complex or dynamic systems. To address this, Schilling et al. [75] developed dual-wavelength RICM (DW-RICM), resolving phase ambiguity by simultaneously capturing interference patterns at two wavelengths, enabling precise, quantitative reconstruction of interfacial topographies. Another limitation was that the accuracy of distance (height) determination by RICM critically depends on the optical model used to relate image intensity to physical height. While numerous models have been developed [76,77], many require complex calculations or idealized geometries. The sophistication of the model often limits its widespread application. To address this, Theodoly et al.[78] extended a multilayer optical model by discretizing curved interfaces (e.g., spherical beads or vesicles) as a stack of infinitesimal horizontal steps and the glass slide/glucose solution/polystyrene bead system as a multilayer of parallel dielectric layers, enabling accurate height mapping in immersed, multilayer systems (Figures 2-5(a)-(c)). Although this method is an approximation, the advantage of this model is that the distance between the substrate and objective can be directly determined by the cosine transformation (simplifying calculations). Subsequently, Wiegand et al. [76] demonstrated DW-RICM's capability for height measurement with an accuracy of ~2 nm and absolute accuracy better than 5 nm within the first 100 nm.

The high spatial and temporal resolution of DW-RICM has facilitated numerous advances in soft contact systems where surfaces are compliant, deformable, or dynamically evolving. For example, Mitra et al. [57] use the DW-RICM to reconstruct the wetting ridge of a water droplet on a soft gel substrate (Figure 2-5(d) and (e)). Besides, Kim et al. [44] tracked contact ridge evolution in glass-gel-glass systems over extended periods (up to 258 hours). Further, Misra et al. [79] applied it to obtain the height profile and 3D topography of a condensed

microdroplet pinned on a substrate. These studies underscore DW-RICM's versatility and precision in characterizing complex interfacial phenomena in soft materials.

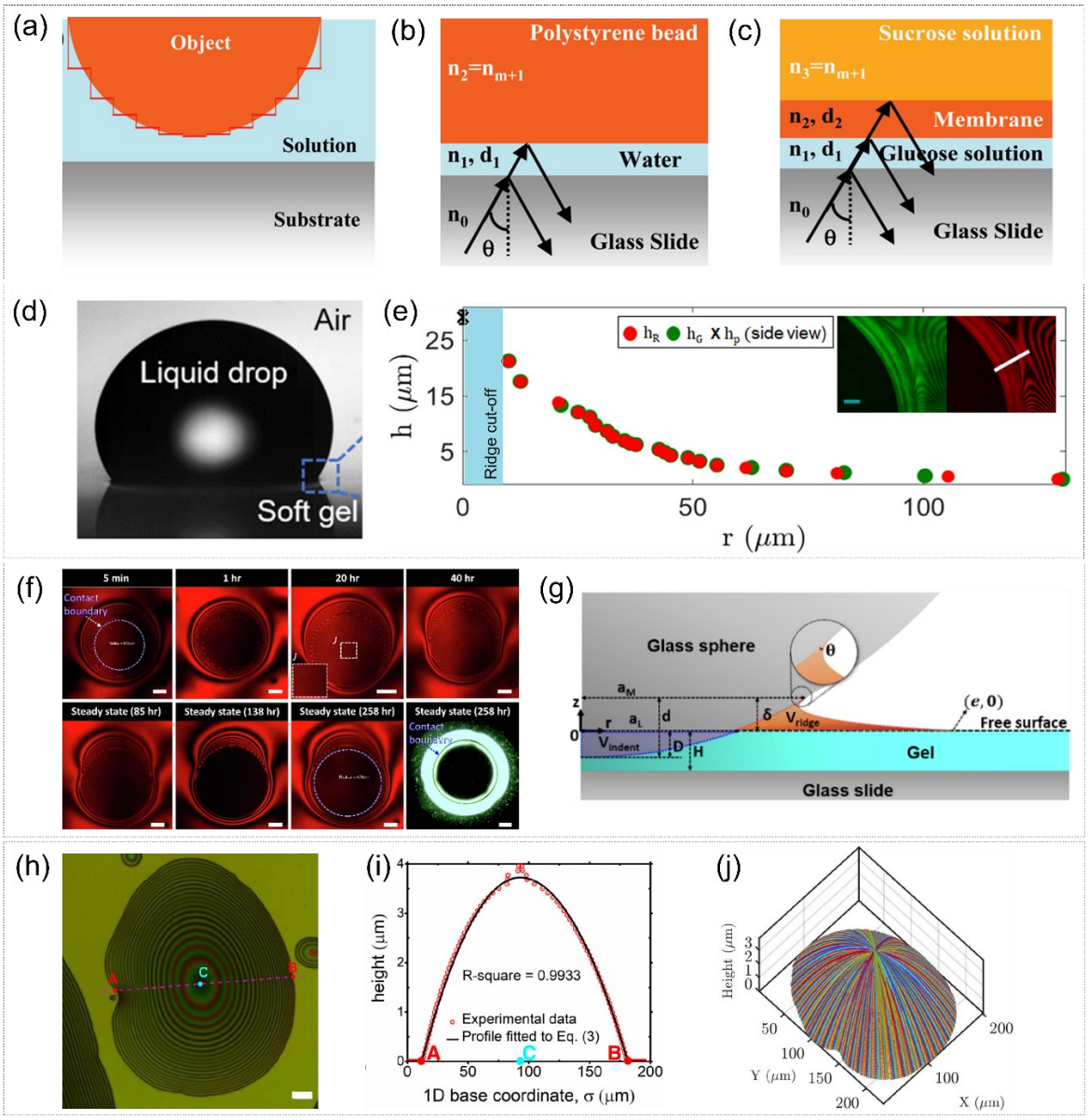


Figure 2-5 Representative applications of DW-RICM in soft contact systems and thin film analysis. (a) Schematics of the RICM model of an immersed object close to a substrate. The interfaces are assumed to be locally parallel. Optical multilayer model used for (b) a spherical polystyrene bead and (c) a vesicle settled on a glass substrate. ((a) (b) and (c) Adapted from ref. [78] with permission. © 2009 American Chemical Society.) (d) A

water drop on a soft gel coated glass surface. (b) The extracted wetting ridge profile for the water drop on soft gel from the intensity distribution along the white line shown in the interference signature (inset), scale bar: 50 μm. Red and green circles represent height extracted from intensity distribution of red and green wavelength, respectively. ((d) and (e) Adapted from ref.[57] with permission. © 2022 American Chemical Society.) (f) Interferograms of glass-gel (thickness: 35 μm)-glass contact at 5 min, 1 hr, 20 hrs, 40 hrs, 85 hrs (steady state), 138 hrs (steady state), and 258 hrs (steady state), and the optical microscopic bottom view of the contact area. Scale bar: 200 μm. (g) Schematics of the contact zone. V_{ridge} includes the volume of the phase-separated liquids and elastic network. ((f) and (g) Adapted from ref. [44] with permission. © 2022 Elsevier Inc.) (h) The experimental snap showing a pinned acetone microdroplet. AB is a randomly chosen vertical slice across the microdroplet of interest. Red dots labeled A and B indicate the locations of the droplet contact line, while the cyan dot labeled C indicates the projected location of the droplet apex on the base plane. Scale bar: 20 μm. (i) Reconstructed height profile of the droplet along the line AB (as shown in part h). (j) Reconstructed 3D topography of the entire droplet. ((h) (i) and (j) Adapted from ref. [79] with permission. © 2021 American Chemical Society.)

Chapter 3

In-situ Raman Spectroscopy for Soft Contacts

Contacting surfaces often experience deformations across multiple length scales. These deformations become particularly complex when one of the materials is soft, such as elastomers. Elastomers are widely used in flexible electronics and intelligent interactive systems, where their surface deformability facilitates the acquisition of multimodal physical information. Therefore, precise identification and effective monitoring of soft contact deformation are crucial. Despite the significant physical insights provided by existing imaging and theoretical tools, inherent approximations affect their precision and granularity. We hypothesize that mapping chemical (molecular) signatures could be a promising approach, as these deformations often originate from molecular properties. In this work, we aim to uncover the physical and chemical signatures of soft contact deformation using in-situ confocal Raman spectroscopy. We first assembled a calibration experimental setup consisting of five spherical glass probes of equal radius that are fixed onto a glass substrate, with an additional glass substrate placed on top. The four glass spheres placed at the corners provide support, while the contact of the central glass sphere with the upper glass substrate is used for measurements. This calibration experiment established the workflow for subsequent Raman mapping measurements. Next, we replaced the upper glass substrate with a PDMS-coated glass substrate, allowing the PDMS layer to contact the central glass sphere and undergo contact deformation. Due to the optical path of a typical Raman spectroscope, an inverted contact configuration was necessary. We then conducted systematic Raman mapping measurements in the x, y, and z directions in and around the contact region of interest. By analyzing the intensity of the 2905 cm^{-1} Raman peak of PDMS, we developed a framework to generate Raman contour maps at different imaging planes. Such Raman mapping embeds crucial chemical signatures of the system that translates into tangible physical insights. Tracking the variation in the relative intensity of the 2905 cm^{-1} Raman peak of PDMS within the contour maps enabled us to monitor

the spatial variation of the contacting interfaces at different vertical planes. In doing so, it allowed us to extract physical parameters like contact radius and indentation depth as well as confirm the non-conformal nature of contact deformation. Our experimental findings showed good agreement with the Hertz theory, although we observed subtle deviations indicating localized inhomogeneities at the contacting interfaces.

3.1 Introduction

Soft materials, which occupy a unique space between ideal solids and fluids [80], have gained prominence across various industries due to their highly tunable mechanical properties, superior adhesion, easy deformability to suit specific applications, and biocompatibility. Upon integration with complementary materials like metal thin films, metal oxides, textiles, and 2D materials, these materials unlock physical and chemical signatures with significant potential in advanced applications, such as soft self-contained grippers [81], Janus on-skin electronics [82], soft-touch panels [83], soft bio-scaffolds [84], and soft bionic robots [85]. In many of these applications, the soft materials inevitably come into contact with other materials and undergo deformations at micro- and nano-scales. However, the contact deformation of soft materials is a complex process, governed by an interplay of factors including their mechanical properties [15–17,86,87], adhesion characteristics [15–17,87], thickness [42,43,88], shape and dimensions of the contact pair [59,89–91], surface roughness [92,93], and chemical composition. Understanding these variables is essential for optimizing performance across various applications. For instance, in interface-dominated fields such as intelligent interactive systems, analyzing physical deformation signatures at soft interfaces enables the decoupling of external stimuli, such as pressing, twisting, and sliding, thus facilitating advanced human-machine interactions [94–98]. However, to understand these signatures, we mostly rely on a fixed set of imaging tools and theoretical models.

Classical contact mechanics theories, such as Hertz theory [14], Johnson-Kendall-Roberts (JKR) theory [15], Derjaguin-Muller-Toporov (DMT) theory [16,87], Maugis-Dugdale (MD)

theory [17] as well as Boussinesq model [89] and Winkler's mattress model [90], have been extensively employed to predict the contact behavior of soft materials. Each theory operates under distinct assumptions about the mechanical interactions involved. These models and their subsequent refinements [42,43,59,88–91,93,99,100] rely heavily on accurate knowledge of key material parameters such as Young's modulus, contact radii, and work of adhesion to select the most appropriate theoretical framework.

To experimentally validate these theories, a range of imaging or visualizing techniques, such as scanning electron microscopy (SEM) [49,50], confocal microscopy [101,102], confocal fluorescence microscopy [51,52,54,55,58], X-ray imaging [56,62], Dual-Wavelength Reflection Interference Confocal Microscopy (DW-RICM) [19,57,103–107] as well as optical tactile sensing system [60,108] are commonly employed (Table 3-1). However, each technique has its benefits and limitations. For instance, SEM provides high-resolution (~1 nm) imaging, but it poses challenges for soft matter insulators like elastomers due to sample charging and radiation damage [109]. These issues arise from the electron emission principle of SEM, requiring careful adjustment of beam energy and dose [109,110]. Confocal microscopes enable deliver high-resolution (~ 200 nm) and high-contrast images by precise localization and focusing on specific regions of a sample. Additionally, it is feasible to scan the sample incrementally and reconstruct a three-dimensional image through optical sectioning techniques. However, as with confocal fluorescence microscopy, it is often combined with dyes or fluorescent particles to avoid strong scattering beyond the limitation of the instrument [111,112], which may alter the intrinsic properties of soft materials being studied. Reflex optical sensing relies on CMOS image sensors to capture optical variations on the elastomer surface and integrate deep learning to improve classification accuracy. Advantages include high spatial resolution, non-contact measurement, and high sensitivity to subtle deformations, making it well-suited for soft-touch sensing and interactive applications. However, there are also limitations: sensitivity to lighting conditions, limited capability for high-speed motion detection, potential occlusion issues in multi-contact scenarios, and computational demands associated with deep learning processing

[60,108]. X-ray Computed Tomography (XRCT) operates by transmitting X-rays through a sample, capturing multiple radiographic projections at different angles, and reconstructing a three-dimensional volume using computational algorithms, enabling non-destructive visualization of internal structures and surface deformations even for non-transparent materials. However, its resolution sensitivity, imaging artifacts, and slow acquisition limit real-time applications, requiring further improvements in resolution and imaging speed [62]. DW-RICM is a powerful technique in capturing high-resolution imaging and extracting absolute height values of micro-nano scale surface undulations by analyzing the interference signatures of the incident light and the reflected light from the interfaces of interest. The limitation lies in the lateral resolution of objective lenses used, making it less effective for highly curved or steep contact geometries [19,57,79,103,104,113]. Furthermore, our previous work has shown that using glass probes in DW-RICM can introduce interference artifacts, complicating the analysis of soft contact deformations [103].

The majority of the existing imaging techniques are optimized for observing relatively larger deformations, such as the formation of contact/wetting ridges [19,52,103] and phase separation phenomena [52,54,58]. However, for materials with relatively higher elastic moduli, contact deformations are often subtle, manifesting as wedge-shaped or Hertzian or Winkler deformation profiles [59–61] near the contact interface with rapidly changing slopes and non-conformal contact geometries. Such features are often manifested due to changes at a molecular scale, such as changes in a group of carbon rings, methyl chains or polymer backbone [67]. Therefore, it is crucial to develop a novel technique capable of capturing chemical signatures and simultaneously provide information on physical parameters involving contact deformation at the micro-nano scales, without prior knowledge of the material properties e.g., shape and dimensions of the probe, elastic modulus of the probe and soft substrate, etc. A dual physical and chemical mapping will ensure a more granular understanding of soft contact mechanics, enable precision and cost-effectiveness, and offer high operational flexibility.

Table 3-1 Imaging techniques for visualizing soft contact deformation of elastomer film. (*R*: Radius of the probe; *E*: Elastic modulus of the soft substrate; *H*: thickness of the soft substrate. Resolution implies spatial resolution: instrument-defined (confocal microscopy, XRCT, Raman) or extracted (DW-RICM).)

References	Probe	Substrate	Instrument	Resolution
R. W. Style, et al. (2013) [18]	Glass sphere (*R*: 3-30 μm)	Silicone elastomer (Sylgard 184, *E*=85, 250 and 500 kPa, *H*:70-72 μm) and silicone gel (CY 52-276 A/B, *E*=3 kPa, *H*:150 μm)	Confocal microscopy	0.3 - 2 μm
Z. Zou et al. (2024) [60,108]	Sphere (*R*: 2, 3, 4mm)	Silicone elastomer (Sylgard 184, 10:1) with a thin layer of white propylene on top	Reflex optical sensing	20 μm
F. Zhao et al. (2024) [103]	Black ink coated glass sphere (*R*: 2615 μm)	Silicon elastomer (Sylgard 184 10:1/45:1/60:1, *H*:30-35 μm) coated glass slide	Dual-wavelength refractive interference confocal microscopy (DW-RICM)	0.09μm (488nm) / 0.15μm (561nm)
V. Acito et al (2023) [62]	Silicon elastomer (Sylgard 184 20:1) hemisphere (*R*: 9.42 mm) mixed with hollow micrometric glass beads)	Poly(methyl methacrylate) PMMA plate	X-ray Computed Tomography (XRCT)	3.3 μm
Current work	Glass sphere (*R*: 2600 μm)	Silicon elastomer (Sylgard 184 10:1, *E*:1.62 MPa, *H*:30-35 μm) coated glass slide	Raman Spectroscopy	0.78 - 10 μm

Raman Spectroscopy is a particularly promising technique for chemical sensing that offers detailed insights into molecular vibrations, making it sensitive to molecular interactions and conformational changes. This non-invasive, label-free technique is renowned for its chemical specificity and is widely used across various disciplines. These applications range from biological and biomedical [114] to surface science [115,116], low dimensional nanostructures

[117], and chemical doping [118,119]. For instance, Raman spectroscopy has been instrumental in elucidating the structure and dynamical processes involving water molecules at the solid-liquid interface [116], investigating phase transition in aqueous polymer gels [120], and quantifying crystallinity in poly(p-phenylene terephthalamide) (PPTA) [121]. Other notable applications include understanding soft elastohydrodynamic tribological contacts [69], analyzing friction and wear of protective coatings [68], the thickness mapping of amorphous silicon in test solar cells [70], and chemical imaging of nano-scale thin film in a surface force apparatus [67].

In contrast to single-point Raman spectroscopy, which provides discrete chemical information at specific positions within a sample, Raman mapping integrates spatial information by scanning a region of interest with a laser [71,72]. Here, the laser spot scans the region of interest in preset step sizes, acquiring Raman spectra pixel by pixel. These spectra are then analyzed using chemometric techniques, resulting in high-precision structural and chemical information of the scanned region, displayed as a pseudo-color map. Such Raman mapping is particularly valuable for applications where the structure and dynamics of the molecular components of soft materials spatially vary, for instance, in confinement [122,123]. For example, existing literature has shown that when Polydimethylsiloxane (PDMS), a commonly used silicone-based organic polymer [124], is confined to a thickness of approximately 3.5 nm without shear, the Raman intensity of the methyl group becomes anisotropic in the x-y plane, indicating that the methyl chains preferentially orient parallel to the confining surfaces [67]. Furthermore, mapping across different vertical planes enables confocal Raman spectroscopy, which provides crucial physical and chemical signatures to differentiate between bulk and interfacial properties. For instance, it has been observed that in confined PDMS, the relative Raman peak intensity of the asymmetric (2967 cm^{-1}) to symmetric carbon-hydrogen stretch (2905 cm^{-1}) is enhanced compared to bulk PDMS [67]. Such findings underscore the significance of confocal Raman mapping as a tool for monitoring chemical (molecular) signatures at micro- or even nanoscales, especially under conditions of contact deformation.

In this work, we perform confocal Raman spectroscopy for a qualitative (chemical) and quantitative (physical) understanding of soft contact deformation. First, we unravel detailed chemical signatures of the contact interface between a glass probe and a soft PDMS substrate across different x, y, and z directions. Consequently, using that chemical signature, we provide valuable insights into the nature of the contact interface (conformal or non-conformal, homogenous or heterogeneous) as well as physical parameters like contact radius and indentation depths.

3.2 Experimental

3.2.1 Preparation of soft substrates

Soft substrates were fabricated by spin-coating silicone elastomer (PDMS) (Sylgard 184, Dow Corning) on freshly cleaned glass slides (Microscope slides, Sail Brand, dimensions: 38.1 mm × 25.4 mm ×1 mm) by controlling the volume of PDMS solution and spin-coating speed. The glass slides were thoroughly cleaned by immersing them in nitrohydrochloric acid for 1 hr and in boiling piranha solution until the solution cooled down to 22-24 ℃. Then, the glass substrates were thoroughly rinsed with DI water and ethanol three times and dried with N_2 gas before use. The PDMS solution was prepared by mixing component A (base: dimethylsiloxane oligomers with vinyl end groups (> 60 %), silica filler (dimethylvinylated and trimethylated silica, 30-60 %), tetra(trimethylsiloxy) silane (1-5 %) and ethylbenzene (< 1 %), and a platinum catalyst) and component B (crosslinker: a cross-linking agent (dimethyl methyl hydrogen siloxane, 40-70 %) and an inhibitor (tetramethyl tetravinyl cyclotetrasiloxane 1-5 %)) at weight ratios of 10:1. The PDMS solution was uniformly mixed and degassed by a planetary mixer (Thinky Corporation, ARE-310), and then 0.3 mL of uncured solution was spin-coated (KE-4A, spin coater) on the glass slides at 2100 rpm and cured at 80 ℃ for 14 hrs. The thickness of the cured soft substrate was 35.43 ± 0.31 μm, determined by a Field Emission Scanning Electron Microscopy (Zeiss UltraPlus FESEMs) (A3.1 and Figure A3-1, Appendix A). The PDMS substrate was named P_{10} based on the aforementioned ratio of the base and

crosslinker. The transmittance and reflectance of the glass slide and the PDMS-coated glass slide (P_{10}) were measured by a UV-Vis spectroscopy (PerkinElmer Lambda 35 &1050 UV-Vis) (Figure A3-2, Appendix A), and the corresponding refractive indices were determined to be 1.53 and 1.44, respectively (A3.3 and Figure A3-3, Appendix A).

3.2.2 Raman measurements

A custom-built Raman spectrometer (HORIBA scientific, XploRA PLUS) equipped with a focused monochromatic laser of wavelength 638 nm (red) was employed (Figure 3-1 (a)). Note that the Raman instrument was mounted on a vibration-isolated optical platform to ensure mechanical stability. All Raman experiments were conducted in a laboratory setting under ambient temperature (23 ± 2 ℃) and humidity (＜50 %) to avoid any measurement variations caused by temperature and humidity changes [125]. Before each experiment, the laser was turned on and warmed up for 30 min to ensure that the laser reached a stable state. Additionally, during measurement, we minimize the effect of ambient light by either turning off the lights in the room or ensuring that the ambient light source is stable. These controls ensure minimum laser spot fluctuations. First, the instrument was calibrated by fitting the typical Raman peak of a silicon wafer at 520.7 cm^{-1} [126]. The sample under test is then placed on the carrier stage with the measured surface upwards. There are two focusing methods: focusing under video mode (using white light) and focusing under laser mode (using laser), with little difference in final results. The two focusing methods could be used alternatively to locate the focal plane (or position) quickly and accurately. However, for experimental consistency, we chose to focus under the video mode, i.e., using white light. Then, the laser was turned on and the instrument was adjusted to laser mode for Raman measurement. This sequence was followed in all our experiments. During Raman measurement, the laser was routed through a 50x objective lens (OLYMPUS, Plan ELWD, 50x) with a numerical aperture (NA) of 0.5 and subsequently focused on the substrate of interest. Consequently, the scattered light was collected by the same 50x objective lens and focused to a 300-μm diameter pinhole using a tube lens to block out-of-focus signals. The in-focus signals were further filtered via a

slit filter, dispersed in the spectrometer using a diffractive optical element, and finally detected by a charged coupled device (CCD).

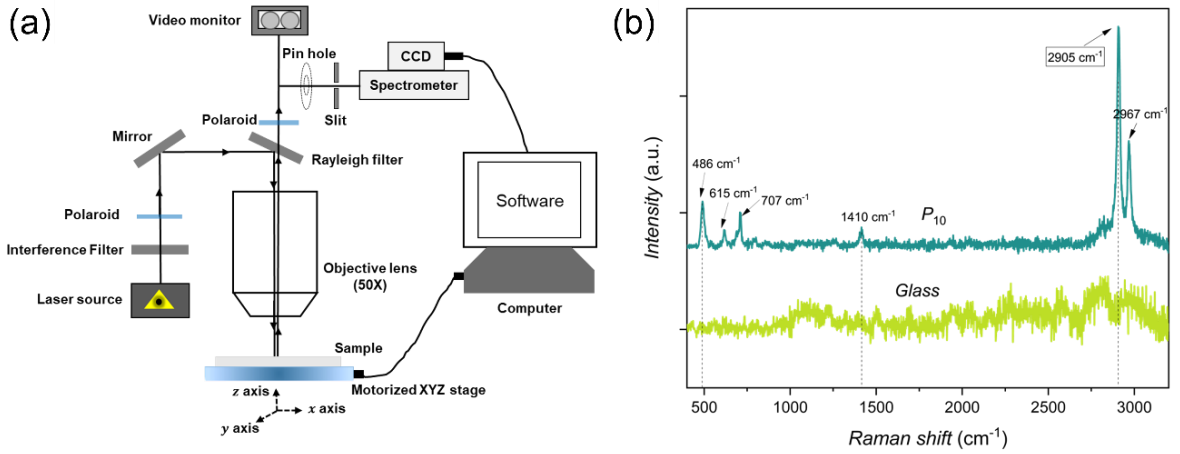


Figure 3-1 (a) Schematic of Raman spectroscopy set-up highlighting the different components. Light source: laser with wavelength λ = 638 nm. CCD: Charged coupled device. (b) The typical Raman spectra of glass and P_{10} at a laser power of 3.77 mW.

To select an appropriate measurement condition, we tried different laser powers of 0.13 mW / 1.41 mW / 3.77 mW with integration time of 1s (Figure A3-4, Appendix A). Since higher laser powers and longer integration times may cause local heating and damage to the PDMS film and lower laser power may not be strong enough to produce sufficiently strong Raman signals of the materials, an optimum laser power and integration time of 3.77 mW and 1 s, respectively were chosen for all the mapping experiments. Unless mentioned otherwise, Raman measurements were performed between 400 cm^{-1} and 3200 cm^{-1} Raman shift. It is to be noted that we have repeated all our experiments three times.

3.3 Results and discussion

The typical Raman spectra of glass and P_{10} are shown in Figure 3-1(b). For glass, a distinct, sharp Raman peak was not observed but a broad peak appears near 1111 cm^{-1} when the laser power is increased to 3.77 mW (Figure A3-4(a), Appendix A), which relates to the structural unit of SiO_2 combined with alkali ions [127,128]. The characteristic Raman peaks of P_{10}

were observed at 486, 615, 707, 1410, 2905, and 2967 cm^{-1} Raman shifts, which corresponds to Si-O stretch, C-Si stretch, SiC_2 antisymmetric stretch, $-CH_2$ bending, $-CH_3$ symmetric stretch and $-CH_3$ antisymmetric stretch, respectively [67,129,130]. We focused on the Raman peaks at 2905 cm^{-1} for our analysis of PDMS contact deformation because of the following reasons: 1) the peak has the strongest signature (intensity) (Figure 3-1(b)), 2) the peak is sensitive to conformational changes [131,132], and 3) the peak exhibits variations from bulk PDMS to confined PDMS [67,133,134]. Additional details regarding this particular selection of PDMS peak are discussed later on in the text. Before delving into the soft contact deformation, we first describe in detail our workflow, i.e., experimental configuration, measurements, and image processing in the form of a calibration experiment performed using a glass sphere - glass substrate contact configuration.

3.3.1 Calibration experiments: glass-glass contact

For calibration, we first performed Raman measurements for the configuration where a glass sphere is in contact with a glass substrate, i.e., solid contact. The calibration experiment of the glass sphere-glass substrate contact setup is shown in Figure 3-2(a). Here, five glass spheres (8996K24, McMaster-Carr) with a radius of 2600 μm, a weight of 1.24 mN, and a refractive index of 1.47 were fixed onto a cleaned glass slide and then another cleaned glass slide was placed on top of the five glass spheres. Note that our focus is on the contact region between the top glass slide and the central glass sphere while the other four glass spheres located at the four corners, together with the center glass sphere, support the top glass plate, and in turn, help maintain contact with the central glass sphere in equilibrium. We assumed that the glass spheres are perfectly spherical and identical in size, and the refractive indices of the glass spheres and the glass slide are assumed to be equivalent, with a representative value of ~1.5. The top glass slide (2.42 g) exerts its weight which is equally distribution among the five glass spheres. Further, a drop of Methylene blue (MB) solution (MB / ethanol: 10^{-3} mol/L) was deposited on the contact surface of the top glass slide ~1.3 mm away from our region of

interest and dried before use to facilitate a reference plane for focusing for subsequent experiments.

To map the region of interest, i.e., the contact region of the central glass sphere with the top glass slide, the workflow of the Raman mapping measurements can be divided into four steps:

(1) **Focusing under video mode**: Using the footprint of the MB droplet as a reference, we initially focused on the free surface (contact surface) of the top glass slide with white light, establishing the reference plane at $z = 0$. Next, by translating the carrier horizontally while maintaining the height of the objective lens and the carrier stage, we set the focus point to the center of the contact area between the top glass slide and the glass sphere (Figure 3-2(a)), designated as the origin $O(0,0,0)$. To clearly illustrate the region of interest, a schematic of the set-up is shown in Figure 3-2(b). The typical Raman spectra of glass with different integration times for a laser power of 3.77 mW are shown in Figure 3-2(c).

(2) **Setting mapping parameters under video mode**: The Raman mapping parameters, including the mapping region and step size, are determined based on the instrument's resolution and the region of interest, specifically the contact area between the central glass sphere and the top glass slide. Here, the minimum achievable laser spot diameter is 1.56 μm (A3.5, Appendix A). The spatial resolution in the x-y axis is 0.78 μm (A3.6, Appendix A), and in the z-axis in the air medium is 2.55 μm (A3.7, Appendix A). A key criterion for setting the mapping parameters is ensuring that the mapping step is greater than the lateral resolution. Our present focus is on investigating the spatial structure of the contact zone. Thus, to be comprehensive, we choose a mapping region of 420 μm in x and y directions with a mapping step of 10 μm (Table 3-2). For the initial calibration experiment, we only performed z-scanning at $z = 4$ μm, $z = 0$ μm and $z = -4$ μm, as shown in Figures 3-2(d)-(f), respectively. Note that, since both the glass sphere and glass slide are transparent and rigid, the contact area of the glass-glass system appears as a dark region with adjoining

interference fringes (Figure 3-2(e)) due to the air separating the glass sphere and the glass substrate. This observation aligns with the existing literature [19,103].

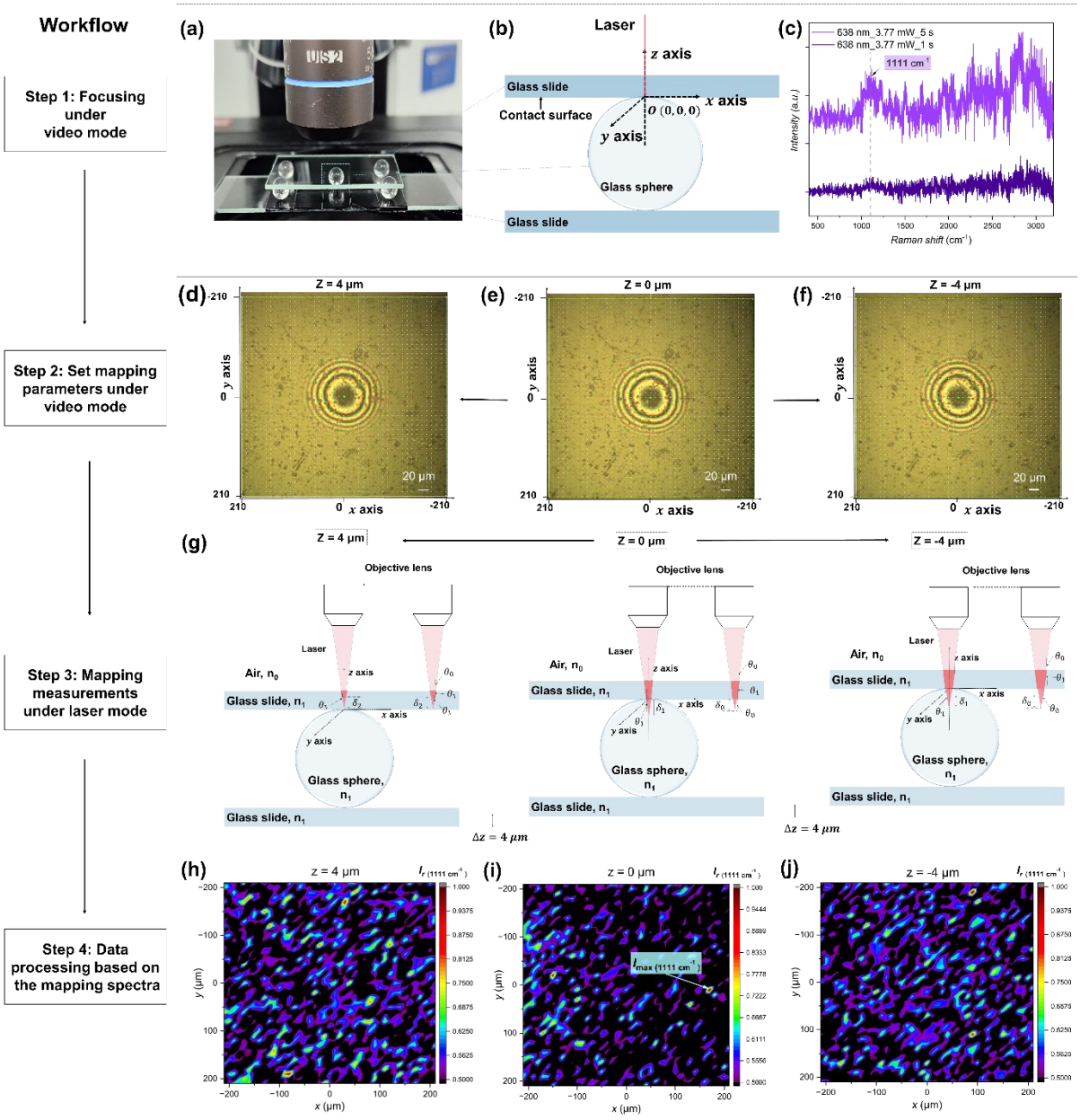


Figure 3-2 Workflow illustration of Raman mapping measurement of the glass sphere - glass substrate contact system. (a) Snapshot of the set-up of the calibration experiment: five glass spheres of 2.6 mm radius each fixed on a glass substrate with another cleaned glass substrate on top of the five glass spheres. The contact between the

central glass sphere and the top glass slide is of interest here. (b) Schematic of the set-up of the calibration experiment (glass-glass system), where the origin $O(0,0,0)$ is located at the center of the contact area between the glass sphere and the top glass substrate. The x and y axis are located on the free surface of the top glass substrate, and the z-axis goes through the center of the contact interface and the top glass substrate. (c) The typical Raman spectra of glass obtained at a laser power of 3.77 mW with integration times of 1 s and 5 s. The peaks at 1111 cm^{-1} are highlighted. (d), (e), and (f) Optical snapshots of the mapping regions of interest at z locations of z = 4 μm, z = 0 μm and z = -4 μm, respectively. (g) The schematic of the laser spot focusing on the z layers of z = 4 μm, z = 0 μm and z = -4 μm. n_0, and n_1 are the refractive index of air (1.0) and glass (1.5), respectively and $n_0 < n_1$. θ_0 and θ_1 are the refraction angle of air and glass, respectively and obey the condition $\theta_0 > \theta_1$ (A3.8, Appendix A). δ_0 and δ_1 are the real penetration depth of laser in air and glass, respectively and obey the condition $\delta_0 < \delta_1$ (A3.8, Appendix A). Note that additional discussion on the penetration depth of the laser in air and glass is included in A3.8, Appendix A. (h), (i) and (j) The Raman mapped images (contour plots) based on the normalized Raman peak intensity of 1111 cm^{-1} (see text) at z layers of z = -4 μm, z = 0 μm and z = -4 μm, respectively.

Table 3-2 Mapping parameters of glass-glass system.

Axis (μm)	From(μm)	To(μm)	Step(μm)
x	-210	210	10
y	-210	210	10
z	4	-4	-4

(3) **Raman mapping measurements under laser mode:** Based on the preset mapping parameters, we scan a region of size 420 μm x 420 μm in x-y directions, symmetric about the origin, using a scanning step of 10 μm in both directions. The z-scanning is performed at z = 4 μm, z = 0 μm, and z = -4 μm, with a scanning step of 4 μm. For the mapping process at each layer, such as at z = 0 μm, the laser spot first passes through the top glass slide and focuses on a region outside the contact zone (Figure 3-2(g)). The mapping measurement begins at position (-210,-210,0) and scans point by point along the x-axis from -210 μm to 210 μm with a 10 μm step interval, totaling 43 points in the first row. The scan then moves to the next row at y = -200 μm and continues until the row at y = 210 μm, ending at the position (210, -210, 0). This results in 1849 points scanned at a single z-plane.

Note that z = +ve implies moving down the stage so that the focal plane of the laser is into the top glass slide and z = -ve implies moving up the stage so that the focal plane is now into the glass sphere (Figure 3-2(g)). Thus, for the 420 μm x 420 μm region in x-y, the mapping provides 43 x 43 or 1849 slices of Raman spectra. Combining three different z measurements, a total of 5547 Raman spectra are obtained and subsequently analyzed.

(4) **Post-processing of Raman spectra:** Here, we select the Raman peak at 1111 cm^{-1}, the most dominant signature for glass, for further analysis. For each z layer, we choose the intensity of the peak at 1111 cm^{-1}, i.e., I_i (1111 cm^{-1}) for all 1849 Raman signatures. As our reference, we choose the Raman signature at a given (x, y) with the maximum peak intensity of 1111 cm^{-1} obtained at z = 0 μm (Figure 3-2(i)). We normalize all 5547 Raman spectra obtained with this reference intensity, i.e., $I_{z=0,max}$(1111 cm^{-1}) obtained at z = 0 as denoted below:

$$I_r(1111\ cm^{-1}) = \frac{I_i(1111\ cm^{-1})}{I_{z=0,max}(1111\ cm^{-1})} \qquad (3\text{-}1)$$

where I_r (1111 cm^{-1}) is the normalized peak intensity of each point. At the reference layer of z = 0, $0 \leqslant I_r(1111\ cm^{-1}) \leqslant 1$. However, the spatial resolution in Raman spectroscopy is commonly defined as the lateral distance at which the measured peak intensity decreases to 50 % of its maximum observed value, which is scientifically valid and aligns with the full width at half maximum (FWHM) criterion commonly used in optical imaging and spectroscopy [135,136]. To further improve the comparison and resolution of the Raman peak image (contour) at each measurement plane, we set the color bar level of the contour as $0.5 \leqslant I_r(1111\ cm^{-1}) \leqslant 1$ and apply it for all the z layers. The distribution of I_r (1111 cm^{-1}) along 420 μm x 420 μm region is thus plotted and represented as a contour plot. The corresponding Raman contour plots for z = 4 μm, z = 0 μm and z = -4 μm are shown in Figure 3-2(f), (g) and (h), respectively. From Figures 3-2(f) - (g), we observe that the glass Raman signature at each layer is relatively weak but uniform and stable, i.e., the normalized intensity I_r (1111 cm^{-1}) is mostly around 0.5. This observation is beneficial for the present study since it indicates the

glass Raman signature emanating from the glass slide and glass sphere will have minimal effect in our subsequent experiments where we intend to resolve the PDMS Raman signature.

3.3.2 PDMS-glass experiments

For glass sphere-PDMS contact experiments, the top glass slide is now replaced with the PDMS-coated glass substrates, with the PDMS coating facing downwards in contact with the five glass spheres. The corresponding schematic of the PDMS-glass set-up is shown in Figure 3-3(a), where point A(0, 0, z_a) represents the lowermost point of the glass sphere-PDMS contact interface, now at a finite z value due to the finite PDMS deformation around the contact region. Note that for the sake of representation, a Hertz-like conformal contact configuration is shown. Based on the schematic, for any $z > z_a$, the mapping region in x, y and z directions is entirely PDMS; for $0 < z < z_a$, both PDMS and glass sphere are present; and for $z < 0$, only the glass sphere is present. Therefore, the gradual progression of the Raman spectra along the z-direction aids us in identifying the contact deformation region of interest.

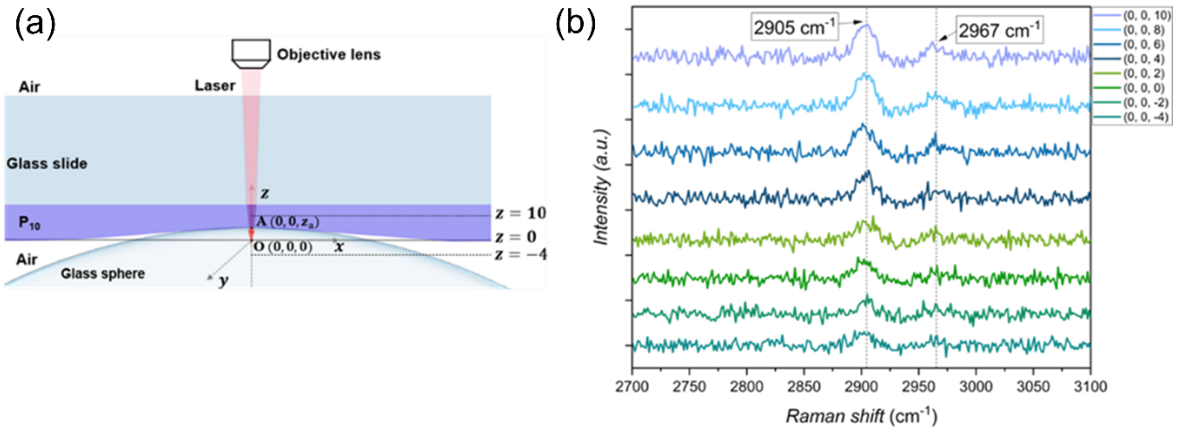


Figure 3-3 (a) Schematic of the set-up of the PDMS-glass system, where the origin $O(0,0,0)$ is located inside the glass sphere, i.e., at the secant of the glass sphere at z = 0 µm. The x and y axis are located on the free surface (lower surface) of the PDMS/glass, and the z axis goes through the center of the contact interface and the upper PDMS/glass slide. (b) Single point Raman scans along z-direction from z = -4 µm to z = 10 µm in 2 µm steps focusing on the center of the glass sphere-PDMS contact configuration.

The Raman mapping measurements were performed similarly to previous calibration experiments, focusing on the central glass sphere in contact with the PDMS. Similarly, the laser spot was initially focused on the free surface of the PDMS layer far away from the contact region using the deposited MB droplet as a reference, identifying the z = 0 μm plane. The focused laser spot was then moved horizontally to the center of the secant line of the glass sphere at z = 0 μm, now designated as the origin O(0,0,0). To identify the Raman peaks of interest, we first perform a systematic z-scanning of the glass sphere-PDMS contact configuration from z = -4 μm to z = 10 μm in 2 μm steps, focusing the laser spot at the center, i.e., (0, 0, z). The corresponding Raman spectra are shown in Figure 3-3(b). From our observations, it is evident that the intensity of Raman peaks relevant to PDMS i.e., 2905 and 2967 cm^{-1} increased significantly as the z distance is larger than 4 μm (glass slide thickness = 1 mm), indicating the approximate vertical location of the glass-PDMS contact interface. However, this does not provide information on the lowermost point A separating the glass sphere and the PDMS, i.e., $z = z_a$. Nevertheless, the gradual progression of the Raman spectra along the z-direction helps identify the most relevant Raman peak. Out of the two peaks that exhibit changes, we choose the Raman peak at 2905 cm^{-1} for subsequent analysis since its change with the z-direction is the most pronounced. It is noteworthy to mention that the Raman peaks at 2905 cm^{-1} and 2967 cm^{-1} in PDMS correspond to the symmetric and asymmetric stretching vibrations of the methyl ($-CH_3$) groups, respectively. The stronger Raman intensity of the 2905 cm^{-1} peak relative to the 2967 cm^{-1} peak in PDMS can be attributed to the inherent characteristics of the symmetric stretching mode of methyl groups. According to Raman selection rules, symmetric stretching vibrations typically result in a greater change in molecular polarizability, thereby producing a stronger Raman signal [137,138]. Furthermore, in PDMS, the methyl groups are preferentially oriented perpendicular to the polymer backbone, which may presumably enhance the intensity of the symmetric stretching mode due to favorable alignment with the incident light's electric field [67,139]. Therefore, the peak intensity at 2905 cm^{-1} is more sensitive to changes in the external environment like confinement. Existing literature has shown how the peak intensity of 2905 cm^{-1} decays from the bulk to the contact region which

is at par with present observations [134]. Consequently, we perform the detailed Raman *z*-mapping across a scan region of 420 µm x 420 µm in *x*-*y* directions focusing on the signature of the Raman peak at 2905 cm^{-1}.

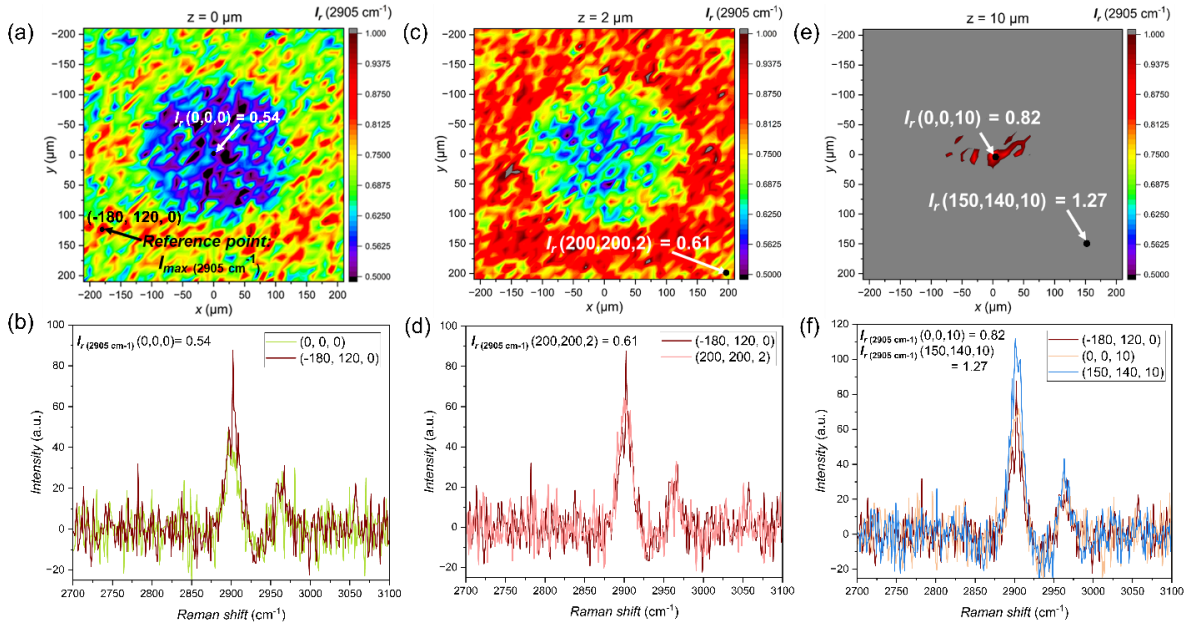


Figure 3-4 Raman mapped images (contour plots) based on the normalized Raman peak intensity (I_r) of 2905 cm^{-1} (see text) at (a) z = 0 µm, (c) z = 2 µm, and (e) z = 10 µm. (b) Raman spectra at the locations (-180, 120, 0) (reference point) and at the origin (0,0,0). The intensity of the 2905 cm^{-1} peak at the location (-180, 120, 0) is used as the reference intensity and denoted as $I_{0,\,max}$ (2905 cm^{-1}). The intensity ratio, i.e., I_r (2905 cm^{-1}) = I_i (2905 cm^{-1})/ $I_{z=0,\,max}$ (2905 cm^{-1}) is highlighted. (d) Raman spectra at the locations (-180, 120, 0) (reference point) and (200, 200, 2), i.e., at a location on the z = 2 µm plane. The corresponding I_r is highlighted. (f) Raman spectra at the locations (-180, 120, 0) (reference point), (0, 0, 10), and (150, 140, 10) i.e., at two different locations on the z = 10 µm plane. The corresponding I_r's are highlighted.

Similar to that performed for the calibration experiments, we first extract the maximum intensity $I_{0,\,max}$(2905 cm^{-1}) obtained at z = 0 out of the 1849 Raman scans at z = 0, and using that normalize all intensity, I_i (2905 cm^{-1}) of all Raman spectra obtained across all x, y and z locations. Thus, we obtain the normalized intensity information as, I_r (2905 cm^{-1}) = I_i (2905 cm^{-1})/ $I_{z=0,\,max}$ (2905 cm^{-1}). As shown in Figure 3-4(a), the maximum Raman intensity of the

peak at 2905 cm^{-1} at z = 0 occurs at the location (x, y) = (-180, 120) and its magnitude is subsequently used to normalize all other intensities of the peak 2905 cm^{-1} (Figure 3-4). For instance, comparing this peak intensity at (-180, 120, 0) with another Raman scan at (200, 200, 2) yields an intensity ratio I_r = 0.61 (Figures 3-4(c)-(d)). Repeating this normalization along x and y enables a color map highlighting the intensity ratio distribution along that particular z-location (Figures 3-4(a), (c) and (e)). Additional examples of intensity ratio calculations at a few other locations are shown in Figures 3-4(b) and (f). Note that the observed Raman signatures across the different x, y, and z locations have negligible peak shifts and uniform peak widths for the peak at 2905 cm^{-1} (Figures 3-4(b), (d) and (f)). Thus, our normalization by using the intensity at 2905 cm^{-1} yields negligible mapping error.

3.3.3 Confocal Raman mapping of contact deformation

In Figure 3-5(a), we show the contour plots, i.e., the distribution of I_r (2905 cm^{-1}) over the mapping area of 420 μm x 420 μm at different z positions. Note that the color bar range of the contour map is $0.5 \leqslant I_r\,(2905\ cm^{-1}) \leqslant 1$ and any ratio above 1 is assigned as grey. The Raman contour plots reveal two distinct regions: an inner circular region indicating the contact interface (or the radius of the secant area of the glass sphere at a different z plane) and an outer region. At z = -4 μm, z = -2 μm, and z = 0 μm, the central region predominantly shows a weak PDMS signature ($I_r < 0.5$) due to the sole presence of the glass sphere without any contact with PDMS (Figure 3-5(a)). At z = 0 μm and z = 2 μm, we observe increasing PDMS signatures (red regions in the contour plot) outside the inner region, possibly arising from the PDMS-air interface drifting away from the contact interface. However, the signature of the inner region indicates that glass-PDMS contact is yet to be established. The density of the red regions increases with increasing z in the +ve direction, towards the PDMS substrate. Consequently, we trace these red regions of the contour plots across different z-locations and use them as a definitive confirmation of either the PDMS-glass contact interface or the PDMS-air interface. Note that regions with an intensity ratio below red in the maps are not considered representative of a significant PDMS signature. Even though discrete red spots are observed at z = 2 μm, the

PDMS signature (red regions) only begins to invade the inner region as a continuous front at z = 4 μm, indicating that a conformal interfacial contact between PDMS and the glass sphere has been established (z = 4 μm, Figure 3-5(a)). The Raman map at z = 4 μm, thus provides the definitive location of the glass sphere-PDMS contact interface. From this map (z = 4 μm, Figure 3-5(a)), the average radius of this inner region is determined to be 127.2 μm, which is close to the value obtained from optical imaging, a_{exp} = 127.6 ± 3.2 μm (Figure 3-5(b)).

The contour map at z = 4 μm additionally reveals trace amounts of grey areas, which have a higher intensity than the red regions, indicating an enhanced PDMS signature (z = 4 μm, Figure 3-5(a)). Note that, in terms of the relative strengths of the intensity ratio I_r, for red regions in the contour plots, $0.8 < I_r < 1$, whereas for grey regions, $I_r > 1$. There are two possible explanations for these two distinct regions in the Raman mapping. First, part of the laser light reflecting from the inner region (glass sphere-PDMS interface) gets scattered away, while another portion is detected. Thus, for $z \geq 4$ μm, the 2905 cm^{-1} signature corresponding to PDMS within the contact region is relatively weaker (red regions) compared to the outer region with a stronger signature (grey regions). Second, the red regions may correspond to the signature of interfacial PDMS where it contacted with either glass sphere or air (either glass- PDMS or PDMS- air) whereas the grey regions correspond to the PDMS signature coming from the 'bulk', i.e., a few micrometers away from the interface. It is expected that as we move away from the glass sphere and approach the PDMS substrate, I_r continues to increase. Proceeding further into the +ve z-direction, we observe that the appearance of the red PDMS signature in the inner region is nearly complete at z = 6 μm (z = 6 μm, Figure 3-5(a)) and then progressively decays. At z = 10 μm, we observe a minimal red PDMS signature indicating the lowermost contact point of the glass sphere with the PDMS (z = 10 μm, Figure 3-5(a)). Thus, we obtain $z_a \approx$ 10 μm. At z = 10 μm, most of the Raman contour map exhibits a predominantly grey PDMS signature. Consequently, our previous assumption that the red regions correspond to the interfacial PDMS signature is likely accurate since at z = 10 μm, there is minimal contact

between the glass sphere and the PDMS substrate, and the PDMS layer away from the interface is at least 10 μm from the free surface.

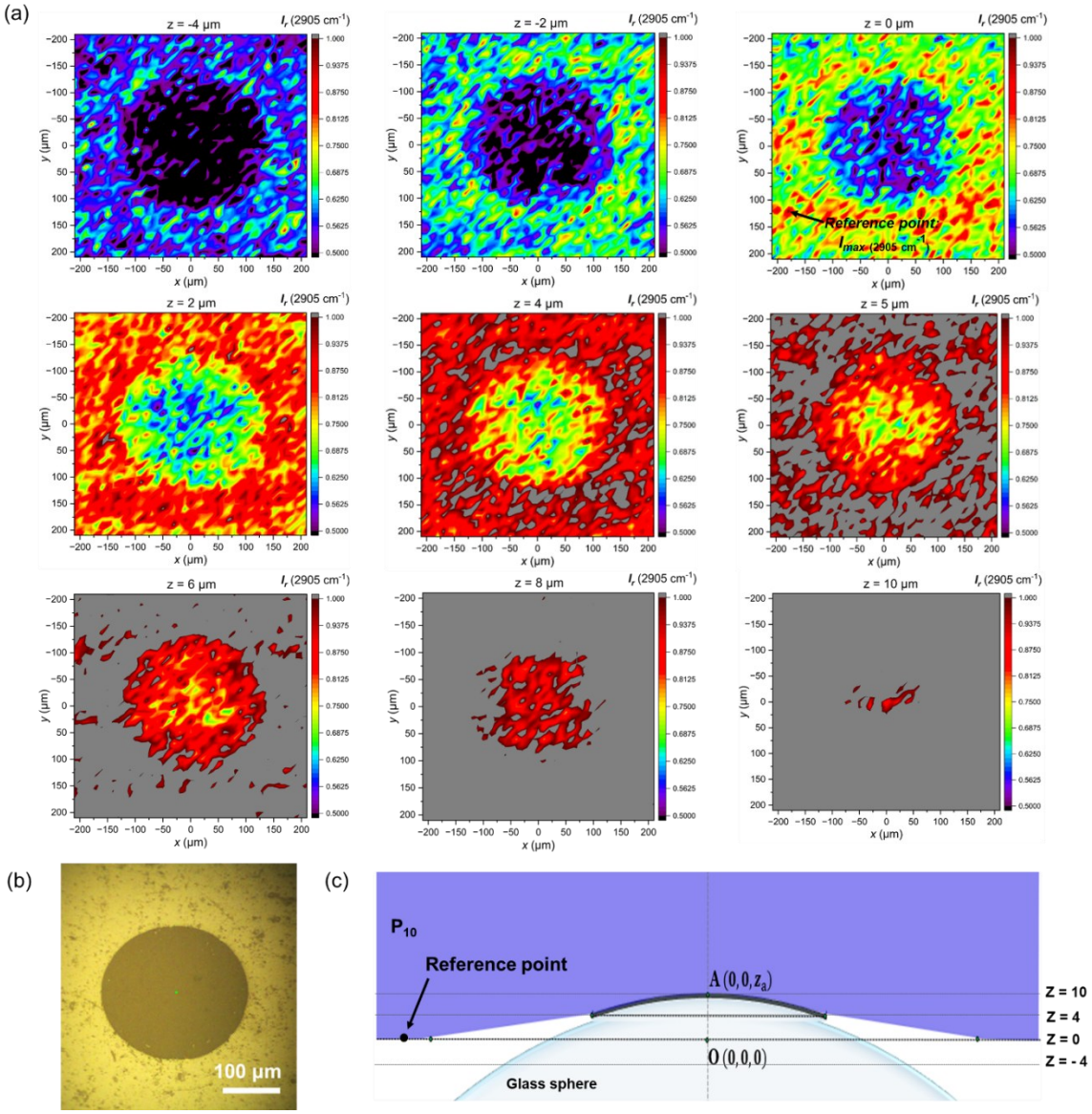


Figure 3-5 (a) The Raman mapped images (contour plots) based on the normalized Raman peak intensity (I_r) of 2905 cm^{-1} (see text) at z = -4 μm, z = -2 μm, z = 0 μm, z = 2 μm, z = 4 μm, z = 5 μm, z = 6 μm, z = 8 μm, and z = 10 μm, respectively. (b) Top view optical imaging snapshot of the glass sphere-PDMS contact interface (dark region) where the green dot is the origin $O(0,0,0)$ or its projection. Note that the central dark region remains

unchanged at neighboring z-planes. (c) Schematic of the contact deformation of glass sphere-PDMS contact pair based on the Hertz theory and the Raman contour plots.

The comprehensive confocal Raman mapping suggests the contact geometry is Hertzian; accordingly, we re-create the approximate schematic of the contact geometry (Figure 3-5(c)). For a contact pair to be Hertzian it needs to meet the criteria of small strain and negligible adhesion which our contact system does obey. While adhesion is often significant in softer PDMS, our previous studies have demonstrated that for the stiff PDMS, adhesion's role in contact can be safely disregarded [19,113]. Further, our Raman mapping shows the radius of the secant of the glass sphere at z = 0 μm to be around 140 μm. Thus, even though the reference point (-180, 120, 0) was initially selected solely based on the maximum intensity of the 2905 cm^{-1} Raman peak at z = 0 μm, we can now confirm its location to be approximately on the free (undeformed) surface of the PDMS (Figure 3-5(c)). Further, evident from the Raman contour maps for $z \geq 8$ μm, contact of soft materials like PDMS with a rigid glass sphere loses homogeneity beyond a certain indentation depth and occurs only in discrete patches. Previous imaging techniques [19,49–52,54–58,60,62,101–107] have failed to resolve this feature of soft contacts. To check if the indentation depth obtained from our analysis is reasonable, we calculate the theoretical contact radius using the Hertz theory, i.e., $a = (3FR/4E^*)^{\frac{1}{3}}$, assuming homogenous and uniform contacts across all contact planes and neglecting the effect of PDMS finite thickness, where R is the glass sphere radius and the effective elasticity $E^* = \left[(1-{\vartheta_1}^2)/E_{glass} + (1-{\vartheta_2}^2)/E_{P_{10}}\right]^{-1} \approx (4/3)E_{P_{10}}$, since $E_{glass} \gg E_{P_{10}} = 1.62$ MPa [113] and Poisson ratios ϑ_1 and ϑ_2 are both 0.5 [140]. For the present configuration, since the weight (25.6 mN) of the P_{10} coated glass slide is equally distributed between the 5 spheres, the central sphere of interest exerts an upward force F = 5.12 mN. Upon subsequent analysis, we observe that a_H = 165.5 μm, i.e., larger than our experimental value of a_{exp} = 127.6 ± 3.2 μm obtained from top-view optical imaging (Figure 3-5(b)) as well as Raman mapping (Figure 3-5(a)). We further use the Hertz formulation to calculate the indentation depth, $\delta_H = {a_H}^2/R$ = 10.53 μm, which is slightly larger than that obtained from confocal Raman mapping δ_{exp} = 10 μm. This is

reasonable considering the discrete non-uniform contact patches and the fact that PDMS is coated onto the glass, making its effective modulus greater than that of the bulk PDMS. It is noteworthy to mention that the ratio of the contact radius (a_{exp}) to the PDMS layer thickness (H) in our system is $\eta = H/a_{exp} = 35.4/127.6 = 0.28$. Hence, we compared our experimentally obtained indentation depth with Winkler's foundation model [90] (A3.9, Appendix A) which holds reasonably well for the condition $\eta << 1$ (thin elastic layers, large contact radius). The model assumes the elastic substrate consists of a mattress of independent springs where deformation at one location does not influence neighboring regions with the effective foundation stiffness $(k = (1-\vartheta)/(1-2\vartheta)\,G)/H$. Here, $G = E/2(1+\vartheta)$ is the shear modulus of the elastic substrate. Consequently, the indentation depth can be estimated using the relation $\delta = F/kS$, where F is the applied force and S is the contact area. Note that in the present study, $F = 5.12$ mN and $S = \pi a_{exp}^2 = 5.1 \times 10^{-8}$ m^2. It is clear that the Winkler theory breaks down for incompressible materials like PDMS with $\vartheta \approx 0.5$ [140] since k diverges. Nevertheless, assuming near incompressibility of the PDMS layer with $\vartheta = 0.45$ - 0.5, the theory predicts indentation depth values of 0.05 μm and 0.02 μm for $\vartheta = 0.45$ and $\vartheta = 0.48$, respectively (A3.9, Appendix A). Both predictions significantly underestimate the experimental value of 10 μm. The severe mismatch with Winkler's model can be due to the near incompressibility of PDMS where deformation is strongly coupled across the material due to volume conservation and thus the independent springs assumption breaks down. Additionally, existing literature has also shown the model to break down in the limit $\eta \to 1$ [90] and a moderate value of 0.28 may very well be beyond the scope of the model. Therefore, we conclude that the Hertz theory is more suitable for our system.

3.3.4 Limitations of the study

Herein, we provide a brief discussion of the merits and demerits of this imaging modality. First, it presents a first-of-its-kind framework using molecular chemical signatures to extract quantifiable microscopic physical parameters of contact deformation. Second, our approach significantly advances existing Raman studies, which probe mostly flat interfaces [141].

By operating in confocal mode and mapping relative intensity, we can qualitatively inspect irregular deformation profiles with varying slopes. Third, the imaging configuration illuminates from the top with a minimum lateral resolution of 0.78 μm and the overall resolution can be adjusted by resetting the mapping step according to the region of interest, offering operational flexibility. Finally, this user-friendly technique allows even novice users to replicate experimental procedures with remote assistance.

In terms of limitations, we highlight several points. First, materials with relatively weak Raman peak intensities cannot be probed using the present imaging modality and will require appropriate surface modifications. Second, Raman mapping involves scanning the sample point by point with a laser beam, according to preset parameters such as the mapping region, step size, and acquisition time of a single spectrum. The mapped region is subsequently divided into a pixel-assigned array of spectral elements [72]. It is crucial that the preset step size is not smaller than the radius of the laser spot, and ideally, it should be equal to the radius of the laser spot. If the step size exceeds the radius of the laser spot, the resulting map will be under-sampled, as not all areas will be scanned [72]. However, in our study, the contact area (average contact radius: 127.6 ± 3.2 μm) is significantly larger than the size of the laser spot (laser spot radius: 0.78 μm). Therefore, our step size of 10 μm is reasonable since using a finer step size to perform this mapping would significantly extend acquisition times and, in turn, the total duration of the experiment. This adjustment highlights the necessity of balancing imaging resolution and image acquisition time when observing large areas and mapping across multiple planes. Finally, the present work only investigated the contact deformation of a relatively stiff PDMS substrate, i.e., P_{10} with an elasticity of 1.62 MPa. Softer materials, such as lightly crosslinked PDMS (45:1, 60:1 Sylgard 184), silicone gel, or hydrogel often exhibit conformal contact configurations with glass spheres in contrast to Hertzian contact [19,51,57,58,103]. Further, they often contain uncrosslinked free chains or free liquids within the polymer network. These free liquids have been observed to form a liquid meniscus at the tip of the contact/wetting ridge and exhibit phase separation [19,51,54,57,103]. For characterizing systems with such fluid separation,

the data-processing methodology of the present work may not be suitable and may need additional consideration.

3.3.5 Assessment of robustness and broader applicability

Despite such limitations, we highlight that the imaging modality is robust and can generate reproducible results with consistent experimental conditions, rigorous calibration, accurate baseline correction and selection of appropriate reference for intensity normalization. These considerations are crucial to minimizing potential errors. For instance, rigorous environmental control ensues minimal laser spot fluctuations. Specifically, the Raman instrument was mounted on a vibration-isolated optical platform to ensure mechanical stability. All measurements were conducted at night under stable temperature and humidity conditions, effectively reducing ambient disturbances. Appropriate selection of mapping resolution compared to the feature size aids in preventing either oversampling or under sampling. Further, selecting accurate reference points for intensity normalization smooths out sample-to-sample intensity fluctuations enhancing reproducibility. However, there is still room for improvement. For materials/systems where a suitable reference point is difficult to ascertain, normalization with respect to an internal standard peak can compensate for variations in laser power and instrumental fluctuations, while advanced baseline subtraction techniques can mitigate background interference [142]. Further, functionally graded materials (FGMs) with spatial heterogeneity may pose additional challenges. In this regard, spatially resolved Raman mapping and spectral deconvolution techniques (e.g., Principal Component Analysis) can improve detection accuracy by distinguishing intrinsic material variations from measurement artifacts [143,144]. Furthermore, complementing intensity-based analysis with Raman peak position shifts and bandwidth changes can enhance robustness, providing a comprehensive approach to material characterization. These methodologies ensure reliable and reproducible Raman measurements, even in complex and inhomogeneous systems.

Moreover, we note that Raman peak position shifts are not particularly a concern for polymeric materials like PDMS as exhibited by our Raman findings. Due to the highly flexible and crosslinked polymer network, mechanical deformation under room temperature primarily affects molecular bond orientations without an increase in crystallinity, which means no significant alteration of phonon energies occurs. As a result, Raman peak shifts do not ideally occur unless the system involves use of low temperatures like -45 ℃ ~ -60 ℃ which allows for crystallization [145]. Thus, changes in Raman intensity serve as a more reliable metric for assessing mechanical and structural modifications. The situation alters for two-dimensional (2D) materials, such as graphene. In these materials, external perturbations, including contact forces and strain, induce significant Raman peak shifts due to changes in phonon dispersion and interatomic bond distances, making spectral shifts an effective indicator of mechanical interactions [146,147]. Hence, peak shifts should be properly monitored for such systems. This distinction highlights the varying applicability of Raman spectroscopy across different material classes and emphasizes the importance of selecting appropriate spectroscopic parameters based on the underlying mechanical response of the material.

3.4 Conclusion

In conclusion, we report an in-situ imaging methodology capable of visualizing soft contact deformation using confocal Raman spectroscopy. Unlike single-point Raman scans, our method involves Raman mapping measurements along the *x*, *y*, and *z* axis around the contact interface. We first performed calibration experiments using a glass probe-on-glass substrate contact configuration to establish the workflow of this methodology. Consequently, we performed soft contact deformation measurements using a similar glass probe indenting a PDMS substrate of finite elasticity. From the observed chemical signatures of PDMS, we identified the relative intensity of the Raman peak at 2905 cm^{-1} and Raman shift to be the most definitive signature embedding crucial spatial information. Using this signature, we developed a framework for generating Raman contour maps that enable us to identify the spatial variation of the glass-PDMS contact interfaces and the non-conformal nature of the contact deformation

profile. The precise identification of contact enabled us to extract parameters like the contact radius and the indentation depth. Our Raman mapping findings and subsequent extrapolations, when compared with the Hertz contact theory, showed reasonable agreement.

As previously mentioned, the present technique offers a first-of-its-kind framework where chemical mapping is used to extract tangible physical information of soft contact deformation. None of the existing methodologies (see Table 3-1) have similar capabilities. Previous studies using Raman mapping to probe soft contact mechanics primarily used chemical signatures, i.e., intensity information to provide qualitative information about either structural change in polymer thin films or the effect of chemical modifications on surface-attached polymers [133,134]. Additionally, similar Raman mapping was employed to study contact mechanics of Si thin films [148]. However, these systems involved much smaller length scales and consequently 3D spatial information extraction was either not relevant or was not performed due to material or length scale-specific challenges. Consequently, the present technique enabling 3D spatial mapping in microscale using chemical signatures in terms of normalization is distinctly different to existing studies and at the same time can be considered as a modest advancement. The ability to probe spatial variations across a finite thickness thus enhances the scope of this technique to include other soft contact configurations, such as conformal contacts exhibited by contact and wetting ridges without phase separation [149]. Further, it can offer new insights into the configuration and distribution of polymer networks under tension or compression, including deformations of elastomer of finite thickness in contact with different solids, liquids, and thin films. From an application point of view, our imaging technique is highly suitable for visualizing the inner structures and distribution of soft or porous materials under deformation as well as lubricant dynamics in dynamic soft contacts [150], which are used in flexible batteries [151], bionic material [152,153], bioelectronics [154] and soft robotics [155]. Lastly, we note that as future work, we aim to expand the capabilities of this imaging technique to map contact deformation of softer polymers and gels.

Chapter 4

Determining effective refractive index and elasticity of nanoscale metal - thin, soft polymer bilayers using interference signatures of a glass probe

Thin metal films like silver (Ag) and gold (Au) on PDMS are perfect candidates for surface-enhanced Raman spectroscopy (SERS) active substrates whose optical and mechanical properties are often subjected to precise tuning. Measurement of such properties often requires multiple sophisticated experimental techniques and numerical analysis. When depositing a nanoscale thin metal film like Ag or Au on the polymer surface, the refractive index and elastic modulus of this bilayer structure could vary with the metal deposition time and properties of soft substrates. In this work, we demonstrate a single experimental methodology to measure the refractive index and elasticity of thin metal films coated on PDMS. Using Dual-Wavelength Reflection Interference Contrast Microscopy (DW-RICM) measurements of a spherical glass probe of known shape, the refractive indices of Ag/PDMS and Au/PDMS substrates of varying metal deposition time, PDMS elasticity, and PDMS coating thickness are extracted corresponding to two different wavelengths. The extracted refractive indices of metal/PDMS substrates decrease with increasing metal deposition time, decreasing PDMS elasticity, and increasing PDMS coating thickness. The extracted refractive indices are found to be in good agreement with corresponding UV/Vis spectroscopy measurements. Lastly, their elastic moduli are also obtained using Hertz's theory on the observed contact radius of the glass sphere on the aforementioned substrates.

4.1 Introduction

Thin metal films deposited on polymer surfaces for enhanced functionality have gained widespread attention due to the ease of integration into emerging technologies. Such structures in combination with inorganic and organic materials have been extensively applied in biomedical devices [156,157], solar cells [158], electronic skins [159], surface-enhanced Raman

spectroscopy (SERS) substrates [160–162], Plasmon Resonance sensors [7,8,163], radiative cooling applications [163] and 5G wireless communications [164]. For these applications, understanding the optical and mechanical properties of the multilayer films is of paramount importance, especially with different film thickness. However, existing literature has mostly focused on film properties, such as, the relationship between deformation and electrical resistance [165], the generation, elimination, and precise control of cracks [166], and the filtering effect on light [167].

Generally, the optical and mechanical properties of metal-polymer films, especially their refractive index (RI) [168–170] and elastic modulus E [171], can be tuned by accurate control of the film thickness. Polydimethylsiloxane (PDMS), a silicon-based organic polymer, is the most commonly used polymer base for different engineering applications, as mentioned earlier. PDMS has high transparency in the visible spectrum and high absorbency near the infrared spectrum. Furthermore, it is chemically inert, bio-compatible, can absorb many solvents and easy to manipulate [26,27]. The ease of manipulation provides an excellent control over the subsequent metal film thickness and elastic properties [171,172]. Consequently, coating PDMS substrates with gold or silver nanoparticles/films provides an ideal playground for fabricating SERS active substrates for chemical and biological imaging [173–178]. However, the deposition of a metal film is expected to change the optical (and mechanical) properties of such substrates. Although the mechanical and optical properties of pristine PDMS substrates are extensively studied [171,179,180], how the same properties change upon coating of a thin metal film, remains unresolved.

For metal/polymer bilayer film, the effective refractive index (RI) plays a crucial role in many optical applications. However, the RI of the majority of polymers is limited to a relatively narrow range between 1.4 and 1.6 [181]. To further broaden the scope of polymeric substrates, considerable effort has been devoted to developing polymeric materials coated with thin metal films to increase or decrease effective RI [181–184]. For example, metal-polymer bilayer structures with a higher effective RI can increase the haze value, which can

consequently improve the light efficiency and viewing-angle characteristics of Organic light-emitting diodes (OLED) and MC-OLED devices without any light loss [185]. In anti-reflection (AR) coating field, the multilayered structure of the AR coating film enables increased transmittance of light in the visible region and selective transmittance or reflectance of light of a certain wavelength [186,187]. Often, to achieve zero reflectance at the interface between the film and the surrounding medium, the AR coating film needs to satisfy two requirements : the optical thickness of the AR coating film should be equal to $\lambda/(4n_{\mathrm{AR-film}})$, and the effective refractive index of the AR coating should be $n_{\mathrm{AR-film}} = \sqrt{n_{\mathrm{air}} n_{\mathrm{substrate}}}$, where n_{air} and $n_{\mathrm{substrate}}$ are the refractive index of air and substrate, respectively, and λ is the wavelength of light source [188]. Knowledge of the effective index of metal-polymer multilayer film is thus crucial for effectively verifying whether the structured film meets the application requirements or not. Hence, measurement of the effective RI of such bilayer films is essential for a detailed understanding of their optical properties and provides the foundation for developing new materials.

In existing literature, various methods of RI measurement have been proposed. For example, the methods reported only for single layer systems are low coherence interferometry [189–191], focus tracking method [192], the combination of low-coherence interferometry and confocal optics [192] and multi-wavelength interferometry [193], and methods for multilayer system are low-coherence confocal interference microscope [194], the combination of a confocal microscope and low-coherence interference [195], wavelength-scanning interferometer with a confocal microscope [196]. However, the majority of methods are time consuming and cumbersome, or even too complex to implement [197]. The techniques that are most applicable for analyzing thin films adhered to soft substrates are surface plasmon resonance (SPR) and ellipsometry. SPR measures the optical thickness, which is based on the Fresnel formulas combined with those of the plasmons [198]. Ellipsometry is commonly used to determine the refractive index and/or thickness of polymer layers, and it provides direct experimental access to the amplitude and phase of the reflected light.

However, the variables directly measured with the ellipsometer are the two elliptical angles Δ and Ψ, which are abstract [199]. Therefore, they cannot be directly translated into the refractive index and thickness, and the model parameter needs to be adjusted several times to finally obtain the refractive index and film thickness. Furthermore, ellipsometry provides precise measurements if the thickness of the bilayer is less than the wavelength of the incident light [199] and thus restrictive in nature for many practical purposes.

To circumvent existing challenges in refractive index measurement, in this work, we report a simple and efficient methodology to measure the refractive index of nanometer scale silver (Ag) and gold (Au) films on soft PDMS coatings: Dual-Wavelength Reflected Interference Contrast Microscopy (DW - RICM) signature of a spherical glass probe. Using intensity information from interference signature and the known profile of the glass sphere, we experimentally investigate the refractive index of PDMS thick/thin coatings with Ag/Au film deposition of varying deposition time. Simultaneously, we quantify the elastic modulus of the bilayer films from the contact radius measured from the same experiment.

4.2 Experimental

4.2.1 Fabrication of soft substrates

Soft substrates were fabricated by spin-coating silicone elastomer (PDMS) (Sylgard 184, Dow Corning) on glass slides (Microscope slides, Sail Brand, dimensions: 76.2 mm×25.4 mm×1 mm). The glass slides were thoroughly rinsed with acetone, IPA, ethanol, and DI water, then dried with N_2 gas before use. The silicone elastomer consists of two components: A (polymer) and B (crosslinker). To obtain different Young's modulus of soft substrates, the PDMS solution was prepared by mixing A and B components at weight ratios of 10:1 and 20:1, respectively. The solution was uniformly mixed and degassed by using a planetary mixer (ARE-310, Thinky Corporation) for 10 min. 0.7 mL of each uncured elastomer solution was spin-coated on clean glass slides at 3000 rpm to obtain a coating thickness of 35 μm. For comparison, we also prepared soft substrates with 1 mm coating

thickness using drop casting technique. All the substrates were cured at 80 ℃ for 14 hrs. Consequently, the substrates were kept at room temperature for 1 day before use. The PDMS substrates of different mixing ratios and coating thickness were named as P_{10} (35 μm), P_{20} (35 μm), P_{10} (1 mm) and P_{20} (1 mm). The elastic moduli of the soft substrates were measured by tensile testing using universal material tester (UMT, T1377, Centre for Tribology Inc.). The PDMS substrate of dimension 300 mm (L) x 1 mm (W) x 1 mm (H) was installed between the moving stage and the double clamps gripper. Then a tensile force through a 1 kg load cell was applied to the PDMS substrate at a constant speed of 8 mm/min. The tensile force and elongation were recorded during the experiment. From the obtained stress-strain curves, the Young's modulus was calculated (B4.1 and Figure B4-1, Appendix B).

4.2.2 Deposition of metal film

A silver (Ag) thin film was deposited on the surface of the PDMS coatings in a magnetron sputter-coater (Denton Vacuum Desk II) at 15 mA at an ambient temperature of 22-24 ℃. The sputter coating rate is 1.5 Å/s, calibrated by measuring the Ag thickness deposited on the glass slide for 120 s using atomic force microscopy (Pacific Nanotechnology AFM Nano-R) with a stylus profilometer (Veeco Dektak 8) (B4.2 and Figure B4-2(a), Appendix B).

For PDMS substrates, direct thickness measurements of Ag films were not reliable because the masking procedure (covered glass slide) induced surface wrinkling (Figure B4-2(b), Appendix B). Therefore, the Ag film thickness on PDMS substrates was controlled by deposition time at a calibrated rate of 1.5 Å/s. By controlling the sputter coating time with 10 s, 30 s, 90 s, and 120 s, we coated Ag on all the soft substrates. The Ag sputtered PDMS coatings are named as P_{10} (35 μm) - Ag(10s), P_{20} (35 μm) - Ag(10s), P_{10} (1 mm) - Ag(10s) and so on. The morphology of the Ag/PDMS substrates was inspected by a field emission scanning electron microscopy (Zeiss UltraPlus FESEMs (with EDX)) (Figure B4-3, Appendix B). The bare PDMS surface (P_{10} (35 μm)) exhibits a smooth and featureless morphology. After 60 s of sputter deposition, the PDMS surface (P_{10} (35 μm) - Ag(60s)) is

fully covered with discrete silver clusters. With increased deposition time to 120 s, a continuous and uniform Ag thin film coverage across the PDMS substrate (P_{10} (35 μm) - Ag(120s)). In a similar manner, thin Au films are also deposited on the PDMS substrates for deposition times of 30 s, 60 s, and 120 s and will be referred to as P_{10} (35 μm) - Au(30s), P_{20} (35 μm) - Au(30s), and so on.

4.2.3 RICM measurements

A custom-built DW-RICM set-up based on LSM 800 (Zeiss, Carl Zeiss, Germany) with two focused monochromatic light beams of wavelengths (488 nm (green) and 561 nm (red)) was employed (Figure 4-1(a)). First, a plane glass sphere (McMaster-Carr, 8996 K24) of the radius 2600 μm, the weight of 1.26 g, and refractive index of 1.47 was placed on a freshly cleaned glass slide for calibration (Figure 4-1(b)). An objective lens with magnification 10x and a numerical aperture (NA) 0.3 (EC Plan-Neofluar, Carl Zeiss, Canada) was used. The interface to be observed was raster scanned simultaneously with the two available focused monochromatic laser beams (488 nm (green) and 561 nm (red)) using a galvanometric mirror (GM). Here, the plane of observation is the glass slide - air interface. Light rays reflecting from the glass sphere - air interface and glass slide - air interface consequently interfere to provide alternate dark and bright fringes. To evaluate the potential impact of uncertainties in the glass sphere radius and refractive index on RICM fringe analysis (height estimation), an error propagation analysis was performed. The results show that the effects of glass sphere radius tolerance (~ ± 2.5 μm) and refractive index uncertainty are negligible (B4.4, Appendix B). Therefore, in the following analysis, the glass sphere is assumed to be perfectly spherical, and its refractive index is taken to be equivalent to that of the glass slide, denoted as n_1. Since both the glass slide and the glass sphere are rigid materials with the same refractive index, the contact region appears dark in the interference images. The reflected light, i.e., the interference pattern is captured through the pinhole of the microscope. Based on the two different light beam wavelengths, the reflected and interference light is split into two signals by a dichroic mirror (DM) and collected by two

photomultiplier tubes (PMT). Finally, the detected optical signal was converted into a digital image by the in-built deconvolution algorithm of the LSM system. Further, to acquire higher resolution images, the pixel size is refined to 1240 pixels × 1240 pixels (1 pixel = 0.52 µm). By doing this calibration experiment, the base plane is identified and will be later used during RICM measurements in confocal mode.

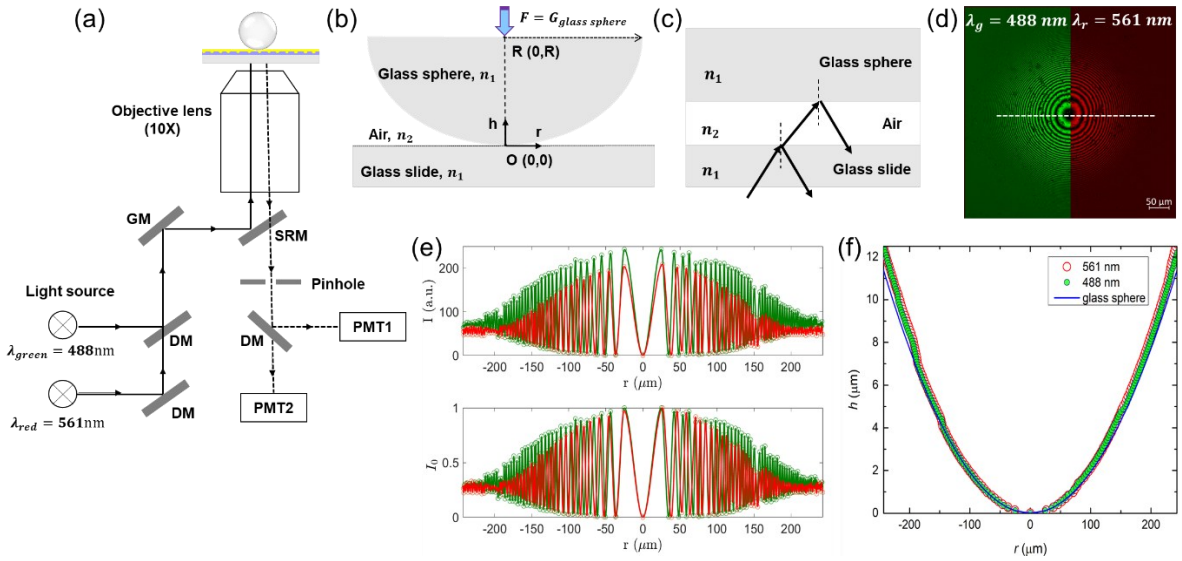


Figure 4-1 (a) Schematic of dual wavelength reflection interference contrast microscopy setup. The light sources are green (λ_g = 488 nm) and red (λ_r = 561 nm). SRM: Semi-refractive Mirror, GM: Galvanometric Mirror, HM: Half Mirror, DM: Dichroic Mirror, PMT: Photomultiplier Tube. (b) Schematic of the calibration experiment: a glass sphere atop a glass slide. n_1 and n_2 are the refractive indices of glass and air, respectively. (c) The curved glass profile represented as a series of three parallel dielectric layers with the air layer sandwiched between two glass layers. (d) Interference signature corresponding to green and red wavelengths for the system shown in (b). (e) Plot of raw (I (a.u.)) and normalized (I_0) intensity with radial location r for the slice shown in (d). (f) Plot of glass sphere profile for the interference signature shown in (d) and (e). The symbols represent the height extracted from experimentally obtained intensity profiles and the solid line represents the theoretical glass profile.

For the soft substrates, samples were kept on the same stage of the microscope. Since the PDMS coated glass slide has a finite coating thickness, it is paramount to identify the plane of contact upon placing the same glass sphere. Therefore, to obtain sufficient intensity information and clear images, imaging was performed in confocal mode, i.e., the Z-stack

multidimensional acquisition function was used to scan from the position of the upper interface of the glass slide that has the PDMS coated to a height approximately 44 μm above the free surface of the PDMS coating. Thus, for a 35 μm PDMS coating, the total scanned range is 79 μm and one slice is scanned at 1 μm interval. 80 slices per sample per experimental run is obtained, which is adequate to identify the interference planes(s) of interest. By comparing the change of fringes and light intensity of the 80 slices per sample, we choose the image where the focal plane is on the free surface of the PDMS coating. The pixel size was also set to 1240 pixels × 1240 pixels (1 pixel = 0.52 μm). Similarly, for Ag/Au coated soft substrates, samples were kept on the same stage of the microscope. The imaging was also performed in confocal mode, i.e., the Z-stack multidimensional acquisition function was used to scan from the position of the upper interface of the glass slide that has the PDMS coating to the height above the free surface of the Ag/PDMS coating, which is sufficient to identify the interference planes(s) of interest. The pixel size was kept consistent throughout.

The basic principle of DW-RICM is summarized in our previous works [19,57,79,200]and existing literature [78,201,202]. Briefly, when a uniform monochromatic plane wave passes through a multilayer sample, the light will reflect from different interfaces. For example, in our calibration experiment of glass - glass contact (glass sphere in contact with glass slide), light reflected from the glass slide air interface (intensity I_1) and the air - glass sphere interface (intensity I_2) interferes. The resultant (measured) light intensity I for any vertical position h can be expressed as,

$$I(h,\lambda) = I_1 + I_2 + 2\sqrt{I_1 I_2}\cos(4\pi nh/\lambda + \varphi) \qquad (4\text{-}1)$$

where φ is the phase difference, n is the refractive index and λ is the wavelength. The unknown intensities I_1 and I_2 can be expressed as, $I_{\max} = I_1 + I_2 + 2\sqrt{I_1 I_2}$ and $I_{\min} = I_1 + I_2 - 2\sqrt{I_1 I_2}$. Thus, the normalized intensity is $(I - I_{min})/(I_{max} - I_{min}) = [\cos(4\pi nh/\lambda) + 1]/2$. Using simultaneous intensity information from the two wavelengths, the height information of any point in the interface can be unambiguously resolved. For the simplest case, when $4\pi nh/\lambda = m\pi$, the height difference between

consecutive bright and dark fringes of the same fringe order m can be expressed as,

$$\Delta h = m\lambda/4n \quad (4\text{-}2)$$

Consequently, by counting the number of bright and dark fringes, the entire profile can be extracted. For the glass sphere/glass slide contact system, since the air - glass sphere interface is curved, we assume that the curved surface consists of a succession of infinitesimal horizontal steps [203]. The glass - glass system is modeled by a 3-layer of parallel dielectric layers (Figure 4-1(c)). The resultant interference from the two interfaces exhibits distinctive bright and dark fringes (see figure 4-1(d)). The raw light intensity I (a.u.) and normalized light intensity I_0 along a particular slice of the interference pattern are shown in Figure 4-1(e). From the intensity distribution, the radial locations of peaks and valleys are obtained. Here, the contact point $O(0, 0)$ of the glass sphere with the glass slide is a dark point (valley) corresponding to zero light intensity (central point in figure 4-1(d)) and thus used as reference, i.e., $h = 0$. Since only air exists between the two interfaces, $n_2 = n_{air} = 1$. Thus, using $n = 1$ in Eq. 4-2, we extract the height of the glass sphere corresponding to both wavelengths. As shown in Figure 4-1(f), the extracted profile is in excellent agreement with the theoretical profile of the glass sphere, i.e., $h(r) = 2600 - \sqrt{2600^2 - r^2}$.

4.3 Results and discussion

In order to predict the elasticity and refractive index of Ag/Au sputtered PDMS coatings, we first performed some baseline experiments on pristine PDMS coatings without any metal thin film deposition. For calculating the elastic properties, the Hertz [14] or JKR [15] theory is typically used whereby the Young's modulus is extracted from the measurement of the contact radius of the glass probe [28]. Considering Hertz theory [14], the reduced Young's modulus can be expressed as $E^* \sim (3FR/(4a^3))$, where F is the applied load, $R = (1/R_1 + 1/R_2)^{-1}$ is the effective radius, a is the contact radius, $E^* = \left[(1 - {\vartheta_1}^2)/E_1 + (1 - {\vartheta_2}^2)/E_2\right]^{-1}$. For our glass sphere- Ag/PDMS system, the applied load is the weight of the glass sphere ($F = mg = 1.24$ mN). E_1 and E_2 are the Young's modulus of the glass sphere (64 MPa)

and soft substrate, respectively. ϑ_1 and ϑ_2 are their Poisson's ratio (both ~ 0.5). $R = (1/R_1 + 1/R_2)^{-1} \approx R_1 = R_0$, where R_1 and R_2 are the radius of the glass sphere (R_0 = 2600 μm) and soft substrate (+∞). $E^* \approx E_2$, since $1/E_1 \approx 0$. Therefore, the Hertz equation relevant to our elasticity calculation can be expressed as,

$$E_{\mathrm{PDMS,PDMS/Ag}} = (3FR_0)/(4a^3) \quad (4\text{-}3)$$

Further, to predict the refractive index of the PDMS coatings, we use the known shape of the glass sphere beyond the region of contact and subsequently calculate *n* using Eq. 4-2.

4.3.1 Pristine PDMS coating

Due to finite elasticity of the PDMS coating, a glass sphere presents a finite deformation of the PDMS free surface upon contact due to its weight. The distinctive bright and dark interference fringes of the glass PDMS contact are shown in Figure 4-2(c). The central dark zone represents the contact zone of the glass sphere and PDMS. The resultant raw light intensity I (a.u.) and normalized light intensity I_0 are shown in Figure 4-2(d). For PDMS 10:1 substrate, upon evaluating the central dark zone with intensity of approximately zero, we found the contact diameter to be 207.4 μm. The diameter measured using RICM is consistent with brightfield microscopy measurements, as well as with experimentally observed previously [19]. Thus, the average contact radius is 103.7 μm. Consequently, using Eq. 4-3, we found that Young's modulus of PDMS 10:1 to be around 1.62 MPa, which is close to the value obtained from tensile testing as well as with existing literature [171,204]. Further, based on the Hertz contact theory, we calculate the deformation of the PDMS due to the glass sphere $\delta \sim a^2/R_0 \approx 4.1$ μm.

Based on the above analysis, we recreate the schematic of the glass - soft contact system at stable state (Figure 4-2(a)). Since the glass sphere deforms the PDMS free surface, the origin of coordinate *O*(0, 0) is inside the glass sphere and the free surface of the PDMS coating is at the point where it meets the glass sphere (h = 0). The lowest point of the glass sphere in contact

with the PDMS is thus at D $\left(0, \delta \approx \sqrt{R_0^2 - a^2} - R_0\right)$ and the point A (a, 0)is at the edge of the contact region between the glass sphere and the PDMS. Consequently, upon RICM imaging, the interfaces that can reflect light are the glass sphere - air, air - PDMS, and PDMS - glass slide. Moreover, it is expected that small deformations will occur at the PDMS - air interface around the contact zone with the glass sphere. However, the deformation of the PDMS - air interface around the contact zone with the glass sphere is mostly obscured by background reflections from the glass sphere above. Since the majority of the interference signature reflects the glass sphere profile and any possible deformation in the PDMS air interface is suppressed, they can be neglected. At the same time, constructing the glass sphere profile from the obtained interference signature is no longer straight forward like the previous case, i.e., glass sphere on a glass slide. Since both the PDMS and air layers contribute to the observed interference fringes, the glass - soft system can be modeled using four parallel dielectric layers (Figure 4-2(b)).

In an ideal scenario, the height extraction from intensity can be extracted simply using n = 1 (air) in Eq. 4-2. However, due to the presence of composite interfaces, we observe that using n = 1 (air) does not fit the theoretical glass sphere profile (Figure B4-4, Appendix B). Neither does n = 1.41 (PDMS) provides accurate extraction of the glass profile (Figure B4-4, Appendix B). Thus, to account for the roles of all the interfaces, we use an effective refractive index, $n_{\text{eff}} = \sqrt{n_{\text{air}} n_{\text{PDMS}}}$ (B4-6 and Figure B4-4, Appendix B), which is conceptually similar to the analytical approximations for effective indices of thin-layer structures reported by A.V. Kozar (2009) [205]. As shown in Figure 4-2(e), the height extracted using n_{eff} in Eq. 4-2 ($\Delta h_{\text{g,r}} = m\lambda_{\text{g,r}}/4\sqrt{n_{\text{air}} n_{\text{PDMS}}}$) can fit the theoretical glass sphere profile $\left(h = \sqrt{2600^2 - a^2} - \sqrt{2600^2 - r^2}\right)$. A detailed description of the data processing procedure is given in Appendix B (B4.7, Appendix B). Further, since the refractive index is wavelength dependent, we used different n_{PDMS} values for the green (n_{g}) and red (n_{r}) wavelengths while extracting the glass

sphere profile. For PDMS 10:1, the best-fit height values were observed for n_g = 1.42 and n_r = 1.42.

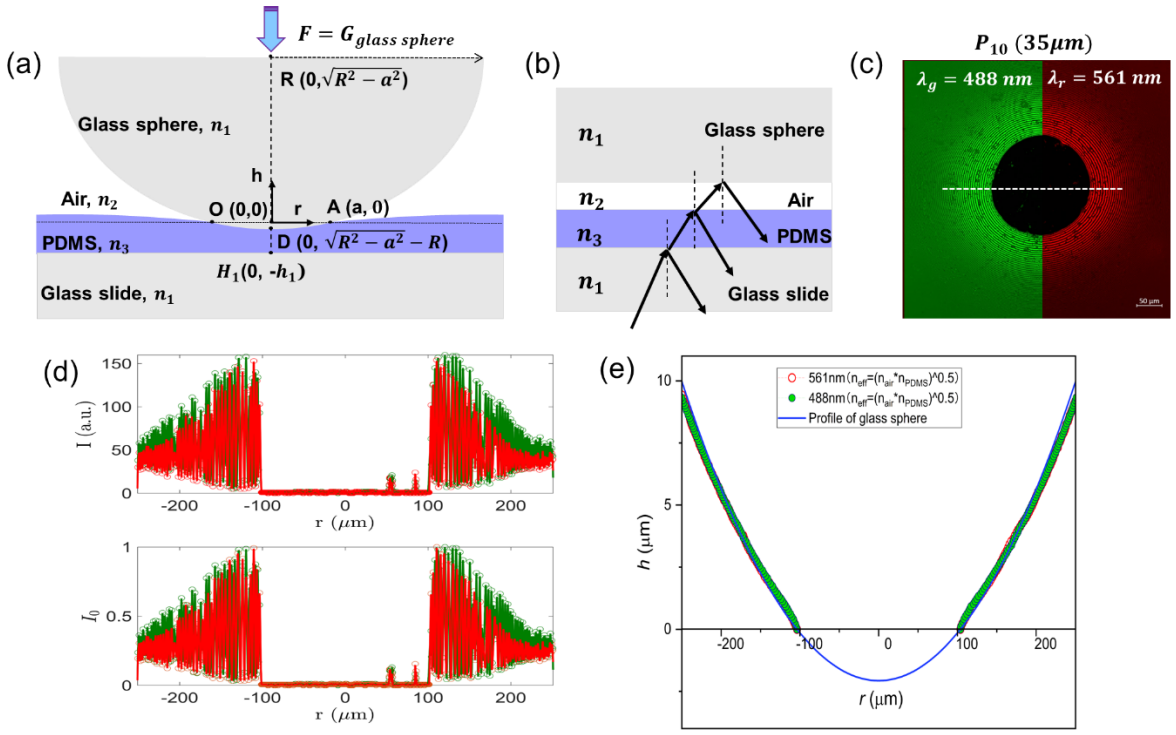


Figure 4-2 (a) Schematic of the glass sphere (R_0 = 2.6 mm) on soft PDMS (10:1) coating of finite coating thickness h_1 = 35 μm. n_1, n_2, and n_3 are the refractive indices of glass, air, and PDMS, respectively. (b) Optical multilayer model used for predicting the curved surface of the glass sphere on the soft substrate shown in (a). (c) Unprocessed interference signature corresponding to the contact system shown in (a). (d) Plot of raw (I) and normalized (I_0) intensity with radial location r for the slice shown in (c). (e) Plot of glass sphere profile for the interference signature shown in (d) along the dashed line. The symbols represent the height extracted using $\Delta h_{g,r} = m\lambda_{g,r}/(4\sqrt{n_{air}n_{PDMS}})$ and the solid lines represent the theoretical glass profile, i.e., $h = \sqrt{2600^2 - a^2} - \sqrt{2600^2 - r^2}$. Here, a is the contact radius.

Here, we verify whether our assumption of the effective refractive index holds for PDMS substrates with different elasticity and coating thickness. It is expected that softer PDMS will create a larger contact area and indentation depth but the unperturbed glass sphere profile above the PDMS will remain unchanged. As shown in Figure 4-3, we observe that using

the effective refractive index successfully predicts the glass sphere profile for P_{20} (35 μm) substrate. Further, using interference intensity variation, we observe the contact radius to be a = 108.2 μm for P_{20} (35 μm). Thus, using Eq. 4-3, we calculate the Young's modulus to be 1.43 MPa. For comparison, we also evaluated the contact radius using the JKR theory with literature reported values of the work of adhesion for PDMS-glass contact. Yu *et al.* (2015) [206] reported $w \approx 64.6 \pm 3.2$ mJ/m^2 for PDMS (10:1)-glass and $w \approx 87.8 \pm 4.3$ mJ/m^2 for PDMS (20:1)-glass, measured by dynamic mechanical analysis. Using these values, the JKR theory predicts contact radii of 170.5 μm (P_{10}) and 188.5 μm (P_{20}), and the DMT theory predicts contact radii of 145.8 μm (P_{10}) and 161.4 μm (P_{20}). Both significantly larger than the experimental values (103.7 μm for P_{10} and 106.7 μm for P_{20}) as well as the Hertzian predictions (104.7 μm for P_{10} and 108.2 μm for P_{20}). These comparisons indicate that the effect of adhesion on contact radius in our PDMS-glass system may be negligible, and Hertz theory provides a more appropriate framework. Detailed calculations are provided in Appendix B (B4.8, Appendix B). The closer agreement with Hertzian predictions can be attributed to the supporting effect of the rigid glass substrate, which increases the effective modulus of the PDMS film, while interfacial adhesion seems to play an insignificant role. Independent methods to assess the work of adhesion, such as pull-off tests or surface force apparatus measurements, could also be employed in future studies to verify the negligible role of adhesion in similar systems [207].

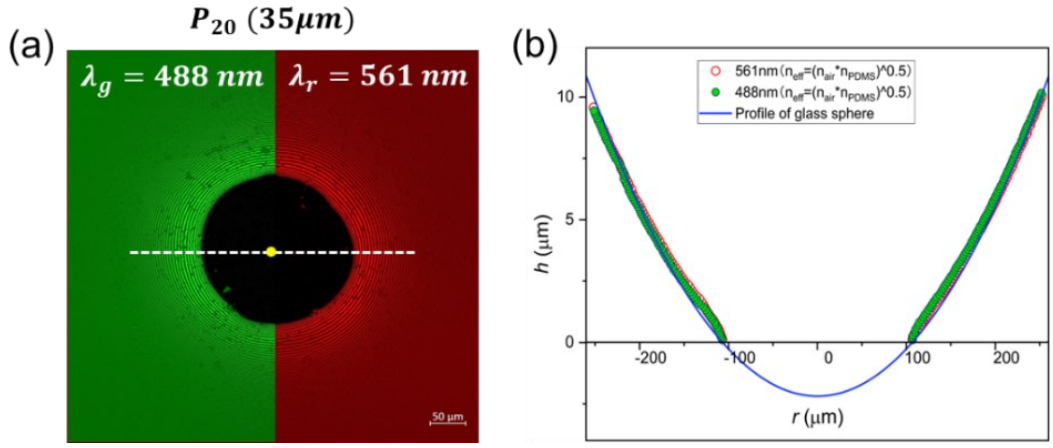


Figure 4-3 (a) Interference signature of glass sphere contact with the soft substrate P_{20} (35 µm). (b) Plot of glass sphere profile for the interference signature shown in (a) along the dashed line. The symbols represent the height extracted using $\Delta h_{g,r} = m\lambda_{g,r}/4\sqrt{n_{air}n_{PDMS}}$ and the solid lines represent the theoretical glass profile.

To further verify the applicability and accuracy of our proposed technique, we consider 1 mm thick coatings of the used soft substrates (P_{10}, P_{20}). The contact radius of P_{10} (1 mm) and P_{10} (1 mm) are found be 145.1 µm and 158.9 µm, respectively (Figure 4-4). Consequently, the modulus of elasticity of the corresponding soft substrates calculated from the Hertzian contact theory provides values of 0.59 MPa and 0.45 MPa. The Young's moduli obtained are smaller than the corresponding thinner substrates, i.e., P_{10} (35 µm) and P_{20} (35 µm). The observed results are reasonable since thicker substrates are likely to undergo larger deformation and have a larger contact area when subjected to the same glass sphere. Further, using the effective refractive index, we were able to obtain the large sphere profile (Figure 4-4(b) and (d)) for thicker coatings as well, albeit with slightly lower n_g and n_r values compared to the thinner films.

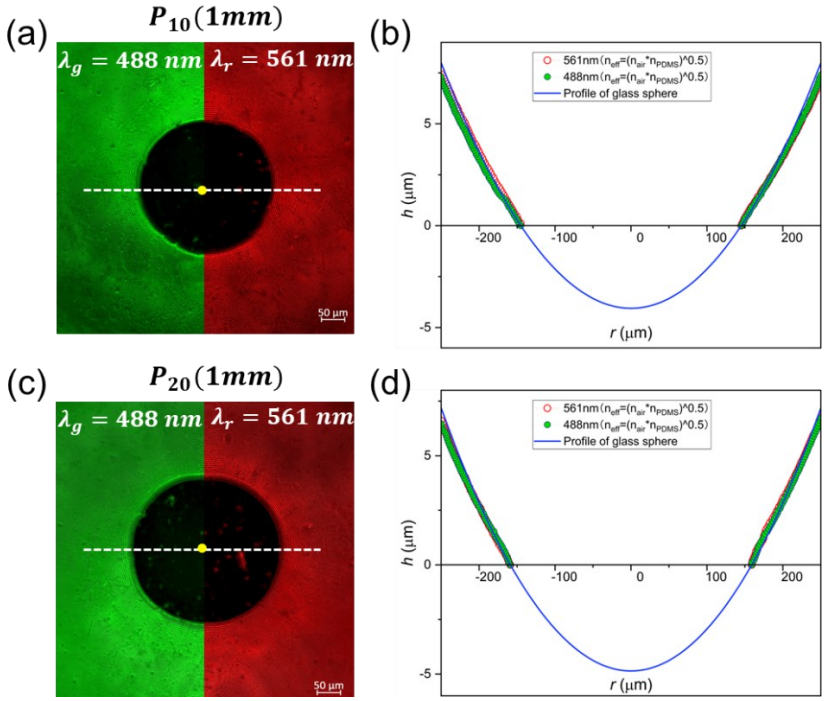


Figure 4-4 (a) and (c) Interference signatures of glass spheres in contact with thick, soft substrates P_{10}(1 mm) and P_{20}(1 mm). (b) and (d) Plots of glass sphere profiles for the interference signature shown in (a) and (c) along the dashed lines. The symbols represent the height extracted using $\Delta h_{g,r} = m\lambda_{g,r}/4\sqrt{n_{air}n_{PDMS}}$ and the solid lines represent the theoretical glass profile.

It should be noted here that the effective refractive index formulation is ideally applicable for medium thickness(s) less than the wavelength of the light sources [188]. However, in the present study, we observe that the applicability of the effective refractive index formulation is surprisingly robust to large thickness values of the existing media, i.e., air and PDMS. Further, as an additional check, we investigated whether this formulation holds upon changing one of the mediums involved. Consequently, we submerged the glass sphere-PDMS system under water and observed that the glass sphere profile could be accurately extracted using the effective refractive index expression, i.e., $n_{\text{eff}} = \sqrt{n_{\text{water}}n_{\text{PDMS}}}$ (Figure B4-5, Appendix B). However, a detailed theoretical justification is beyond the scope of the present work.

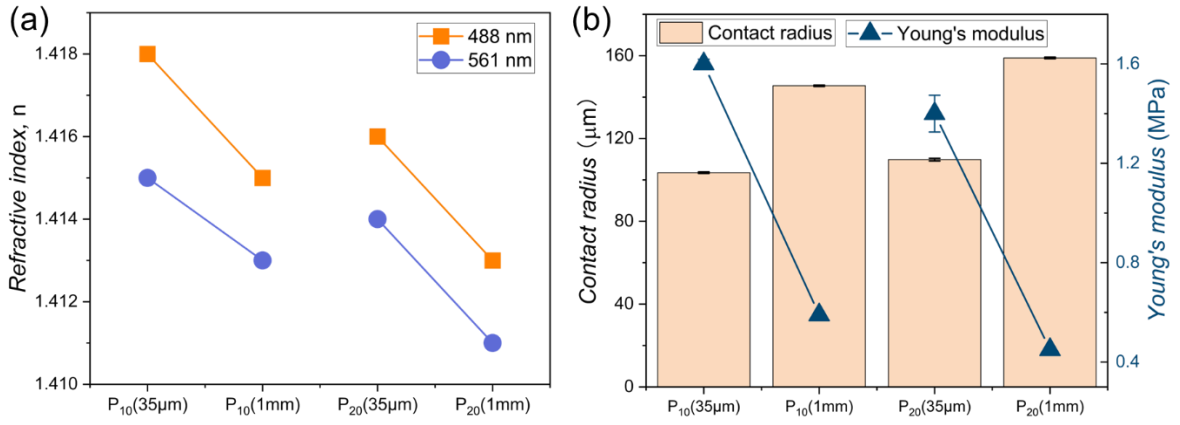


Figure 4-5 (a) The refractive index of soft substrates predicted by fitting the profile of the glass sphere. (b) The contact radius of the spherical glass probe on the soft substrates surface and the calculated elastic (Young's) modulus based on the Hertz theory (Eq. 4-3). Error bars represent standard deviations calculated from three independent experiments. In some cases, they are smaller than the symbol size and thus not visible.

In Figure 4-5, we highlight the predicted refractive indices and Young's moduli for pristine PDMS coatings. As shown in Figure 4-5(a), the predicted refractive index of the soft substrates decreases with increasing substrate thickness and decreasing weight of the curing agent, i.e., decreasing stiffness. The dependence on coating thickness is due to the fact that for the spin coated sample, the polymer chain space configuration is more orderly because of rotational speed, resulting in a greater density of polymer chain stacking per unit volume, and thus its refractive index is larger. For 1 mm thick coatings prepared by drop casting, the polymer chain conformation is more disordered, and the overall density decreases, resulting in a smaller refractive index. A lower degree of curing means a smaller molecular mass in general and therefore a smaller mass density than a soft substrate with a higher degree of curing. The dependence of the refractive index on material density is given by the Lorentz-Lorentz equation [168,169,203].

$$\frac{n^2-1}{n^2+2}=\frac{4\pi\alpha N_a}{3M\varepsilon_0}\rho_m \tag{4-4}$$

where, ρ_{m} is the mass density, N_{a} is the Avogadro number, M is the molecular weight, ϵ_0 is the vacuum permittivity, and α is the average polarizability of the polymer. For spin coated PDMS, ρ_{m} is higher, leading to higher n. Here, we note that a more rigorous treatment of refractive index - density dependence is beyond the scope of the present work. Further, the refractive index exhibits wavelength dependence: decreasing with increasing wavelength. This behavior is consistent with existing literature where a similar wavelength dependence of refractive index was observed for PDMS [208,209]. For the predicted Young's modulus, the observed trend (Figure 4-5(b)), i.e., decreasing magnitudes with increasing thickness and polymer ratio is expected and well established in the literature [171,172,210].

4.3.2 Ag film on PDMS coating

In the preceding sections, we have demonstrated the applicability of the proposed method to accurately predict Young's modulus and refractive index of pristine PDMS coatings. Here, we will extend this technique, i.e., using RICM observations of a spherical glass probe, to empirically calculate the refractive indices and elasticity of Ag film of nanoscale thickness sputtered on PDMS coatings of different curing ratio, Ag sputtering time and PDMS coating thickness.

Based on the same analysis method, we recreate the schematic of a glass sphere settled on the surface of the Ag sputtered soft PDMS coating in Figure 4-6(a). As the thickness of the Ag film is extremely thin ($\leqslant$ 18 nm), which is far below the wavelengths of 488 nm and 561 nm, the majority of the incident light can pass through the Ag sputtered PDMS layer and reach the edge of the glass sphere. And most of the reflected light can also penetrate the Ag coated PDMS layer and interfere with other reflected light, and finally be received by the PMT. In Figure 4-6(b), we show the optical multilayer model used in the glass- Ag coated PDMS substrate contact system. Thus, the effective refractive index for the present condition is $n_{\mathrm{eff}} = \sqrt{n_{\mathrm{air}} n_{Ag/PDMS}}$. We show two test cases, where the glass sphere was placed on two different Ag-on-PDMS substrates, namely, P_{10} (35 μm) – Ag (10s) (Figures 4-6(c)-(e) and P_{20} (35 μm)

– Ag (60s) (Figures 4-6(f)-(h)) and extracted its profile in the undisturbed part, i.e., above the free surface of Ag film. By using our effective refractive index expression and fitting the theoretical profile of the glass sphere, the predicted refractive index, i.e., $n_{Ag/PDMS}$ values for P_{10} (35 µm) – Ag (10s) are 1.30 (488 nm) and 1.28 (561 nm) and that of P_{20} (35 µm) – Ag (60s) are 1.18 (488 nm) and 1.16 (561 nm). It should be noted here that the above-mentioned n values for Ag-on-PDMS substrates are lower than that of pristine PDMS substrates ($n_{g,\,r} \approx 1.4$) but considerably higher than that of bare Ag film ($n_g = 0.08$, $n_r = 0.12$, Figure B4-6, Appendix B). Further, from the obtained RICM signature, the contact radius of P_{10} (35 µm) – Ag (10s) and P_{20} (35 µm) – Ag (60s) is found to be 78.8 µm and 86.1 µm, respectively. In contrast to pristine PDMS coatings, the contact area is no longer an all-black center, but a brighter contact center as the Ag sputter coating time increases (Figure 4-6(f)). The corresponding elastic moduli calculated are 3.71 MPa and 2.81 MPa, which are higher than the pristine PDMS substrates. Consequently, we use this approach to calculate the refractive index empirically and elastic modulus of Ag sputtered thick/thin PDMS coatings of different elasticity and sputtering time.

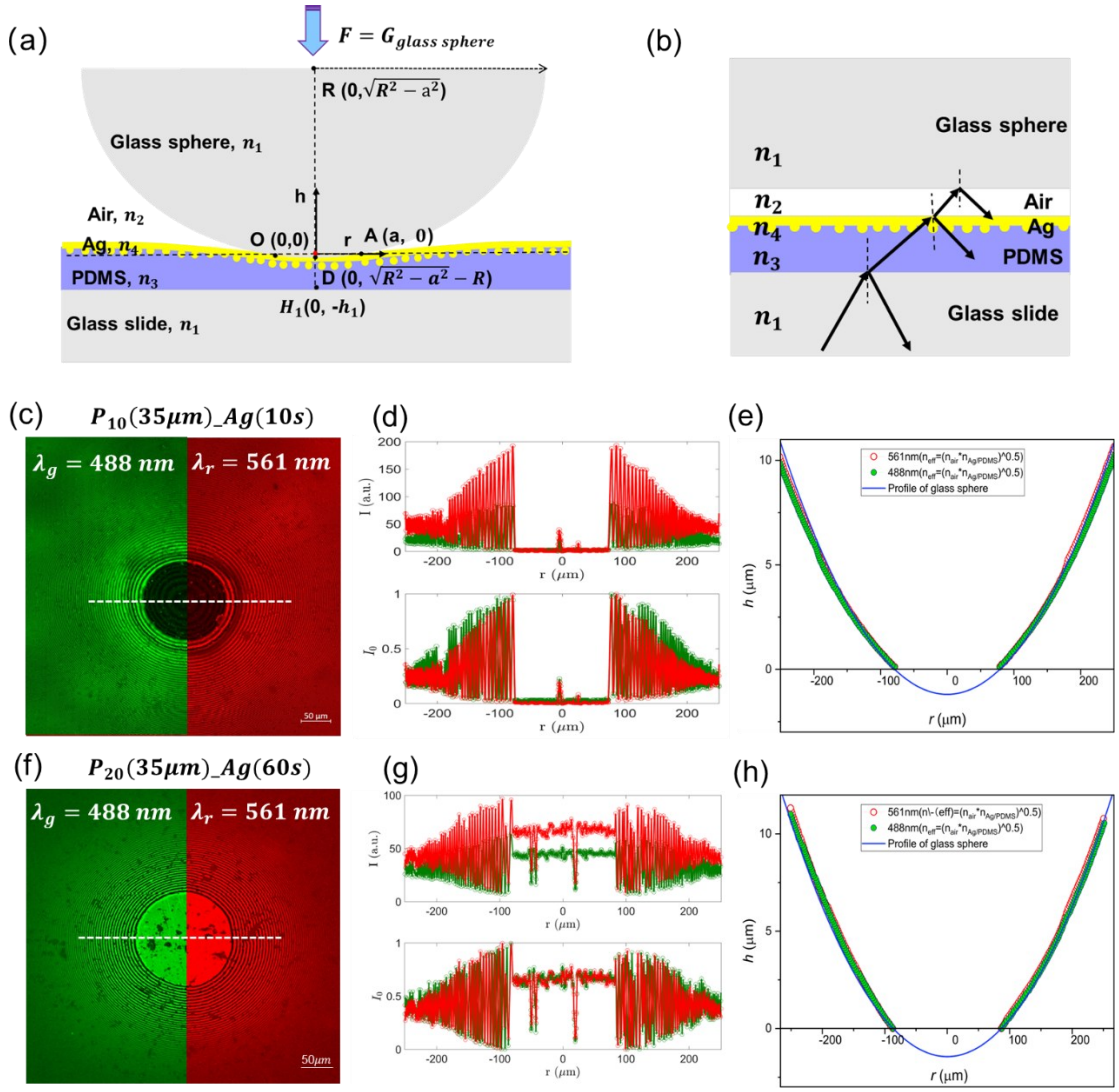


Figure 4-6 (a) Schematic of a glass sphere atop a Ag coated PDMS film of finite thickness h_1. n_1, n_2, n_3, and n_4 are the refractive indices of glass, air, PDMS, and Ag, respectively. (b) Optical multilayer model used for predicting the curved surface of the glass sphere on the soft substrate shown in (a). (c) and (f) Interference signatures of glass sphere in contact with Ag coated PDMS films, P_{10} (35 μm) - Ag (10s) and P_{20} (35 μm) - Ag (10s). (d) and (g) Plots of raw (I (a.u.)) and normalized (I_0) intensity with radial location r for the slices shown in (c) and (f). (e) and (h) Plots of glass sphere profile for the interference signature shown in (c) and (f). The symbols represent the heights extracted from experimentally obtained intensity profiles using $\Delta h_{g,r} = m\lambda_{g,r}/4\sqrt{n_{air}n_{Ag/PDMS}}$ and the solid lines represent the theoretical glass profile.

As shown in Figures 4-7(a) and (b), we observe that the refractive index of Ag-on-PDMS substrates decreases with increasing sputtering time, i.e., increasing Ag film thickness. The behavior is consistent for the thicker PDMS coatings as well (Figure 4-7(c)). Also, the refractive indices of Ag-on-PDMS substrates are lower than the corresponding pristine PDMS substrates for all cases. The observed decrease of RI for Ag sputtered PDMS is due to boundary effects [167,180]. The RI of metallic silver is much smaller than that of PDMS. Thus, its deposition changes the interfacial properties of PDMS coatings, which finally contributes to the decrease of effective RI of the whole structure. Briefly, at the early stage of silver deposition process, Ag particles partially diffuse inside the PDMS coating and combine with the elastomer to form PDMS-encapsulated nanoparticles [211,212]. Subsequently, with increasing deposition time, more Ag will appear on the top surface of the PDMS coating, forming silver clusters [211–213]. When the deposition time is long enough, more Ag will cover the cluster and form a continuous, thin Ag film of certain thickness. The different metal-polymer structures thus formed contribute to different decreasing trends of effective RI for P_{10} and P_{20} substrates with Ag deposition (Figures 4-7(a) and (b)). Further, similar to pristine PDMS coatings, here also, the predicted refractive index corresponding to the green wavelength is marginally higher than the one for the red wavelength. In this regard, exceptions are observed for a few cases, i.e., P_{20} (35 µm) – Ag (10s) and P_{20} (35 µm) – Ag (90s) substrates (Figure 4-7(b)). On the other hand, the measured contact radii of glass spheres on Ag-on-PDMS substrates are lower than that observed on pristine PDMS substrates and monotonically decreases with increasing Ag sputtering time (Figures 4-7(d)-(e)). Further details on the variation of glass sphere profile and contact radius for different Ag sputtered thick/thin PDMS coatings are included in the Appendix B (Figures B4-7-11, Appendix B). Consequently, the predicted Young's modulus of Ag-on-PDMS substrates increases with increasing sputtering time (Figures 4-7(d)-(e)). The trend is consistent for thick PDMS coatings as well (Figure 4-7(f)). For the predicted elastic modulus of Ag-on-PDMS substrates, we consistently used the Hertz theory. Using JKR theory provides an overestimation for elastic modulus values (Figure B4-12, Appendix B). As a result,

we can safely assume that the role of adhesion is negligible since the PDMS substrates used are on the stiffer limit rather than very soft.

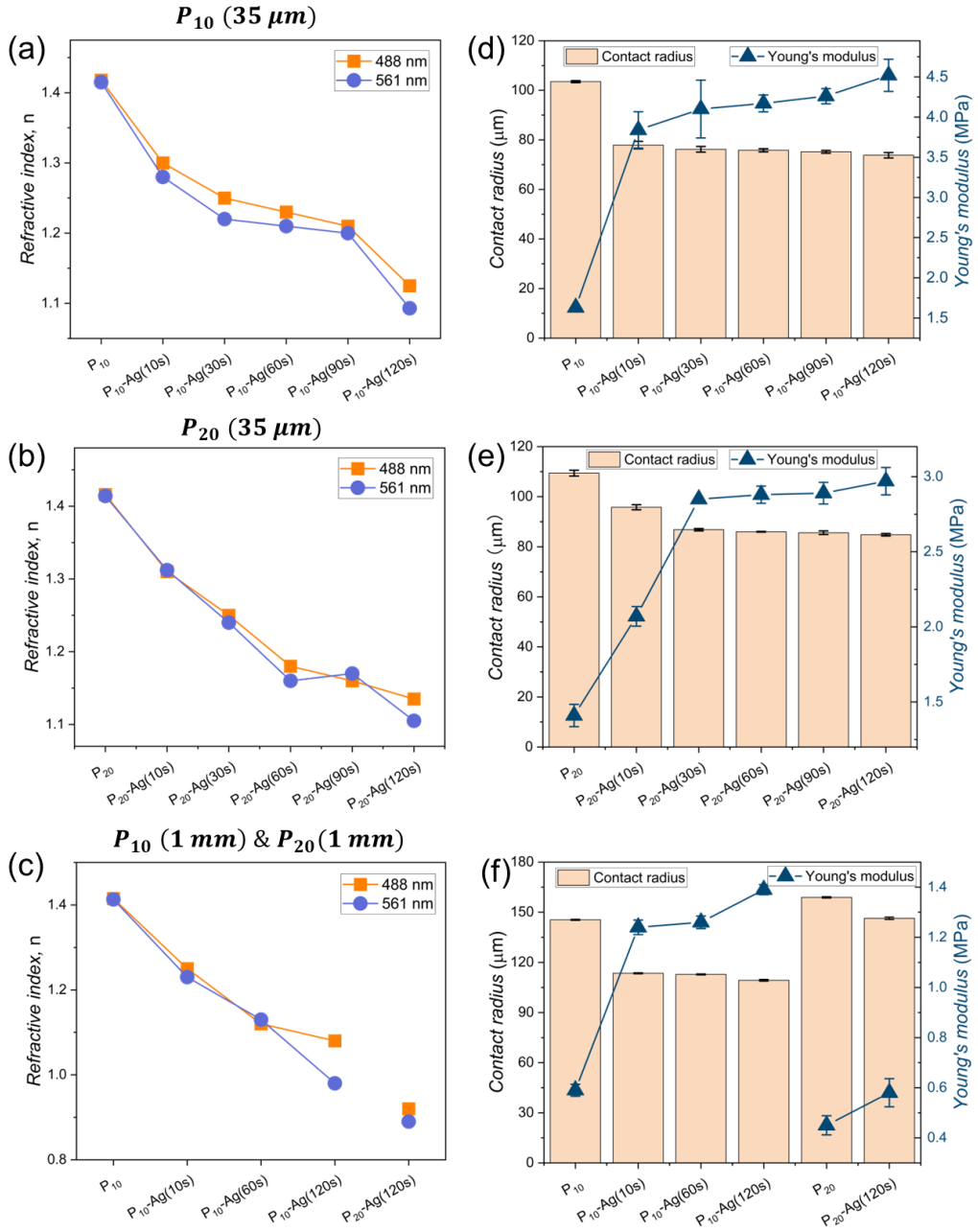


Figure 4-7 (a) Variation of the refractive index corresponding to both green and red wavelengths with Ag sputtering time for 35 μm thin PDMS 10:1 substrate. (b) Variation of the refractive index corresponding to both

green and red wavelengths with Ag sputtering time for 35 µm thin PDMS 20:1 substrate. (c) Variation of the refractive index corresponding to both green and red wavelengths with Ag sputtering time for 1mm thick PDMS 10:1 and PDMS 20:1 substrate. (d) Variation of experimentally obtained contact radius of glass probe and calculated Young's modulus (using Hertz theory) with Ag sputtering time for 35 µm thin PDMS 10:1 substrate. (e) Variation of experimentally obtained contact radius of glass probe and calculated Young's modulus (using Hertz theory) with Ag sputtering time for 35 µm thin PDMS 20:1 substrate. (f) Variation of experimentally obtained contact radius of glass probe and calculated Young's modulus (using Hertz theory) with Ag sputtering time for 1mm thick PDMS 10:1 and PDMS 20:1 substrate. Error bars represent standard deviations calculated from three independent experiments. In some cases, they are smaller than the symbol size and thus not visible.

4.3.3 Au film on PDMS coating

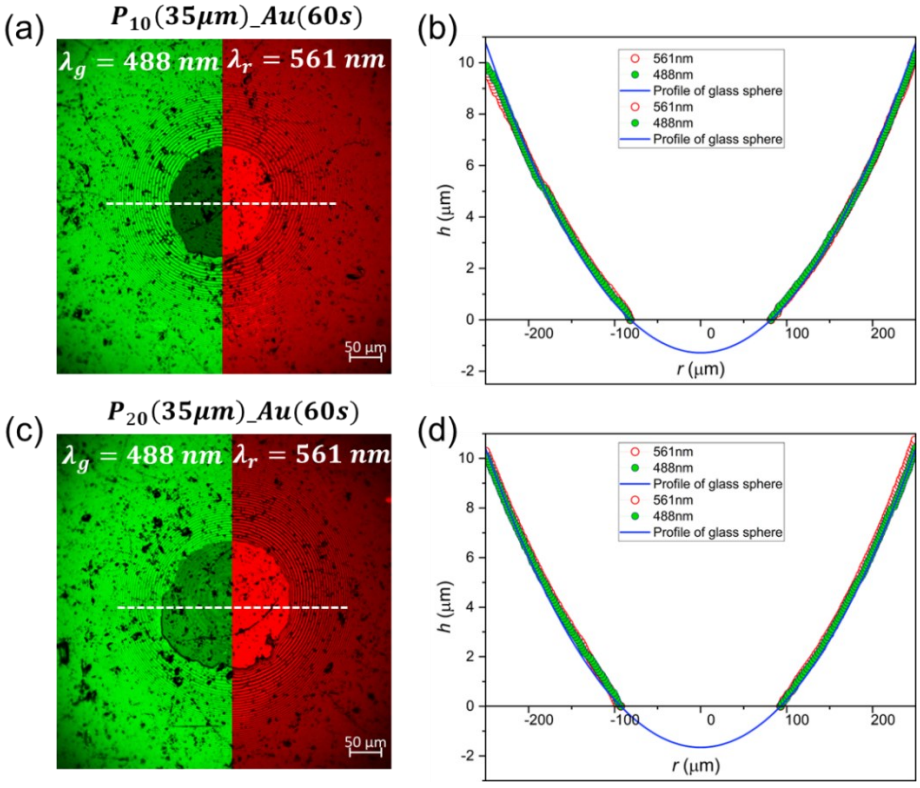


Figure 4-8 (a) and (c) Interference signatures of glass spheres in contact with Au coated soft PDMS substrates P_{10} (35 µm) **-** Au (60s) and P_{20} (35 µm) **-** Au (60s). (b) and (d) Plots of glass sphere profiles for the interference signature shown in (a) and (c) along the dashed lines. The symbols represent the height extracted using $\Delta h_{g,r} = m\lambda_{g,r}/4\sqrt{n_{air}n_{Au/PDMS}}$ and the solid lines represent the theoretical glass profile.

Here, we reveal our findings for Au sputtered PDMS substrates of 35 μm thickness for Au deposition times of 30 s, 60 s, and 120 s. Consequently, in a manner consistent with pristine PDMS and Ag sputtered PDMS substrates, we used a glass probe and extracted its profile using the corresponding effective refractive medium relation, i.e., $\Delta h_{\mathrm{g,r}} = m\lambda_{\mathrm{g,r}}/4\sqrt{n_{air}n_{Au/PDMS}}$. As shown in Figures 4-8(b)-(d), the fitted profile perfectly matches the glass sphere shape. Here, the used refractive index, i.e., $n_{\mathrm{Au/PDMS}}$ values for P_{10} (35 μm) – Au (60s) are 1.23 (488 nm) and 1.16 (561 nm) and that for P_{20} (35 μm) – Au (60s) are 1.22 (488 nm) and 1.16 (561 nm). Similar to Ag sputtered PDMS substrates, here also, the refractive indices are lower than that of pristine PDMS substrates. As shown in Figures 4-8(a) and (c), we observe that the contact region has a bright center due to Au deposition. To elaborate further on the experimentally obtained refractive index values, in Figures 4-9(a) and (b) we show the variation of refractive index values with Au deposition times on PDMS 10:1 and PDMS 20:1 substrate. We observe that refractive index gradually decreases with increasing Au deposition times. The refractive indices obtained for the green wavelength (n_{g}) are larger than those obtained corresponding to the red wavelength (n_{r}) for all cases. In contrast to Ag-on-PDMS substrates, here the difference between n_{g} and n_{r} are comparatively large. Here, we note the refractive index of Au exhibits a significant change in the wavelength range of 450 nm - 600 nm, which is reflected on Au/PDMS bilayers as well. In addition, we also observed that the contact area appeared slightly non-circular (Figure 4-8(a) and (c)), which may arise from variations in the roughness/coverage of the thin Au film. While such effects are not expected to substantially affect the refractive index fitting presented here, they highlight aspects that merit further investigation in future. Besides, from the observed footprint of the glass probe on the Au sputtered PDMS substrates, we observed that the contact radius is marginally higher than that for Ag sputtered PDMS of same deposition time. For instance, for a sputtering time of 120 s, the contact radius on Au-on-PDMS (P_{10}) is 78.4 μm, whereas the corresponding contact radius on the Ag-on-PDMS substrate (P_{10}) is 75.7 μm. Consequently, as shown in Figures 4-9(c)-(d), using the experimentally extracted contact radius and Hertz theory, we

evaluate the elastic modulus of Au sputtered PDMS substrates. In a manner consistent with Ag-on-PDMS substrates, here also increased Au sputtering enhances the stiffness of the bilayers. For instance, a 120 s sputtering duration of Au enhances the Young's modulus by approximately a factor of 2 for both the curing ratios.

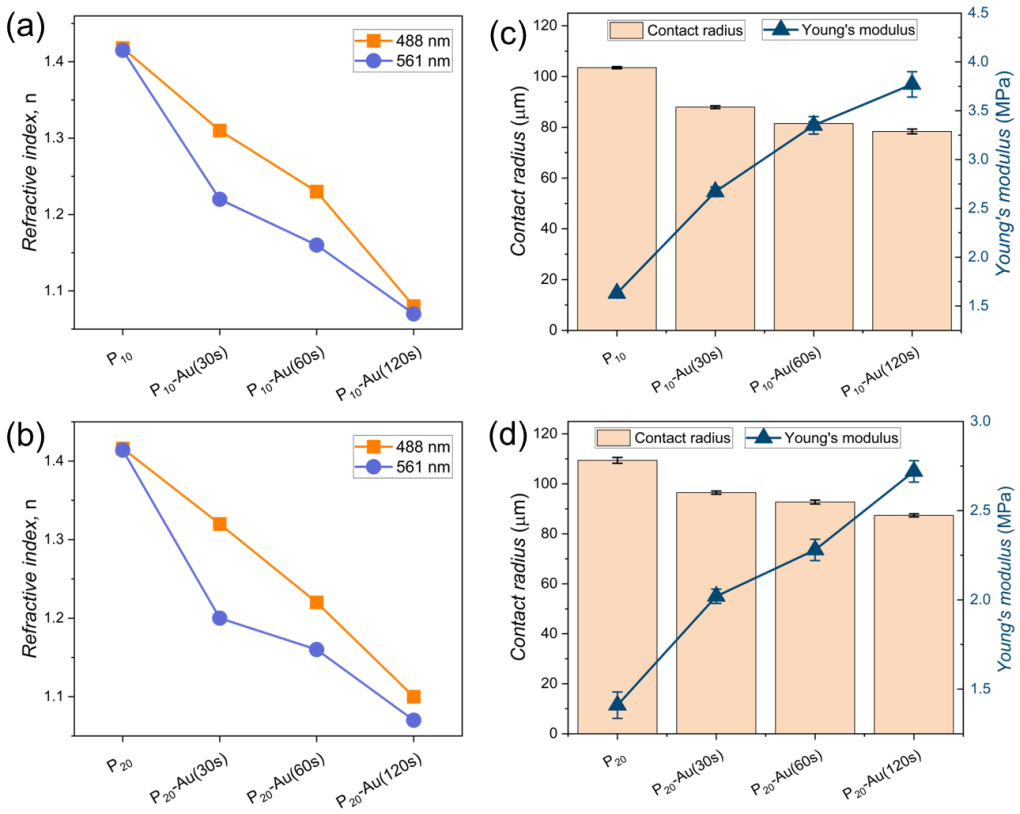


Figure 4-9 (a) and (b) Variation of the refractive index corresponding to both green and red wavelengths with Au sputtering time for 35 μm thin PDMS 10:1 and PDMS 20:1 substrate. (c) and (d) Variation of experimentally obtained contact radius of glass probe and calculated Young's modulus (using Hertz theory) with Au sputtering time for 35 μm thin PDMS 10:1 and PDMS 20:1 substrate. Error bars represent standard deviations calculated from three independent experiments. In some cases, they are smaller than the symbol size and thus not visible.

4.3.4 Comparison with UV/Vis measurements

Here, we compare our predicted refractive index values with those measured using UV-Vis spectroscopy measurements. It should be noted here that we performed the comparison for only thin PDMS coatings. For spectroscopy measurements, the Transmittance and Reflectance measurements are performed, and the refractive index is calculated using known relations (B4-9 and Figures B4-13-15, Appendix B). As shown in Figure 4-10, the predicted refractive index values from RICM measurements are in close agreement with those obtained from spectroscopy measurements. Notably, for bare PDMS, the refractive indices obtained from RICM are slightly lower than those from UV-Vis. This can be attributed to RICM probing local effective optical paths that are sensitive to nanometric air gaps or interfacial deformation at the soft substrate, whereas UV-Vis assumes a laterally uniform, fully dense PDMS layer with negligible absorption. In contrast, for metal-coated PDMS, RICM yields slightly higher refractive indices than UV-Vis, likely due to additional phase shifts upon reflection introduced by the metallic layer, while UV-Vis fitting underestimates the refractive index when absorption is negligible. For example, for the substrate P_{10} (35 μm) – Ag (10s), the refractive indices calculated using RICM measurements are n_g = 1.25 and n_r = 1.22, whereas those measured using UV/Vis are n_g = 1.18 and n_g = 1.18. Further, for the substrate P_{10} (35 μm) – Au (30s), the refractive indices calculated using RICM measurements are n_g = 1.32 and n_r = 1.20, whereas those measured are n_g = 1.27 and n_r = 1.17. Thus, for the aforementioned cases, the predicted values are within 5.9 % (n_g) and 3.4 % (n_r) of the measured values for the Ag/PDMS substrate whereas they are within 3.6 % (n_g) and 1.7 % (n_r) for the Au/PDMS substrate. Overall, the predicted values are within 5.6 ± 1.3 % of the measured values for PDMS 10:1 substrate with Ag film and within 5.7 ± 1.8 % for PDMS 20:1 substrate with Ag film. Similarly, for the Au sputtered substrates, the predicted values are within 6.1 ± 3.2% for PDMS 10:1 substrate and within 6.0 ± 3.5 % for PDMS 20:1 substrate. We highlight that for UV/Vis measurements, knowledge of refractive indices of the different mediums involved is required as a priori. However, the current technique offers the unique advantage of predicting

the effective refractive index of metal-polymer bilayer films without knowledge of the refractive indices of individual mediums, i.e., metal and polymer. Consequently, the current technique can be extended to different compositions of metal-polymer bilayers and thus provides broad applicability. At the same time, the assumption of parallel stratified layers is valid within a certain spatial range but begins to deviate when the probe curvature becomes significant. Specifically, for radial distances $r \leq 200$ μm, the reconstructed profiles fitted with effective refractive index n_{eff} closely matches the true profile of the glass probe. However, for $r > 200$ μm, slight deviations were observed (Figures 4-4(b) and (d), 4-6(c), and 4-8(b)), with the reconstructed profiles fitted with effective refractive index n_{eff} tending to underestimate the true probe profile. This deviation can be attributed to the increasing slope of the spherical curvature at larger r, which leads to an increase in the effective air gap thickness in the optical path. Since our analysis region is confined to relatively small areas, we approximated the glass slide / PDMS (or Ag- /Au- coated PDMS) /glass sphere system is as three parallel layers. While this approximation is reasonable within the analyzed region, its limitations should be acknowledged when extending to larger r where curvature effects become non-negligible. Future studies should investigate the transition between the parallel-layer and curvature-dominated regimes in a more systematic manner. In particular, additional optical factors such as the numerical aperture of the objective, the pinhole size in confocal detection, and the angular distribution of incident light should be considered. These parameters are expected to influence the effective optical path length and the sensitivity of the interference signal to curvature, thereby determining the range of validity of the current approach. Lastly, we note that the proposed technique does not provide any information regarding the complex part of the refractive index since RICM is inherently limited to reflected light only.

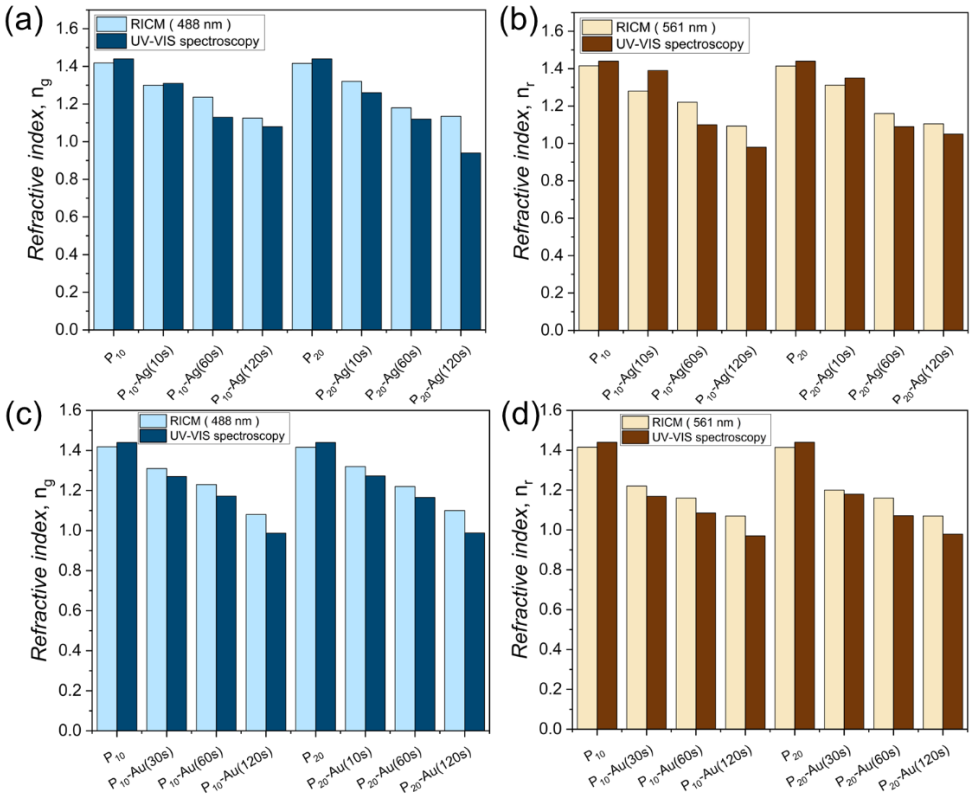


Figure 4-10 (a) Comparison of refractive index n_g values between RICM and UV/Vis spectroscopy measurements corresponding to wavelength, λ = 488 nm for Ag/PDMS bilayer films of varying deposition times for PDMS coating thickness of 35 µm. (b) Comparison of refractive index n_r values between RICM and UV/Vis spectroscopy measurements corresponding to wavelength, λ = 561 nm for Ag/PDMS bilayer films of varying deposition times for PDMS coating thickness of 35 µm. (c) Comparison of refractive index n_g values between RICM and UV/Vis spectroscopy measurements corresponding to wavelength, λ = 488 nm for Au/PDMS bilayer films of varying deposition times for PDMS coating thickness of 35 µm. (d) Comparison of refractive index n_r values between RICM and UV/Vis spectroscopy measurements corresponding to wavelength, λ = 561 nm for Au/PDMS bilayer films of varying deposition times for PDMS coating thickness of 35 µm.

4.4 Conclusion

In summary, we propose a simple and convenient methodology to predict the refractive index and elasticity of silver (Ag) and gold (Au) sputtered PDMS thick/thin coatings. Using the interference signature of a glass sphere of known shape atop the Ag/PDMS and Au/PDMS

bilayer substrates, the measurements of refractive index are first standardized for pristine PDMS coatings and then applied for PDMS coatings with Ag and Au films of varying thickness. It was found that the conventional procedure of glass sphere height extraction from interference fringes does not apply to such PDMS coatings on glass slides. Consequently, we proposed a modified refractive index n_{eff} accounting for refractive indices of both PDMS (or Ag/PDMS and Au/PDMS) medium and air medium to accurately extract the height profile of the glass sphere. Upon successful fitting of glass sphere profiles on the two different metal-polymer bilayer substrates using n_{eff}, the refractive index of Ag/PDMS and Au/PDMS bilayer substrates of varying deposition times are extracted. The use of dual wavelength enables refractive index extraction corresponding to the two different wavelengths, i.e., n_{g} (488 nm) and n_{r} (561 nm). For both Ag/PDMS and Au/PDMS substrates, it was observed that the refractive index decreases with increasing metal deposition times, i.e., metal film thicknesses. The behavior is consistent for PDMS substrates of two different elasticities and coating thickness. Comparison of predicted n values with corresponding UV/Vis spectroscopy measurements yield satisfactory results. Using the same experiment, we were further able to measure the contact radius of glass spheres atop the metal sputtered PDMS substrates. Consequently, using Hertz theory, we were able to predict the elastic modulus of such thin metal films on PDMS.

4.5 Outlook

The proposed methodology is simple and robust and might be extended to other metal films like Cr, Pt, etc., deposited on polymers since knowledge of individual refractive indices is not required as a priori. Apart from not being able to quantify the complex part of the refractive index, the only other limitation in the proposed technique appears to be characterizing optical properties of thick PDMS coatings, which exhibit a decrease of refractive index values due to possible variation of material density. Using a single experiment to predict two different material properties should boost efforts characterizing such bilayer

films, which typically involves multiple, complex measurements and calculations, and is thus of immense utility towards designing SERS active substrates for diverse applications.

Chapter 5

Profiling contact ridge of soft substrates with metallic thin films using a novel interference technique

As technology moves toward flexibility, embedded systems, and miniaturization, which often have metallic elements integrated with the functional substrates, understanding the contact deformation of such soft substrates coated with thin metallic films is crucial. However, probing nanoscale deformations optically, typically in a few hundred nanometers, poses challenges. DW-RICM holds promise in unveiling nanoscale deformations. However, when paired with conventional glass probes to measure deformation of underlying soft substrates, DW-RICM faces limitations due to light reflection at the glass-air interface, impeding accurate determination of the contact zone (e.g., contact area, contact ridge). Here we hypothesize that using alternative probes to eliminate unwanted reflections can enhance understanding of soft substrate deformation with thin metallic films (bilayer substrates). In this work, we investigate the deformation profile of viscoelastic soft substrates with sputter-coated gold thin films (referred to herein as bilayer substrates) using DW-RICM. We employ millimeter-sized black ink-coated glass spheres as probes, absorbing most light under DW-RICM. We focus our laser beams associated with DW-RICM in the contact zone between the probe and the underlying soft substrates. Our new technique of using black ink-coated glass probes in contact with soft bilayer substrates enables us to accurately extract the deformation profile, particularly the contact ridge. With the increase in the gold sputter coating time, the contact area and contact ridge of gold-polymer bilayer substrates decrease. Further, long-term contact analysis of gold-coated soft substrates reveals a steady increase in the contact ridge height over time, unlike the gradual decrease observed in their bare counterparts until reaching a steady state.

5.1 Introduction

Contact deformation of soft substrates is of fundamental importance in fields ranging from colloid science and biomedicine to sustainable energy generation [214–216]. For example, the measurements of the contact area and the contact ridge have been utilized to determine the adhesive and elastic properties of soft substrates [217]. In the increasingly widespread application of multifunctional flexible materials, for instance, bilayer or multilayer metal-polymer laminate substrates, understanding their contact deformation behaviours plays a pivotal enabling role in enhancing and optimizing its distinctive synergistic properties, including exceptional thermal and electrical conductivity with remarkable impact resistance [218–221]. However, these deformations are often in the micro and nano scales, making it notoriously difficult to probe with high accuracy. Conventional techniques to measure such small-scale deformations include fluorescence microscopy [58,222–224], confocal microscopy [101,102], and X-ray imaging [225]. However, these conventional techniques are faced with many challenges, as described later. Therefore, it is desired to develop a visualization or imaging technique that circumvents the existing challenges to decipher micro/nano-scale deformation of soft substrates, especially the bilayer/multilayer metal-polymer substrates.

Fluorescence microscopy utilizes the advantages of site-specific fluorescent labeling to provide a method of imaging structures with a micrometer resolution. The imaging resolution, however, is predominantly constrained by the UV-visible wavelength range, which is subject to limitations imposed by either Abbe's law or Rayleigh's law [222]. Laser scanning confocal microscopy (LSCM) is built around a conventional epifluorescence light microscope, which can serially produce thin optical sections of 0.5 ~ 1.5 μm through fluorescent specimens with the thickness more than 50 μm [226,227]. The limitation lies in the restricted availability of excitation wavelengths from common lasers, which are confined to narrow bands and incur high production costs in the ultraviolet (UV) region [228]. Besides, high-intensity laser irradiation poses potential risks to the viability and integrity of living cells and tissues [229]. X-ray imaging is an effective modality of medical imaging due to exceptional penetrative capacity with

wavelengths of 0.01 nm ~ 10 nm [222,230,231]. It is extensively applied for non-destructive measurements, such as material thickness gauging and internal defects inspection [232,233]. A major concern of X-rays is that they can ionize, which damages living cells [234].

Dual-Wavelength Reflection Interference Contrast Microscopy (DW-RICM) is a particularly promising technique whereby an object either in contact or close to a surface is illuminated from bottom using two monochromatic light sources operating at low power and the reflected light is collected to form the interference fringes. The interference signature is subsequently analyzed with relative ease. The method is convenient, requires no fluorescent labeling, and can be combined with other detection instruments [235–237]. It has already produced a significant impact in cell and lipid adhesion studies, particles-soft substrates interactions as well as energy generation due to the vast potential behind RICM's operational simplicity, adequately high spatial (nanometer-scale) and temporal resolution (microsecond-scale), and distinctive non-invasive 'view from below' perspective [214,234,237]. For example, RICM was used to investigate the impact of random multiscale surface roughness on triboelectric nanogenerators' performance by directly visualizing the contact interface [214]. It has also been an imaging modality of choice for investigating soft contact [105–107], wetting dynamics [44,57,79,99,200,238–241], the existence and impact of surface hydration of regenerated cellulose underwater [242] as well as topography of thin films in microfluidic channels [243]. For example, in soft contact of gels, RICM enables the probe of the microscale contact area of interest, observes the long-term development of contact deformation, and constructs the profile of free liquid under compression by observing the contact area as well as the interference fringes outside the contact area over time without dye molecules [44]. Moreover, RICM has been successfully employed to probe droplet evolution (evaporation and condensation) on rigid substrates [44,79,200] as well as the morphology of the three-phase contact line of water droplets resting on soft substrates [57]. In a recent study, we have demonstrated how RICM can successfully determine the elastic moduli and refractive indices of metal-polymer bilayer films by combining the known weight and profile of a glass probe in contact with the said films [113].

The principle of DW-RICM is based on the interference of reflected light at different optical interfaces (see details in C5.1, Appendix C), which has been summarized in our previous works [44,57,79,113,200,210] and existing literature [78,202,235,244]. In the study of contact systems with multiple components, the characteristic fringe patterns contain information of an upper component's deformation profile near the contact boundary with a lower component. A glass sphere is commonly employed as a probe in combination with RICM [44,105–107,113,241]. However, this method has difficulties in measuring the contact deformation of soft substrates because the interface of the glass sphere reflects light, thereby interfering with the light associated with the deformation information of underlying soft coatings.

Herein, we report a simple approach to negate background interference and obtain high-quality interference fringes solely providing the deformation information of the underlying soft substrates. We coated the probes with black ink that absorbed almost all the incident light. And we hypothesize that using a black ink-coated glass can eliminate unwanted light reflections so as to allow us to probe soft substrate deformation through interference fringes. Thus, the interference fringes allow us to visualize the contact zone between the probe and soft substrates, which is otherwise not optically accessible, and to quantitatively characterize the contact ridge near the three-phase contact boundary.

5.2 Experimental

5.2.1 Preparation of black ink-coated probe

The black ink used for coating the glass sphere (probe) consists of two different types of black ink to enhance the bonding between the glass sphere and black ink. Black ink #1 (Musou Black, KOYO Orient Japan Co., Ltd.) is a water-based acrylic paint with a light absorption up to 99.4%. Black ink #2 (Glass Paint black, DecoArt) is a commonly used black ink for glass coating. The final black coating was prepared by mixing black ink #1 and black ink #2 at a weight ratio of 1:1 using a planetary mixer (ARE-310, Thinky Corporation) for 6 mins. Before coating, the glass spheres with a radius of 2.6 mm (8996 K24, McMaster-Carr)

were rinsed thoroughly with isopropanol (IPA) and ethanol and finally dried with N_2. The cleaned glass spheres were coated with the prepared black ink using dip-coating with a coating speed of 2 mm/s. A hold time of 1 minute was maintained to ensure stable contact between the glass sphere and the ink bath. Finally, the ink-coated glass probe was dried at 22˚C - 24˚C for 24 hrs. Before each experiment, the ink-coated glass probe was sonicated in IPA for 3 mins to remove any pigment particles adhering to the surface, and subsequently dried at 22˚C - 24˚C for 4 hrs. The morphology and radius of the black ink-coated glass probe before and after sonication were inspected by handheld digital microscopy (Dino-Lite, AM73915MZT Edge) (Figure C5-2, Appendix C). The final radius and weight of the black ink-coated glass probe are 2.615 mm and 1.3 mN, respectively. The roughness of black ink coating after sonication in IPA was measured by a surface profiler (KLA-Tencor P-6 profiler, HERZAN) (Figure C5-3, Appendix C), which is 1.29 μm. Besides, we obtained black ink-coated probes with different sizes and weights by replacing the glass sphere with other materials, like steel balls. For instance, we prepared a series of truncated black ink-coated steel probes with a diameter of 19 mm and a weight of 299.3 mN.

5.2.2 Optical loss measurement of black ink

The transmittance (T) and reflectance (R) of the black ink (ink #1: ink #2 = 1:1) mixture were confirmed by coating the ink on a glass slide and then performing UV-Vis measurements (PerkinElmer Lambda 35 &1050 UV-Vis) over the wavelength range of 200 nm - 1100 nm at 20°C. For these measurements, we spin-coated 0.7 mL of the prepared black ink on freshly cleaned glass slides (Microscope slides, Sail Brand, dimensions: 76.2 mm x 25.4 mm x 1 mm) at 2000 -3000 rpm, resulting in a uniform ink film thickness of around 15 μm and consequently dried the film under ambient conditions for 12 hrs. The optical loss (L) of the black ink was calculated by the equation $L = 1 - T - R$, which includes the absorption (A) and scattering (S) (see Figures C5-4 and C5-5, Appendix C) [203]. The optical loss (L) of black ink #1 is 98.5 % at 466 nm and 561 nm. The reflectance of black ink #1 is less than 2 %. Similarly, the observed optical loss (L) of the mixed black ink mixture (ink #1: ink #2 = 1:1) is 97.3 % at 466 nm and

561 nm. The reflectance of the ink mixture is less than 3 %. It was indicated that the reflected light from the black ink-coated probe is extremely weak and thus does not superimpose on the interference fringes of interest, i.e., from the metal-polymer bilayer substrate.

5.2.3 Preparation of soft coatings

Soft coatings were spin-coated on a cleaned glass slice (dimensions: 76.2 mm × 25.4 mm ×1 mm) by adjusting the volume of the silicone elastomer (PDMS) (Dow Corning, Sylgard 184) and spin rate. The soft substrates with different Young's modulus were prepared by mixing base and curing agent at weight ratios of 10:1, 20:1, 35:1, 45:1, and 60:1, respectively. The PDMS solutions were mixed and degassed for 10 mins by the planetary mixer. To achieve the coating thickness at 35 μm, each mixture (volume: 0.7 mL) was spin coated on the glass slice at 3000 rpm. For simplicity, throughout the remainder of the text, the soft substrates with weight ratios of 10:1, 20:1, 35:1, 45:1, and 60:1 are referred to as P_{10}, P_{20}, P_{35}, P_{45}, and P_{60}, respectively.

5.2.4 Preparation of Au-coated soft substrates

A gold (Au) thin film was sputtered on the soft substrates by magnetron sputtering coater (Denton Vacuum Desk II) with a current of 15 mA at 22 ˚C - 24 ˚C. The thickness of the Au film was manipulated by adjusting the sputtering time with a deposition rate of 1.38 Å/s. For instance, the thickness of Au sputtered on a glass slice for 120 s was ~16.5 nm (Figure C5-6, Appendix C), measured by an atomic force microscopy (Pacific Nanotechnology AFM Nano-R). We sputter-coated Au on the soft substrates of P_{35}, P_{45}, and P_{60} with the sputtering time of 10 s, 30 s, and 60 s. Those sputtered PDMS coatings are named P_{35} (35 μm)-Au (10 s), P_{35} (45 μm)-Au (30 s), and P_{60} (35 μm)-Au (60 s).

5.2.5 Measurements of RICM

The custom-built DW-RICM unit that we used was consisted of LSM 800 (Carl Zeiss, Germany) and equipped with two focused monochromatic laser with wavelengths λ_{green} = 488

nm and λ_{red} = 561 nm (Figure 5-1(a) and Figure C5-7, Appendix C). To confirm the feasibility of black ink, the ink-coated glass probe of radius 2.615 mm was carried on a cleaned glass slide, as shown in Figure 5-1(b). We assume the ink-coated probe is perfectly spherical. As the black probe-air interface is curved, the curved surface is assumed to be composed of numerous succession of infinitesimal horizontal steps [78]. Hence, the black probe-glass slide structure is simulated by a three-layer of parallel dielectric layers [228] (Figure 5-1(c)). Even though this approach involves a fair amount of approximation, the advantage of this model is that the distance between the substrate and the objective can be directly determined by the cosine transformation, i.e., it simplifies the calculations and can be employed for any complex multi-layer system. Further, we note that Theodoly et al. [78] successfully employed this model for their RICM image reconstruction to obtain the profiles of polystyrene beads in close proximity to a glass slide in a glucose solution. For imaging in the DW-RICM mode, we used an objective lens with a magnification of 10× and a numerical aperture (NA) of 0.3 (EC Plan-Neofluar, Carl Zeiss, Canada). The interfaces of interest were raster scanned simultaneously using two laser beams by the galvanometric mirror. In this system, the glass slide - air interface is the observation plane. In stark contrast to observations for bare glass spheres (Figure C5-1, Appendix C) [44,113], we observe that there are no interference fringes, indicating negligible reflection from the glass sphere for the ink-coated probe on glass slide (Figure 5-1(d)). This is because incident light rays are only reflected from the interference of glass slide-air while a majority of the incident laser that reached the air-black ink-coated probe interface was absorbed or scattered away. We confirm the validity of the black ink coating, which is essential for the subsequent experiments and analysis from this calibration experiment.

A black ink-coated probe of appropriate weight and size was selected and placed on the soft substrates. To obtain clear interferograms, imaging was conducted in confocal mode with a pixel size of 1240 pixels × 1240 pixels, where 1 pixel = 0.52 μm. The Z-stack multidimensional acquisition function was applied to scan from the PDMS/glass slide interface up to a height upper the free surface of the soft substrates. Each slice was scanned at 1 μm

intervals. Furthermore, the time-series multidimensional acquisition function was applied to scan the interference planes of interest with a minimal time interval of 1 s, which was sufficient to record the evolving processes and confirm the stable state. Through these two functions, sufficient slices were obtained to obtain the interference planes of interest. For each sample, we selected and confirmed the images where the focal plane was located on the free undeformed surface of soft substrates and when the deformation reached the steady state through comparing the variation of interference fringes and laser intensity of those slices. In a similar manner, gold-coated soft substrates were examined using the black-inked probe.

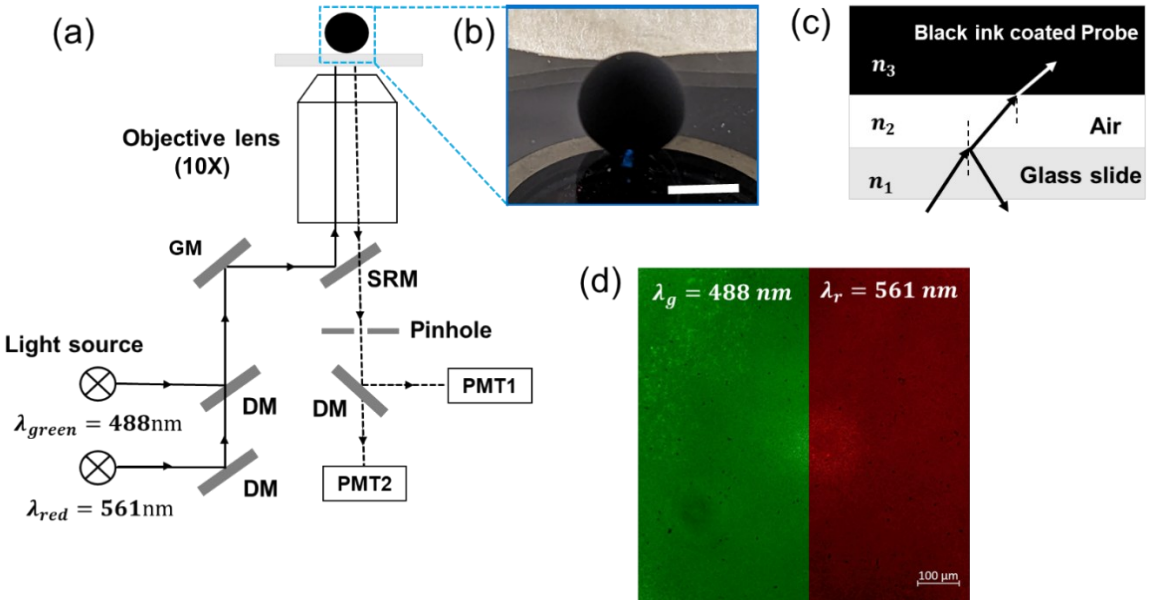


Figure 5-1 (a) Schematic of Dual Wavelength - Reflectance Interference Contrast Microscopy (DW-RICM) set-up. Light sources: $\lambda_g = 488$ nm and $\lambda_r = 561$ nm. DM: Dichroic Mirror. GM: Galvanometric Mirror. SRM: Semi-refractive Mirror. PMT: Photomultiplier Tube. (b) Photo of a black ink-coated glass probe atop a glass slide used in the calibration experiment. Scale bar: 2 mm. (c) Schematic of optical configurations: the three parallel dielectric layers of black ink coated probe / air / glass slide represented the curved probe profile. n_1, n_2 and n_3 are the indices of refraction of glass, air, and black ink, respectively. (d) Images from DW-RICM at green and red wavelengths.

5.2.6 Refractive indices of soft substrates and Au-coated soft substrates

To determine the contact deformation of the metal-polymer substrates, it is crucial to determine their refractive indices first. In this regard, we used the methodology reported in our previous work where we used the RICM signature of a bare glass probe and fitted the known glass sphere profile to extract the refractive indices of Au-coated PDMS substrates [113]. Briefly, RICM measurements were performed in ways similar to that described in section 5.2.5 except that the ink coated glass probe was replaced by the bare glass probe. By using the confocal mode of the RICM set-up, we obtain the interference fringes solely from the bare glass probe (see Figure C5-1, Appendix C). Consequently, from the RICM interference fringes, the refractive indices were determined by comparing the real profile of the bare glass probe ($h = \sqrt{2600^2 - a^2} - \sqrt{2600^2 - r^2}$) with the reconstructed profile ($h = m\lambda/4\sqrt{n_{air}n_{PDMS}}$). Here, h is the profile of the probe; a is the contact radii between the probe and soft substrates; r is the radius; m is the order of consecutive bright and dark fringes; λ is the wavelength of laser; n_{air} is the refractive index of air (n_{air} = 1); n_{PDMS} is the refractive index of PDMS. The determined results are illustrated in Figure 5-2 and C5-8, Appendix C. The refractive indices of Au-coated soft substrates were measured in the same method using $h_{g,r} = m\lambda/4\sqrt{n_{air}n_{Au/PDMS}}$, where $n_{\text{Au/PDMS}}$ is the refractive indices of Au-coated soft substrate (see Figures 5-2 and 5C-9, Appendix C).

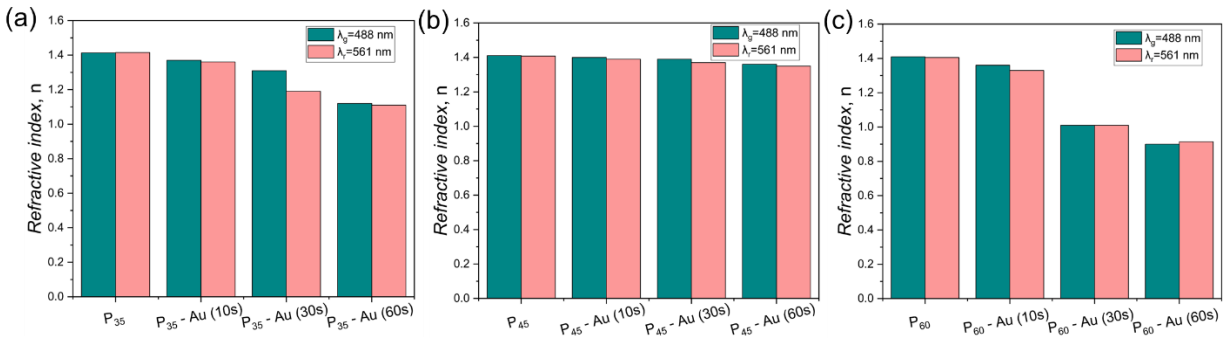


Figure 5-2 Calculated refractive indices. Au-coated soft substrates: (a) P_{35}, (b) P_{45}, and (c) P_{60} with different sputter coating times of 0 s, 10 s, 30 s, and 60 s under wavelengths of 488 nm and 561 nm.

5.2.7 Measurements using Raman spectroscopy

A Raman spectrometer (HORIBA scientific, XploRA Plus) equipped with a microscope (OLYMPUS, LMPlanFL N) was employed to further confirm the long-term deformation dynamics associated with the contact deformation of the substrate P_{60}-Au (10 s). The wavelength of the excitation laser was 638 nm. The diameter of the laser spot focused on the substrate is less than 5 μm. The scattered laser was collected by a 50× objective lens with a numerical aperture (NA) of 0.5. The laser power was set as 1.41 mW with an integration time of 10 s. For Raman measurements without a glass probe, the laser was focused directly on the sample surface. For measurements with a glass probe, a 2.5-mm-radius hemispherical lens (BOHR OPTICS, H-K9L Half Ball Lens) was used to replace the glass probe and ink-coated probe used in the RICM measurements since the glass probe affects the laser path, inducing scattering. The actual image of the experimental measurement setup of Raman spectroscopy incorporating a hemispherical lens and the comparison of the effect of a hemispherical lens and glass probe on the laser spot are shown in Figures C5-10 and -11, Appendix C. During the Raman measurements, the laser spot was focused on the sample surface, which was close to the center contact area and within the contact deformation region (between points A and C in Figure 5-3(a) (right)). To ensure the same test point, the sample was kept stationary on the carrier table until the end of the test. The Raman spectra of the surface and internal of bare P_{10} and P_{60} (Figure C5-12, Appendix C), and the surface of P_{60}-Au (10s) without placing a hemispherical lens (Figure C5-13, Appendix C) were examined for comparison.

5.3 Results and discussion

The schematic of the RICM laser paths of a glass probe in contact with a soft substrate is shown in Figures 3a and b. For a millimeter-sized glass probe on a P_{10} substrate, the contact area and contact deformation are determined by the elastic modulus and finite thickness of the soft substrate [44,113]. In Figure 3b, for contact on P_{10} with finite thickness, a clean uniform pattern of concentric Newton's rings occurred outside the contact area (the central dark region). However, the observed fringes offered no information regarding the deformation of the

underlying soft coating. In this system, three interfaces reflect light: the interface of a glass slide-PDMS, the interface of PDMS-air, and the interface of air-the edge of a glass probe. For P_{10}, the contact interface is below the free surface of the soft coating, and the deformation profile of the soft substrate gradually goes up from its lowest position at the bottom of the probe to the free surface (see Figure 5-3(a) (left)). Since the elastic modulus of P_{10} is relatively large, the indentation depth is as small as a few nanometers. Under this condition, the incident angle is small, and most incident light goes through PDMS up to the edge of the glass probe. Consequently, the reflected light from the PDMS–air interface is negligible, being weak compared to the reflected light from the glass probe–air interface. Therefore, the clear interference fringes shown in Figure 5-3(b) (left) represent the profile of the glass probe [113]. For the glass probe on a relatively softer substrate, i.e., P_{60}, the periodic and sharp interference fringes often disappear over time and are replaced by partial complex interference fringes close to the contact zone of the probe with the PDMS (Figure 5-3(b) (pink box)). On the one hand, away from the contact zone, the interference fringes become progressively clearer, showing different periodicity (Figure 5-3(b) (right blue box)). Thus, though the outer ring of interference fringes originates from the deformation of the underlying soft coating, the inner ring of complex fringes results from the superposition of interference fringes from the glass probe and the soft substrate, making it difficult to determine the deformation profile near the contact boundary.

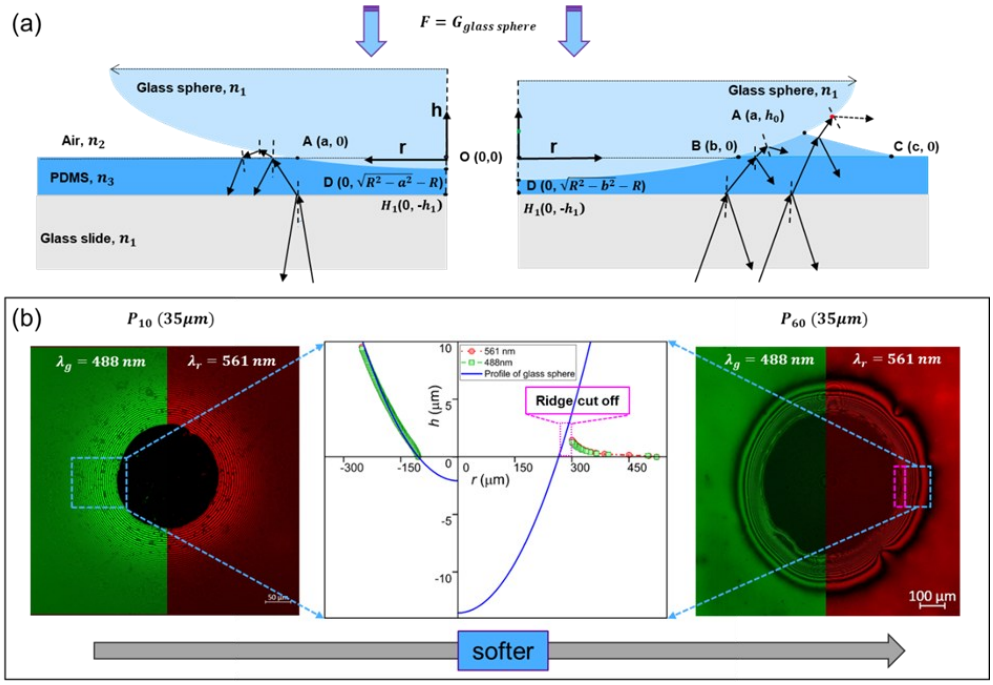


Figure 5-3 (a) Schematics of a 2.6-mm-radius glass probe in contact with PDMS 10:1 (P_{10}) (left) and PDMS 60:1 (P_{60}) (right) coating of finite thickness of 35 μm and the laser path. n_1, n_2 and n_3 are the indexes of refraction of glass slice, air, and PDMS coating, respectively. The origin O is inside the glass probe. Point D is the lowest point of the glass probe that contacted with soft coating. Point H_1 is located at the interface between the PDMS coating and the glass slide. Point A is located at the contact boundary between the glass probe and the PDMS coating. Point B is the crossing point of the free surface of soft coating with the *r*-axis. Point C is the base of the contact ridge. (b) RICM observation of a bare 2.6-mm-radius glass sphere sitting on a soft substrate with different elasticities: P_{10} (35 μm) and P_{60} (35 μm), and the corresponding reconstructed profile of glass probe (left: blue box) and partial contact deformation profile of P_{60} (35 μm) (right: blue box) based on the interference fringes.

We initially tried a wide range of probe materials, such as steel balls, ceramic balls, rubber balls, black polymer-coated glass spheres (uniform surfaces), and blue dye / Rhodamine 6G / mark pen-dyed glass balls to overcome the challenges of analyzing complex interference fringes around the contact area of softer substrates caused by the contact with probes. However, all of them still reflected light from the probes. The challenge appears to be a trade-off between the smoothness of the probe and light absorption capability. To confirm the feasibility of using black ink-coated probe and reconstruct the deformation profile of Au-sputtered PDMS

substrates, we first applied the ink-coated probe on pristine PDMS substrates without thin metal films.

5.3.1 Deformation profiles of pristine polymer substrates

In Figure 5-4, we show the interferograms of P_{45} (35 μm) and P_{60} (35 μm) soft substrates using a black ink-coated probe of a weight of 1.3 mN, and a radius of 2.615 mm. Compared to the bare glass probe, the interference fringe pattern is significantly clearer near the contact boundary. The contact areas (central dark zone in Figures 5-4(c) and (e)) are mostly dark except at the edges where the roughness of the black ink surface induces local inhomogeneity. By summing areas of all the dark regions, the average contact radii of P_{45} (35 μm) and P_{60} (35 μm) are determined to be 187.96 μm and 265.67 μm, respectively. The advantages of the ink-coated probe are illustrated in Figure 5-4a, where we set the free, undeformed part of the soft substrate as the horizontal zero-axis (*r*-axis). The probe deforms the free surface of PDMS; the lowest point D of the probe contacts and then compresses the PDMS soft substrate until it reaches the equilibrium configuration. The origin O (0,0) is inside the probe. The point B (b, 0) is on the interface between the probe and the *r*-axis. The final position of point D (0, $\sqrt{R^2 - b^2} - R$) is below the *r*-axis. The point A $\left(a, \sqrt{R^2 - b^2} - \sqrt{R^2 - a^2}\right)$ is located at the boundary of the contact region of the probe and soft coating, which is also below the horizontal *r*-axis. Near the boundary of the contact zone ($a < r < c$), the deformation profile of the soft substrates forms a ridge-like structure and eventually levels with the free surface at the point C (c, 0). For the region $r \geq c$, the soft substrates are undeformed (Figure 5-4(a)).

To reconstruct the deformation profile of the soft substrates, height information at point B is a prerequisite, which can only be resolved using the black ink-coated probe with no background reflections from the probe surface. From the interferograms, we extract the entire profile of the deformed soft substrate by setting the free undeformed surface as $h = 0$ and calculating the gradual increase in height using the relation:

$$\Delta h = m\lambda/4n \tag{5-1}$$

where $m = 1$ is the fringe order; λ is the wavelength of the laser (488 nm and 561 nm); n is the refractive index of PDMS. We thus extract the contact ridge of P_{45} and P_{60} soft substrates where the maximum height and ridge width are represented as h_0 and l_0, respectively (Figures 5-4(c)-(f)). For a better representation of how the ridge deformation approaches the probe surface, we assume the ink-coated probe is a perfectly spherical and show the theoretical profile of the probe using $h = \left(\sqrt{R^2 - a^2} + h_0\right) - \sqrt{R^2 - r^2}$. As opposed to a bare glass probe which severely restricted measurement capabilities close to the contact boundary between the soft substrate and the probe, i.e., the tip of the contact ridge (Figure 5-3(b)), here we enable the reconstruction of the entire deformation profile. From our experimentally extracted deformation profiles corresponding to the two wavelengths, P_{45} has h_0 = 2.07 μm at 488 nm and 2.00 μm at 561 nm, and P_{60} has h_0 = 2.68 μm at 488 nm and 2.59 μm at 561 nm. Note that since the surface of the ink-coated probe is not as smooth as the bare glass probe, the contact area and interference fringes are not completely symmetrical. These features may have two implications: (1) it is impossible to do any angular averaging of the interference profiles to improve the signal-to-noise ratio, which may greatly enhance the determination of the location of the interference fringes and the associated resolution of the contact profiles; (2) it is impossible to extract quantitative data on the mechanical behavior of the soft layers from the contact mechanics description of the deformation ridge. Thus, partial fringes were chosen for analysis (white, dotted lines in Figures 5-4c and e, and Figure C5-14, Appendix C). Lastly, we observe that the maximum lateral extent of the ridge is at c = 305.51 μm for P_{45} and c = 413.53 μm for P_{60}. Consequently, upon subtracting the contact radius, we obtain the ridge width: l_0 = 117. 55 μm for P_{45} and l_0 = 147.86 μm for P_{60}.

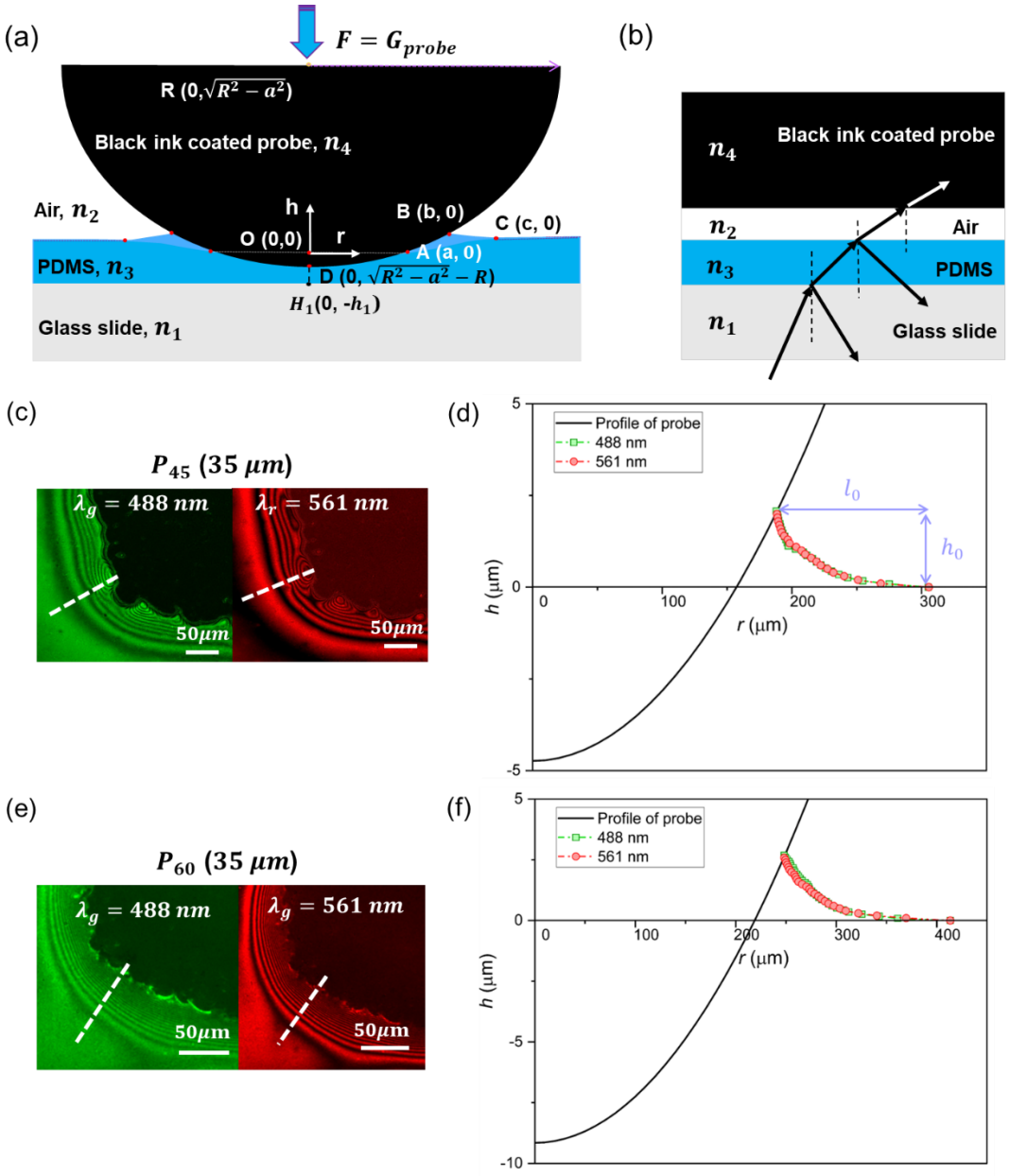


Figure 5-4 (a) Schematic of the ink-coated probe (R = 2.615 mm) on a soft PDMS substrate of finite thickness ~ 35 µm. (b) Optical configurations of a four parallel dielectric layers model for simulating the curved surface of the black probe on the PDMS coating as illustrated in (a). n_1, n_2, n_3 and n_4 are the indexes of refraction of glass slice, air, PDMS coating, and ink, respectively. (c) and (e) The obtained interference signature generated by the ink-coated probe in contact with PDMS 45:1 (P_{45}) and PDMS 60:1 (P_{60}) with a thickness of 35 µm. (d) and (f)

Reconstructed profiles of the ink-coated probe and contact deformation of the soft substrates based on the interference signature along the white, dotted lines drawn in (c) and (e). The green and red symbols indicate the extracted height using $h_{g,r} = m\lambda_{g,r}/4n_{PDMS}$. The dark solid line indicates the theoretical profile of the ink-coated probe using $h = \left(\sqrt{R^2 - a^2} + h_0\right) - \sqrt{R^2 - r^2}$, h_0 and l_0 are the peak ridge height and width, respectively.

5.3.2 Deformation profiles of metal-polymer bilayer substrates

As demonstrated in the above section, the black ink-coated probe combined with DW-RICM allowed us to reconstruct the entire contact deformation profile of pristine soft substrates, which is crucial for the in-depth understanding of soft contact deformation. Since bilayer or multilayer thin films composed of different characteristic materials are increasingly being used for technologies relying on miniaturization and multifunctionalities, such as metal-coated polymer/gel films in e-skin [245] and wearable sensors [246], investigating the contact deformation of such bilayers is both scientifically and technically important.

To further extend the application of this technique, here, we demonstrate how the black ink-coated probe can measure the contact deformation of metal-PDMS bilayer substrates. For this, we prepared metal-PDMS substrates with Au-sputter depositions. The PDMS substrates used are P_{35}, P_{45}, and P_{60} with metal deposition times of 10 s (thickness ≈ 1.5 nm), 30 s (thickness ≈ 4.5 nm), and 60 s (thickness ≈ 9 nm). In Figure 5-5(a), we show the interferograms of a black ink-coated probe on Au-sputtered P_{60} substrates with deposition times of 10 s, 30 s, and 60 s. We observed that the contact area was not uniformly black, but rather a hybrid of localized bright (gold) and dark areas due to the roughness of the black ink coating and the presence of a thin layer of gold. Here, the black-inked surface absorbs most of the incident light that reaches the probe surface. At the same time, the existence of the Au layer enhances the intensity of reflected light, which in turn makes the interference fringes appear brighter. Therefore, the interference signature obtained using the ink-coated probe is distinctly clear and contains the relevant intensity information required for extraction of the deformation profile of the metal-polymer bilayer substrates (Figure 5-5(b)). As noted earlier, the difference in local height between two consecutive extrema, a minimum, and an adjacent maximum, is $\lambda/4n$ and

vice versa. Consequently, we can extract the deformation profile of the Au-sputtered soft substrate with a resolution of $\lambda/4n$ (0.09 μm for 488 nm and 0.15 μm for 561nm) from the interferograms, where n is the refractive index of Au-sputtered soft substrates ranging from 1.41 ~ 0.90. As shown in Figure 5-5(c), the ridge-like deformation profile has a ridge height h_0 ~ 2.46 μm which gradually decays away from the contact zone, i.e., the edge of the glass probe.

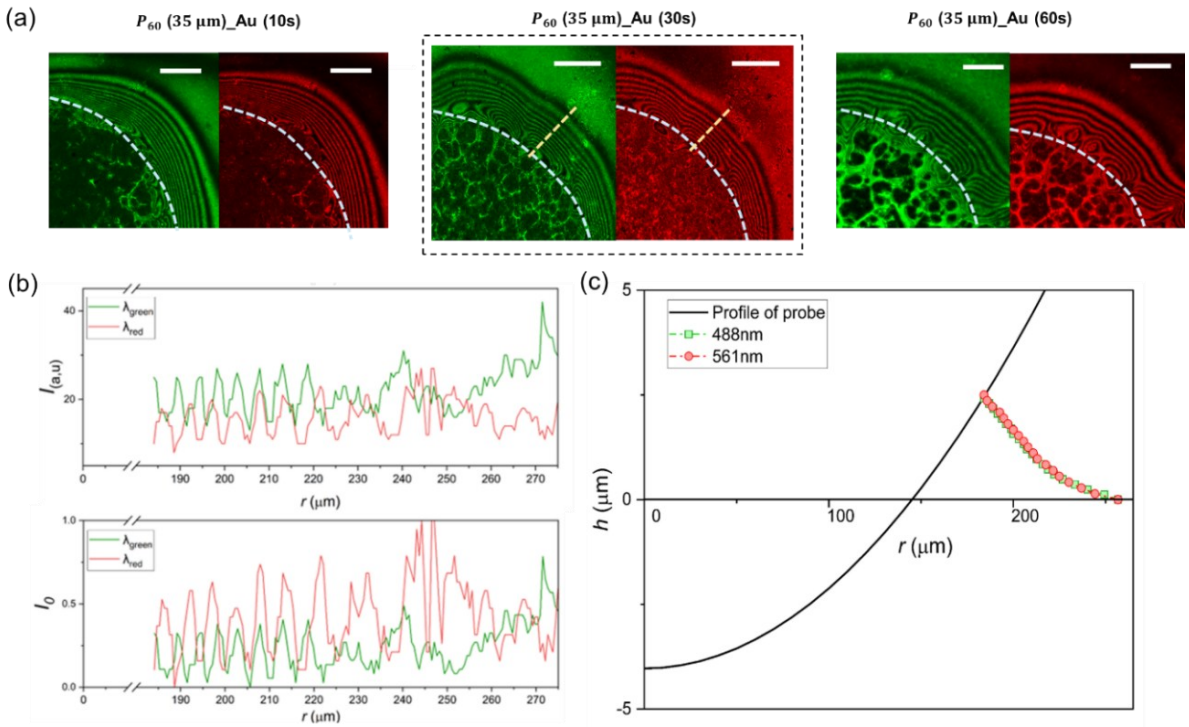


Figure 5-5 (a) Unprocessed interference signature corresponding to the contact of the ink-coated probe with the Au sputtered soft substrates P_{60} with varying sputtering times. Scale bars: 50 μm. (b) A plot of raw and normalized intensity distribution for the P_{60} - Au (30 s) substrate along the white dashed line in (a). (c) Profile of the ink-coated probe and contact deformation of the Au sputtered soft substrate based on the interference signature along the dashed line shown in (a). The green and red symbols indicate the height extracted using $h_{g,r} = m\lambda_{g,r}/4n_{PDMS}$. The dark solid line indicates the theoretical profile of the ink-coated probe using $h = \left(\sqrt{R^2 - a^2} + h_0\right) - \sqrt{R^2 - r^2}$.

In Figure 5-6, we show the contact deformation for the ink-coated probe on Au-sputtered soft substrates with varying deposition times. For all the soft substrates, the contact radius decreases with increasing Au deposition times, indicating the substrates become stiffer with increasing Au deposition time (or increasing Au film thickness) [113]. For instance, for the P_{45} substrate with Au deposition time increase from 10 s to 60 s, the average contact radius decreases from 170.30 μm to 146.82 μm. Here, we note that the contact radius of the bare P_{45} substrate is 187.96 μm. In addition, the ridge height h_0 is higher for the bare PDMS and progressively decreases with increasing Au deposition (Figure 5-6(d)). Note that the marginal variation in the ridge height with Au deposition is most likely due to the finite thickness of the underlying soft coatings. A more pronounced change in the ridge height can be observed for thicker PDMS coatings. It is worthwhile to mention that the black ink coating may alter the mechanical properties at the contact interface. To evaluate this, we compare the contact radius of the bare glass probe and the ink-coated probe on the bare PDMS substrates as well as the PDMS-Au bilayer substrates (Figure C5-15, Appendix C). Note that there are limitations in accurately measuring the contact radius using the bare glass probe close to the ridge tip. Nevertheless, considering measurement errors, a rough comparison of the contact radius measured using a bare glass and ink-coated glass probe indicates that the contact radius is slightly lower for the ink-coated probe and the trend is consistent across all the substrates (Figure C5-15, Appendix C). Note that such slight alteration in mechanical properties of the contact interface due to the ink-coated probe does not affect the primary objective of our imaging modality, i.e., visualize the contact ridge with higher accuracy.

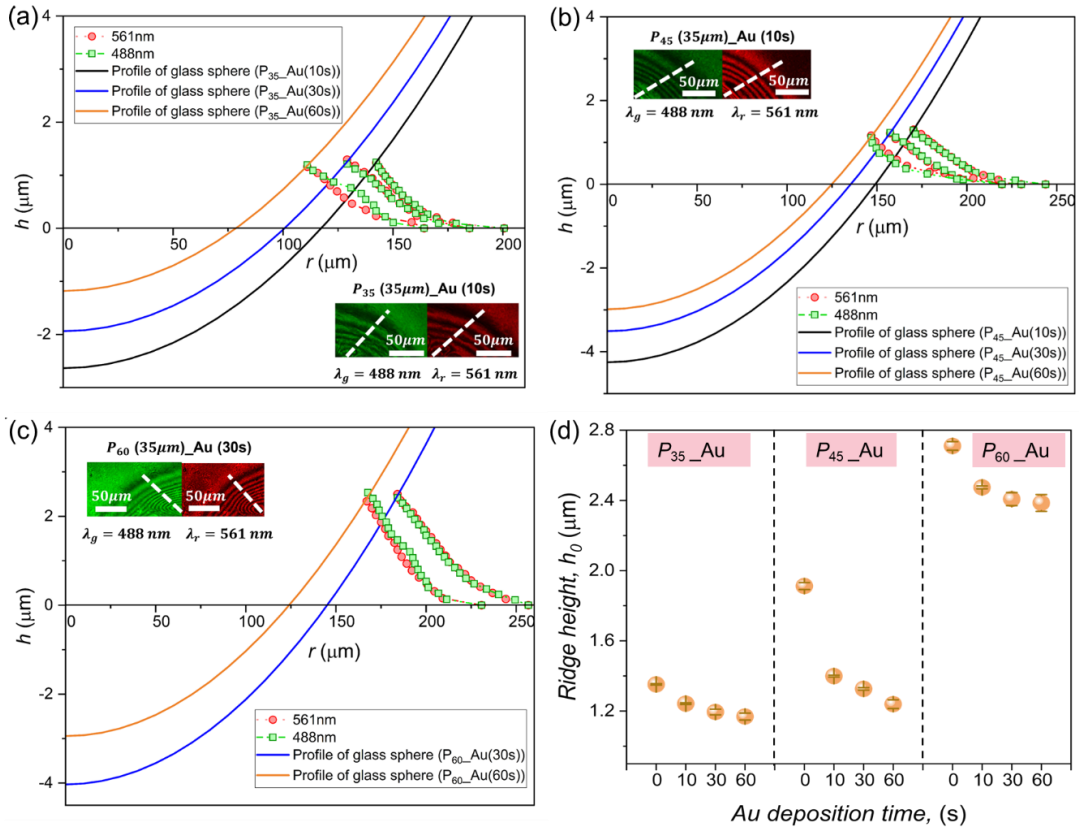


Figure 5-6 Reconstructed profiles of the ink-coated probe with a radius of 2.615 mm and the contact deformation of Au-coated (a) P_{35}, (b) P_{45}, and (c) P_{60} substrates at different Au deposition times of 10 s, 30 s, and 60 s based on the interferograms. The green and red symbols indicate the height extracted using $h_{g,r} = m\lambda_{g,r}/4n_{Au/PDMS}$. The solid lines indicate the theoretical profile of ink-coated probes using $h = \left(\sqrt{R^2 - a^2} + h_0\right) - \sqrt{R^2 - r^2}$. (d) Ridge height h_0 of different PDMS-Au bilayer substrates. Error bars represent the standard deviations of the reconstructed h_0 obtained from measurements at the laser wavelengths (488 nm and 561 nm). In some cases, the error bars are smaller than the data symbols.

5.3.3 Evolution of contact deformation

The stability of metal-polymer bilayer substrates is vital for many applications. Hence, a thorough understanding of the long-term contact effects is necessary. The long-time deformation dynamics is particularly relevant for the thin metal film deposited on the gel-like PDMS, P_{60} substrates, containing a higher fraction of liquid-like non-crosslinked chains in the

polymer network. Together with the fact that the weight of the ink-coated probe will continuously compress the soft surface, increasing the indentation depth, the temporal contact dynamics offers rich physics. In Figure 5-7(a), we highlight the temporal interferograms for an ink-coated probe on a bare P_{60} substrate. Over a span of 35 hours, the surfaces exhibit significant changes. First, the contact radius and indentation depth increase (Figures 5-7(a) and (c)) due to the probe weight. And then, the ridge height decreases over time since long-term poroelasticity entails a viscous flow of free liquids away from the ridge; thus, lowering the ridge height. However, for the Au/PDMS substrate, the ridge height also increases while the contact radius and indentation depth increase over time (Figures 5-7(b) and (d), and Figure 5-8). Although the metal deposition increases the elasticity of the bilayer substrates [113], free liquids in the PDMS can still flow away from the ridge lowering its height over time (see Figure 5-8). The counter-intuitive phenomenon of ridge height increase can be interpreted considering the long-term diffusion of the Au into the soft gel-like substrate. As shown in Figure 5-7(b), at the early stage, the contact area between the ink-coated probe and the P_{60} - Au (10 s) bilayer substrate is noticeably rough. However, over time, the contact area appears smoother and darker. Thus, two possible scenarios can occur that lead to ridge growth rather than decay: a) the Au gradually diffuses within the layer which leads to a decrease in stiffness or an increase in adhesive energy of the bilayer system. b) The contact deformation increases indentation depth and consequently the probe-gel interface gradually goes out of focus.

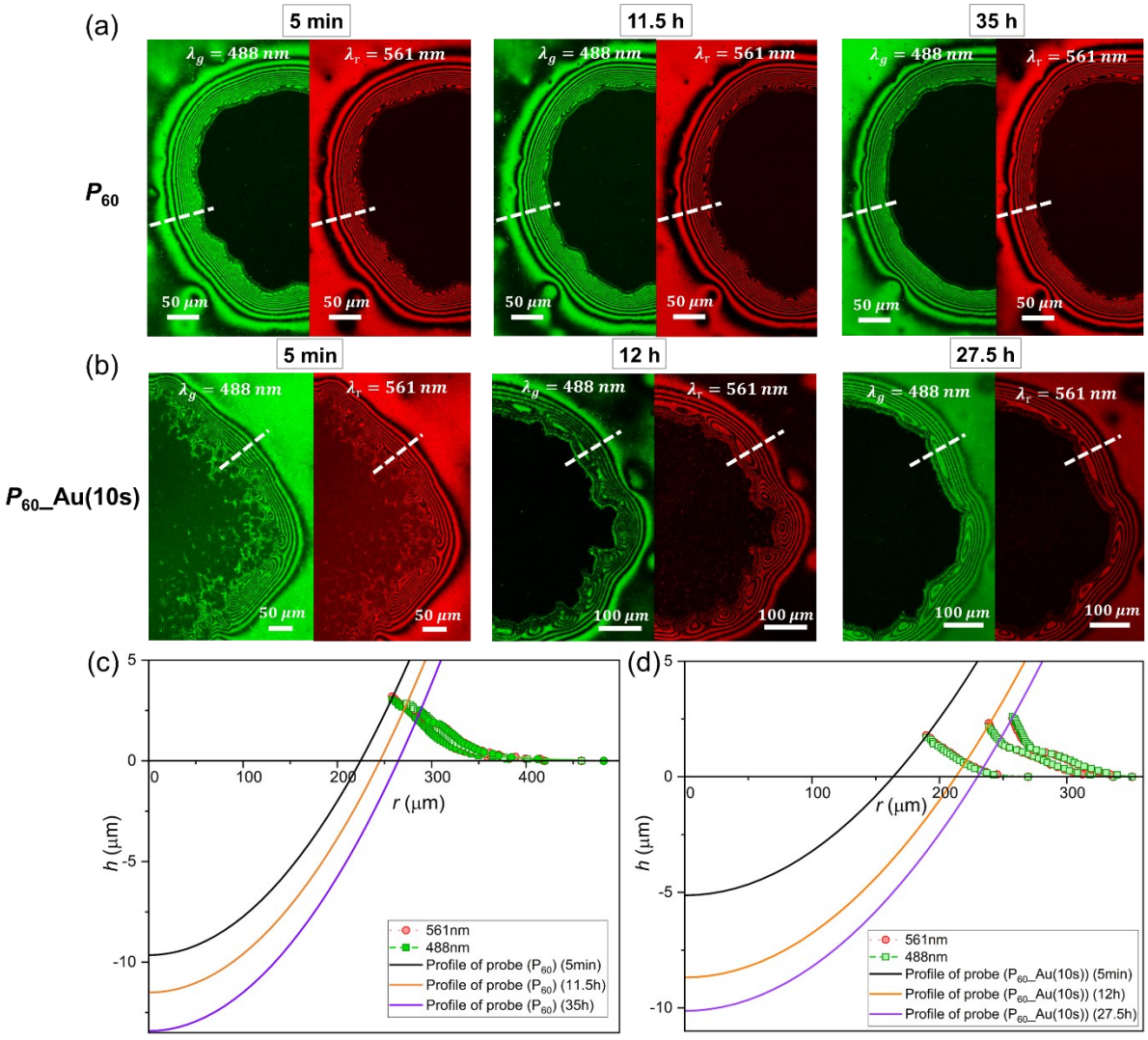


Figure 5-7 (a) Interferograms of a 2.615-mm-radius ink-coated probe on P_{60} soft substrate at 5 min, 11.5 hrs., and 35 hrs. after contact. (b) Interferograms of a 2.615-mm-radius ink-coated probe on P_{60} - Au (10s) metal - polymer bilayer substrate at 5 min, 12 hrs., and 27.5 hrs. after contact. (c) Plots of the ink-coated probe and contact deformation profiles for the interferograms shown in (a) at the location of the white dashed lines. (d) Plots of the ink-coated probe and contact deformation profiles for the interferograms (shown in (b)) at the location of the white dashed lines. The green and red symbols indicate the height extracted using $h_{g,r} = m\lambda_{g,r}/4n_{PDMS,Au/PDMS}$. The solid lines indicate the theoretical profiles of the ink-coated probes using $h = \left(\sqrt{R^2 - a^2} + h_0\right) - \sqrt{R^2 - r^2}$.

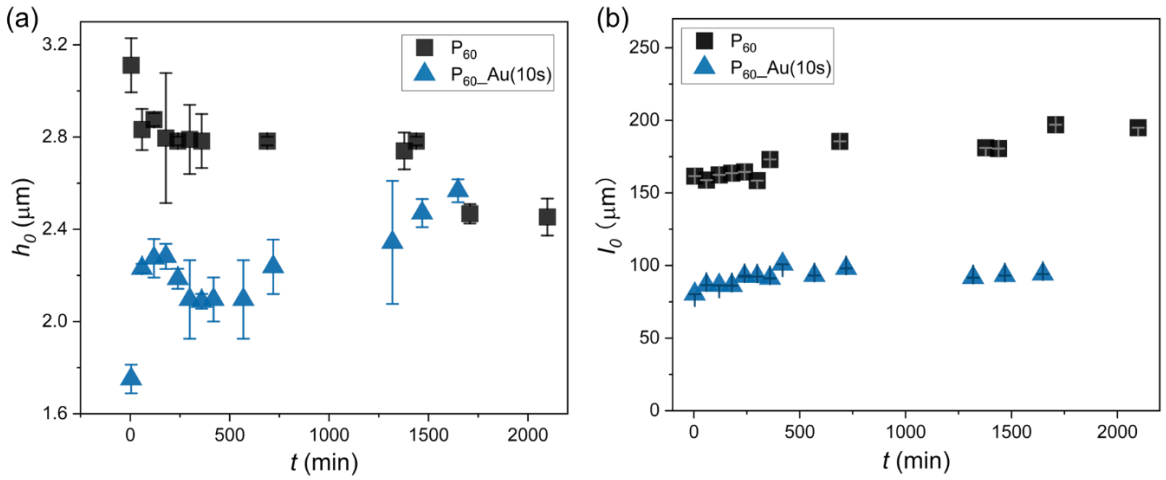


Figure 5-8 Evolution of ridge height h_0 (a) and maximum lateral deformation, i.e., ridge width l_0 (b) for bare P_{60} and P_{60} with Au sputtering for 10 s. Error bars represent the standard deviations of the reconstructed h_0 and l_0 obtained from measurements at the laser wavelengths (488 nm and 561 nm). In some cases, the error bars are smaller than the data symbols and are therefore not visible in the figure.

The long-time deformation of P_{60}-Au (10s) was further investigated by Raman spectroscopy to monitor the typical peak intensity of surface chemicals, as shown in Figure 5-9. Note that the hemispherical lens was used instead of the glass probe because the hemispherical lens enables a better focus spot with less scattering and clearer signals under Raman Spectroscope (Figure C5-11, Appendix C) after a series of preliminary trials (C5.11, Appendix C). When the hemispherical lens is in direct contact with the surface of the soft substrate, the soft substrate deformed under the weight of the hemispherical lens, forming a contact deformation zone similar to the contact between a glass sphere and the soft substrate. Then the laser spot of Raman spectroscopy went through the center of the hemispherical lens and focused on the surface of deformation region. The Raman spectra (typical Raman peaks) we eventually obtain relates to the deformation region of the P_{60}-Au (10s) as we shown in Figure 5-9 are same as the P_{60}-Au (10s) without placing the hemispherical lens (Figure C5-13, Appendix C), which indicates that the Raman measurements results are not affected by the hemispherical lens. The characteristic bands of cured PDMS were observed at 486, 615, 707, 1260, 1415, 2905, and 2967 cm^{-1}, corresponding to Si-O stretch, C-Si stretch, SiC_2

antisymmetric stretch, CH_2 bending, CH_3 symmetric stretch and CH_3 antisymmetric stretch, respectively [129,247]. The characteristic peaks that distinguish PDMS base from cured PDMS are related to vibration bands of the Si-CH=CH_2 group at 1608 cm^{-1} (overlap with the phenyl group vibration) and 1400 cm^{-1} [129,247]. The Raman peaks related to Au were in the region from 1300 to 1600 cm^{-1} and 2130 cm^{-1} [248]. Thus, all the characteristic peaks of cured PDMS and Au were observed even without the probe (hemispherical lens) in contact with the substrate. However, upon placing the probe, the intensities of all peaks became weaker. This is because the scattering of the laser by the probe led to a reduction in the intensity of reflected light. Furthermore, we observed that upon placing the probe on the metal-polymer bilayer substrate, the intensity of the peak at 2130 cm^{-1} decreased with increasing contact time and finally saturated when the contact time was longer than 24 hrs. This observation reiterates that close to the center contact area; the surface of the soft substrate continuously deforms as the contact time increases. As the Au diffuses into the PDMS, its intensity decays. Besides, the peak at 1608 cm^{-1} corresponding to the Si-CH=CH_2 group was observed up to the contact time of 15 hrs, beyond which the observed peak disappeared. This illustrates that as the contact time increases and Au diffuses into the PDMS substrate, the Raman signature of the unreacted PDMS base, i.e., the free liquid inside the polymer network progressively decays since it is no longer being enhanced by the Au.

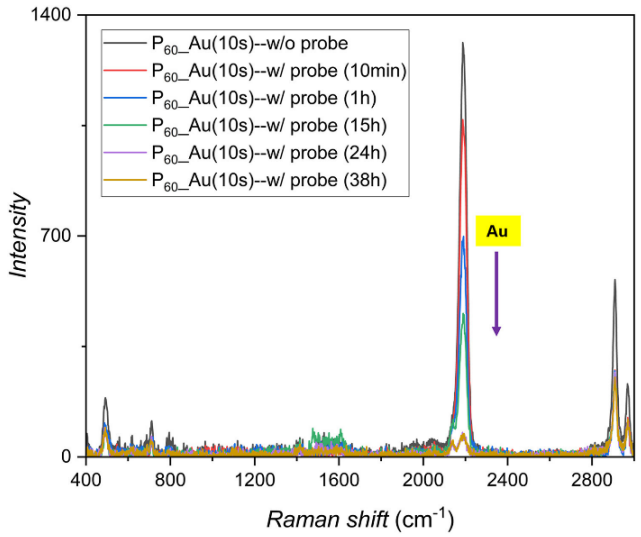


Figure 5-9 Raman spectra of P_{60} - Au (10 s) in contact with the glass probe (hemispherical lens) and its variation over time.

Finally, it is worthwhile to note that the present experimental modality is simple and easy to use; and probes with other materials can be coated with black ink. Thus, this technique could be applied to other materials as well, such as steel balls. There is also flexibility in terms of probe size and weight making the method suitable for studies involving loading-unloading stress/stain cycles where control of applied force is highly desired. In Figure C5-16 (Appendix C), we demonstrated an example where an ink-coated steel probe with a larger diameter of 19 mm is used to probe the contact deformation of a soft PDMS substrate. As revealed from the interference signature, the deformation profile, i.e., the contact ridge up to the contact boundary is reconstructed. The present study aligns well with the ongoing efforts to understand the contact deformation of bilayer soft substrates, as well as how nanoscale thin metal films affect soft contact behaviors. Hence, it is inspiring to contemplate how our work fits into the framework of soft contact, coatings development, and advancement of e-skin. Though contact dynamics of soft substrates have been reported previously [18,44,52,53,223,224,249,250], the contact deformation behaviors of viscoelastic substrates with sputtered metallic thin films were seldom investigated, such as the long-term contact behaviors of bilayer soft substrates with finite-thickness. For the majority of studies, the contact ridge was observed where the underlying

soft substrates with semi-infinite thickness [18,223,224,250] or soft substrates swollen with silicon oil or modified with fluorescein molecules [223,224]. Jensen, et al showed that the phase-separation of gel films formed the contact ridge near the contact line when a microscale silica sphere was on a gel film, which is consistent with our observations [224]. Recently, Kim et al. investigated the long-term contact dynamic of gel film with finite-size effect and preload shown time-dependent by DW-RICM because of the simultaneous existence of solid and liquid phases and the ridge evolution arises from the combining effect of the external preload, finite-size effect, and viscoelasticity [44]. However, due to the limitation of the method using a bare glass sphere combing with DW-RICM, the contact ridge that was close to the contact boundary encountered interference by reflected light from the glass sphere and was predicted based on the volume of indentation of the glass sphere and the partial reconstruction of deformation profile [44,113]. Our study provides a novel method to visualize the formation and change of contact ridges, resulting in a deeper insight into the soft contact systems.

5.4 Conclusion

As a proof-of-concept, we have demonstrated a novel interference modality for quantifying the contact deformation profiles of PDMS coatings, both bare and metal-deposited, with a finite coating thickness of 35 μm while varying the elastic modulus and metal deposition time. To achieve high-resolution quantification, we combine the use of a black ink-coated probe and dual wavelength-reflection interference contrast microscopy (DW-RICM). The interference fringes that were obtained embedded only the deformation signature of the bare or metal-polymer bilayer substrate enabling accurate extraction of the contact ridge profile in the vicinity of the contact region. Stray light is efficiently absorbed by the black ink coating. As a result, complete visualization of the contact ridge is possible, extending to the ridge tip where it meets the probe surface. For soft substrates with varying elasticity and metal (Au) deposition times, the ridge height, the ridge width, and the contact radius are examined. We note that regardless of Au deposition, soft substrates have a contact ridge, which is consistent with earlier studies using such soft substrates [18,44]. Our analysis of long-term contact

deformation presents crucial insights. With increasing contact times, the soft substrates undergo increasing deformation, i.e., increasing indentation depth, and increasing ridge width but decreasing ridge height. The decreasing ridge height is well documented and highlights the role of long-term poroelasticity [44,224,251]. However, when a thin metal film is deposited, the deformation increase is accompanied by a counter-intuitive observation of an increase in the ridge height. Using both RICM and Raman signatures, we have shown how the diffusion of the metal, i.e., Au into the PDMS contributes to this ridge growth either by decreasing the effective elasticity of the interface or by increasing the adhesion.

The research findings not only offer fundamental insight into soft contact of thin metal-polymer bilayer substrates but might also have profound technical implications for engineering applications, such as flexible pressure sensors [252,253], e-skin [254,255] and intelligent robotics [256]. In those applications, soft surfaces are inevitably in contact with other objects and deform, affecting their performance. Understanding the contact deformation mechanism of such bilayer soft substrates will contribute to a deeper comprehension of the relationship between deformation and performance, which will contribute to the development of more targeted and application-specific industrial products. Future studies will need to address the composition and distribution of phase separation and elastic compressive deformation of substrates during the formation of contact ridge, as well as the contact ridge of different types of gels, such as hydrogel, having varying compressibility of the elastic network [257,258]. A smooth surface, light-absorbing probe is critically needed to complement the DW-RICM, thus enabling the proposed optical-based technology to be utilized in a broader application field.

Chapter 6

Solvent-induced triradial pattern formation on solid-supported viscoelastic thin films and gel

Solvent-driven surface instabilities in soft materials offer a powerful route to generate spontaneous patterns without external templating, yet the mechanisms governing their emergence, evolution, and long-term modulation remain elusive. Here, we uncover the time-dependent formation of quasi-periodic triradial patterns on the surface of thin, soft films undergoing hexane extraction and drying. Using DW-RICM, we observe a reproducible morphological progression: from shallow circular domains at short extraction times to a well-defined array of triradial, three-armed patterns at longer durations, driven by the buildup of internal stress, surface-to-bulk modulus gradients and network densification. Systematic studies across silicone elastomers and gels reveal that while the triradial patterning is broadly conserved, its geometry is tunable by factors such as cross-link density and solvent retention. These results establish a general mechanism of solvent-mediated pattern formation in soft films and offer a new strategy for designing dynamic and programmable surface architectures through controlled solvent processing.

6.1 Introduction

Surface pattern formation in soft materials represents a hallmark of out-of-equilibrium processes in both natural and engineered systems [259,260]. Such patterns manifest across multiple length scales and functional contexts, from the morphological buckling of fruits and vegetables [261], the folding of the cerebral cortex in biological tissues [262] and the wrinkling of human skin [263,264], to desiccation-induced cracking in dried mud flats [265], and the controlled buckling of thin elastic films for flexible electronics and biomimetic surfaces [266–268]. These structurally rich morphologies not only reflect underlying mechanical instabilities but also serve as functional architecture in nature inspiring diverse technological applications. Mechanically induced

surface instabilities, such as wrinkling [262], creasing [269], and buckling [259] have been widely studied in thin elastomer films, where stress gradients, elastic modulus gradients, and boundary constraints drive spontaneous symmetry breaking and ordered morphologies [259,262,266,269]. Beyond mechanical triggers, external stimuli, including thermal gradients [270], electric fields [271], light-induced molecular reconfigurations [272,273], magnetic fields [274] and plasma [275] have also been employed to modulate surface instabilities in soft materials. These features enable dynamic and programmable patterning, providing versatile platforms for tuning wettability, adhesion, optics, and mechanotransduction, with applications spanning flexible electronics, soft robotics, and bioinspired coatings [268,273,275,276].

Solvent-induced polymer reorganization represents a particularly effective strategy for triggering surface instabilities [20–25], which has been employed to achieve reversible modulation of cellular microstructural topologies [277], enhancement of mechano-sensitivity for mechano-chromic polymers [278] and gelation of hydrogel [279]. Particularly, upon swelling, soft films supported on to a rigid substrate are subjected to spatial gradients in elastic modulus and compressive stresses, decreasing from the top to the bottom, which can lead to buckling, wrinkling, or delamination after drying [21–25,280,281]. While several studies have investigated surface wrinkling from such solvent processes [280,282,283], the full dynamic pathway from swelling to surface patterning remains elusive, especially in systems involving significant free-liquid content and heterogeneous network densification [284,285].

Here, we report the time-dependent formation of highly ordered triradial (three-armed) surface micro-nano structures (patterns) on soft elastomeric and gel films containing significant free liquid polymer chains, which are spin coated onto a rigid glass substrate (hereafter referred to as confined soft films) and are driven by prolonged solvent extraction. By immersing these confined soft, thin films in hexane for controlled durations and subsequently drying them under ambient conditions, we observe a reproducible evolution of surface morphology: from disordered circular domains for low extraction times to well-defined, periodic triradial ridge-like patterns upon extended solvent removal. Through Dual-

wavelength reflection interference contrast microscopy (DW-RICM), atomic force microscopy (AFM), and Raman spectroscopy, we reveal that these patterns arise from solvent-induced gradients in modulus and internal compressive stress, which drive buckling instabilities and subsequent pattern formation. Furthermore, through systematic variation of material composition, i.e., different base-crosslinker ratios of the polymers, extraction time, and drying conditions, we demonstrate that the geometry and fidelity of the resulting surface patterns are governed by the coupling of the removal rate of the free liquid polymer chains, solvent uptake, structured surface network formation, and stress relaxation. These findings establish a general, lithography-free strategy for programmable surface patterning in soft matter systems and offer new insights into the mechanics of stress-driven self-organization in solvent-responsive polymeric materials. This work not only elucidates the underlying mechanism of stress-guided pattern formation but also opens new avenues for scalable, self-organized surface engineering in soft functional materials.

6.2 Materials and experiments

6.2.1 Materials

Silicone elastomer Polydimethylsiloxane (PDMS) (SYLGARD^{TM} 184 Silicone Elastomer Kit, Dow Corning) consisted of component A (base, Molecular weight (Mw): 27 kg/mol) and component B (curing agent) was purchased from Sigma Aldrich. Silicone gel consisted of component C (base, Mw: 28 kg/mol, Gelest, DMS-V31), component D: (catalyst, Mw: 474.68 g/mol, Gelest, SIP6831.2), and component E: (curing agent, Mw: 1.95 kg/mol, Gelest, HMS-301) and all purchased from Gelest, Inc. Organic liquids, including hexane, ethanol, and isopropanol, were purchased from CHEM STORE of the University of Waterloo. All chemicals were used as received without further treatment.

6.2.2 Fabrication of silicone elastomer thin films

The silicone elastomer thin films were fabricated by spin-coating PDMS solution on freshly cleaned glass slides (Microscope slides, Sail Brand, dimensions: 38.1 mm × 25.4 mm ×1 mm) by a spin coater (Specialty Coating Systems, Spincoat G3-8). The thickness of the elastomer substrates was regulated by adjusting the volume of PDMS solution to 0.3 mL and the spin-coating speed to 2100 rpm. The glass slides were first thoroughly rinsed with isopropanol and ethanol, then dried with N_2 gas before use. The PDMS solution was prepared by mixing component A and component B at weight ratios of 60:1, 64:1, and 80:1, respectively. The PDMS solution was uniformly mixed and degassed by a planetary mixer (Thinky Corporation, ARE-310) for 5 min, respectively, then spin-coated on the glass slides and cured at 80 ℃ for 14 hrs. The thickness of the elastomer thin films was determined using Field Emission Scanning Electron Microscopy (Zeiss UltraPlus FESEM). The PDMS substrate was named P_{60}, P_{64}, and P_{80} based on the aforementioned ratio of the base and crosslinker.

6.2.3 Fabrication of silicone gel thin films

The silicone gel thin film was fabricated in a manner similar to the PDMS. First, solution #1 was prepared by mixing component C (base) with component D (catalyst) using weight ratio of 10:0.005 using the planetary mixer for 5 min**.** Then the solution #2 was prepared by mixing component C (base) with component E (curing agent) at a weight ratio of 10:1 using the planetary mixer for 5 min. Finally, solutions #1 and #2 were mixed in a weight ratio of 9:1, degassed, coated on the freshly cleaned glass slides, and cured at 80 ℃ for 14 hrs.

6.2.4 Hexane-induced pattern formation

The pre-cured soft substrates (silicone elastomer films and silicone gel films) were placed in a beaker with the soft coating side on top and the glass substrate at the bottom. 200 mL of hexane was carefully introduced along the inner walls of the beaker to minimize surface disturbance. Consequently, the beaker was covered with aluminum foil to suppress solvent evaporation. Substrates were swollen for 96 hrs, with hexane refreshed every 48 hrs.

Subsequently, the soft substrates were removed from the solvent and dried in air or an oven to ensure complete evaporation of the solvent. The regular pattern was formed during the evaporation process. Swelling experiments were also performed for 8 min, 1 hr, and 10 hrs.

6.2.5 DW-RICM measurement

To analyze the hexane-induced pattern formation on the soft substrates, DW-RICM measurements were performed on a Zeiss LSM 800 inverted microscope using a microscope objective of 10x and a numerical aperture (NA) 0.3 (EC Plan-Neofluar) under two focused monochromatic light beams of wavelengths (488 nm (green) and 561 nm (red)). From the interferometric images, we first extract the intensity distribution for both wavelengths along a chosen slice. The intensity distribution reveals alternate peaks and valleys corresponding to bright and dark fringes. Consecutive bright and dark fringe represents a height variation of $\Delta h = m\lambda/4n$, where λ_g = 488 nm, λ_r = 561 nm, m is the order of the interference fringes and n (PDMS) ≈ 1.4. Using this relation, the entire height variation is calculated corresponding to both wavelengths. Note that intensity normalization is performed using the relation $I_0 = (I - I_{min})/(I_{max} - I_{min})$, where I_{max} and I_{min} are the minimum and maximum intensities for a particular intensity distribution.

6.2.6 Optical Microscopic measurement

To analyze the pattern formation on soft substrates, optical microscopy measurements were performed on a Zeiss LSM Observer.Z1m instrument with a magnification of 5×.

6.2.7 AFM measurement

To analyze the height and structure of the hexane-induced microstructural features on soft substrates surface, atomic force microscopy (AFM) was conducted using a Pacific Nanotechnology AFM Nano-R with a stylus profilometer (Veeco DekTak 8).

6.2.8 SEM measurement

To analyze the thickness of the soft substrates before and after extraction of hexane for 96 h, SEM measurements were conducted on a field emission scanning electron microscope (Zeiss UltraPlus FESEMs). The soft substrates were cut into 8 mm × 10 mm (width × length) pieces and mounted on the stub aligned at an angle of 90° with a conductive tape, with the soft coating layer facing outward and the glass slide in contact with the conductive tape, for SEM measurements.

6.2.9 Rheological measurement

To evaluate the viscoelastic properties of the soft substrates, rheological measurements were performed using a dynamic shear rheometer (AR 2000, TA Instruments) under a frequency sweep from 0.01 to 100 Hz at a strain amplitude of 1% and a normal force of 1 N. The PDMS mixtures, prepared at the specified base-to-curing agent ratios, were cast into 60-mm diameter Petri dishes to a thickness of 2 mm and cured at 80 °C for 14 h. The cured PDMS samples were then cut into circular specimens of 25-mm diameter. Tests were carried out using a 25-mm parallel plate geometry at a constant temperature of 25 ℃. Prior to each measurement, the samples were allowed to equilibrate for 10 min to ensure stability. The shear storage modulus (G') and loss modulus (G'') were recorded, and each measurement was repeated three times for reproducibility. The measured shear modulus values were later converted to Young's modulus (E) using $E = 2G(1 + \vartheta)$ with Poisson ratio ϑ (PDMS) ≈ 0.5.

6.2.10 Raman spectroscopy measurement

To analyze chemical signatures of the soft substrates before and after extraction of hexane for 96 h, as well as the formed patterns on soft substrates, Raman spectroscopy measurements were conducted on an alpha300 R Raman microscope (OXFORD instruments) using the 532 nm laser wavelength. To ensure spatial accuracy, a two-step focusing protocol was employed. The region of interest was first identified in video mode using a 10× (Zeiss EC Epiplan-Neofluar DIC) objective (NA = 0.25), followed by laser focusing with a 100× (Zeiss

EC Epiplan-Neofluar DIC objective) (NA = 0.9) to minimize the laser spot size. Raman spectra were acquired using the same 100× objective, with the laser power set to 50% and an integration time of 5 s. For unextracted samples, spectra were acquired at the substrate center. For extracted samples, spectra were collected at four positions: a reference point away from the pattern, the central vertex of the triradial structure, and two points along the selected arm: midpoint (Line1-1) and foot (Line1-2). This enabled spatially resolved comparison of chemical composition between patterned and non-patterned regions.

6.3 Results and discussion

6.3.1 Formation and characterization of solvent-induced patterns on silicone elastomer thin films.

Figure 6-1(a) illustrates the schematic of the solvent-induced (swelling and evaporation) pattern formation process on a solid-supported soft PDMS coating (P_{60}) of 30.76±0.28 μm thickness and Young's modulus, E = 9.6 kPa (Figures D6-1(a) and (b), Appendix D). A typical experiment involved swelling in hexane for 96 hrs followed by drying in ambient conditions for 10 mins. Post drying, the surface instabilities, i.e., the morphology of the patterns, were observed using DW-RICM (Figure 6-1(b)) and bottom-view optical microscopy (Figure 6-1(c)). Both images reveal a quasi-periodic array of *Y-shaped* triradial (three-armed) microstructures on the overall surface, while DW-RICM imaging (Figure 6-1(b)) reveals a higher resolution with further zooming in on the pattern. The observed patterns display some common features: a characteristic inter-arm angle of approximately 120°, an average arm length of 53.82 ± 9.66 μm, and a center-to-center distance (pitch) of 91.02 ± 8.99 μm. From the DW-RICM measurements, we observe a uniform distribution with approximately 200 such patterns on a 1.02 mm x 1.02 mm region. The observed color variations in Figure 6-1(b) (last row) arise from the combined effects of laser wavelengths of 488 nm (green) and 561 nm (red), with each wavelength corresponding to a distinct interference condition related to the local surface topography. To investigate whether the quasi-periodic array of triradial (three-armed)

patterns exhibits any polarization-dependent optical response, polarized light microscopy was performed to examine the surface patterns under varying polarization angles (Figure D6-2, Appendix D). As expected for an isotropic material like PDMS, the observed surface morphologies remained unchanged with the rotation of the polarization angle. This result confirms that the surface pattern does not induce polarization effects and exhibits no optical anisotropy under polarized light. The atomic force microscopy (AFM) images (Figure 6-1(d)) and corresponding three-dimensional (3D) surface reconstructions (Figure 6-1(e)) further confirm that the triradial structures protrude above the substrate surface, with the central vertex reaching a height of approximately 450 nm. Thus, the instability reflects a ridge-like formation, rather than creases or wrinkles, with a ridge opening angle close to π. Such ridge-like instabilities are common for wetting and adhesion on soft substrates where elasticity and capillarity compete. However, unlike the smooth morphologies commonly observed for wetting or contact ridges [18,44,53,55,103,223], here, we observe that the morphology of the ridge is rugged with multiple undulations. Note that it is likely that these undulations are not actual pattern features and may have been induced by the AFM tip. Furthermore, we observe that the ridge half-width is maximum at the ridge tip with a typical value of approximately 8 μm and gradually decays to zero at the foot (Figures 6-1(b) and (d)).

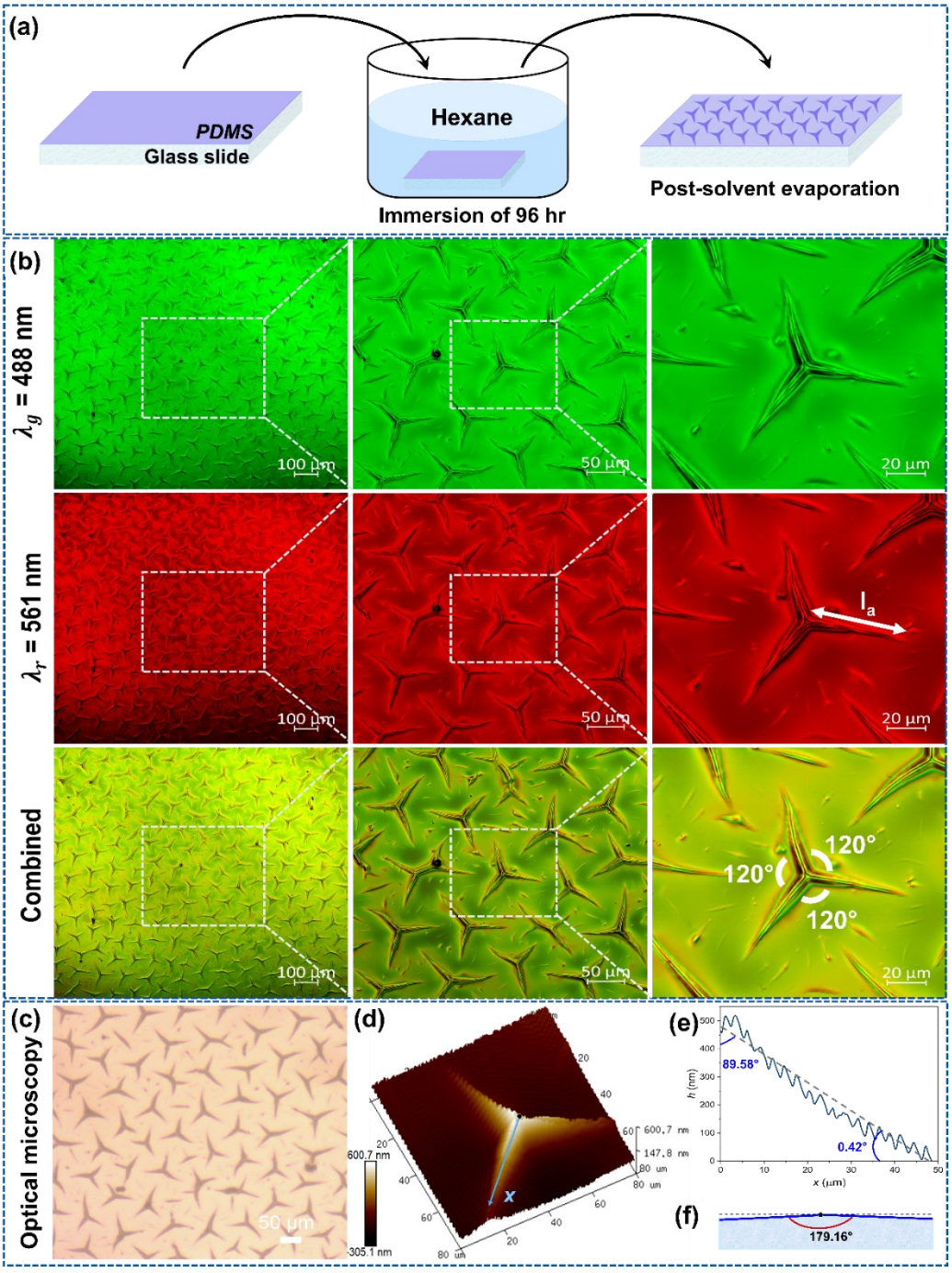


Figure 6-1 (a) Schematic of the hexane-extraction experimental set-up. (b) Dual-Wavelength Reflection Interference Microscopy (DW-RICM) snapshots of the pattern formation. The green and the red channels reflect

imaging using 488 nm and 561 nm wavelengths, respectively. The combined channel image is the overlay of the green and red channel images. l_a represents the pattern arm length. (c) Optical microscopy snapshot of the pattern formation. (d) Atomic force microscopy scan and profile reconstruction of a pattern. (e) Profile of the ridge along the blue line highlighted in (d). The angles are shown for clarity. The dashed line is an approximate linear fit of the profile shown to highlight the angles. (f) Schematic of the ridge tip highlighting the opening angle.

It is noteworthy to mention that for surface-attached polymers, swelling-induced formation of creases and wrinkles on the free surface results from compressive stress release. Ridges can also occur by a phenomenon called *buckle delamination,* where the soft coating delaminates locally from the underlying rigid substrate [25]. For both these cases, swelling induces an increase in the thickness of the soft layer. Interestingly, Y-shaped creases having an inter-arm angle of 120° have also been observed for swelled confined gels [23,286]. However, for the present experiments, where swelling is followed by solvent evaporation, the Y-shaped ridge formation follows a decrement in its thickness of roughly 58.06 %, i.e., significant shrinking. Thickness measurements before and after extraction, conducted by scanning electron microscopy (SEM, Figure D6-3, Appendix D), revealed a reduction from 30.76± 0.28 μm to 12.9 ± 0.31 μm. A corresponding weight loss of approximately 60.02% indicates that the shrinkage is due to significant removal of free liquid chains within the PDMS network by hexane. Note that a pristine, unswollen PDMS substrate usually contains 60% free liquid phase by weight (labelled as P_{60}) [54]. Thus, the initially swollen elastomer may have formed creases. However, following solvent evaporation, free liquids are extracted, the soft layer shrinks, and the associated compressive stresses result in out-of-plane ridge-like pattern formation. Lastly, we compare the ridge height with the characteristic elastocapillary length-scale, $l_{EC} = \gamma/E$, where γ is the PDMS surface tension. Considering $\gamma \approx 21$ mN/m [287], $l_{EC} \approx 2.18$ μm, which is approximately four times the ridge height of 450 nm. The overestimation may either be due to the enhanced elastic modulus of the PDMS layer of finite thickness or due to the elasticity increase post-extraction of free liquids. Longer time observation reveals that the pattern is highly stable and irreversible: a random incision on the surface does not affect the neighbouring patterns (Figure D6-4, Appendix D), i.e., there are no residual compressive

stresses and trapped liquid phase. Thus, surface tension and elasticity predominantly dictate equilibrium pattern profiles.

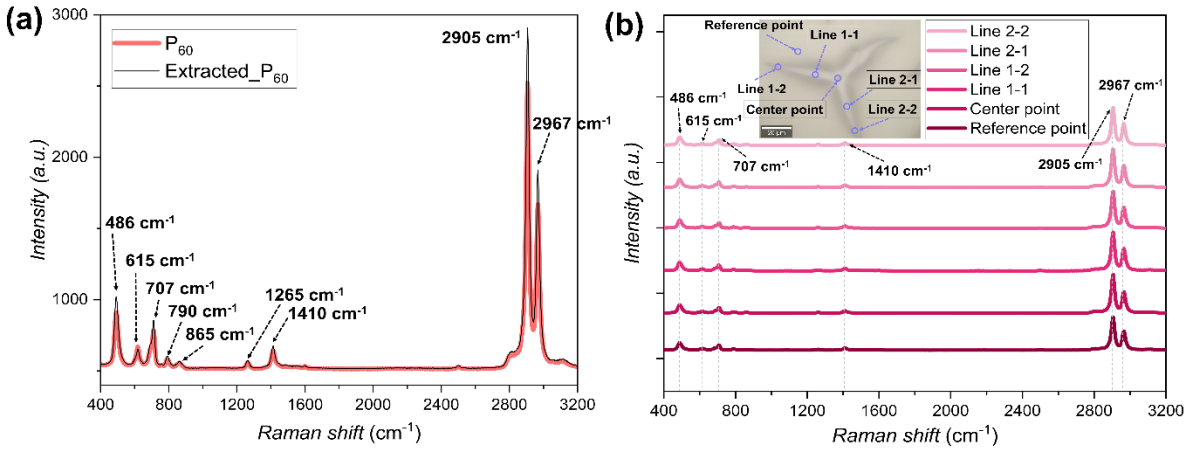


Figure 6-2 (a) Raman spectra of pristine P_{60} and hexane-extracted P_{60} soft substrates. (b) Raman spectra of multiple selected positions around a pattern on the surface of the hexane-extracted P_{60} soft substrate.

To shed further light on the pattern formation, we first assess the changes in the chemical signature of the substrates before and after solvent extraction and drying using Raman spectroscopy. As shown in Figure 6-2(a), the Raman spectra of pristine P_{60} and hexane-extracted P_{60} with patterns exhibit identical peak positions, with characteristic signatures at 486, 615, 707, 790, 865, 1265, 1410, 2905, and 2967 cm^{-1} Raman shift, corresponding to Si-O stretching, Si-C asymmetric stretching/ Si-CH_3 rocking, Si-C symmetric stretching, -CH_3 asymmetric rocking/ Si-C asymmetric stretching, -CH_3 symmetric rocking, -CH_3 symmetric bending/rocking, -CH_3 asymmetric bending, -CH_3 symmetric stretching, and -CH_3 antisymmetric stretching modes, respectively [67,129,247]. Notably, no new peaks were observed after swelling in solvent and drying, and only a slight increase in Raman intensity was detected, indicating that hexane removal did not induce chemical bond cleavage or residue retention. The intensity enhancement is attributed to the densification of the polymer network structure following immersion and solvent evaporation [288]. Further confirmation of chemical uniformity was obtained by comparing Raman spectra at multiple locations: a reference point on the

surface without patterns, the central vertex, and along two arms (both at the mid-arm and base regions) (Figure 6-2(b)). All spectra exhibited nearly identical profiles, verifying the chemical homogeneity of the patterned surfaces. Our Raman measurements reaffirm our earlier hypothesis of the removal of free liquid chains inducing polymer densification. Moreover, due to the absence of any hexane signature, we confirm that the developed ridges do not contain any trapped solvent close to the ridge tip.

From our experiments, we observed that once the soft substrates are removed from the solvent and dried in air, the patterns gradually appear as the hexane evaporates. Consequently, we assess the influence of drying conditions on the final pattern morphology. To do that, we systematically compared the effects of different air flow rates (ambient air versus fume hood), drying durations, and drying temperatures. Figure 6-3 shows the surface morphology of the P_{60} soft substrate after drying under four different conditions: in ambient air for 10 mins (Figure 6-3(a)), in ambient air for 12 hrs (Figure 6-3(b)), in a fume hood for 12 hrs (Figure 6-3(c)), and in an oven at 80 °C for 12 hrs (Figure 6-3(d)). Evident from Figure 6-3, no significant morphological differences were observed between the samples dried in ambient air or in the fume hood (Figures 6-3(a)-(c)); however, the pattern height increased from approximately 450 nm to 590 nm (Figure D6-5, Appendix D) under fume hood conditions, suggesting a modest influence of evaporation rate on vertical pattern amplitude. While the patterns obtained for the samples dried at elevated temperatures, i.e., in the oven exhibited lesser elevation (Figure 6-3(d)). Notably, the characteristic pattern lengths or the pattern density remained consistent across all drying conditions, with an average arm length of 52.42 ± 7.99 μm (Figure D6-6(a), Appendix D). The corresponding histograms (Figure D6-6(b), Appendix D) further reveal that the distributions of arm length are unimodal and largely overlapping across different drying environments. In all cases, the majority of measured lengths fall within a range of approximately 40-70 μm. Neither the mean values nor the overall statistical distribution of arm lengths is substantially affected by the drying condition. These results indicate that the nature of pattern formation is insensitive to air flow rate and drying

time but may be influenced by the drying temperature. Based on these observations, subsequent drying experiments were performed under ambient air conditions.

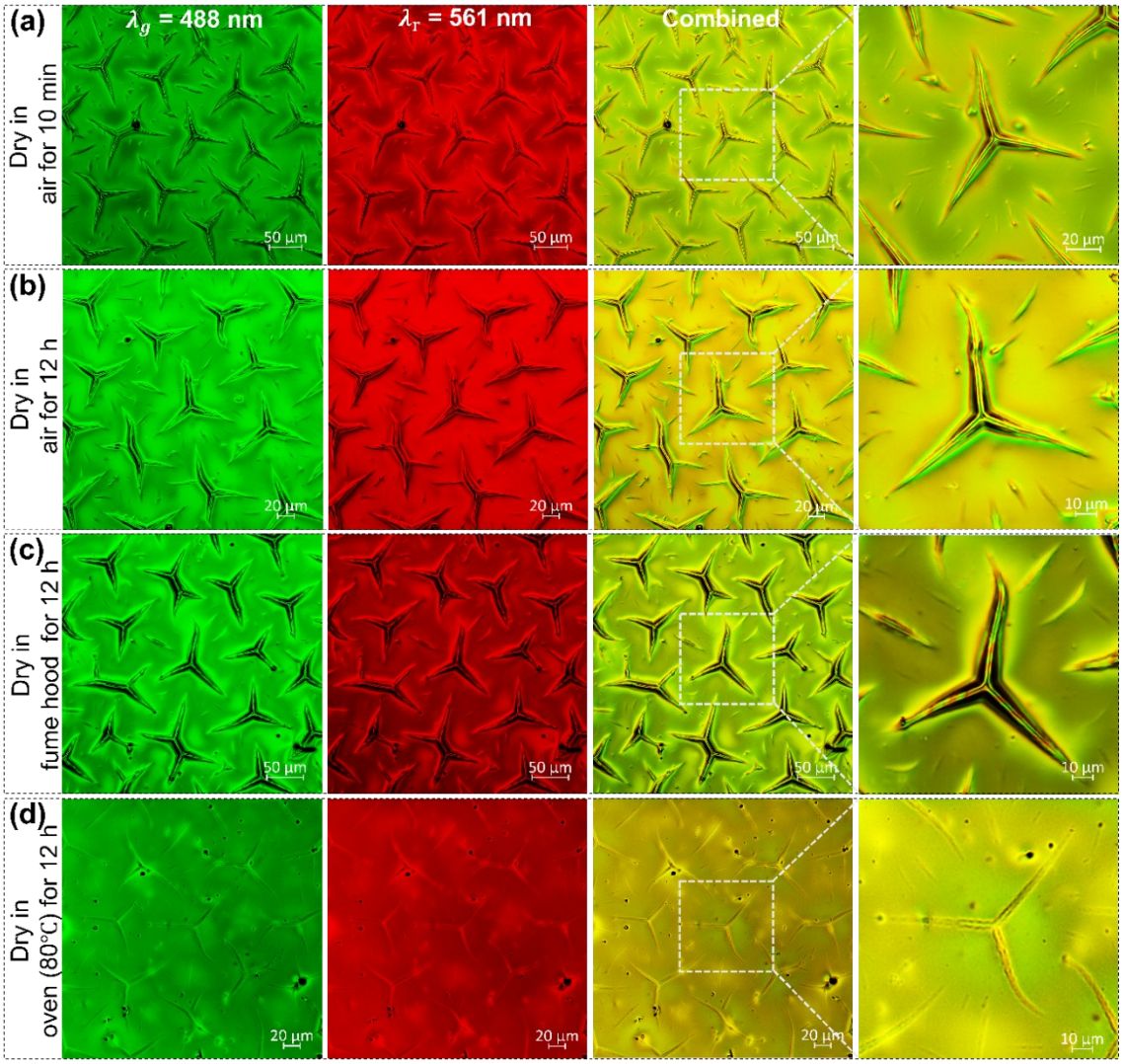


Figure 6-3 Effect of drying conditions on the pattern formation: (a) In air for 10 min, (b) In air for 12 hrs, (c) In a fume hood for 12 hrs, and (d) In an oven for 12 hrs at 80 °C. The green (first column) and the red channels (second column) reflect imaging using 488 nm and 561 nm wavelengths, respectively. The combined channel image (third column) is the overlay of the green and red channel images. The final column images are zoomed-in versions of the combined channel images, highlighting a single pattern.

Pattern evolution with varying immersion times. To gain deeper insight into the dynamics of pattern formation, the soft substrates were immersed in hexane for varying durations (t_E) of 8 min, 1 hr, 10 hrs, and 96 hrs, followed by air drying to facilitate solvent evaporation. Note that during the first 10 min of evaporation, the majority of the hexane absorbed by the substrate is evaporated, and the weight of the soft substrate reaches a stable state. Subsequently, representative surface morphologies of the soft PDMS substrates with varying immersion times were characterized by DW-RICM (Figures 6-4(a)-(d)) for varying drying times (t_0) of 10 min and 90 min, respectively.

At short solvent extraction time (t_E = 8 min), the DW-RICM images (Figure 6-4(a)) reveal the presence of isolated, circular surface features sparsely distributed across the substrate. These circular domains, with radii ranging from 10 - 50 μm, exhibit weak optical contrast and gradual transitions at the circular edges without defined interference fringes under both wavelengths of 488 nm and 561 nm, indicative of shallow_out-of-plane deformations on the order of hundreds of nanometers or less [78,235]. Further, the signature appears to be sensitive to the imaging wavelength, i.e., bright fringes for green and dark fringes for red. Within the circle of some larger circular domains, the three arms can be faintly observed with an average length of 36.61 ± 8.86 μm (Figures 6-4(e) and D6-7(a), Appendix D). This morphology indicates that minimal swelling, likely induced by spatially heterogeneous solvent uptake, leads to slight expansion in regions of higher hexane absorption relative to their surroundings during solvent evaporation. Upon drying, this internal swelling mismatch generates weak in-plane compressive stresses, which are relieved through subtle surface deformation. Such local swelling instabilities have been reported in other soft polymer systems where non-uniform solvent exposure gives rise to stress-driven morphological transitions even in the absence of large bulk deformation [289,290]. And the observed weak triangular (Y-shaped) pattern may be associated with localized solvent swelling and volatilization, resulting in radially inward relaxation of compressive stresses [291,292]. Consistent with this interpretation, optical microscopy images (Figure 6-4(e)) shows largely featureless surfaces, with only faint circular

features visible across the substrate. The weak optical contrast and lack of structural organization confirm that minimal shrinkage-induced reorganization has occurred at this stage. Further, the sample weight decreased by approximately 45.35% after 8 minutes of hexane immersion and evaporation, primarily due to the removal of unreacted PDMS base (Figure 6-4(f)).

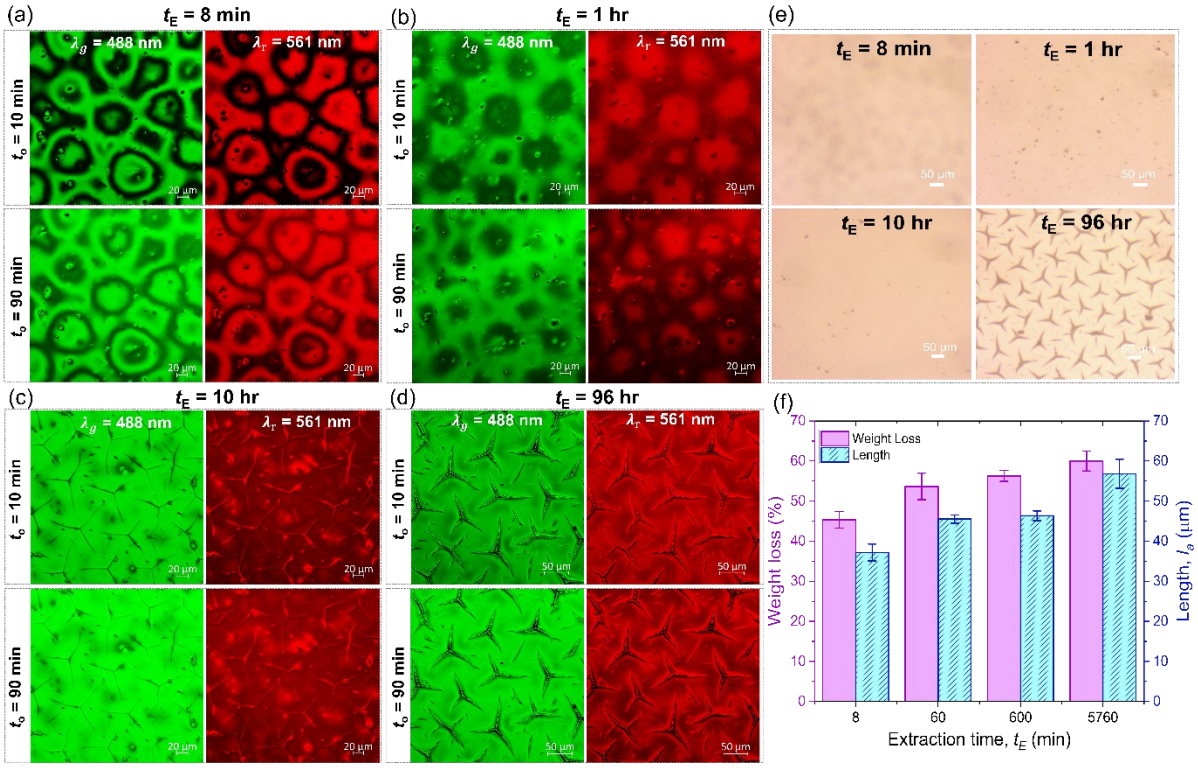


Figure 6-4 Effect of hexane extraction time (t_E) on the pattern formation on P_{60} substrates of 35 μm thickness: (a) t_E = 8 min, (b) t_E = 1 hr, (c) t_E = 10 hrs and (d) t_E = 96 hrs. Observations at two different drying times, t_O = 10 min and t_O = 90 min, are shown. The green and the red channels reflect imaging using 488 nm and 561 nm wavelengths, respectively. (e) Corresponding optical microscopy images of the patterns. (f) Variation of post-solvent extraction weight loss and arm length of the pattern l_a with different extraction times. Error bars for weight loss and length represent standard deviation from three independent experiments.

Despite this weight loss, the limited morphological evolution observed indicates that the compressive stress or equivalently the strain has not reached the critical value necessary

for the formation of organized surface patterns. Importantly, analysis of the surface morphology across different drying times (10 min and 90 min) shows no significant evolution of these circular patterns. The faint circular features remain largely unchanged even after prolonged drying, indicating that the surface morphology stabilizes rapidly once solvent removal begins.

Following a longer extraction time of t_E = 1 hr, the surface morphology exhibits diffuse, patchy circular domains distributed across the substrate (Figure 6-4(b)). Within these domains, elongated and discernible three-armed structures with an average arm length of 45.12 ± 12.15 μm (Figures 6-4(e) and D6-7(b), Appendix D) emerge at the centers, displaying partial spatial periodicity under DW-RICM imaging. Complementary optical microscopy imaging (Figure 6-4(e)) reveals no discernible triradial features, suggesting that the surface deformations are shallow and below the resolution limit of conventional optical techniques. Even after extended drying (up to 90 mins), the pattern morphology shows no significant evolution. Similarly, due to the removal of unreacted PDMS base, the sample weight decreased up to 53.67% after 1 hr of hexane extraction (Figure 6-4(f)). The increase in pattern length and weight loss with higher extraction duration indicates greater removal of unreacted PDMS base and deeper solvent penetration into the network, resulting in enhanced swelling. Upon drying, this generates larger internal compressive stress differentials, yet still insufficient to initiate ordered mechanical instabilities. The substrate thus remains in a transitional regime driven by anisotropic swelling and solvent evaporation, without progressing to fully periodic surface instabilities.

Upon further increase of the extraction time, i.e., t_E = 10 hr, the surface morphology undergoes a significant transformation (Figure 6-4(c)). DW-RICM images reveal the formation of more continuous and interconnected surface features across the substrate. Within these domains, triradial patterns become more distinctly defined, with an average arm length of 45.20 ± 8.37 μm (Figures 6-4(c) and (f)). The arms extend radially from a central vertex and

show increased spatial regularity compared to the structures observed at t_E = 1 hr. The clearer periodicity and enhanced feature size suggest that sufficient solvent induced swelling has occurred to induce the critical modulus gradients [23] and compressive stresses required for distinct, ordered pattern formation. Nevertheless, complementary optical microscopy imaging (Figure 6-4(e)) shows that while faint outlines of larger features can be distinguished, full structural resolution remains limited at the optical scale, indicating that the surface topography is becoming more pronounced but still largely requires high-sensitivity wavelength-dependent imaging techniques to resolve finer details. The observed weight loss of approximately 56.31% after 10 hrs of hexane extraction reflects extensive removal of unreacted PDMS base and partial network reorganization.

Notably, only after a prolonged extraction time of t_E = 96 hrs, DW-RICM imaging reveals a clear quasi-periodic array of triradial microstructures uniformly distributed across the substrate (Figure 6-4(d). As mentioned previously, each microstructure consists of three arms spaced approximately 120° apart, with an average arm length of 53.82 ± 9.66 μm, indicating high geometric regularity (Figures 6-4(d)-(f)). This suggests that the mechanical instabilities, seeded during swelling and driven by stress accumulation and modulus gradients upon solvent evaporation, have fully developed and stabilized into an energetically favorable surface configuration. Complementary optical microscopy imaging (Figure 6-4(e)) resolves the surface pattern, confirming that the deformations are sufficiently large to be distinguished without high-resolution techniques. Notably, no significant morphological changes are observed after drying times of 10 and 90 minutes, indicating rapid stabilization of the surface features following solvent evaporation. A weight loss of approximately 60.02% reflects the near-complete removal of unreacted PDMS base and substantial network densification (Figure 6-4(f)). Thus, it is likely that large compressive stresses accumulated during drying exceeded the critical threshold for long-range mechanical ordering, resulting in highly periodic and mechanically stable surface patterns.

6.3.2 Formation and characterization of solvent-induced patterns on silicone gel thin films

To further validate the universality of the observed pattern formation, glass substrates coated with a commercially available silicone gel with a thickness of 26.88 ± 1.05 μm were also used. The Young's modulus (E) of the silicone gel is 5.6 kPa [51] and the amount of uncross-linked free liquid chains here is around 64 % [44] i.e., higher than that of P_{60} (60%). In a manner consistent with previous experiments, the confined gel substrates were immersed in hexane, followed by drying in air to allow solvent evaporation. Figure 6-5(a) shows the representative RICM snapshots for a silicone gel substrate immersed in hexane for 96 hrs, followed by 10 mins of air drying. Similar to PDMS substrates, triradial (three-armed) ridge-like patterns were observed with a uniform distribution throughout the substrate. However, the arms are significantly broader here, yielding a flower-petal-like morphology. Image analysis reveals a consistent arm length of 38.6 ± 5.31 μm (measured at the arm axis) and an average center-to-center distance (pitch) of 65.79 ± 7.62 μm between neighbouring patterns. Thus, compared to PDMS, both the average arm length and the pitch of the patterns are lower here. However, the patterns observed here are significantly broader, with a maximum width of approximately 20 μm at the peak. The black regions observed in our interference signature may reflect trapped liquid phase or high interface slopes. Interference fringes only along the central axis of the arm, i.e., top of the ridge are distinctly visible (Figure 6-5(a), last column). Interference intensity and corresponding height extraction along the ridge reveal the maximum ridge height to be around 3 μm, i.e., significantly higher than that observed for patterns on PDMS. Comparison with the characteristic elastocapillary length-scale of the gel, i.e., $l_{EC} = \gamma/E \approx 4$ μm, yields satisfactory agreement with the magnitude of the peak ridge height. Furthermore, compared to the sharp peak profiles on PDMS, the ridge profile close to the peak here suffers a shape inversion. In other words, close to the peak, the pattern appears to have folded upon itself, forming a localized crease. Independently performed AFM scans confirm this crease formation (Figure D6-8, Appendix D). Consequently, it is difficult to define a ridge opening angle.

Additionally, interference fringes in the space between adjacent patterns indicate some height variations on the free surface of the gel. It is likely that the final pattern forms on a wrinkled surface induced by initial swelling. Finally, SEM measurements (Figure D6-9, Appendix D) exhibit a reduction in film thickness from 26.88 ± 1.05 μm to 3.6 ± 0.21 μm after extraction, providing evidence of coating shrinkage due to the removal of unreacted PDMS base. Silimarly, longer time observation reveals that the pattern is highly stable and irreversible: a random incision on the surface does not affect the neighbouring patterns (Figure D6-10, Appendix D), i.e., there are no residual compressive stresses and trapped liquid phases. Thus, surface tension and elasticity predominantly dictate equilibrium pattern profiles.

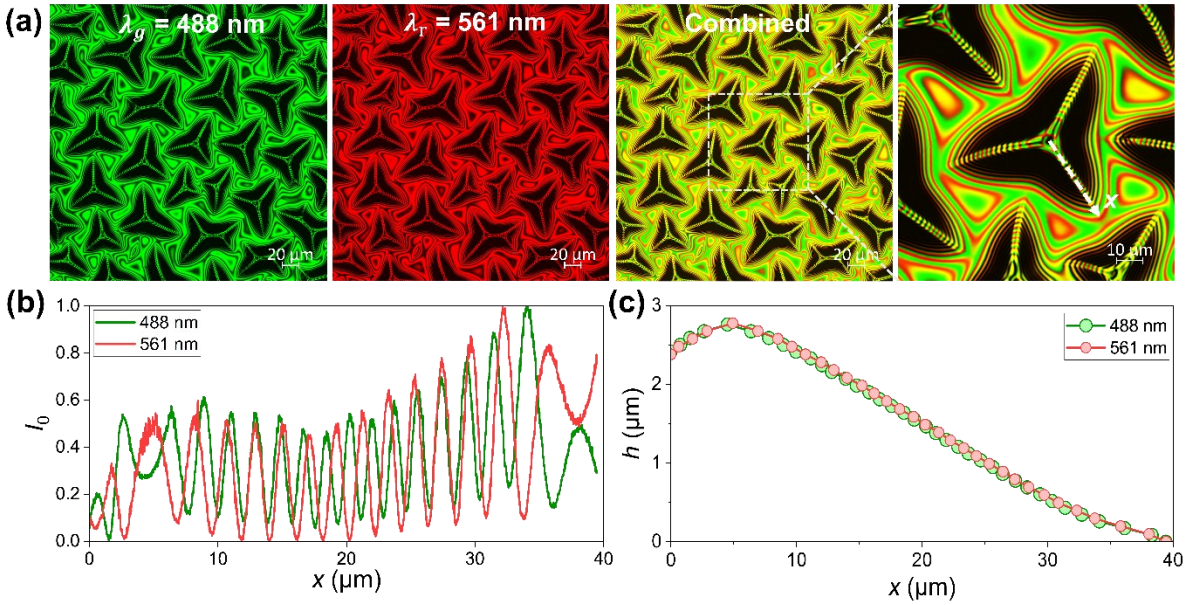


Figure 6-5 (a) Pattern formation on silicone gel substrates after 96 hrs of hexane immersion followed by drying in air. The green (first column) and the red channels (second column) reflect imaging using 488 nm and 561 nm wavelengths, respectively. The combined channel image (third column) is the overlay of the green and red channel images. The final column images are zoomed-in versions of the combined channel images, highlighting a single pattern. (b) Variation of normalized intensity I_0 corresponding to the green and red wavelengths along the white dashed line shown in the last image of (A). (c) Height profile (h) extracted from the intensity distribution of (B). The green and the red symbols represent height extracted from 488 nm and 561 nm wavelengths, respectively (see methods).

In a manner consistent with patterns on PDMS, here also, we observed that the instabilities are sensitive to solvent immersion times (Figure 6-6 and Figures D6-11 and 12, Appendix D). For low extraction times (t_E = 8 min), the DW-RICM images of the silicone gel substrate (Figure 6-6(a)) reveal the presence of isolated, circular surface features sparsely distributed across the substrate, consistent with the topology observed in the PDMS system (Figure 6-6(a)). However, the circular domains in the gel substrate are generally smaller in size, with radii ranging approximately from 5 to 40 μm. Notably, the internal triradial motifs, which could be faintly observed in PDMS (Figure 6-6(a)), are extremely distinct in the gel system (Figure 6-6(a) and Figures D6-11 and 12, Appendix D). These structures exhibit well-defined radial symmetry with visible arms extending from a central point, often separated by approximately 120°, even at this early extraction stage. The average arm length is measured to be 38.19 ± 5.15 μm. Despite the clear visibility of these patterns under DW-RICM, they remain undetectable under conventional optical microscopy, indicating that the surface deformations, while morphologically defined, are still relatively shallow in height. This suggests that although mechanical instability has been initiated, the overall amplitude of deformation remains below the resolution threshold of standard optical imaging techniques. A weight loss of approximately 50.95% at this stage indicates substantial solvent uptake and extraction. The early manifestation of well-defined triradial patterns may be attributed to the lower crosslinking density or higher solvent absorption capacity of the gel matrix, which facilitates earlier development of modulus gradients and the associated compressive stresses that drive surface buckling. These observations underscore a potentially greater sensitivity of the gel network to solvent-induced stress gradients and suggest that the mechanical instability threshold may be reached more rapidly in this system, even at shorter extraction durations.

At a longer extraction duration of t_E = 1 hr, the surface morphology of the silicone gel substrate exhibits a notable evolution: a significant increase in the number and size of patterned features, with triradial patterns now dominating the surface (Figure 6-6(b) and Figures D6-11 and 12, Appendix D). These structures display well-defined three-armed

geometries with enhanced contrast and spatial regularity. Each arm radiates symmetrically from a central vertex, forming angles of approximately 120°, consistent with isotropic compressive stress release. The average arm length is measured to be 53.66 ± 9.38 μm. Importantly, the triradial patterns are now clearly visible under conventional optical microscopy (Figure 6-6(e)), indicating that the surface deformations have increased sufficiently. The improved pattern visibility at both low and high magnification suggests that not only the lateral dimensions but also the vertical height variations of the features have significantly increased. A weight loss of approximately 62.13 % at this stage reflects extensive extraction of unreacted PDMS base and a higher degree of network densification compared to the 8-minute swelling duration. This substantial solvent removal likely contributes to a sharper modulus gradient between the drying surface and the still-soft interior, thereby amplifying compressive stresses and facilitating the robust formation of surface patterns. Overall, these results indicate that the silicone gel matrix, due to its high solvent uptake capacity and compliant network structure, rapidly accumulates sufficient stress to initiate and sustain organized surface instabilities. The appearance of well-developed, optically visible triradial patterns at this early time point underscores the high responsiveness of the gel system to solvent-induced mechanical instabilities.

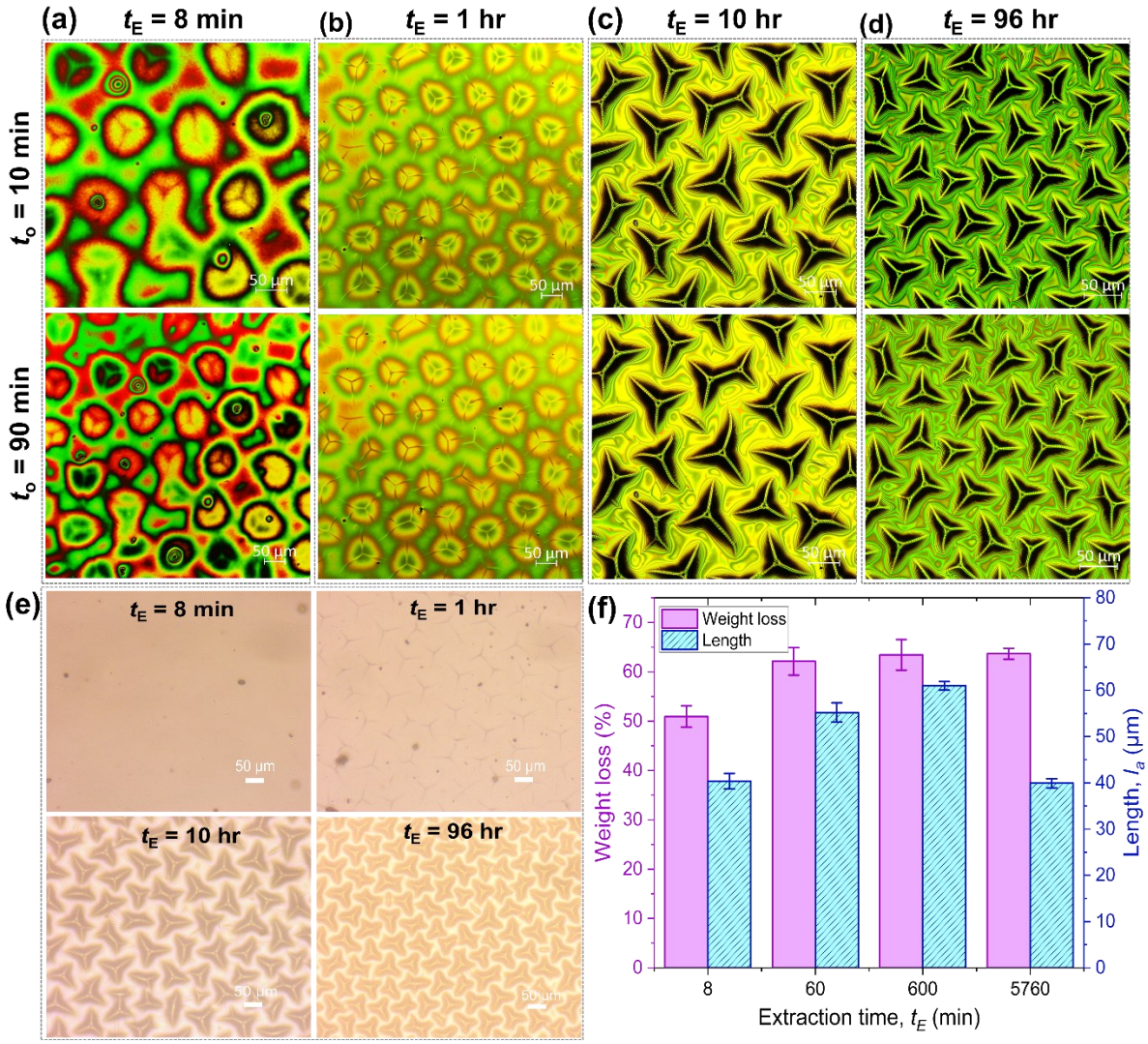


Figure 6-6 Effect of hexane extraction time (t_E) on the pattern formation on silicone gel substrates of 35 µm thickness: (a) t_E = 8 min, (b) t_E = 1 hr, (c) t_E = 10 hrs, and (d) t_E = 96 hrs. Observations at two different drying times, t_O = 10 min and t_O = 96 min, are shown. The overlay of the green and the red channels images are shown here. Individual channel images are shown in the Appendix D (Figure D6-11, Appendix D). (e) Corresponding optical microscopy images of the patterns. (f) Variation of post-solvent extraction weight loss and arm length of the pattern l_a with different extraction times. Error bars for weight loss and length represent standard deviation from three independent experiments.

When the extraction time was extended to t_E = 10 hrs, the surface morphology of the silicone gel substrate underwent a pronounced transformation, presenting a well-developed and highly ordered triradial structure (Figure 6-6(c)). Compared to earlier stages, the patterns exhibited improved clarity, uniformity, and spatial regularity. The average arm length increased to 59.78 ± 12.04 μm, significantly longer than that observed at shorter extraction times, indicating continued growth and relaxation of the surface features. Importantly, the triradial structures became clearly visible under conventional optical microscopy (Figure 6-6(e)), with individual arms and central vertices sharply resolved without the need for high-sensitivity imaging techniques. This enhanced visibility suggests that both the lateral dimensions and vertical amplitudes of the surface deformations increased substantially, reflecting a more advanced stage of mechanical buckling. A mass loss of approximately 63.44 % after 10 hrs of extraction, suggesting near-complete removal of extractable unreacted PDMS base. This extensive solvent extraction likely generates a pronounced surface-to-bulk modulus gradient, wherein a stiffened surface layer overlays a softer interior. The resulting strong compressive stresses are sufficient not only to induce buckling but also to drive the formation of highly regular and energetically favorable surface microstructures. Collectively, these observations demonstrate that silicone gel matrices can rapidly evolve into highly ordered arrays of triradial patterns upon prolonged solvent extraction. The marked improvement in structural clarity and uniformity underscores the critical role of extraction time and solvent-induced mechanical gradients in directing the pattern formation process.

After an extended extraction time of t_E = 96 hrs, the surface morphology of the silicone gel substrate (Figure 6-6(d)) remains largely consistent with that observed at t_E = 10 hrs (Figure 6-6(c)), presenting a dense and well-organized array of triradial microstructures with high spatial regularity and uniformity. These features are also distinctly visible under conventional optical microscopy (Figure 6-6(e)), with clear resolution of the individual arms and central vertices. Interestingly, despite the overall morphological similarity, the average arm length of the triradial structures decreases to 38.6 ± 5.31 μm at this stage, compared to 59.78 ± 12.04 μm

after 10 hrs of extraction. The weight loss of approximately 63.67 %, nearly identical to that observed at 10 hrs, suggesting that solvent extraction had effectively reached saturation and that further extraction no longer significantly alters the bulk composition. The observed reduction in arm length, despite the stable mass, likely reflects a densification and structural relaxation process within the surface layer. Prolonged solvent depletion and continued drying can induce additional network rearrangements and compaction, leading to contraction of pre-formed surface features without further material removal [281]. Specifically, secondary relaxation phenomena, such as polymer chain reorganization and residual stress relaxation within the stiffened surface layer, can cause slight retraction of the buckled structures [23,293], thereby reducing the characteristic arm length while preserving the overall pattern morphology and spatial distribution. These findings highlight that while the primary pattern formation is governed by solvent-induced mechanical gradients and compressive instabilities at early to intermediate extraction stages, prolonged solvent extraction and drying introduce secondary network relaxation processes that can subtly reshape the final surface morphology. This behavior is consistent with prior observations of post-buckling evolution in solvent-processed polymeric systems [281].

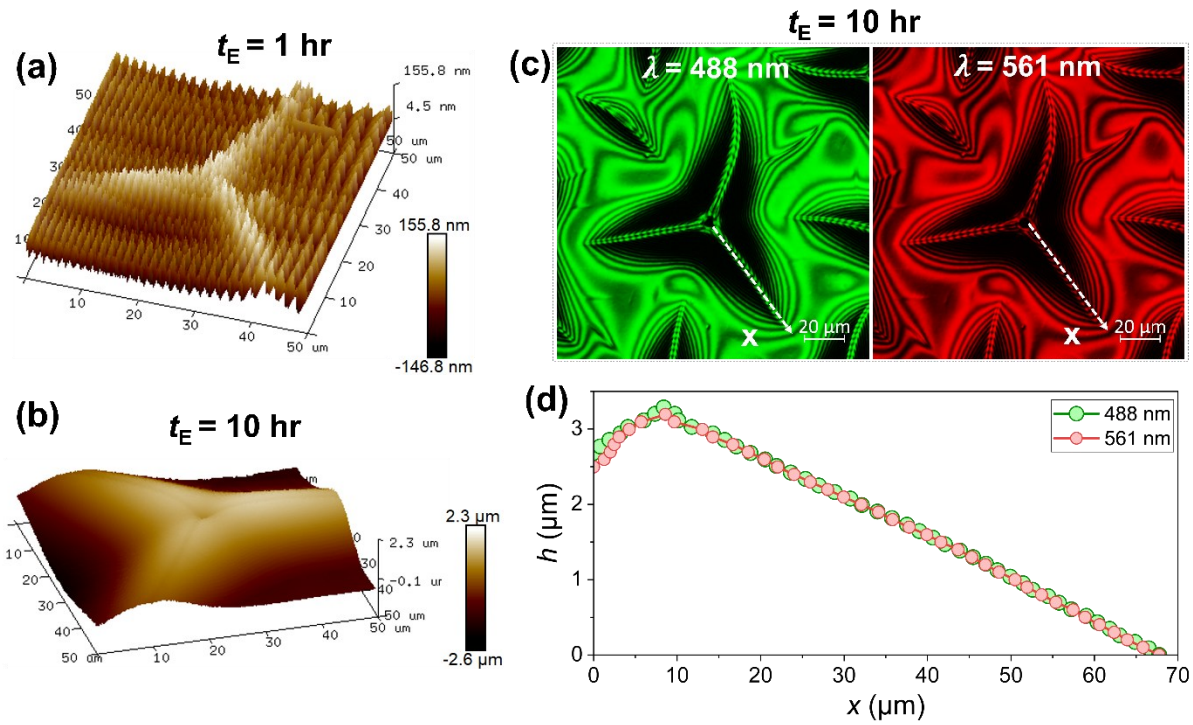


Figure 6-7 Atomic force microscopy scans of the pattern formation on silicon gel substrates for swelling durations of (a) t_E = 1 hr and (b) t_E = 10 hrs. (c) DW-RICM images of a similar pattern formation for swelling duration of 1 hr. The green (first column) and the red channels (second column) reflect imaging using 488 nm and 561 wavelengths, respectively. (d) Height profile (h) extracted from RICM images along the white dashed line in (c). The green and the red symbols represent height extracted from 488 nm and 561 nm wavelengths, respectively (see methods). The patterns in (b) and (c) are not the exact same pattern.

To further quantify the evolution of surface deformation during hexane extraction, the height of the patterns formed in the silicone gel substrates after extraction times of 1 hr and 10 hrs were analyzed by atomic force microscopy (AFM) (Figures 6-7(a) and (b)). AFM scans reveal that for t_E = 1 hr, the pattern morphology reflects a sharp ridge-like profile where the peak height reaches 0.16 µm (Figure 6-7(a)**)**. This formation is similar to that observed for PDMS substrates (Figure 6-1(d)**)**. The similarity can be interpreted from a comparing the fraction of uncrosslinked free liquid chains between PDMS and silicone gel: a minimally swollen gel surface extracts amount of free liquid similar to moderately or fully swollen PDMS.

However, the AFM scan reveals that the free surface of the gel is wrinkled, which was not observed for PDMS. As the extraction time increases to 10 hrs, the pattern, however, experiences a morphological change: close to the center, a sharp crease appears. This feature is independently confirmed using DW-RICM imaging and height extraction (Figures 6-7(c) and (d)**)**. The maximum height occurs at a slight offset whose magnitude varies between 2-3 μm. Further, these measurements confirm a substantial increase in vertical deformation with gel swelling time, consistent with enhanced internal stress generation and modulus gradient development due to enhanced network swelling [23]. The trend remains consistent for substrates swollen for 96 hrs, as previously shown (Figure 6-5). It is noteworthy to mention that the appearance of the dark regions on the patterns (Figures 6-5(a), 6-6(a) and 6-7(c)) and the localized crease formation for gel substrates swollen for 10 hrs or longer (Figures 6-5(c) and 6-7(d)) reiterates our previous hypothesis that some fraction of either the solvent or the free-liquid chains may have gotten trapped within the evolving pattern peak during swelling. Existing literature has shown that during the drying stage of surface folds, flow reversal can cause formation of creases close to the fold tip, i.e., the ridge peak [294]. Thus, the appearance of the dark regions may very well correspond to the trapped hexane phase ($n = 1.37$) or the trapped free liquid phase ($n \approx 1.4$), both of whose refractive indices are close to that of silicon gel ($n \approx 1.4$), resulting in no interference fringe formation. This feature becomes more evident when different drying conditions are used (Figure 6-8).

Even though the overall morphology of the patterns remain insensitive to drying conditions with a marginally smaller pattern dimesion (arm lengths) for drying in oven, we observe that for drying in oven the black regions are not observed (Figure 6-8(c)) indicating complete removal of hexane or the free liquid phase. Further, height extraction along pattern arm reveals that the ridge profile does not exhibit the crease formation close to the ridge peak (Figure D6-13, Appendix D). Note that independently performed Raman spectroscopy measurements, before and after solvent extraction, reveal no new peaks, and thus may not be able to resolve the trapped phase, possibly due to evaporation under the laser intensity (Figure

D6-14, Appendix D). Taken together, these results confirm that the formation of triradial patterns in the silicone gel arises from physical reorganization and stress-driven deformation, albeit with a possible presence of a trapped free-liquid phase.

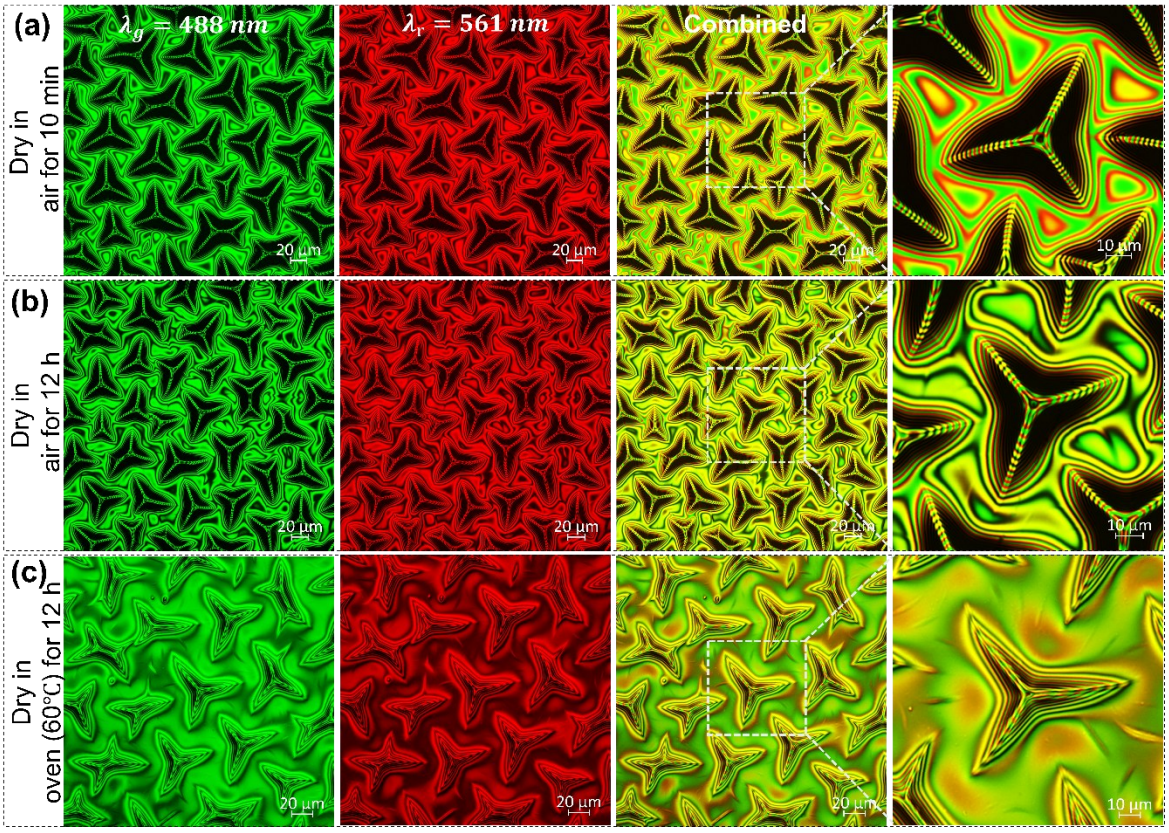


Figure 6-8 Effect of drying conditions on the pattern formation: (a) In air for 10 min, (b) In air for 12 hrs, (c) In an oven for 12 hrs at 60 °C. The green (first column) and the red channels (second column) reflect imaging using 488 nm and 561 nm wavelengths, respectively. The combined channel image (third column) is the overlay of the green and red channel images. The final column images are zoomed-in versions of the combined channel images, highlighting a single pattern.

To further validate the generality of the observed post-extraction morphological evolution, particularly the reduction in triradial arm length likely caused by secondary relaxation and network compaction, two additional silicone-based elastomer systems, P_{64} (PDMS base and crosslinker ratio = 64:1, see methods and $E \approx 4$ kPa [295]) and P_{80} (PDMS base

and crosslinker ratio = 80:1, see methods and $E \approx 1$ kPa [295]), were prepared and analyzed (Figure 6-9). The formulation P_{64} was selected to match the free liquid content of the silicone gel (approximately 64 wt%, as the weight loss of silicone gel extracted in hexane for 10 hrs and 96 hrs), thereby serving as a compositional analogue. In contrast, P_{80}, with a higher fraction of uncross-linked fluid and lower network stiffness, was employed to assess the response of even softer elastomer networks. By comparing the pattern evolution in these materials, we aim to elucidate whether similar secondary relaxation-induced morphological retraction occurs across elastomer systems of varying mechanical compliance and free-liquid content. From our RICM signature, we observe that the morphology is like the silicone gel substrate with a broad flower petal-like configuration with significant dark regions indicating trapped free liquid phase (Figure 6-9(a) and 9(b)). Further, the ridge profiles also exhibit the crease formation close to the ridge tip (Figure 6-9(c) and 9(d)) with an average vertical height at par with that observed in silicone gel substrates. However, quantitative analysis reveals that the average arm length of patterns is 57.62 ± 5.79 μm and 59.43 ± 9.02 μm for P_{64} and P_{80}, respectively. Both these values are significantly higher that that observed for patterns on the silicone gel substrate and more at par with that observed for P_{60} (Figure 6-4(f) and Figure D6-15(a), Appendix D). The histograms and corresponding fitted distributions of the arm length l_a (Figure D6-15(b), Appendix D) show a systematic shift with increasing free liquid content. For substrates with lower free liquid (e.g., P_{60}), the distribution is centered at shorter lengths (∼50 μm) with a relatively narrow spread. With increasing free liquid fraction (P_{64} and P_{80}), the distributions progressively broaden and shift toward larger values, with mean lengths exceeding 60 μm and a noticeably wider variance. This trend indicates that the presence of free liquid promotes the formation of longer and more heterogeneous arms. Consequently, even though the pattern size increases as the elasticity of the PDMS decreases and free liquid content increases, the correlation across elastomer (PDMS) and silicone gel substrate is not straightforward. Furthermore, similar to previous surfaces, here also, the patterns are fully developed and exhibit no transient states beyond the extraction time of 10 hrs (Figure D6-16, Appendix D).

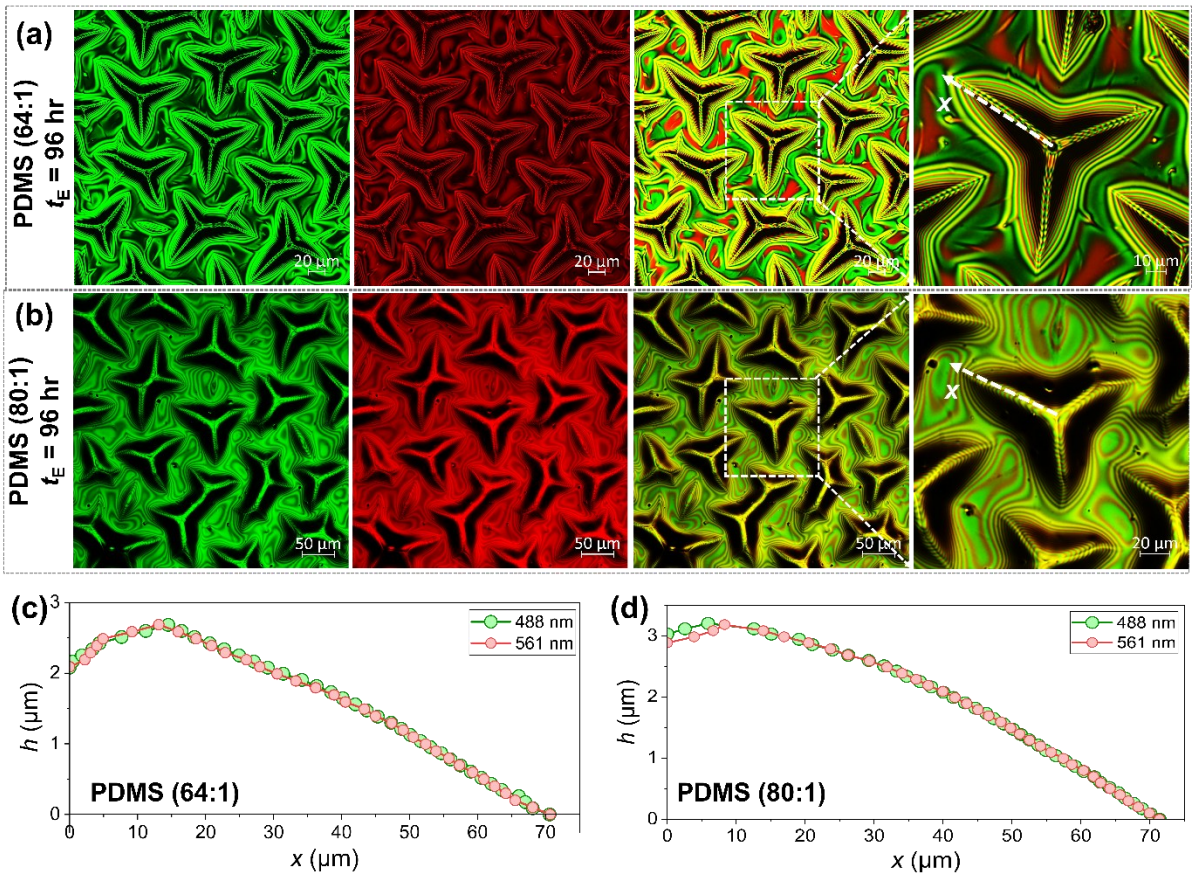


Figure 6-9 Pattern formation for PDMS substrates with different base-crosslinker ratios: (a) PDMS 64:1 and (b) PDMS 80:1. The green (first column) and the red channels (second column) reflect imaging using 488 nm and 561 nm wavelengths, respectively. The combined channel image (third column) is the overlay of the green and red channel images. The final image in each row is the zoomed-in image of a pattern. Compared to PDMS 60:1, these surfaces have a higher fraction of free liquid chains and lower elasticity. (c) and (d) Height profiles (h) extracted from RICM images along the white dashed lines in (a) and (b). The green and the red symbols represent height extracted from 488 nm and 561 nm wavelengths, respectively (see methods).

6.3.3 Mechanism of solvent-induced soft thin film surface patterning

Time-resolved observations of surface morphology evolution in confined soft substrates (P_{60} and silicone gel) during n-hexane extraction and drying reveal a multistage pattern formation process governed by the massive removal of unreacted free liquid polymer

chains, solvent uptake, internal stress buildup, ordered lattice structure arrangement, mechanical instability, and final stabilization. The process occurs in five distinct stages:

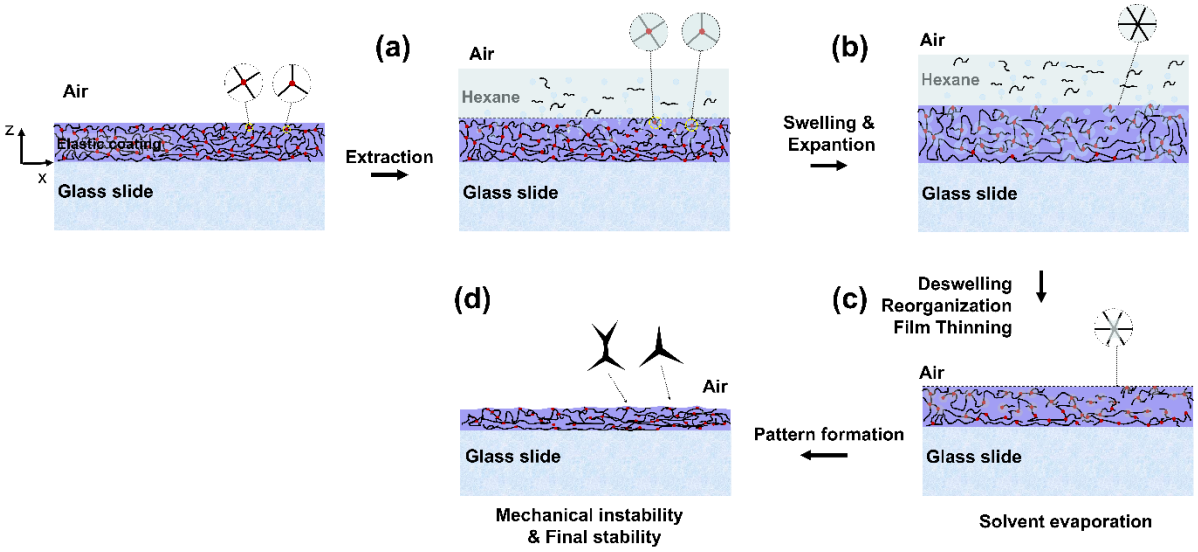


Figure 6-10 Schematic of the solvent-induced surface pattern formation mechanism in confined soft elastomer films, highlighting the five distinct stages: (a) Pre-extraction and early solvent extraction (see step 1 in the main text), (b) Progressive swelling (see step 2 in the main text), (c) Solvent evaporation (see step 3 in the main text), (d) Mechanical instability, and pattern formation and stabilization (see steps 4 and 5 in the main text).

1. **Initial Extraction. Selective removal of free liquid chains:** At early stages of solvent extraction, hexane preferentially removes unreacted, free liquid polymer chains from the soft polymer network. This results in a reduction of the spatial density within the network, effectively loosening the polymer mesh and allowing solvent molecules to more easily diffuse into the crosslinked matrix (Figure 6-10(a)). The ensuing modest swelling leads to minor, localized perturbations in the film, but remains insufficient to generate the compressive stress required for the onset of surface instability.
2. **Progressive Swelling. Solvent Penetration, Network Expansion, and Ordered Lattice Structure Arrangement:** As the extraction time increases, a greater proportion of free, unreacted chains are removed, allowing more hexane molecules to infiltrate the crosslinked three-dimensional (3D) polymer network. This process results

in pronounced swelling, accompanied by internal polymer reorganization (Figure 6-10(b)). Further, during this process, prominent surface-to-bulk gradients in both elastic modulus and internal stress begin to emerge. Specifically, the top surface layer, being less constrained and more accessible to solvent, undergoes greater expansion compared to the underlying bulk. This differential swelling continues until the compressive stress accumulated in the surface layer is counterbalanced by the surface elasticity. As the swelling progresses, the polymer network on the free surface tends to self-organize into locally ordered lattice-like arrangements, likely due to cooperative molecular realignment under solvent-mediated plasticization [296,297].

3. **Solvent Evaporation. Asymmetric Deswelling, Reorganization and Film Thinning:** Upon removing the sample from the solvent bath, rapid evaporation of hexane from the free surface initiates contraction of the swollen polymer chains, particularly in the previously expanded surface layer (Figure 6-10(c)). Meanwhile, hexane retained in the deeper regions of the film, especially within the denser, bulk network, evaporates more slowly. This deswelling asymmetry induces molecular rearrangement within the bulk polymer network, promoting polymer chain aggregation in the bulk. As a result, the center of the crosslinker network of the film becomes denser and thicker than the surrounding areas. Once most of the solvent has evaporated, the vertical redistribution of polymer becomes frozen in time, and the film exhibits a thinner profile overall due to the combined effects of free molecules extraction and post-swelling contraction.
4. **Mechanical Instability. Pattern Formation via Buckling:** The surface pattern arises at this point: as the topmost crosslinked layer attempts to contract and match the underlying polymer height, which now features localized polymer densification and height differences, mechanical instabilities are triggered due to the mismatch in shrinkage and elastic constraint. This stress imbalance leads to the formation of surface buckling patterns, particularly the observed triradial (Y-shaped) microstructures (Figure 6-10(d)).

5. **Final Stabilization. Quasi-periodic Pattern Emergence:** At sufficiently long extraction times (e.g., 96 hrs), the cumulative effects of solvent-induced swelling, network densification, and stress accumulation culminate in the emergence of a quasi-periodic array of ordered patterns. Weight loss, thickness reduction, and topographic analysis confirm extensive free molecules loss and polymer reorganization, indicating that these surface features represent an energetically stabilized, mechanically equilibrated configuration.

6.4 Conclusion

Collectively, the results presented here establish a generalized framework for solvent-induced surface patterning in soft elastomer and gel networks. Across multiple material systems with varying crosslink densities and solvent affinities, we observe a reproducible transition from shallow, disordered swelling domains to well-defined triradial microstructures, driven by free liquid chains removal, solvent-induced swelling, internal stress accumulation, and the development of surface-to-bulk modulus gradients. The emergence of a quasi-periodic array of triradial patterns reflects a mechanically favorable mode of stress release, while the subsequent dimensional retraction observed at extended extraction durations highlights the role of post-buckling relaxation and network densification. Importantly, the spatial fidelity, symmetry, and long-term stability of the resulting patterns are strongly modulated by intrinsic material parameters such as free liquid content, elastic compliance, and swelling capacity. These insights enable rational design strategies for encoding surface patterns through controlled solvent processing and material selection.

Beyond fundamental interest, these findings offer practical implications for soft surface engineering in applications ranging from optical interference structures [298] and tunable wetting surfaces [299] to bioinspired topographies [300] and stretchable devices [301]. By coupling simple solvent extraction protocols with tailored elastomer formulations, a broad range of hierarchical, self-organized surface architectures can be generated without the need for lithography or

templating. Unlike conventional lithographic techniques, solvent-induced pattern formation is inherently self-organized, substrate-conformal, and scalable, making it attractive for applications in flexible electronics [302] and smart coatings [303,304]. This work thus bridges fundamental understanding with application-oriented design, paving the way for solvent-responsive materials in next-generation surface engineering. Moreover, the high-resolution and morphologically rich patterns generated here present an opportunity for integration with data-driven approaches such as machine learning. By leveraging image-based pattern recognition or correlating polymers and solvent parameters with pattern geometries, these structures could be used to train predictive models for topography control, enabling inverse design in soft material systems. Beyond scientific insights, our experiments using advanced microscopic techniques can generate beautiful images, which demonstrate the artistry of science and even rival the beauty of nature.

Chapter 7

Conclusions and Future Outlook

7.1 Conclusions of present research

The objective of this dissertation was to investigate the interfacial behaviors of soft polymer thin films and metal-polymer bilayers under contact and solvent stimuli. To address the four interconnected scientific questions identified at the outset, two advanced techniques: confocal Raman spectroscopy and DW-RICM, were employed to explore localized interfacial deformation of polymer thin films under external loading, optical and mechanical properties of metal-polymer bilayers, dynamic contact behavior of softer metal-polymer bilayers, and solvent-induced surface instabilities and pattern formation in polymer thin films. These studies have demonstrated correlations between microscopic structures and macroscopic mechanical behaviors, contributing to the scientific understanding of functional soft interfaces and providing effective experimental methodologies for their characterization and practical applications. The conclusions and some scientific and practical insights acquired from each chapter are listed below.

In chapter 3, confocal Raman spectroscopy was used to establish an in-situ imaging technique capable of visualizing soft contact deformation. This technique involves Raman mapping measurements along the x, y, and z axis around the contact interface of a silicone elastomer on a glass substrate. Consequently, the present technique provides chemical signatures across different confocal planes around the region of interest. The mapping identified the relative intensity of the Raman peak at 2905 cm^{-1} to be the most definitive signature enabling detection of the spatial variation of the silicone contacting interfaces. Using this signature, we developed a framework of generating Raman contour maps that embed crucial information, such as the position of the contact interface, contact radius, and indentation depth, without extensive reliance on predefined material parameters. It reveals that, for stiffer

PDMS (P_{10}), Hertz theory remains valid even a/H = 3.6. This novel Raman-based framework provided unprecedented insights by linking chemical signatures with measurable physical parameters, thus establishing a robust analytical approach for characterizing soft contact. It raises promising prospects of future work following the onset of inside molecular distributions within deformation region of soft contact and would provide guidance for the characterization of such elastomer across a wide array and would benefit emerging technologies.

In chapter 4, DW-RICM was used as an efficient method for simultaneously measuring the effective refractive index and elastic modulus of metal-polymer bilayers. By employing interference signatures at wavelengths of 488 nm and 561 nm from a spherical glass probe of known geometry, the refractive indices and elastic moduli of nanoscale Ag and Au coatings deposited on PDMS substrates with varying stiffness and thickness were quantitatively determined. Results demonstrated a notable decrease in the effective refractive index with increased metal deposition time, showing excellent agreement with independent UV-Vis spectroscopy measurements. Furthermore, elastic moduli derived using Hertz contact theory exhibited a clear increase with increasing metal deposition time. This robust yet straightforward methodology addresses limitations of traditional techniques that require multiple complex experimental procedures, thereby providing valuable experimental and theoretical foundations for the precise design and characterization of metal-polymer bilayer materials with tailored optical and mechanical properties.

In chapter 5, DW-RICM was innovatively advanced by employing black ink coated probes to effectively eliminate optical interference inherent to transparent glass probes. This enabled precise characterization of the dynamic behavior of contact ridges. Through detailed analysis of PDMS substrates with varying Au deposition times, it was found that increasing metal deposition time enhanced substrate stiffness, consequently decreasing both the contact radius and ridge height. Additionally, it revealed that the metal-polymer bilayers exhibited a continuous increase in ridge height over time, which is different with bare PDMS. Raman spectroscopy confirmed this phenomenon arises from the long-term diffusion of metal into the

soft substrate, decreasing interfacial stiffness or enhancing adhesion. This newly developed methodology overcomes measurements challenges, providing essential experimental tools and theoretical insights for better understanding interfacial behaviors in flexible electronics, intelligent sensors, and wearable devices based on metal-polymer composite thin films.

In chapter 6, DW-RICM was utilized to reveal the mechanism behind solvent-induced patterns formation on soft polymer films. Systematic variation of solvent extraction time and drying conditions clearly showed morphological evolution from shallow circular domains into stable, well-defined triradial structures. Studies of silicone elastomer and gel with varying stiffness and crosslink densities indicated that lower crosslinking densities and higher free-liquid contents enhance the pattern size and accelerate their formation. Raman spectroscopy further confirmed that these patterns arise not from chemical changes. These insights not only elucidate a general mechanism for solvent-driven self-organized surface pattern formation on soft polymer thin films, but also provide a scalable, lithography-free approach to creating tailored microstructures relevant to flexible electronics, smart coatings, and bio-inspired surfaces.

In summary, this dissertation integrates spectroscopic and optical methodologies to systematically address aforementioned questions in soft interfaces. The analytical frameworks and key findings presented herein advance the fundamental understanding and provide robust experimental tools essential for the rational design, precise characterization, and practical application of advanced soft-material interfaces.

7.2 Suggestions for future research

The spectroscopic and optical methods developed in this dissertation have significantly advanced our understanding of soft interface mechanics. However, further refinements are necessary to broaden their applicability and enhance analytical precision. Based on the methodological limitations identified, this section proposes several directions for future

research, aimed at both deepening fundamental insights and enabling practical applications of the interfaces of soft materials.

Firstly, future work could extend confocal Raman spectroscopy methodologies to non-Hertz (conformal) contact configurations. While the current study primarily focused on relatively stiff PDMS substrates (~1.6 MPa), softer materials, such as lightly crosslinked PDMS [103], silicone gels [19], or hydrogels [104], often exhibit more complex deformation features, including pronounced contact ridges, liquid menisci, or phase separation phenomena [51,58]. Such features complicate Raman spectral analysis, necessitating the adaptation of existing data processing frameworks. Besides, integrating Raman spectroscopy with DW-RICM may provide complementary chemical and topographical data, significantly enhancing the capability to interpret complex interfacial phenomena.

Regarding DW-RICM, in Chapter 4, it was successfully applied to determine the refractive index of polymer thin films and metal-polymer bilayers. The glass slide / PDMS (or Ag-/Au-coated PDMS) / glass sphere system were analyzed under the simplifying assumption of three parallel stratified layers with normal incidence. While this approximation is valid within the analyzed region, deviations emerge at larger radial distances where curvature effects become significant. Future studies should investigate the transition between the parallel-layer and curvature-dominated regimes in a more systematic manner. In particular, additional optical factors such as the numerical aperture of the objective, the pinhole size in confocal detection, and the angular distribution of incident light should be considered. These parameters are expected to influence the effective optical path length and the sensitivity of the interference signal to curvature, thereby determining the range of validity of the current approach. Incorporating such considerations through experimental calibration or optical modeling would provide a more comprehensive framework for extending RICM analysis to broader geometries and material systems. Besides, although its efficacy in probing soft contacts has been demonstrated, future efforts should focus on engineering probe coatings with tailored spectral absorption or reflectance characteristics to substantially enhance the accuracy of height

measurements and interfacial morphology characterization. Current techniques suppress unwanted reflections using black-ink coatings; however, achieving an optimal balance between optical absorption and surface smoothness remains challenging. In addition, integrating DW-RICM with advanced data-driven methods presents exciting opportunities. As demonstrated in Chapter 6, DW-RICM effectively captured solvent-induced surface instabilities, revealing detailed morphological features. Future research could leverage image processing techniques and machine learning algorithms to systematically extract morphological descriptors, correlate them to underlying material and solvent parameters, and develop predictive models. This approach could facilitate inverse design strategies, enabling precise control of interfacial architecture and functionality in soft materials.

Furthermore, the solvent-induced pattern formation described in Chapter 6 deserves deeper theoretical and computational investigation. Numerical modeling methods, such as finite-element simulations, would clarify key mechanisms underlying these observed morphological changes, particularly internal stress accumulation, solvent transport dynamics, and modulus heterogeneity. Additionally, systematic studies on factors including polymer properties, solvent polarity, film thickness, and crosslink density will enhance reproducibility and enable better control over pattern formation. Moreover, incorporating optically active materials (e.g., nanoparticles or two-dimensional materials) into PDMS could further tailor the optical properties of these surface patterns, thus broadening their potential function.

References

1. Polymer-Based Flexible Materials. (2024). MDPI - Multidisciplinary Digital Publishing Institute.
2. Shahid, Md. A., Rahman, Md. M., Hossain, Md. T., Hossain, I., Sheikh, Md. S., Rahman, Md. S., Uddin, N., Donne, S. W., & Hoque, Md. I. U. (2025). Advances in Conductive Polymer-Based Flexible Electronics for Multifunctional Applications. Journal of Composites Science, 9(1), 42.
3. Fang, Y., Bai, Z., Xu, W., Xiong, X., Wei, J., Hu, Q., Wang, H., & Cui, J. (2025). Mechanical Design Principles of Conductive Gels Applied for Flexible Electronics. Advanced Functional Materials, 35(10).
4. Bok, M., Zhao, Z.-J., Hwang, S. H., Ahn, J., Ko, J., Jung, J.-Y., Lee, J., Jeon, S., & Jeong, J.-H. (2022). Functional Asymmetry-Enabled Self-Adhesive Film via Phase Separation of Binary Polymer Mixtures for Soft Bio-Integrated Electronics. ACS Nano, 16(11), 18157–18167.
5. Kashef Tabrizian, S., Terryn, S., & Vanderborght, B. (2025). Toward Autonomous Self-Healing in Soft Robotics: A Review and Perspective for Future Research. Advanced Intelligent Systems.
6. Lu, X., Lu, D., Xu, L., Wang, D., Shao, S., Zhang, A., & Zhang, J. (2025). Ionic conductive elastomer with enhanced tensile strength and Skin-Like modulus for artificial skin based on dynamic Polyurethane-urea. Chemical Engineering Journal (Lausanne, Switzerland : 1996), 505, Article 159292.
7. Chang, C.-Y., Lin, H.-T., Lai, M.-S., Shieh, T.-Y., Peng, C.-C., Shih, M.-H., & Tung, Y.-C. (2018). Flexible Localized Surface Plasmon Resonance Sensor with Metal–Insulator–Metal Nanodisks on PDMS Substrate. Scientific Reports, 8(1), Article 11812.
8. Hu, S., Chen, J., Liang, J., Luo, J., Shi, W., Yuan, J., Chen, Y., Chen, L., Chen, Z., Liu, G.-S., & Luo, Y. (2022). Hyperbolic-Metamaterials-Based SPR Temperature Sensor

Enhanced by a Nanodiamond-PDMS Hybrid for High Sensitivity and Fast Response. ACS Applied Materials & Interfaces, 14(37), 42412–42419.

9. Liu, S., Rao, Y., Jang, H., Tan, P., & Lu, N. (2022). Strategies for body-conformable electronics. Matter, 5(4), 1104-1136.
10. Cordill, M. J., Kreiml, P., & Mitterer, C. (2022). Materials engineering for flexible metallic thin film applications. Materials, 15(3), 926.
11. Xiang, C., Guo, J., & Rossiter, J. (2019). Soft-smart robotic end effectors with sensing, actuation, and gripping capabilities. Smart Materials and Structures, 28(5), 55034.
12. Jung, H. S., Kim, J. Y., Yang, S. Y., Kim, K., Park, J. H., Gong, Y. J., Moon, S. J., & Choi, H. R. (2023). Shape-Adaptive Electrostatic Soft Gripper With Transform Mechanism for Multifunctional Grips. Journal of Mechanisms and Robotics, 15(5).
13. Zhang, X., Yang, T., Zhang, D., & Lepora, N. F. (2024). TacPalm: A Soft Gripper With a Biomimetic Optical Tactile Palm for Stable Precise Grasping. IEEE Sensors Journal, 24(22), 38402–38416.
14. Hertz, H. (1882). Ueber die Berührung fester elastischer Körper. Journal für die reine und angewandte Mathematik, 92, 156–171.
15. Johnson, K. L., Kendall, K., & Roberts, A. D. (1971). Surface energy and the contact of elastic solids. Proceedings of the Royal Society of London. Series A, Mathematical and Physical Sciences, 324(1558), 301–313.
16. Derjaguin, B. V., Muller, V. M., & Toporov, Yu. P. (1994). Effect of contact deformations on the adhesion of particles. Progress in Surface Science, 45(1), 131–143.
17. Maugis, D. (1992). Adhesion of spheres: The JKR-DMT transition using a dugdale model. Journal of Colloid and Interface Science, 150(1), 243–269.
18. Style, R. W., Hyland, C., Boltyanskiy, R., Wettlaufer, J. S., & Dufresne, E. R. (2013). Surface tension and contact with soft elastic solids. Nature Communications, 4(1), Article 2728.
19. Kim, A.-R., Mitra, S. K., & Zhao, B. (2022). Capillary pressure mediated long-term dynamics of thin soft films. Journal of Colloid and Interface Science, 628(Pt B), 788–797.

20. Mukherjee, R., & Sharma, A. (2015). Instability, self-organization and pattern formation in thin soft films. Soft matter, 11(45), 8717-8740.
21. Singamaneni, S., McConney, M. E., & Tsukruk, V. V. (2010). Spontaneous self-folding in confined ultrathin polymer gels. Advanced Materials, 22(11), 1263-1268.
22. Ortiz, O., Vidyasagar, A., Wang, J., & Toomey, R. (2010). Surface instabilities in ultrathin, cross-linked poly (N-isopropylacrylamide) coatings. Langmuir, 26(22), 17489-17494.
23. Trujillo, V., Kim, J., & Hayward, R. C. (2008). Creasing instability of surface-attached hydrogels. Soft matter, 4(3), 564-569.
24. Metze, F. K., Sant, S., Meng, Z., Klok, H. A., & Kaur, K. (2023). Swelling-activated, soft mechanochemistry in polymer materials. Langmuir, 39(10), 3546-3557.
25. Velankar, S. S., Lai, V., & Vaia, R. A. (2012). Swelling-induced delamination causes folding of surface-tethered polymer gels. ACS applied materials & interfaces, 4(1), 24-29.
26. Algorri, J. F., Poudereux, D., García-Cámara, B., Urruchi, V., Sánchez-Pena, J. M., Vergaz, R., Caño-García, M., Quintana, X., Geday, M. A., & Otón, J. M. (2016). Metal nanoparticles-PDMS nanocomposites for tunable optical filters and sensors. Optical Data Processing and Storage, 2(1), 1–6.
27. Hua, F., Sun, Y., Gaur, A., Meitl, M. A., Bilhaut, L., Rotkina, L., Wang, J., Geil, P., Shim, M., Rogers, J. A., & Shim, A. (2004). Polymer Imprint Lithography with Molecular-Scale Resolution. Nano Letters, 4(12), 2467–2471.
28. Butt, H.-J., Cappella, B., & Kappl, M. (2005). Force measurements with the atomic force microscope: Technique, interpretation and applications. Surface Science Reports, 59(1), 1–152.
29. Russel, W. B., Russel, W. B., Saville, D. A., & Schowalter, W. R. (1991). Colloidal dispersions. Cambridge university press.
30. Van Oss, C. J. (2006). Interfacial forces in aqueous media. CRC press.
31. Israelachvili, J. N. (2011). Intermolecular and surface forces. Academic press.

32. Carpick, R. W., Ogletree, D. F., & Salmeron, M. (1999). A General Equation for Fitting Contact Area and Friction vs Load Measurements. Journal of Colloid and Interface Science, 211(2), 395–400.
33. Schwarz, U. D. (2003). A generalized analytical model for the elastic deformation of an adhesive contact between a sphere and a flat surface. Journal of Colloid and Interface Science, 261(1), 99–106.
34. Grierson, D. S., Flater, E. E., & Carpick, R. W. (2005). Accounting for the JKR-DMT transition in adhesion and friction measurements with atomic force microscopy. Journal of Adhesion Science and Technology, 19(3–5), 291–311.
35. Dillard, D. A., Mukherjee, B., Karnal, P., Batra, R. C., & Frechette, J. (2018). A review of Winkler's foundation and its profound influence on adhesion and soft matter applications. Soft Matter, 14(19), 3669–3683.
36. Winkler, E. (1867). Theory of elasticity and strength.
37. Johnson, K. L. (1987). Contact mechanics. Cambridge university press.
38. Dillard, D. A. (1989). Bending of plates on thin elastomeric foundations.
39. Chandler, T. G., & Vella, D. (2020). Validity of Winkler's mattress model for thin elastomeric layers. Proceedings: Mathematical, Physical and Engineering Sciences, 476(2242), 1-27.
40. Skotheim, J. M., & Mahadevan, L. (2004). Soft lubrication. Physical review letters, 92(24), 245509.
41. Zhao, F., Mitra, S., Qi, Z., Xu, M., Yuan, Y., Yao, J., ... & Zhao, B. (2025). In-situ Raman spectroscopy for soft contacts. Journal of Colloid and Interface Science, 138084.
42. Shull, K. R., Ahn, D., Chen, W. L., Flanigan, C. M., & Crosby, A. J. (1998). Axisymmetric adhesion tests of soft materials. Macromolecular Chemistry and Physics, 199(4), 489-511.
43. Shull, K. R. (2002). Contact mechanics and the adhesion of soft solids. Materials Science and Engineering: R: Reports, 36(1), 1-45.
44. Kim, A. R., Mitra, S. K., & Zhao, B. (2022). Capillary pressure mediated long-term dynamics of thin soft films. Journal of Colloid and Interface Science, 628, 788-797.

45. Hay, J. L., & Pharr, G. M. (2000). Instrumented indentation testing.
46. Poon, B., Rittel, D., & Ravichandran, G. (2008). An analysis of nanoindentation in linearly elastic solids. International Journal of Solids and Structures, 45(24), 6018-6033.
47. He, D., Malu, D., & Hu, Y. (2024). A comprehensive review of indentation of gels and soft biological materials. Applied Mechanics Reviews, 76(5), 050802.
48. Nguyen, H. K., Fujinami, S., & Nakajima, K. (2016). Elastic modulus of ultrathin polymer films characterized by atomic force microscopy: The role of probe radius. Polymer, 87, 114-122.
49. Rimai, D. S., DeMejo, L. P., & Bowen, R. C. (1989). Adhesion-induced deformations of polymeric substrates: Particle size dependence of the contact area. Journal of Applied Physics, 66(8), 3574-3578.
50. Rimai, D. S., DeMejo, L. P., Vreeland, W. B., & Bowen, R. C. (1994). Adhesion induced deformations of a highly compliant elastomeric substrate in contact with rigid particles. Langmuir, 10(11), 4361-4366.
51. Jensen, K. E., Sarfati, R., Style, R. W., Boltyanskiy, R., Chakrabarti, A., Chaudhury, M. K., & Dufresne, E. R. (2015). Wetting and phase separation in soft adhesion. Proceedings of the National Academy of Sciences, 112(47), 14490-14494.
52. Pham, J. T., Schellenberger, F., Kappl, M., & Butt, H. J. (2017). From elasticity to capillarity in soft materials indentation. Physical Review Materials, 1(1), 015602.
53. Glover, J. D., & Pham, J. T. (2020). Capillary-driven indentation of a microparticle into a soft, oil-coated substrate. Soft Matter, 16(25), 5812-5818.
54. Cai, Z., Skabeev, A., Morozova, S., & Pham, J. T. (2021). Fluid separation and network deformation in wetting of soft and swollen surfaces. Communications Materials, 2(1), 21.
55. Pericet-Camara, R., Auernhammer, G. K., Koynov, K., Lorenzoni, S., Raiteri, R., & Bonaccurso, E. (2009). Solid-supported thin elastomer films deformed by microdrops. Soft Matter, 5(19), 3611-3617.

56. Park, S. J., Weon, B. M., Lee, J. S., Lee, J., Kim, J., & Je, J. H. (2014). Visualization of asymmetric wetting ridges on soft solids with X-ray microscopy. Nature communications, 5(1), 4369.
57. Mitra, S., Misra, S., Tran, T., & Mitra, S. K. (2022). Probing liquid drop induced deformation on soft solids using dual-wavelength reflection interference contrast microscopy. Langmuir, 38(25), 7750-7758.
58. Hauer, L., Cai, Z., Skabeev, A., Vollmer, D., & Pham, J. T. (2023). Phase separation in wetting ridges of sliding drops on soft and swollen surfaces. Physical Review Letters, 130(5), 058205.
59. Li, J., Zhang, G., Wang, L., & Dai, Z. (2025). Indentation of a plate on a thin transversely isotropic elastic layer. Acta Mechanica Solida Sinica, 38(2), 331-340.
60. Zou, Z., Li, Z., Zhou, Y., Zhou, G., Xu, W., Wu, W., ... & Li, X. (2024). Monitoring soft shape surface deformation via optical images for the distinction of contact state. Advanced Intelligent Systems, 6(3), 2300535.
61. Barber, J. R. (2018). Contact mechanics (Vol. 20). Berlin: Springer International Publishing.
62. Acito, V., Dancette, S., Scheibert, J., Oliver, C., Adrien, J., Maire, E., & Dalmas, D. (2023). On the use of in situ X-ray computed tomography for soft contact mechanics. European Journal of Mechanics-A/Solids, 101, 105057.
63. Smekal, A. (1928). Zur Quantentheorie der Streuung und Dispersion. Naturwissenschaften, 16(31), 612-613.
64. Raman, C. V. (1928). A change of wave-length in light scattering. Nature, 121(3051), 619-619.
65. Long, D. A. (2002). The Raman effect : a unified treatment of the theory of Raman scattering by molecules (1st ed.). Wiley.
66. Klockenkämper, R. E. I. N. H. O. L. D. (1997). Chemical Analysis. A series of monographs on Analytical Chemistry and its Applications. ed. JD Winefordener, 140.

67. Coman, C., & Leopold, L. F. (2017). Raman mapping: Emerging applications. Raman Spectroscopy and Applications, 59-77.
68. Foucher, F., Guimbretière, G., Bost, N., Westall, F., & Maaz, K. (2017). Petrographical and mineralogical applications of Raman mapping. Raman spectroscopy and applications, 163-180.
69. Bae, S. C., Lee, H., Lin, Z., & Granick, S. (2005). Chemical imaging in a surface forces apparatus: confocal Raman spectroscopy of confined poly (dimethylsiloxane). Langmuir, 21(13), 5685-5688.
70. Singer, I. L., Dvorak, S. D., Wahl, K. J., & Scharf, T. W. (2003). Role of third bodies in friction and wear of protective coatings. Journal of Vacuum Science & Technology A: Vacuum, Surfaces, and Films, 21(5), S232-S240.
71. Bongaerts, J. H. H., Day, J. P. R., Marriott, C., Pudney, P. D. A., & Williamson, A. M. (2008). In situ confocal Raman spectroscopy of lubricants in a soft elastohydrodynamic tribological contact. Journal of Applied Physics, 104(1).
72. Ledinský, M., Paviet-Salomon, B., Vetushka, A., Geissbühler, J., Tomasi, A., Despeisse, M., ... & Fejfar, A. (2016). Profilometry of thin films on rough substrates by Raman spectroscopy. Scientific reports, 6(1), 37859.
73. Curtis, A. S. G. (1964). The mechanism of adhesion of cells to glass: a study by interference reflection microscopy. The Journal of cell biology, 20(2), 199-215.
74. Velde, I. C. T., Bonnet, J., Tanke, H. J., & Ploem, J. S. (1988). Reflection contrast microscopy: visualization of (peroxidase-generated) diaminobenzidine polymer products and its underlying optical phenomena. Histochemistry, 89(2), 141-150.
75. Schilling, J., Sengupta, K., Goennenwein, S., Bausch, A. R., & Sackmann, E. (2004). Absolute interfacial distance measurements by dual-wavelength reflection interference contrast microscopy. Physical Review E, 69(2), 021901.
76. Wiegand, G., Neumaier, K. R., & Sackmann, E. (1998). Microinterferometry: three-dimensional reconstruction of surface microtopography for thin-film and wetting studies by reflection interference contrast microscopy (RICM). Applied optics, 37(29), 6892-6905.

77. Wiegand, G., Jaworek, T., Wegner, G., & Sackmann, E. (1997). Studies of structure and local wetting properties on heterogeneous, micropatterned solid surfaces by microinterferometry. Journal of colloid and interface science, 196(2), 299-312.
78. Theodoly, O., Huang, Z. H., & Valignat, M. P. (2010). New modeling of reflection interference contrast microscopy including polarization and numerical aperture effects: application to nanometric distance measurements and object profile reconstruction. Langmuir, 26(3), 1940-1948.
79. Misra, S., Teshima, H., Takahashi, K., & Mitra, S. K. (2021). Reflected laser interferometry: A versatile tool to probe condensation of Low-surface-tension droplets. Langmuir, 37(27), 8073-8082.
80. De Gennes, P. G. (1992). Soft matter. Science, 256(5056), 495-497.
81. Guo, X., Tang, W., Qin, K., Zhong, Y., Xu, H., Qu, Y., ... & Zou, J. (2024). Powerful UAV manipulation via bioinspired self-adaptive soft self-contained gripper. Science Advances, 10(19), eadn6642.
82. Zhao, G., Ling, Y., Su, Y., Chen, Z., Mathai, C. J., Emeje, O., ... & Yan, Z. (2022). Laser-scribed conductive, photoactive transition metal oxide on soft elastomers for Janus on-skin electronics and soft actuators. Science advances, 8(25), eabp9734.
83. Nam, M., Chang, J., Kim, H., Son, Y. H., Jeon, Y., Kwon, J. H., & Choi, K. C. (2024). Highly reliable and stretchable OLEDs based on facile patterning method: toward stretchable organic optoelectronic devices. npj Flexible Electronics, 8(1), 17.
84. Xie, R., Cao, Y., Sun, R., Wang, R., Morgan, A., Kim, J., ... & Stevens, M. M. (2024). Magnetically driven formation of 3D freestanding soft bioscaffolds. Science Advances, 10(5), eadl1549.
85. Xu, Y., Sun, Z., Bai, Z., Shen, H., Wen, R., Wang, F., ... & Lee, C. (2024). Bionic e-skin with precise multi-directional droplet sliding sensing for enhanced robotic perception. Nature Communications, 15(1), 6022.

86. Muller, V. M., Derjaguin, B. V., & Toporov, Y. P. (1983). On two methods of calculation of the force of sticking of an elastic sphere to a rigid plane. Colloids and Surfaces, 7(3), 251-259.
87. Boussinesq, J. (1878). Équilibre d'élasticité d'un sol isotrope sans pesanteur, supportant différents poids. CR Math. Acad. Sci. Paris, 86(86), 1260-1263.
88. Chandler, T. G., & Vella, D. (2020). Validity of Winkler's mattress model for thin elastomeric layers: beyond Poisson's ratio. Proceedings of the Royal Society A, 476(2242), 20200551.
89. Li, J., Zhang, G., Wang, L., & Dai, Z. (2025). Indentation of a plate on a thin transversely isotropic elastic layer. Acta Mechanica Solida Sinica, 38(2), 331-340.
90. Yu, C., & Dai, Z. (2024). Premature jump-to-contact with elastic surfaces. Journal of the Mechanics and Physics of Solids, 193, 105919.
91. Greenwood, J. A., Johnson, K. L., & Matsubara, E. (1984). A surface roughness parameter in Hertz contact. Wear, 100(1-3), 47-57.
92. Ciavarella, M. (2018). An approximate JKR solution for a general contact, including rough contacts. Journal of the Mechanics and Physics of Solids, 114, 209-218.
93. Ge, J., Wang, X., Drack, M., Volkov, O., Liang, M., Cañón Bermúdez, G. S., ... & Makarov, D. (2019). A bimodal soft electronic skin for tactile and touchless interaction in real time. Nature communications, 10(1), 4405.
94. Han, J., Yang, J., Gao, W., & Bai, H. (2021). Ice-templated, large-area silver nanowire pattern for flexible transparent electrode. Advanced Functional Materials, 31(16), 2010155.
95. Lan, X., Li, W., Ye, C., Boetje, L., Pelras, T., Silvianti, F., ... & Loos, K. (2022). Scalable and degradable dextrin-based elastomers for wearable touch sensing. ACS Applied Materials & Interfaces, 15(3), 4398-4407.
96. Adepu, V., Yoo, C., Jung, Y., & Sahatiya, P. (2023). Large area matrix of MXene/MoSe2 nanohybrid-based flexible piezoresistive pressure sensors for artificial e-skin application. Applied Physics Letters, 122(26).

97. He, Y., Liang, H., Chen, M., Jiang, L., Zhang, Z., Heng, X., ... & Yang, Z. (2021). Optical fiber waveguiding soft photoactuators exhibiting giant reversible shape change. Advanced Optical Materials, 9(21), 2101132.
98. Kim, A. R., Mitra, S., Shyam, S., Zhao, B., & Mitra, S. K. (2024). Flexible hydrogels connecting adhesion and wetting. Soft Matter, 20(28), 5516-5526.
99. Jensen, K. E., Style, R. W., Xu, Q., & Dufresne, E. R. (2017). Strain-dependent solid surface stress and the stiffness of soft contacts. Physical Review X, 7(4), 041031.
100. Tress, M., Karpitschka, S., Papadopoulos, P., Snoeijer, J. H., Vollmer, D., & Butt, H. J. (2017). Shape of a sessile drop on a flat surface covered with a liquid film. Soft matter, 13(20), 3760-3767.
101. Schellenberger, F., Xie, J., Encinas, N., Hardy, A., Klapper, M., Papadopoulos, P., ... & Vollmer, D. (2015). Direct observation of drops on slippery lubricant-infused surfaces. Soft Matter, 11(38), 7617-7626.
102. Zhao, F., Mitra, S., Kim, A. R., Xu, M., Yao, J., Mitra, S. K., & Zhao, B. (2024). Profiling contact ridge of soft substrates with metallic thin films using a novel interference technique. Surfaces and Interfaces, 49, 104458.
103. Kim, A. R., Mitra, S. K., & Zhao, B. (2024). Unravelling soft interfaces: Visualization of gel ridges. Journal of Colloid and Interface Science, 676, 1109-1117.
104. Delavoipière, J., Tran, Y., Verneuil, E., Heurtefeu, B., Hui, C. Y., & Chateauminois, A. (2018). Friction of poroelastic contacts with thin hydrogel films. Langmuir, 34(33), 9617-9626.
105. Delavoipiere, J., Tran, Y., Verneuil, E., & Chateauminois, A. (2016). Poroelastic indentation of mechanically confined hydrogel layers. Soft Matter, 12(38), 8049-8058.
106. Ciapa, L., Delavoipière, J., Tran, Y., Verneuil, E., & Chateauminois, A. (2020). Transient sliding of thin hydrogel films: the role of poroelasticity. Soft Matter, 16(28), 6539-6548.

107. Zou, Z., Li, Z., Zhou, Y., Zhou, G., Xu, W., Huang, M., ... & Li, X. (2025). A Real‐Time Imaging Sensing System to Visualize Elastomer Surface Profile Evolution for Dynamic Tactile Recognition. Advanced Functional Materials, 35(10), 2416731.
108. Wandrol, P., & Slouf, M. (2017). Polymer imaging in SEM—Charge, damage and coating free. Microscopy and Microanalysis, 23(S1), 1816-1817.
109. Mohammed, A., & Abdullah, A. (2018, November). Scanning electron microscopy (SEM): A review. In Proceedings of the 2018 international conference on hydraulics and pneumatics—HERVEX, Băile Govora, Romania (Vol. 2018, pp. 7-9).
110. Fang, N., Chan, V., Wan, K. T., Mao, H. Q., & Leong, K. W. (2002). Colloidal adhesion of phospholipid vesicles: high-resolution reflection interference contrast microscopy and theory. Colloids and Surfaces B: Biointerfaces, 25(4), 347-362.
111. Matsuzaki, T., Sazaki, G., Suganuma, M., Watanabe, T., Yamazaki, T., Tanaka, M., ... & Yoshikawa, H. Y. (2014). High contrast visualization of cell–hydrogel contact by advanced interferometric optical microscopy. The journal of physical chemistry letters, 5(1), 253-257.
112. Zhao, F., Mitra, S., Kim, A. R., Xu, M., Yao, J., Mitra, S. K., & Zhao, B. (2023). Determining effective refractive index and elasticity of nanoscale metal-thin, soft polymer bilayers using interference signatures of a glass probe. Colloids and Surfaces A: Physicochemical and Engineering Aspects, 674, 131861.
113. Zhou, H., Llanes, J. P., Lotfi, M., Sarntinoranont, M., Simmons, C. S., & Subhash, G. (2023). Label-free quantification of microscopic alignment in engineered tissue scaffolds by polarized Raman spectroscopy. ACS Biomaterials Science & Engineering, 9(6), 3206-3218.
114. Wang, Y. H., Li, S., Zhou, R. Y., Zheng, S., Zhang, Y. J., Dong, J. C., ... & Li, J. F. (2023). In situ electrochemical Raman spectroscopy and ab initio molecular dynamics study of interfacial water on a single-crystal surface. Nature Protocols, 18(3), 883-901.

115. Wang, Y. H., Zheng, S., Yang, W. M., Zhou, R. Y., He, Q. F., Radjenovic, P., ... & Li, J. F. (2021). In situ Raman spectroscopy reveals the structure and dissociation of interfacial water. Nature, 600(7887), 81-85.
116. Krishnamoorthy, K., & Kim, S. J. (2021). Raman Spectroscopy and Mapping Analysis of Low-Dimensional Nanostructured Materials and Systems. In Recent Developments in Atomic Force Microscopy and Raman Spectroscopy for Materials Characterization. IntechOpen.
117. Colomban, P. (2002). Analysis of strain and stress in ceramic, polymer and metal matrix composites by Raman spectroscopy. Advanced engineering materials, 4(8), 535-542.
118. Gupper, A., Wilhelm, P., Schmied, M., & Ingolic, E. (2002, August). Morphology of a PA/PTFE blend studied by Raman imaging. In Macromolecular Symposia (Vol. 184, No. 1, pp. 275-286). Weinheim: WILEY‐VCH Verlag.
119. Kato, E., & Murakami, T. (2002). Study of the volume phase transition of poly (N-isopropylacrylamide) gels in aqueous solutions of pyridine by depolarized Rayleigh and Raman scattering. Polymer, 43(21), 5607-5613.
120. Sun, H., Meng, X., Luo, C., Qian, Y., Men, Y., & Su, Z. (2024). Quantifying Crystallinity in Poly (p-phenylene terephthalamide) by Raman Spectroscopy. Macromolecules, 57(15), 7390-7397.
121. Drake, J. M., Klafter, J., Levitz, P., Overney, R., & Urbach, M. (1993). Dynamics in small confining systems. In MRS Symposia Proceedings (No. 651).
122. Granick, S. (1999). Soft matter in a tight spot. Physics Today, 52(7), 26-31.
123. Li, S., Zhang, J., He, J., Liu, W., Wang, Y., Huang, Z., ... & Chen, Y. (2023). Functional PDMS elastomers: bulk composites, surface engineering, and precision fabrication. Advanced Science, 10(34), 2304506.
124. Mestari, A., Gaufrès, R., & Huguet, P. (1997). Behaviour of the calibration of a Raman spectrometer with temperature changes. Journal of Raman spectroscopy, 28(10), 785-789.

125. De Wolf, I. (1996). Micro-Raman spectroscopy to study local mechanical stress in silicon integrated circuits. Semiconductor science and technology, 11(2), 139.
126. Mysen, B. O., Finger, L. W., Virgo, D., & Seifert, F. A. (1982). Curve-fitting of Raman spectra of silicate glasses. The American Mineralogist, 67(7–8), 686–695.
127. Fukumi, K., Hayakawa, J., & Komiyama, T. (1990). Intensity of raman band in silicate glasses. Journal of Non-Crystalline Solids, 119(3), 297–302.
128. Ma, Y., Du, Y., Chen, Y., Gu, C., Jiang, T., Wei, G., & Zhou, J. (2020). Intrinsic Raman signal of polymer matrix induced quantitative multiphase SERS analysis based on stretched PDMS film with anchored Ag nanoparticles/Au nanowires. Chemical Engineering Journal (Lausanne, Switzerland : 1996), 381, Article 122710.
129. Cai, D., Neyer, A., Kuckuk, R., & Heise, H. M. (2010). Raman, mid-infrared, near-infrared and ultraviolet–visible spectroscopy of PDMS silicone rubber for characterization of polymer optical waveguide materials. Journal of Molecular Structure, 976(1-3), 274-281.
130. Jayes, L., Hard, A. P., Séné, C., Parker, S. F., & Jayasooriya, U. A. (2003). Vibrational spectroscopic analysis of silicones: A Fourier transform-Raman and inelastic neutron scattering investigation. Analytical chemistry, 75(4), 742-746.
131. Colthup, N. B. (1980). Molecular Orbitals and CH_3, CH_2, and CH Deformation Group Frequencies. Applied Spectroscopy, 34(1), 1-6.
132. Jiang, S., Bae, S. C., & Granick, S. (2008). PDMS melts on mica studied by confocal Raman scattering. Langmuir, 24(4), 1489-1494.
133. Rathnayake, D. T., Malik, N., Milone, S., Morin, S. A., & Guo, Y. (2024). Interference effects in micro-raman spectroscopy enable mapping of chemical gradients on an elastomer surface. The Journal of Physical Chemistry Letters, 15(33), 8467-8476.
134. Gouadec, G., & Colomban, P. (2007). Raman Spectroscopy of nanomaterials: How spectra relate to disorder, particle size and mechanical properties. Progress in crystal growth and characterization of materials, 53(1), 1-56.
135. Toporski, J., Dieing, T., & Hollricher, O. (Eds.). (2018). Confocal Raman Microscopy (Vol. 66). Springer.

136. Long, D. (2002). A unified treatment of the theory of Raman scattering by molecules. The Raman Effect.
137. McCreery, R. L. (2005). Raman spectroscopy for chemical analysis. John Wiley & Sons.
138. Weber, W. H., & Merlin, R. (Eds.). (2013). Raman scattering in materials science (Vol. 42). Springer Science & Business Media.
139. Dogru, S., Aksoy, B., Bayraktar, H., & Alaca, B. E. (2018). Poisson's ratio of PDMS thin films. Polymer Testing, 69, 375-384.
140. Baldwin, K. J., & Batchelder, D. N. (2001). Confocal Raman microspectroscopy through a planar interface. Applied Spectroscopy, 55(5), 517-524.
141. He, S., Zhang, W., Liu, L., Huang, Y., He, J., Xie, W., ... & Du, C. (2014). Baseline correction for Raman spectra using an improved asymmetric least squares method. Analytical Methods, 6(12), 4402-4407.
142. Beams, R., Cançado, L. G., & Novotny, L. (2015). Raman characterization of defects and dopants in graphene. Journal of Physics: Condensed Matter, 27(8), 083002.
143. Bocklitz, T., Walter, A., Hartmann, K., Rösch, P., & Popp, J. (2011). How to pre-process Raman spectra for reliable and stable models?. Analytica chimica acta, 704(1-2), 47-56.
144. Zhao, J., Chen, P., Lin, Y., Chang, J., Lu, A., Chen, W., ... & Li, L. (2018). Stretch-induced crystallization and phase transitions of poly (dimethylsiloxane) at low temperatures: an in situ synchrotron radiation wide-angle X-ray scattering study. Macromolecules, 51(21), 8424-8434.
145. Ferrari, A. C., & Basko, D. M. (2013). Raman spectroscopy as a versatile tool for studying the properties of graphene. Nature nanotechnology, 8(4), 235-246.
146. Mohiuddin, T. M. G., Lombardo, A., Nair, R. R., Bonetti, A., Savini, G., Jalil, R., ... & Ferrari, A. C. (2009). Uniaxial strain in graphene by Raman spectroscopy: G peak splitting, Grüneisen parameters, and sample orientation. Physical Review B—Condensed Matter and Materials Physics, 79(20), 205433.

147. Gayle, A. J., Friedman, L. H., Beams, R., Bush, B. G., Gerbig, Y. B., Michaels, C. A., ... & Cook, R. F. (2017). Two-dimensional strain-mapping by electron backscatter diffraction and confocal Raman spectroscopy. Journal of applied physics, 122(20).

148. Hao, Z., Ghanekarade, A., Zhu, N., Randazzo, K., Kawaguchi, D., Tanaka, K., ... & Zuo, B. (2021). Mobility gradients yield rubbery surfaces on top of polymer glasses. Nature, 596(7872), 372-376.

149. Cuccia, N. L., Pothineni, S., Wu, B., Méndez Harper, J., & Burton, J. C. (2020). Pore-size dependence and slow relaxation of hydrogel friction on smooth surfaces. Proceedings of the National Academy of Sciences, 117(21), 11247-11256.

150. Xia, X., Yang, J., Liu, Y., Zhang, J., Shang, J., Liu, B., ... & Li, W. (2023). Material choice and structure design of flexible battery electrode. Advanced Science, 10(3), 2204875.

151. Zhao, W., Zhang, Y., Zhao, X., Sheng, W., Ma, S., & Zhou, F. (2024). Mechanically robust lubricating hydrogels beyond the natural cartilage as compliant artificial joint coating. Advanced Science, 11(31), 2401000.

152. Chen, Q., Zhang, X., Chen, K., Feng, C., Wang, D., Qi, J., ... & Zhang, D. (2022). Bilayer hydrogels with low friction and high load-bearing capacity by mimicking the oriented hierarchical structure of cartilage. ACS Applied Materials & Interfaces, 14(46), 52347-52358.

153. Zhao, C., Park, J., Root, S. E., & Bao, Z. (2024). Skin-inspired soft bioelectronic materials, devices and systems. Nature Reviews Bioengineering, 2(8), 671-690.

154. Gu, Y., Zheng, J. J., Otake, K. I., Sugimoto, K., Hosono, N., Sakaki, S., ... & Kitagawa, S. (2020). Structural‐deformation‐energy‐modulation strategy in a soft porous coordination polymer with an interpenetrated framework. Angewandte Chemie, 132(36), 15647-15651.

155. Endo, T., Yanagida, Y., & Hatsuzawa, T. (2007). Colorimetric detection of volatile organic compounds using a colloidal crystal-based chemical sensor for environmental applications. Sensors and Actuators B: Chemical, 125(2), 589-595.

156. Yao, C., Storey, D., & Webster, T. J. (2007). Nanostructured metal coatings on polymers increase osteoblast attachment. International journal of nanomedicine, 2(3), 487-492.
157. Tang, R., Huang, H., Tu, H., Liang, H., Liang, M., Song, Z., ... & Yu, H. (2014). Origami-enabled deformable silicon solar cells. Applied Physics Letters, 104(8).
158. Liu, Y. Q., Zhang, J. R., Han, D. D., Zhang, Y. L., & Sun, H. B. (2019). Versatile electronic skins with biomimetic micronanostructures fabricated using natural reed leaves as templates. ACS applied materials & interfaces, 11(41), 38084-38091.
159. Zhang, H., Zhao, N., Li, H., Wang, M., Hao, X., Sun, M., ... & Wang, C. (2022). 3D flexible SERS substrates integrated with a portable Raman analyzer and wireless communication for point-of-care application. ACS Applied Materials & Interfaces, 14(45), 51253-51264.
160. Yin, L., Wu, Q., Zhang, C., Xu, M., Yuan, Y., & Yao, J. (2022). Real-time visualization of the Suzuki reaction using surface enhanced Raman spectroscopy and a moveable magnetic nanoparticle film. Chemical Communications, 58(45), 6538-6541.
161. Lin, J., Zhang, C., Xu, M., Yuan, Y., & Yao, J. (2018). Surface-enhanced Raman spectroscopic identification in fingerprints based on adhesive Au nanofilm. RSC advances, 8(43), 24477-24484.
162. Zhou, L., Song, H., Liang, J., Singer, M., Zhou, M., Stegenburgs, E., ... & Gan, Q. (2019). A polydimethylsiloxane-coated metal structure for all-day radiative cooling. Nature Sustainability, 2(8), 718-724.
163. Kim, J., Kim, M., Jung, H., Park, J., Jun, B. O., Kang, B., ... & Lee, Y. (2022). High-quality microprintable and stretchable conductors for high-performance 5G wireless communication. ACS Applied Materials & Interfaces, 14(47), 53250-53260.
164. Xiang, Y., Li, T., Suo, Z., & Vlassak, J. J. (2005). High ductility of a metal film adherent on a polymer substrate. Applied Physics Letters, 87(16).
165. Sun, S., Pan, Z., Yang, F. K., Huang, Y., & Zhao, B. (2016). A transparent silica colloidal crystal/PDMS composite and its application for crack suppression of metallic coatings. Journal of Colloid and Interface Science, 461, 136-143.

166. Nikolaou, P., Mina, C., Constantinou, M., Koutsokeras, L. E., Constantinides, G., Lidorikis, E., ... & Patsalas, P. (2015). Functionally graded poly (dimethylsiloxane)/silver nanocomposites with tailored broadband optical absorption. Thin Solid Films, 581, 14-19.
167. Ritland, H. N. (1955). Relation between refractive index and density of a glass at constant temperature. Journal of the American Ceramic Society, 38(2), 86-88.
168. Anderson, O. L., & Schreiber, E. (1965). The relation between refractive index and density of minerals related to the Earth's mantle. Journal of Geophysical Research, 70(6), 1463-1471.
169. Mukhopadhyay, M. K., Lurio, L. B., Jiang, Z., Jiao, X., Sprung, M., DeCaro, C., & Sinha, S. K. (2010). Measurement of the interior structure of thin polymer films using grazing incidence diffuse x-ray scattering. Physical Review E—Statistical, Nonlinear, and Soft Matter Physics, 82(1), 011804.
170. Liu, M., Sun, J., Sun, Y., Bock, C., & Chen, Q. (2009). Thickness-dependent mechanical properties of polydimethylsiloxane membranes. Journal of micromechanics and microengineering, 19(3), 035028.
171. Chen, L., Bonaccurso, E., Deng, P., & Zhang, H. (2016). Droplet impact on soft viscoelastic surfaces. Physical Review E, 94(6), 063117.
172. Lu, G., Li, H., & Zhang, H. (2011). Nanoparticle-coated PDMS elastomers for enhancement of Raman scattering. Chemical Communications, 47(30), 8560-8562.
173. Lu, G., Li, H., & Zhang, H. (2012). Gold‐Nanoparticle‐Embedded Polydimethylsiloxane Elastomers for Highly Sensitive Raman Detection. Small, 8(9), 1336-1340.
174. Yang, F. K., Zhang, W., Han, Y., Yoffe, S., Cho, Y., & Zhao, B. (2012). “Contact” of nanoscale stiff films. Langmuir, 28(25), 9562-9572.
175. Fortuni, B., Inose, T., Uezono, S., Toyouchi, S., Umemoto, K., Sekine, S., ... & Uji-i, H. (2017). In situ synthesis of Au-shelled Ag nanoparticles on PDMS for flexible, long-life, and broad spectrum-sensitive SERS substrates. Chemical Communications, 53(82), 11298-11301.

176. Li, Z., Huang, X., & Lu, G. (2020). Recent developments of flexible and transparent SERS substrates. Journal of Materials Chemistry C, 8(12), 3956-3969.
177. Xia, D., Guo, Q., Ge, M., Yuan, Y., Xu, M., & Yao, J. (2016). On-line sensitive detection of aromatic vapor through PDMS/C 3 H 7 S-assisted SERS amplification. Rsc Advances, 6(58), 53289-53295.
178. Wolf, M. P., Salieb-Beugelaar, G. B., & Hunziker, P. (2018). PDMS with designer functionalities—Properties, modifications strategies, and applications. Progress in Polymer Science, 83, 97-134.
179. Martinček, I., Turek, I., & Tarjányi, N. (2014). Effect of boundary on refractive index of PDMS. Optical Materials Express, 4(10), 1997-2005.
180. Yasir, M., Sai, T., Sicher, A., Scheffold, F., Steiner, U., Wilts, B. D., & Dufresne, E. R. (2021). Enhancing the Refractive Index of Polymers with a Plant‐Based Pigment. Small, 17(44), 2103061.
181. Badur, T., Dams, C., & Hampp, N. (2018). High refractive index polymers by design. Macromolecules, 51(11), 4220-4228.
182. Kleine, T. S., Nguyen, N. A., Anderson, L. E., Namnabat, S., LaVilla, E. A., Showghi, S. A., & Pyun, J. (2016). High refractive index copolymers with improved thermomechanical properties via the inverse vulcanization of sulfur and 1, 3, 5-triisopropenylbenzene. ACS Macro Letters, 5(10), 1152-1156.
183. Higashihara, T., & Ueda, M. (2015). Recent progress in high refractive index polymers. Macromolecules, 48(7), 1915-1929.
184. Park, C. H., Kim, J. G., Jung, S. G., Lee, D. J., Park, Y. W., & Ju, B. K. (2019). Optical characteristics of refractive-index-matching diffusion layer in organic light-emitting diodes. Scientific reports, 9(1), 8690.
185. Shanbhogue, H. G., Nagendra, C. L., Annapurna, M. N., Kumar, S. A., & Thutupalli, G. K. M. (1997). Multilayer antireflection coatings for the visible and near-infrared regions. Applied Optics, 36(25), 6339-6351.

186. Asghar, M. H., Placido, F., & Naseem, S. (2007). Reactively evaporated multilayer antireflection coatings for Ge optical window. Journal of Physics D: Applied Physics, 40(7), 2065.
187. Macleod, H. A., & Macleod, H. A. (2010). Thin-film optical filters. CRC press.
188. Chen, L., Guo, X., & Hao, J. (2013). Refractive index measurement by fiber point diffraction longitudinal shearing interferometry. Applied Optics, 52(16), 3655-3661.
189. Hussain, B., Ahmed, M., Nawaz, M., Saleem, M., Razzaq, M., Zia, M. A., & Iqbal, M. (2012). Simultaneous determination of thickness and refractive index based on time-of-flight measurements of terahertz pulse. Applied Optics, 51(21), 5326-5330.
190. Fukano, T., & Yamaguchi, I. (1996). Simultaneous measurement of thicknesses and refractive indices of multiple layers by a low-coherence confocal interference microscope. Optics letters, 21(23), 1942-1944.
191. Fukano, T., & Yamaguchi, I. (1999). Separation of measurement of the refractive index and the geometrical thickness by use of a wavelength-scanning interferometer with a confocal microscope. Applied optics, 38(19), 4065-4073.
192. Binding, J., Ben Arous, J., Léger, J. F., Gigan, S., Boccara, C., & Bourdieu, L. (2011). Brain refractive index measured in vivo with high-NA defocus-corrected full-field OCT and consequences for two-photon microscopy. Optics express, 19(6), 4833-4847.
193. Labiau, S., David, G., Gigan, S., & Boccara, A. C. (2009). Defocus test and defocus correction in full-field optical coherence tomography. Optics letters, 34(10), 1576-1578.
194. Zhou, Y., Chan, K. K., Lai, T., & Tang, S. (2012). Characterizing refractive index and thickness of biological tissues using combined multiphoton microscopy and optical coherence tomography. Biomedical optics express, 4(1), 38-50.
195. Srinivasan, V. J., Radhakrishnan, H., Jiang, J. Y., Barry, S., & Cable, A. E. (2012). Optical coherence microscopy for deep tissue imaging of the cerebral cortex with intrinsic contrast. Optics express, 20(3), 2220-2239.

196. Min, G., Kim, J. W., Choi, W. J., & Lee, B. H. (2012). Numerical correction of distorted images in full-field optical coherence tomography. Measurement Science and Technology, 23(3), 035403.
197. Rothenhäusler, B., & Knoll, W. (1988). Surface-plasmon microscopy. Nature, 332(6165), 615-617.
198. Nestler, P., & Helm, C. A. (2017). Determination of refractive index and layer thickness of nm-thin films via ellipsometry. Optics Express, 25(22), 27077-27085.
199. Teshima, H., Misra, S., Takahashi, K., & Mitra, S. K. (2020). Precursor-film-mediated thermocapillary motion of low-surface-tension microdroplets. Langmuir, 36(19), 5096-5105.
200. Limozin, L., & Sengupta, K. (2009). Quantitative reflection interference contrast microscopy (RICM) in soft matter and cell adhesion. ChemPhysChem, 10(16), 2752-2768.
201. Rädler, J., & Sackmann, E. (1993). Imaging optical thicknesses and separation distances of phospholipid vesicles at solid surfaces. Journal de Physique II, 3(5), 727-748.
202. Stenzel, O. (2005). The physics of thin film optical spectra: an introduction. Berlin, Heidelberg: Springer Berlin Heidelberg.
203. Palchesko, R. N., Zhang, L., Sun, Y., & Feinberg, A. W. (2012). Development of polydimethylsiloxane substrates with tunable elastic modulus to study cell mechanobiology in muscle and nerve. PloS one, 7(12), e51499.
204. Yu, Y., Sanchez, D., & Lu, N. (2015). Work of adhesion/separation between soft elastomers of different mixing ratios. Journal of Materials Research, 30(18), 2702–2712.
205. She, H., & Chaudhury, M. K. (2000). Estimation of Adhesion Hysteresis Using Rolling Contact Mechanics. Langmuir, 16(2), 622–625.
206. Kozar, A. V. (2009). Optical properties of aperiodic thin-layer structures: Effective refractive index. Moscow University Physics Bulletin, 64(3), 291-293.
207. Prajzler, V., Nekvindova, P., Spirkova, J., & Novotny, M. (2017). The evaluation of the refractive indices of bulk and thick polydimethylsiloxane and polydimethyl-

diphenylsiloxane elastomers by the prism coupling technique. Journal of Materials Science: Materials in Electronics, 28(11), 7951-7961.

208. Meichner, C., Schedl, A. E., Neuber, C., Kreger, K., Schmidt, H. W., & Kador, L. (2015). Refractive-index determination of solids from first-and second-order critical diffraction angles of periodic surface patterns. AIP Advances, 5(8).

209. Mitra, S., Vo, Q., & Tran, T. (2021). Bouncing-to-wetting transition of water droplets impacting soft solids. Soft Matter, 17(24), 5969-5977.

210. Cortelli, G., Patruno, L., Cramer, T., Murgia, M., Fraboni, B., & de Miranda, S. (2021). Atomic force microscopy nanomechanics of hard nanometer-thick films on soft substrates: Insights into stretchable conductors. ACS Applied Nano Materials, 4(8), 8376-8382.

211. Lee, D., Barber, J. R., & Thouless, M. (2009). Indentation of an elastic half space with material properties varying with depth. International journal of engineering science, 47(11-12), 1274-1283.

212. Wei, H., & Eilers, H. (2009). From silver nanoparticles to thin films: Evolution of microstructure and electrical conduction on glass substrates. Journal of Physics and Chemistry of Solids, 70(2), 459-465.

213. Kumar, C., Perris, J., Bairagi, S., Min, G., Xu, Y., Gadegaard, N., & Mulvihill, D. M. (2023). Multiscale in-situ quantification of the role of surface roughness and contact area using a novel Mica-PVS triboelectric nanogenerator. Nano Energy, 107, 108122.

214. Wu, D., Yamada, K. M., & Wang, S. (2023). Tissue morphogenesis through dynamic cell and matrix interactions. Annual review of cell and developmental biology, 39(1), 123-144.

215. Yang, Q., & Loos, K. (2017). Janus nanoparticles inside polymeric materials: interfacial arrangement toward functional hybrid materials. Polymer Chemistry, 8(4), 641-654.

216. Mary, P., Chateauminois, A., & Frétigny, C. (2006). Deformation of elastic coatings in adhesive contacts with spherical probes. Journal of Physics D: Applied Physics, 39(16), 3665.

217. Walden, R., Kumar, C., Mulvihill, D. M., & Pillai, S. C. (2022). Opportunities and challenges in triboelectric nanogenerator (TENG) based sustainable energy generation technologies: a mini-review. Chemical Engineering Journal Advances, 9, 100237.
218. Wu, C., Kim, T. W., Park, J. H., An, H., Shao, J., Chen, X., & Wang, Z. L. (2017). Enhanced triboelectric nanogenerators based on MoS2 monolayer nanocomposites acting as electron-acceptor layers. ACS nano, 11(8), 8356-8363.
219. Komvopoulos, K. (2020). A multiscale theoretical analysis of the mechanical, thermal, and electrical characteristics of rough contact interfaces demonstrating fractal behavior. Frontiers in Mechanical Engineering, 6, 36.
220. Sakai, M. (2010). Substrate-affected contact deformation and hardness of an elastoplastic film coated on purely elastic substrates. Surface and Coatings Technology, 204(8), 1247-1251.
221. Ou, X., Chen, X., Xu, X., Xie, L., Chen, X., Hong, Z., ... & Yang, H. (2021). Recent development in x-ray imaging technology: Future and challenges. Research.
222. Cai, Z., Skabeev, A., Morozova, S., & Pham, J. T. (2021). Fluid separation and network deformation in wetting of soft and swollen surfaces. Communications Materials, 2(1), 21.
223. Jensen, K. E., Sarfati, R., Style, R. W., Boltyanskiy, R., Chakrabarti, A., Chaudhury, M. K., & Dufresne, E. R. (2015). Wetting and phase separation in soft adhesion. Proceedings of the National Academy of Sciences, 112(47), 14490-14494.
224. Park, S. J., Weon, B. M., Lee, J. S., Lee, J., Kim, J., & Je, J. H. (2014). Visualization of asymmetric wetting ridges on soft solids with X-ray microscopy. Nature communications, 5(1), 4369.
225. Claxton, N. S., Fellers, T. J., & Davidson, M. W. (2006). Laser scanning confocal microscopy. Encyclopedia of Medical Devices and Instrumentation, 21(1), 1-37.
226. Sandison, D. R., & Webb, W. W. (1994). Background rejection and signal-to-noise optimization in confocal and alternative fluorescence microscopes. Applied optics, 33(4), 603-615.

227. Gratton, E., & VandeVen, M. J. (2006). Laser sources for confocal microscopy. In Handbook of biological confocal microscopy (pp. 53-67). Boston, MA: Springer US.
228. Ashkin, A., Dziedzic, J. M., & Yamane, T. (1987). Optical trapping and manipulation of single cells using infrared laser beams. Nature, 330(6150), 769-771.
229. Scatliff, J. H., & Morris, P. J. (2014). From Roentgen to magnetic resonance imaging: the history of medical imaging. North Carolina medical journal, 75(2), 111-113.
230. Cao, F., Yu, D., Ma, W., Xu, X., Cai, B., Yang, Y. M., ... & Zeng, H. (2019). Shining emitter in a stable host: design of halide perovskite scintillators for X-ray imaging from commercial concept. ACS nano, 14(5), 5183-5193.
231. Holler, M., Guizar-Sicairos, M., Tsai, E. H., Dinapoli, R., Müller, E., Bunk, O., ... & Aeppli, G. (2017). High-resolution non-destructive three-dimensional imaging of integrated circuits. Nature, 543(7645), 402-406.
232. Kotwaliwale, N., Singh, K., Kalne, A., Jha, S. N., Seth, N., & Kar, A. (2014). X-ray imaging methods for internal quality evaluation of agricultural produce. Journal of food science and technology, 51(1), 1-15.
233. Farkas, J. (2006). Irradiation for better foods. Trends in food science & technology, 17(4), 148-152.
234. Limozin, L., & Sengupta, K. (2009). Quantitative reflection interference contrast microscopy (RICM) in soft matter and cell adhesion. ChemPhysChem, 10(16), 2752-2768.
235. Erath, J., Schmidt, S., & Fery, A. (2010). Characterization of adhesion phenomena and contact of surfaces by soft colloidal probe AFM. Soft Matter, 6(7), 1432-1437.
236. Sychev, D., Schubotz, S., Besford, Q. A., Fery, A., & Auernhammer, G. K. (2023). Critical analysis of adhesion work measurements from AFM-based techniques for soft contact. Journal of Colloid and Interface Science, 642, 216-226.
237. Daniel, D., Timonen, J. V., Li, R., Velling, S. J., & Aizenberg, J. (2017). Oleoplaning droplets on lubricated surfaces. Nature Physics, 13(10), 1020-1025.

238. De Ruiter, J., Lagraauw, R., Van Den Ende, D., & Mugele, F. (2015). Wettability-independent bouncing on flat surfaces mediated by thin air films. Nature physics, 11(1), 48-53.

239. Contreras-Naranjo, J. C., & Ugaz, V. M. (2013). A nanometre-scale resolution interference-based probe of interfacial phenomena between microscopic objects and surfaces. Nature Communications, 4(1), 1919.

240. Glover, J. D., & Pham, J. T. (2020). Capillary-driven indentation of a microparticle into a soft, oil-coated substrate. Soft Matter, 16(25), 5812-5818.

241. Koh, J. J., Pang, P., Chakraborty, S., Kong, J., Sng, A., Anukunwithaya, P., ... & He, C. (2023). Presence, origins and effect of stable surface hydration on regenerated cellulose for underwater oil-repellent membranes. Journal of colloid and interface science, 635, 197-207.

242. Huerre, A., Jullien, M. C., Theodoly, O., & Valignat, M. P. (2016). Absolute 3D reconstruction of thin films topography in microfluidic channels by interference reflection microscopy. Lab on a Chip, 16(5), 911-916.

243. Weber, I. (2003). Reflection interference contrast microscopy. In Methods in enzymology (Vol. 361, pp. 34-47). Academic Press.

244. Wang, B., & Facchetti, A. (2019). Mechanically flexible conductors for stretchable and wearable e‐skin and e‐textile devices. Advanced Materials, 31(28), 1901408.

245. Idumah, C. I. (2023). Design, fabrication, characterization and properties of metallic and conductive smart polymeric textiles for multifunctional applications. Nano-Structures & Nano-Objects, 35, 100982.

246. Cai, D., Neyer, A., Kuckuk, R., & Heise, H. M. (2010). Raman, mid-infrared, near-infrared and ultraviolet–visible spectroscopy of PDMS silicone rubber for characterization of polymer optical waveguide materials. Journal of Molecular Structure, 976(1-3), 274-281.

247. Jedrzejczak-Silicka, M., Trukawka, M., Piotrowska, K., & Mijowska, E. (2020). Few-Layered Hexagonal Boron Nitride: Functionalization, Nanocomposites, and

Physicochemical and Biological Properties. In Biochemical Toxicology-Heavy Metals and Nanomaterials. IntechOpen.

248. Rimai, D. S., DeMejo, L. P., & Bowen, R. C. (1989). Adhesion-induced deformations of polymeric substrates: Particle size dependence of the contact area. Journal of Applied Physics, 66(8), 3574-3578.

249. Karpitschka, S., Das, S., van Gorcum, M., Perrin, H., Andreotti, B., & Snoeijer, J. H. (2015). Droplets move over viscoelastic substrates by surfing a ridge. Nature communications, 6(1), 7891.

250. Hu, Y., Zhao, X., Vlassak, J. J., & Suo, Z. (2010). Using indentation to characterize the poroelasticity of gels. Applied Physics Letters, 96(12).

251. Gao, F., Zhao, X., Zhang, Z., An, L., Xu, L., Xun, X., ... & Wang, L. (2022). A stretching-insensitive, self-powered and wearable pressure sensor. Nano Energy, 91, 106695.

252. Kou, H., Zhang, L., Tan, Q., Liu, G., Lv, W., Lu, F., ... & Xiong, J. (2018). Wireless flexible pressure sensor based on micro-patterned Graphene/PDMS composite. Sensors and Actuators A: Physical, 277, 150-156.

253. Yang, J. C., Mun, J., Kwon, S. Y., Park, S., Bao, Z., & Park, S. (2019). Electronic skin: recent progress and future prospects for skin-attachable devices for health monitoring, robotics, and prosthetics. Advanced Materials, 31(48), 1904765.

254. Varshini, J. A., Sree, J. A., Dineshan, A., Anjali, T., Jayakumar, O. D., & Bharadwaj, A. (2021, November). Face mask detection and recognition using an IoT enabled PDMS-Ag e-skin sensor that works in contact and non-contact modes. In 2021 Fourth International Conference on Microelectronics, Signals & Systems (ICMSS) (pp. 1-4). IEEE.

255. Wang, W., Xiang, C., Zhu, Q., Zhong, W., Li, M., Yan, K., & Wang, D. (2018). Multistimulus responsive actuator with GO and carbon nanotube/PDMS bilayer structure for flexible and smart devices. ACS applied materials & interfaces, 10(32), 27215-27223.

256. Cai, S., Hu, Y., Zhao, X., & Suo, Z. (2010). Poroelasticity of a covalently crosslinked alginate hydrogel under compression. Journal of Applied Physics, 108(11).

257. Oyen, M. L. (2014). Mechanical characterisation of hydrogel materials. International Materials Reviews, 59(1), 44-59.
258. Bowden, N., Brittain, S., Evans, A. G., Hutchinson, J. W., & Whitesides, G. M. (1998). Spontaneous formation of ordered structures in thin films of metals supported on an elastomeric polymer. nature, 393(6681), 146-149.
259. Li, B., Cao, Y. P., Feng, X. Q., & Gao, H. (2012). Mechanics of morphological instabilities and surface wrinkling in soft materials: a review. Soft Matter, 8(21), 5728-5745.
260. Dai, H. H., & Liu, Y. (2014). Critical thickness ratio for buckled and wrinkled fruits and vegetables. Europhysics Letters, 108(4), 44003.
261. Cerda, E., & Mahadevan, L. (2003). Geometry and physics of wrinkling. Physical review letters, 90(7), 074302.
262. Tallinen, T., Chung, J. Y., Rousseau, F., Girard, N., Lefèvre, J., & Mahadevan, L. (2016). On the growth and form of cortical convolutions. Nature Physics, 12(6), 588-593.
263. Efimenko, K., Rackaitis, M., Manias, E., Vaziri, A., Mahadevan, L., & Genzer, J. (2005). Nested self-similar wrinkling patterns in skins. Nature materials, 4(4), 293-297.
264. Sáez, P., & Zöllner, A. M. (2017). Mechanics reveals the biological trigger in wrinkly fingers. Annals of biomedical engineering, 45(4), 1039-1047.
265. Goehring, L., Nakahara, A., Dutta, T., Kitsunezaki, S., & Tarafdar, S. (2015). Desiccation cracks and their patterns: Formation and Modelling in Science and Nature. John Wiley & Sons.
266. Yang, S., Khare, K., & Lin, P. C. (2010). Harnessing surface wrinkle patterns in soft matter. Advanced Functional Materials, 20(16), 2550-2564.
267. Hu, X., Liu, Z., & Zhang, Y. (2025). Three-Dimensionally Architected Tactile Electronic Skins. ACS nano, 19(15), 14523-14539.
268. Zhu, Y., Li, J., Ma, T., Gao, X., Li, K., Ma, X., & Jiang, X. (2025). Self‐Wrinkling‐Induced Mechanically Adaptive Patterned Surface of Photocuring Coating for Abrasion Resistance. Advanced Materials, 37(7), 2414352.

269. Hong, W., Zhao, X., & Suo, Z. (2009). Formation of creases on the surfaces of elastomers and gels. Applied Physics Letters, 95(11).
270. Ahmad, Z., Parias M. R, B., Barr, H., & Cabral, J. T. (2024). Thermal Conduction Suppresses Cracks in PDMS Wrinkling by Plasma Oxidation. Nano Letters, 25(2), 740-746.
271. Schäffer, E., Thurn-Albrecht, T., Russell, T. P., & Steiner, U. (2000). Electrically induced structure formation and pattern transfer. Nature, 403(6772), 874-877.
272. Li, F., Hou, H., Yin, J., & Jiang, X. (2018). Near-infrared light–responsive dynamic wrinkle patterns. Science Advances, 4(4), eaar5762.
273. Bai, C., Kang, J., & Wang, Y. Q. (2025). Light-induced wrinkling in annulus anisotropic liquid crystal elastomer films. Physical Review E, 111(1), 015421.
274. Kim, Y., Yuk, H., Zhao, R., Chester, S. A., & Zhao, X. (2018). Printing ferromagnetic domains for untethered fast-transforming soft materials. Nature, 558(7709), 274-279.
275. Kastania, A. S., Mouchtouris, S., Stai, E., Zeniou, A., Kokkoris, G., Constantoudis, V., ... & Tserepi, A. (2025). Plasma‐Induced Maskless Formation of Quasi‐Periodic Nanoripples on Polymeric Substrates. Advanced Engineering Materials, 27(7), 2402729.
276. Wang, Z., Li, S., & Shen, G. (2025). Advanced Sensory Hardware for Intelligent Eye‐Machine Interfacing: from Wearables to Bionics. Advanced Functional Materials, 2503519.
277. Li, S., Deng, B., Grinthal, A., Schneider-Yamamura, A., Kang, J., Martens, R. S., ... & Aizenberg, J. (2021). Liquid-induced topological transformations of cellular microstructures. Nature, 592(7854), 386-391.
278. Kim, D. W., Medvedev, G. A., Caruthers, J. M., Jo, J. Y., Won, Y. Y., & Kim, J. (2020). Enhancement of mechano-sensitivity for spiropyran-linked poly (dimethylsiloxane) via solvent swelling. Macromolecules, 53(18), 7954-7961.
279. Moreau, D., Chauvet, C., Etienne, F., Rannou, F. P., & Corté, L. (2016). Hydrogel films and coatings by swelling-induced gelation. Proceedings of the National Academy of Sciences, 113(47), 13295-13300.

280. Zheng, B. X., Chan, T. S., van Brummelen, E. H., & Snoeijer, J. H. (2025). Dynamics of Poro-viscoelastic Wetting with Large Swelling. arXiv preprint arXiv:2505.18968.
281. Cai, S., Chen, D., Suo, Z., & Hayward, R. C. (2012). Creasing instability of elastomer films. Soft Matter, 8(5), 1301-1304.
282. Ogieglo, W., van der Werf, H., Tempelman, K., Wormeester, H., Wessling, M., Nijmeijer, A., & Benes, N. E. (2013). n-Hexane induced swelling of thin PDMS films under non-equilibrium nanofiltration permeation conditions, resolved by spectroscopic ellipsometry. Journal of membrane science, 437, 313-323.
283. Reiter, G., Khanna, R., & Sharma, A. (2000). Enhanced instability in thin liquid films by improved compatibility. Physical review letters, 85(7), 1432.
284. Kopecz-Muller, C., Gaunand, C., Tran, Y., Labousse, M., Raphael, E., Salez, T., ... & Mcgraw, J. D. (2025). Swelling and evaporation determine surface morphology of grafted hydrogel thin films. Langmuir, 41(4), 2400-2410.
285. Curatolo, M., Nardinocchi, P., Puntel, E., & Teresi, L. (2017). Transient instabilities in swelling dynamics. arXiv:1704.08201.
286. Dervaux, J., & Amar, M. B. (2012). Mechanical instabilities of gels. Annu. Rev. Condens. Matter Phys., 3(1), 311-332.
287. Kuo, A. C. (1999). Poly (dimethylsiloxane). Polymer data handbook, 1999, 411-435.
288. Schaefer, C., van der Schoot, P. P. A. M., & Michels, J. J. (2015). Structuring of polymer solutions upon solvent evaporation. Physical Review E, 91(2), 022602.
289. Cai, S., Breid, D., Crosby, A. J., Suo, Z., & Hutchinson, J. W. (2011). Periodic patterns and energy states of buckled films on compliant substrates. Journal of the Mechanics and Physics of Solids, 59(5), 1094-1114.
290. Li, B., Jia, F., Cao, Y. P., Feng, X. Q., & Gao, H. (2011). Surface wrinkling patterns on a core-shell soft sphere. Physical review letters, 106(23), 234301.
291. Cerda, E., & Mahadevan, L. (2003). Geometry and physics of wrinkling. Physical review letters, 90(7), 074302.

292. Holmes, D. P., & Crosby, A. J. (2010). Draping films: A wrinkle to fold transition. Physical review letters, 105(3), 038303.
293. Jin, L., Cai, S., & Suo, Z. (2011). Creases in soft tissues generated by growth. Europhysics Letters, 95(6), 64002.
294. Sahoo, S., & Mukherjee, R. (2023). Pattern formation in evaporative drying of a polymer solution droplet over a soft swellable substrate. Langmuir, 39(27), 9526-9537.
295. Chen, Y., Askounis, A., Koutsos, V., Valluri, P., Takata, Y., Wilson, S. K., & Sefiane, K. (2019). On the effect of substrate viscoelasticity on the evaporation kinetics and deposition patterns of nanosuspension drops. Langmuir, 36(1), 204-213.
296. Pula, P., Leniart, A., & Majewski, P. W. (2022). Solvent-assisted self-assembly of block copolymer thin films. Soft Matter, 18(21), 4042-4066.
297. Nguyen, D. H., Bazaka, O., Bazaka, K., Crawford, R. J., & Ivanova, E. P. (2020). Three-dimensional hierarchical wrinkles on polymer films: From chaotic to ordered antimicrobial topographies. Trends in Biotechnology, 38(5), 558-571.
298. Ma, L. L., Li, C. Y., Pan, J. T., Ji, Y. E., Jiang, C., Zheng, R., ... & Lu, Y. Q. (2022). Self-assembled liquid crystal architectures for soft matter photonics. Light: Science & Applications, 11(1), 270.
299. Chen, D., McKinley, G. H., & Cohen, R. E. (2016). Spontaneous wettability patterning via creasing instability. Proceedings of the National Academy of Sciences, 113(29), 8087-8092.
300. Tan, Y., Hu, B., Song, J., Chu, Z., & Wu, W. (2020). Bioinspired multiscale wrinkling patterns on curved substrates: An overview. Nano-Micro Letters, 12(1), 101.
301. Yu, X., Mahajan, B. K., Shou, W., & Pan, H. (2016). Materials, mechanics, and patterning techniques for elastomer-based stretchable conductors. Micromachines, 8(1), 7.
302. Kahn, B. E. (2015). Patterning processes for flexible electronics. Proceedings of the IEEE, 103(4), 497-517.
303. Hou, H., Yin, J., & Jiang, X. (2019). Smart patterned surface with dynamic wrinkles. Accounts of chemical research, 52(4), 1025-1035.

304. Sarabia-Vallejos, M. A., Cerda-Iglesias, F. E., Pérez-Monje, D. A., Acuña-Ruiz, N. F., Terraza-Inostroza, C. A., Rodríguez-Hernández, J., & González-Henríquez, C. M. (2023). Smart polymer surfaces with complex wrinkled patterns: Reversible, non-planar, gradient, and hierarchical structures. Polymers, 15(3), 612.

305. Rayleigh, L. (1880). Investigations in optics, with special reference to the spectroscope. Monthly Notices of the Royal Astronomical Society, Vol. 40, p. 254, 40, 254.

306. Born, M., & Wolf, E. (2013). Principles of optics: electromagnetic theory of propagation, interference and diffraction of light. Elsevier.

307. Conrady, A. E., & Kingsla ke, R. (1957). Applied optics and optical design. Dover Publications.

308. Glover, J. D., McLaughlin, C. E., McFarland, M. K., & Pham, J. T. (2020). Extracting uncrosslinked material from low modulus sylgard 184 and the effect on mechanical properties. Journal of Polymer Science, 58(2), 343-351.

309. Zhang, D., Ding, G., & Chen, C. (1998). Theoretical Analysis of Guided Mode and Effective Refractive Index at 1.53\;\mum in Ti: LiNbO3 Strip Waveguides. Journal of lightwave technology, 16(3), 459.

310. Ho, K. P., Kahn, J. M., Kaminow, I. P., Li, T., & Willner, A. E. (2013). Mode coupling and its impact on spatially multiplexed systems. Optical Fiber Telecommunications VI, 17, 1386-1392.

311. Kihm, K. D. (2011). Near-field characterization of micro/nano-scaled fluid flows. Springer Science & Business Media.

312. Rastogi, P. K. (Ed.). (2013). Holographic interferometry: principles and methods (Vol. 68). Springer.

Appendix A

Supporting Information for Chapter 3

A3.1 The thickness of the PDMS film measurement:

The thickness of the soft substrate was determined by a Field Emission Scanning Electron Microscopy (Zeiss UltraPlus FESEMs). After preparation, the soft substrate was cut into 8 mm × 10 mm (width × length) pieces and mounted on the stub aligned at an angle of 90° with a conductive tape, with the PDMS layer facing outward and the glass slide in contact with the conductive tape, for SEM measurements. The corresponding cross-sectional SEM image is shown in Figure A3-1. To assess the spatial uniformity, the PDMS film thickness was measured at three different positions in each of three independent images. From these measurements, the average thickness of the PDMS layer was determined to be 35.43 ± 0.31 μm.

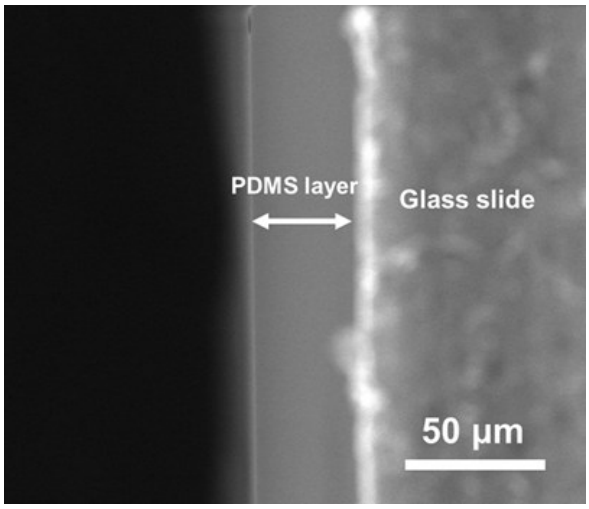


Figure A3-1 The cross sectional SEM image of the PDMS layer coated on a glass slide.

A3.2 The transmittance and reflectance of the glass slide and PDMS coated glass slide

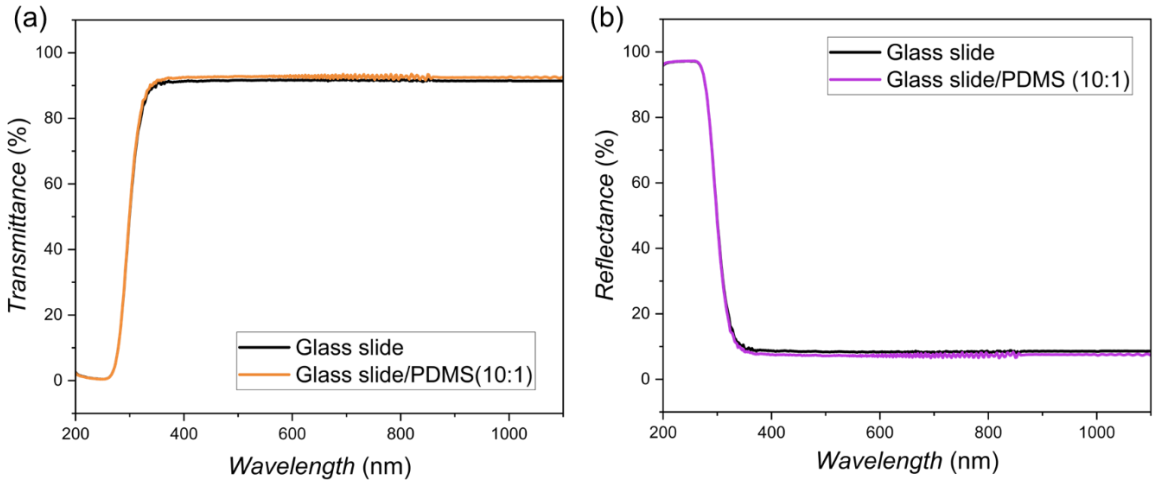


Figure A3-2 (a) Plots of transmittance using UV/Vis spectroscopy measurements for glass slide and PDMS coated glass slide. (b) Plots of reflectance using UV/Vis spectroscopy measurements for glass slide and PDMS coated glass slide.

A3.3: The calculated refractive indices of the glass slide and PDMS thin film

From transmittance and reflectance measurements, the refractive indices of the glass slide and the PDMS thin film were determined. As shown in Figure A3-3(a), the total transmittance of the glass slide system can be expressed as [203],

$$T = T_{12}T_{21}/(1 - R_{21}^2) \quad \text{(A3-1)}$$

where, the reflectance between medium 1 and medium 2, $R_{12} = R_{21} = ((n_2 - n_1)/(n_2 + n_1))^2$ and the transmittance between medium 1 and medium 2, $T_{12} = T_{21} = (4n_1n_2)/(n_1 + n_2)^2$. n_1 and n_2 are the refractive indices of medium 1 and medium 2, respectively. In this system, $n_1 = 1$, the transmittance $T = 91.7\%$. Accordingly, the refractive index of the glass slide is obtained as $n_2 = T^{-1} + \sqrt{T^{-2} - 1} = 1.53$. Similarly, the total transmittance of the PDMS coated glass slide system (Figure A3-3(b)) can be expressed as [203],

$$T = T_{12}T_{23}T_{31}/((1 - R_{23}^2)(1 - R_{31}^2)) \quad \text{(A3-2)}$$

where, the reflectance between medium 2 and medium 3, $R_{23} = ((n_2 - n_3)/(n_2 + n_3))^2$, the reflectance between medium 3 and medium 1, $R_{31} = ((n_3 - n_1)/(n_3 + n_1))^2$, $T_{23} = (4n_2n_3)/(n_2 + n_3)^2$, and the transmittance between medium 3 and medium 1, $T_{31} = (4n_3n_1)/(n_3 + n_1)^2$. In this system, $n_1 = 1$, $n_2 = 1.53$, and the transmittance $T = 92.3\%$. The refractive index of PDMS was determined to be 1.44.

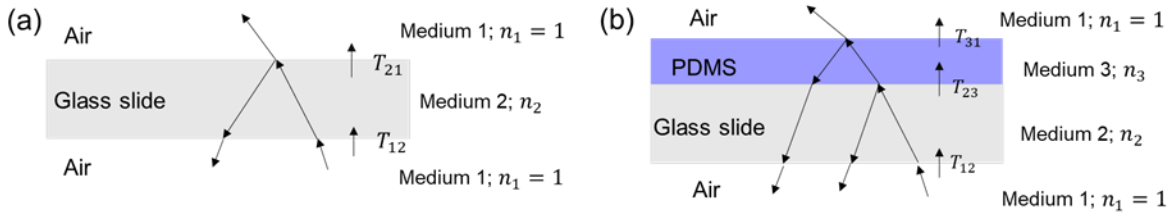


Figure A3-3 (a) Schematic of light transmitting through a glass slide. (b) Schematic of light transmitting through the PDMS coated glass slide. n_1, n_2, and n_3 are the refractive indices of air, glass, and PDMS, respectively.

A3.4 The Raman spectra of glass and P_{10} (PDMS 10:1) at different laser powers

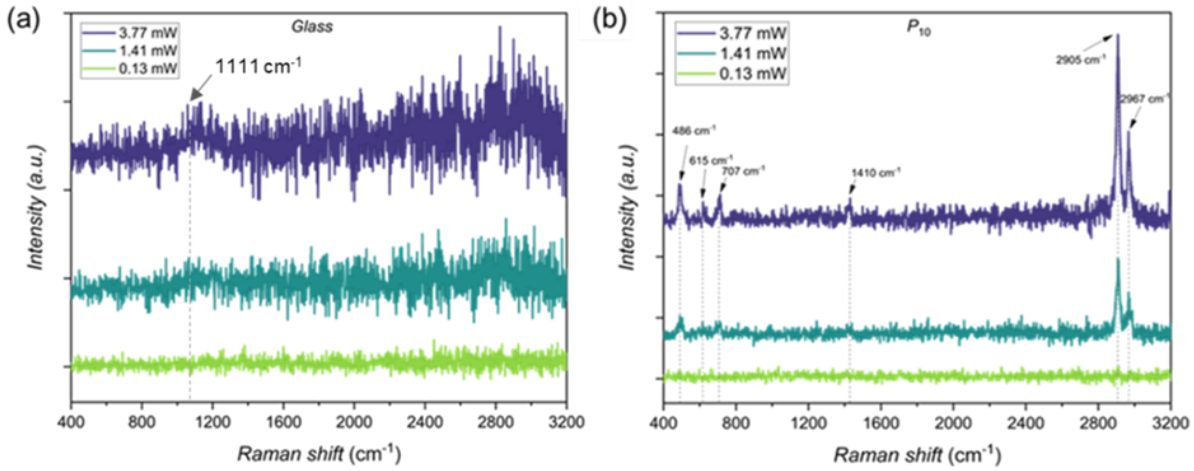


Figure A3-4 The Raman spectra of (a) glass and (b) P_{10} (PDMS 10:1) at laser powers of 0.13 mW, 1.41 mW, and 3.77 mW between 400 cm^{-1} to 3200 cm^{-1} Raman shift.

A3.5: Laser spot diameter of conventional Raman spectroscopy

Based on the laws of optics, the minimum achievable laser spot size (diameter, *D*) is diffraction-limited and is determined by the wavelength of the laser (λ) and the numerical aperture of the microscope objective lens (NA) [72]:

$$D = 1.22\lambda/\mathrm{NA} \quad \text{(A3-3)}$$

In our experiments, the laser wavelength λ is 638 nm, NA is 0.5 and thus, the corresponding laser spot diameter *D* is 1.56 μm.

A3.6: Lateral resolution of Raman spectroscopy

The lateral resolution in *x*- and *y*- axis ($\Delta x, \Delta y$) of Raman spectroscopy is defined as the minimum distance between two points that can be clearly distinguished on a microscope image, i.e. half the width of the Airy disk [135]. Based on the Rayleigh criterion [305],

$$\Delta x, \Delta y = 0.61\lambda/\mathrm{NA} \quad \text{(A3-4)}$$

where λ is the laser wavelength, NA is the numerical aperture of the objective lens. In our experiments, the laser wavelength is 638 nm, NA is 0.5 and the corresponding lateral resolution in *x*- and *y*- axis ($\Delta x, \Delta y$) is 0.78 μm.

A3.7: In-depth resolution of Raman spectroscopy

The in-depth resolution (Δz) of Raman spectroscopy is defined as half the width of the axial intensity profile and can be approximated by the following expression [135,306,307]

$$\Delta z = \lambda/(n_0 \sin\theta)^2 \quad \text{(A3-5)}$$

where λ is the laser wavelength and n_0 is the refractive index of the medium separating the objective from the target substrate (air, in our case). In our experiments, the laser wavelength is 638 nm, $n_0 \sin\theta = \mathrm{NA} = 0.5$. Thus, $\Delta z(through\ air, n_0 = 1) = \lambda/(\mathrm{NA})^2 = 2.55\ \mu m$.

A3.8: The penetration depth of laser in air, glass and PDMS

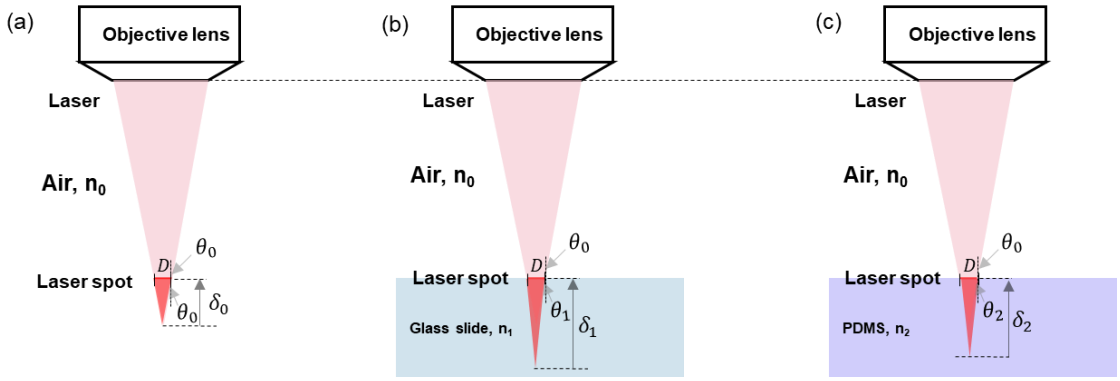


Figure A3-5 Schematic of the laser spot focused on the interface of different materials (a) air, (b) glass, and (c) PDMS film. n_0, n_1, and n_2 are the refractive index of air (1.0), glass (1.5) and PDMS (1.4), respectively and $n_0 < n_2 < n_1$. θ_0, θ_1, and θ_2 are the maximum angle with respect to the optical axis in the observation medium (here is air) and in the analyzed material: glass and PDMS, respectively and $\theta_0 > \theta_2 > \theta_1$ (see text). δ_0, δ_1, and δ_2 are the real penetration depth of laser in air, glass and PDMS, respectively.

During Raman mapping measurement, the optical path of the laser first goes through the air medium and then focuses on the target substrate, where the diameter of the laser spot is D. The volume of light used for Raman spectroscopy depends on the size of the pin hole, the objective lens and the laser wavelength. In our experiments, the laser wavelength (~638 nm), pinhole (~300 μm) and the objective lens (50x) used are constant. During measurements, the penetration depth of laser beam depends on the refractive index of the target substrates. In our system, the surrounding medium is air ($n_0 = 1$) and the target substrates are glass ($n_1 = 1.53$) and PDMS ($n_2 = 1.44$) creating the condition $n_0 < n_2 < n_1$. Therefore, we set the penetration depth in air as the apparent depth δ_0 and illustrate the schematic of the penetration depth in air

during Raman mapping in Figure A3-5(a). According to Snell's law, we know that $n_0 \sin\theta_0 = n_1 \sin\theta_1 = n_2 \sin\theta_2$. Since $n_0 < n_2 < n_1$, we can infer that from Snell's law that $\theta_0 > \theta_2 > \theta_1$. The schematics of the penetration depth in glass and PDMS during Raman mapping are depicted in Figure A3-5(b) and (c), respectively. The penetration depths of analysis in glass and PDMS can be expressed as:

$$\delta_1 = (\tan\theta_0 / \tan\theta_1)\delta_0 \quad \text{(A3-6)}$$

$$\delta_2 = (\tan\theta_0 / \tan\theta_2)\delta_0 \quad \text{(A3-7)}$$

Since, $\theta_0 > \theta_2 > \theta_1$, and tangent is an increasing function its principal interval (-π/2, π/2), therefore, $\tan\theta_0 > \tan\theta_2 > \tan\theta_1$. Then, we can conclude $\delta_1 > \delta_2 > \delta_0$.

A3.9: Comparison with Hertz contact theory and Winkler model

Both Hertz contact theory and the Winkler foundation model describe elastic deformation under external loading but apply to distinct scenarios. Several studies have examined the transition in contact response from Hertz theory (for elastic half-spaces) to the Winkler model (for thin elastic layers on a rigid substrate) as the layer thickness varies, providing mathematical formulations for the transition between these regimes [37–40]. To elucidate this transition, we consider an elastic layer of finite thickness *H*, subjected to indentation by a rigid spherical indenter (Hertzian configuration), with a rigid substrate beneath (Winkler-like boundary condition).

Hertz contact theory describes the deformation of semi-infinite elastic bodies, where the stress and displacement fields are governed by elastic half-space theory:

$$\delta = \left(9\mathrm{F}^2/16RE^{*2}\right)^{\frac{1}{3}} \quad \text{(A3-8)}$$

The contact radius a, and the applied force F satisfy the relationship:

$$a = (3\mathrm{FR}/4E^*)^{\frac{1}{3}} \quad \text{(A3-9)}$$

where F is the applied force, $R = (1/R_1 + 1/R_2)^{-1}$ is the reduced radius, R_1 and R_2 are the radii of the glass probe (~2600 μm) and the soft substrate (~ +∞), respectively. $E^* =$

$[(1-\vartheta_1^2)/E_1 + (1-\vartheta_2^2)/E_2]^{-1}$ is the effective Young's modulus where E_1 and E_2 are the Young's moduli of the glass probe and the soft substrate, respectively. Here, ϑ_1 and ϑ_2 are the Poisson's ratios of the glass probe and the soft substrate, respectively, and δ is the indentation depth.

The Winkler model assumes that 1) the substrate consists of independent springs, meaning deformation at one location does not influence neighboring regions. 2) the deformation occurs only in the normal direction, with no lateral interactions. 3)the foundation stiffness is characterized by a modulus k (unit: N/m^3), which relates the local pressure $q(x)$ to displacement $w(x)$ via:

$$q(x) = k\omega(x) \tag{A3-10}$$

For a thin elastic layer of finite thickness H, the effective foundation stiffness is approximated by:

$$k \approx 2G(1-\vartheta)/H(1-2\vartheta) \tag{A3-11}$$

where E and ϑ are Young's modulus and the Poisson's ratio of the elastic layer, respectively. Such that the indentation force and displacement exhibit a linear relationship:

$$F \approx kS\delta \tag{A3-12}$$

where S is the contact area. The transition from Hertzian to Winkler-like behavior is governed by the dimensionless thickness parameter λ:

$$\lambda = H/a \tag{A3-12}$$

where a is the contact radius. The model transition occurs as follows: For $\lambda \gg 1$ (thick elastic layers, small contact radius): the substrate has negligible influence, and Hertzian contact mechanics applies. For $\lambda \ll 1$ (thin elastic layers, large contact radius): the substrate imposes a dominant influence, and a Winkler-type foundation better describes the response [39,40].

In our case, the thickness (H) of P_{10} film is 35.43 ± 0.31 μm and the contact radius obtained from optical imaging is a_{exp}= 127.6 ± 3.2 μm, therefore, $\lambda = H/a$ = 35.43/127.6 = 0.28 < 1, which means the Winkler-type foundation may be suitable for our system.

Consequently, we calculated the indentation depth based on the Winkler theory, assuming near incompressibility of PDMS and using two test cases $\vartheta = 0.45$ and $\vartheta = 0.48$ [140]. In our system, the applied force F = 5.12 mN, the thickness of the PDMS layer, H = 35.43 μm, and S = $\pi a_{exp}^2 = 5.1\times10^{-8}$ m^2. Further, since $G = E/2(1+\vartheta)$ and E = 1.62 MPa, we calculate G = 0.66 MPa and G = 0.65 MPa for $\vartheta = 0.45$ and $\vartheta = 0.48$, respectively. Consequently, using Eq. (A3-12), we calculate $k(\vartheta = 0.45) = 2.0 \times 10^{11}$ N/m^3 and $k(\vartheta = 0.48) = 4.8 \times 10^{11}$ N/m^3. Using these values in Eq. (A3-13), we estimate $\delta = F/kS = \frac{5.12\times0.001}{2\times10^{11}\times3.14\times(127.6\times10^{-6})^2} =$ 0.5 μm for $\vartheta = 0.45$ and $\delta = F/kS = \frac{5.12\times0.001}{4.8\times10^{11}\times3.14\times(127.6\times10^{-6})^2} = 0.2$ μm for $\vartheta = 0.48$.

Appendix B

Supporting Information for Chapter 4

B4.1: Calculation of Young's modulus from UMT experiments

The tensile stress σ and strain ε of the soft PDMS substrates were determined using $\sigma = F/A_0$ and $\varepsilon = \Delta L/L_0$, where F is the tensile force and L_0 is the length of the substrates. Since PDMS is an elastomer, the true stress and true strain can be expressed as $\sigma^* = \sigma(1+\varepsilon)$ and $\varepsilon^* = \ln(1+\varepsilon)$ [171]. Consequently, the Young's modulus E can be obtained from Hooke's law in the low strain limit using $E = \sigma^*/\varepsilon^*$ [52,206,308], as shown in Figure B4-1. Linear regression was performed within the initial strain regime to minimize error, ensuring that the modulus was extracted from the elastic response.

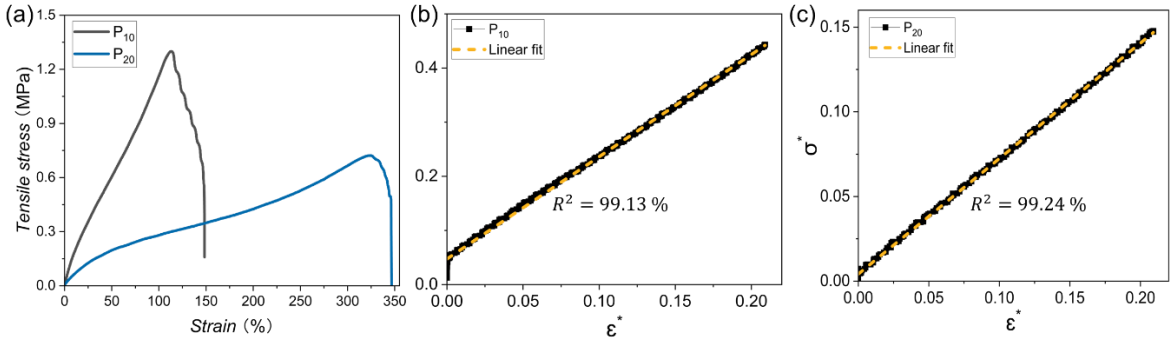


Figure B4-1 (a) Tensile stress-strain curves for PDMS 10:1 (P_{10}) and 20:1 (P_{20}) substrates. (b, c) True tensile stress versus true strain for P_{10} and P_{20}, respectively, along with the fitted slopes corresponding to the Young's modulus (E (P_{10}): 1.88 MPa; E (P_{20}): 0.68 MPa). The linear regressions were performed in the low-strain regime, and the fitted slopes were confirmed to lie within the 95% confidence interval.

B4.2: Calibration of the sputter coating rate

For calibration, a clean glass slide was placed horizontally on the substrate holder inside the vacuum sputtering chamber with the Ag target positioned above it. The chamber was

evacuated to a base pressure of 0.5 - 100 mTorr to remove residual gases, and high-purity argon gas was introduced as the working medium. Upon applying a voltage (target as the cathode and the substrate as the anode), the argon atoms were ionized to generate a plasma. Energetic Ar+ ions bombarded the target surface, ejecting Ag atoms that condensed onto the glass slide to form a uniform thin-film coating.

To verify the sputtering rate, part of the glass slide surface was masked with another glass slide during deposition. After sputtering, the mask was removed, and the step height of the Ag film was measured by atomic force microscopy (Pacific Nanotechnology AFM Nano-R) and confirmed with a stylus profilometer (Veeco Dektak 8) (Figure B4-2(a) and (b)). Typically, the thickness of Ag deposited on the glass slide for 120s was observed to be 18 nm.

Attempts to apply the same method to measure the thickness of the Ag coating on PDMS surface, the masking procedure resulted in surface wrinkles, making direct thickness measurements unreliable (Figure B4-2(c) and (d)).

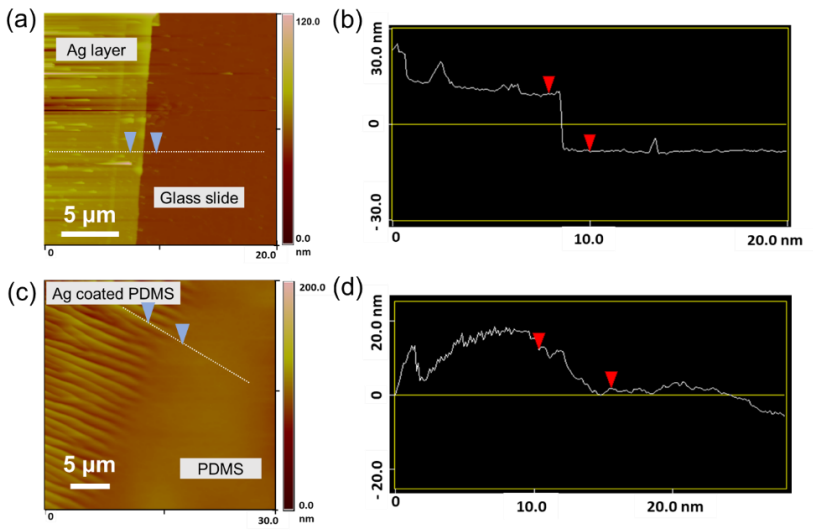


Figure B4-2 (a) and (c) Atomic force microscopy (AFM) scans of sputtered Ag layer on bare and PDMS 10:1 coated glass slides. (b) and (d) Plot of Ag layer thickness corresponding to the micrographs shown in (a) and (c) along the marked lines.

B4.3: Surface Morphology of Bare and Ag-Coated PDMS Substrate

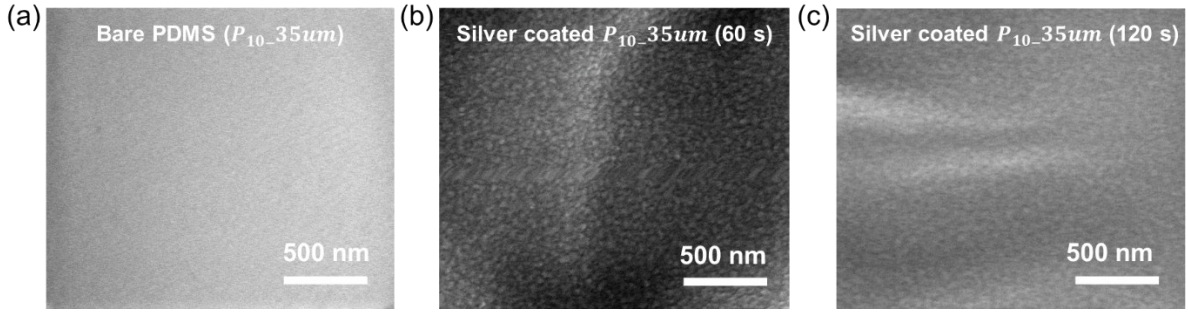


Figure B4-3 SEM micrographs of (a) bare PDMS (10:1), (b) PDMS (10:1) coated with Ag for 60 s, and (c) PDMS (10:1) coated with Ag for 120 s.

B4.4: Uncertainty in glass sphere radius and refractive index for RICM height estimation

For a sphere (with radius of R) - plane geometry, the gap height at a lateral distance r can be approximated as:

$$h(r) = r^2/2R \tag{B4-1}$$

The error propagation gives:

$$\partial h/\partial R = -r^2/2R^2 = -h/R \tag{B4-2}$$

The relative error is $\Delta h/h \approx \Delta R/R$. For the glass sphere used in this work (R_0 = 2600 μm), the typical manufacturing tolerance is ± 5 μm in diameter ($\Delta R \approx 2.5$ μm in radius). This corresponds to a relative uncertainty of $\frac{\Delta R}{R_0} \approx 0.096$ %. Taking a representative height scale around $h \approx 8$ μm (calculated based on: $R_0 - \sqrt{{R_0}^2 - {r_0}^2} = 7.7$ μm, the perfect fitting range $r_0 \approx 200$ μm (see B4.6)), the propagated uncertainty is $\Delta h \approx 0.008\ \mu m$, which is below the pixel size and can be negligible. Hence, the glass sphere can be reasonably assumed to be perfectly spherical.

To assess the impact of the glass sphere refractive index uncertainty on RICM height reconstruction, we apply a similar error-propagation analysis. For normal incidence, the

reconstructed height depends inversely on the refractive index, giving $\Delta h \approx (h/n)\Delta n$. Using the same representative height scale $h \approx 8$ μm and $n = 1.47$, the refractive index uncertainty as $\Delta n = 0.03$ (1.47 vs. 1.50) results in $\Delta h \approx 0.16$ μm. This is far smaller than the micrometer-scale feature of interest in the experiments.

Therefore, both the glass sphere radius tolerance and the uncertainty in refractive index introduce negligible errors in RICM height estimation.

B4.5: Reconstructed profiles based on different expressions of n_{eff}

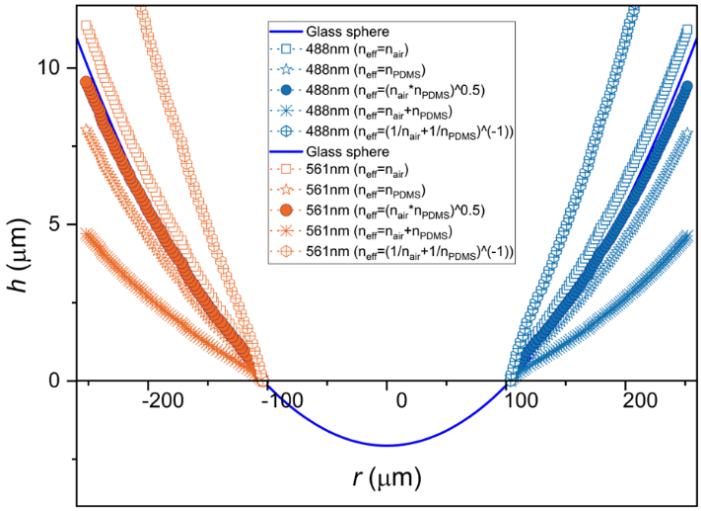


Figure B4-4 Plot of glass sphere profiles, i.e., variation of h over r on PDMS 10:1 substrates corresponding to interference signature using various expressions of n_{eff} in Eq. 4-2 (see main text): $n_{\text{eff}} = n_{\text{air}}$ (squares), $n_{\text{eff}} = n_{\text{PDMS}}$ (pentagram), $n_{\text{eff}} = \sqrt{n_{\text{air}} n_{\text{PDMS}}}$ (circles), $n_{\text{eff}} = n_{\text{air}} + n_{\text{PDMS}}$ (cross), $n_{\text{eff}} = (1/n_{\text{air}} + 1/n_{\text{PDMS}})^{-1}$ (crossed circles). The solid line shows the geometrical glass profile.

B4.6: Comment on effective refractive index

In our extraction of glass sphere profiles on Ag/PDMS substrates, we have used an effective refractive index accounting for refractive indices of both PDMS (Ag/PDMS) and air mediums. The concept of effective refractive index (n_{eff}) is often used in optical fiber field to

define the guided model through the fiber core and clad [309,310]. The n_{eff} must follow below equation:

$$\min[n_1, n_2] \leq n_{\text{eff}} \leq \max[n_1, n_2] \quad \text{(B4-3)}$$

The single mode structure of the optical fiber is made up of two kinds of materials: core and clad with different refractive index of n_1 and n_2. In our system, the light also goes through two types of mediums: PDMS (or Ag/PDMS) and air. We observe that our proposed effective refractive index $n_{\text{eff}} = \sqrt{n_{\text{air}} n_{\text{Ag/PDMS}}}$ in glass-Ag/PDMS system meets the condition of Eq. (B4-3).

B4.7: Data processing procedure for extracting effective refractive index from DW-RICM measurements

As described in Section 4.2.3 during confocal RICM measurements, the Z-stack multidimensional acquisition function was employed to scan from the upper interface of the glass slide to a height of approximately 44 μm above the free surface of the PDMS coating. 80 slices per sample per experimental run is obtained, which is adequate to identify the interference planes(s) of interest. The procedure for processing DW-RICM images, extracting interference fringe profiles, and subsequently fitting refractive indices is described in the following steps:

Step 1: **Selection of analysis region**. The scanned image file was opened in the DW-RICM software (ZEISS ZEN 2.6 lite). A line was drawn across the center of the contact area to extract a one-dimensional fringe intensity profile. The line was positioned such that the interference fringes were symmetrically distributed on both sides of the contact region. Areas containing impurity particles or surface defects were deliberately avoided to minimize artifacts.

Step 2: **Identification of the interference planes(s) of interest**. The focal plane of interest was determined by inspecting the variation of fringe intensity with respect to the z-axis position. Typically, both image clarity and overall fringe intensity increased with

increasing z. At a critical z position, the image reached the maximum sharpness and contrast, and the overall intensity of interference fringes attained its maximum. This position was considered the focal plane of interest. Beyond this plane, further increase in z-axis position caused the contact edge to brighten in sharply, while the location of the maximum fringe intensity shifted laterally outward .

Step 3: **Extraction of fringe intensity and images**. After identifying the focal plane, the interference fringe intensity profile along the selected line was extracted using the DW-RICM software, and the corresponding image at that position was saved. To ensure the accuracy of the focal plane determination, fringe patterns within a ±5 μm range around the focal plane along the z-axis were typically included for analysis.

Step 4: **Reconstruction of the glass sphere profile**. From the extracted images, the average contact radius *a* was determined, and the center of the contact area was set as the origin *O*(0,0). The real geometrical profile of the glass sphere (with radius R_0 = 2600 μm) was calculated according to:

$$h = \sqrt{2600^2 - r^2} - \sqrt{2600^2 - a^2} \tag{B4-4}$$

where *r* is the radial coordinate.

Step 5: **Fringes normalization and refractive index extraction**. The raw intensity *I*(a, u) together with the positional information was extracted. The fringe intensity was normalized using the relation:

$$I_0 = (I - I_{min})/(I_{max} - I_{min}) \tag{B4-5}$$

where I_0 is the normalized intensity of the fringes, I is the measured intensity, I_{max} is the maximum intensity of a particular distribution, I_{min} is the minimum intensity of a particular distribution. Subsequently, based on the contact radius and origin position, the *r*-coordinates corresponding to the maxima and minima of the normalized fringes were identified, and the total number of data points for each set of maxima and minima was recorded. We introduced the effective refractive index $n_{eff} = \sqrt{n_{air} n_{PDMS,\ Ag/Au-PDMS}}$. These data were then fitted to the theoretical relation:

$$\Delta h_{g,r} = \mathrm{m}\lambda/4\sqrt{n_{air} n_{PDMS,\ Ag/Au-PDMS}} \quad \text{(B4-6)}$$

where $\Delta h_{g,r}$ is the reconstructed profile based on the interference fringes, m is the fringes order, and λ is the illumination wavelength (488 nm and 561 nm). By fitting the profile of $\Delta h_{g,r}$ with the geometric profile of the glass sphere h, the refractive indices of PDMS (n_{PDMS}) and metal-polymer bilayers ($n_{Ag/PDMS}$, $n_{Au/PDMS}$) were obtained.

During this fitting process, we first observed that the interference fringe intensity generally increased with radial distance *r*, then decreased beyond a certain point, and became nearly constant around $r \approx 200$ μm. This behavior suggests that $r \approx 200$ μm represents a transition region in the optical response. Consistently, for radial distances $r \leq 200$ μm, all of the reconstructed profiles based on eq. (B4-7) were closely matched with the true profile of the glass probe. However, for $r > 200$ μm, slight deviations were observed (Figures 4-4(b) and (d), 4-6(c), and 4-8(b)), with the reconstructed profiles fitted with effective refractive index n_{eff} tending to underestimate the true probe profile. This deviation can be attributed to the increasing slope of the spherical curvature at larger *r*, which leads to an increase in the effective air gap thickness in the optical path. Therefore, a reliable fitting range can be identified as $r_0 \approx 200$ μm, within which the RICM fringe-based reconstruction matches the geometric profile well. Since our analysis region is confined to relatively small areas, we approximate the glass slide / PDMS (or Ag- /Au- coated PDMS) /glass sphere system as three parallel layers. Nevertheless, the limitations of this approximation should be acknowledged when extending to larger r, where curvature effects become non-negligible.

B4.8: Comparison of Hertz and JKR Predictions for P_{10} and P_{20}

Hertzian prediction: in our experiment, the glass sphere contacts with the soft substrates (P_{10} and P_{20}, respectively). The weight of the glass sphere applied to the force ($F = 1.24$ mN), and the Hertzian contact radius a_H is

$$a_H = (3\mathrm{FR}^*/4E^*)^{\frac{1}{3}} \quad \text{(B4-7)}$$

where the reduced radius $R^* = (1/R_1 + 1/R_2)^{-1}$, $R_1$and R_2 are the radii of the glass probe (~2600 μm) and the soft substrates (~+∞), respectively; the effective Young's modulus $E^* = [(1-\vartheta_1^2)/E_1 + (1-\vartheta_2^2)/E_2]^{-1}$ where $E_1$and E_2 are the Young's moduli of the glass probe (64 MPa) and the soft substrates (P_{10}:1.58 MPa; P_{20}:1.43 MPa), and ϑ_1 and ϑ_2 are their Poisson's ratios (both ~ 0.5). Based on these parameters, the Hertzian predictions are for P_{10}, a_H = 104.7 μm and for P_{20}, a_H = 108.2 μm.

The JKR contact radius is given by:

$$a_{JKR} = \left[3R^*\left(F + 3\pi w R^* + \sqrt{6\pi w R^* F + (3\pi w R^*)^2}\right)/4E^*\right]^{\frac{1}{3}} \quad \text{(B4-8)}$$

where w is the is the work of adhesion. According to Yu *et al.* (2015) [206], the measured values of w: for P_{10} with glass lens, w = 64.6 ± 3.2 mJ/m^2 and for P_{20} with glass lens, w = 87.8 ± 4.3 mJ/m^2. Based on these parameters, the JKR predictions are for P_{10}, a_{JKR} = 170.5 μm and for P_{20}, a_{JKR} = 188.5 μm.

The DMT contact radius is given by:

$$a_{DMT} = [3R^*(F + 4\pi w R^*)/4E^*]^{\frac{1}{3}} \quad \text{(B4-9)}$$

where w is the is the work of adhesion. Based on above mentioned parameters, the DMT predictions are for P_{10}, a_{MDT} = 145.8 μm and for P_{20}, a_{DMT} = 161.4 μm. Both are far larger than the experimental results (P_{10}: a_{exp} = 103.7 μm; P_{20}: a_{exp} = 106.7 μm). Thus, Hertz theory provides a more appropriate description for our PDMS-glass contact system, as the effective adhesion is negligible under the present conditions.

B4.9: Calculation of refractive index from UV/VIS spectroscopy measurements

From Transmittance and Reflectance measurements, we can calculate the refractive index of pristine PDMS substrates as well as Ag coated PDMS substrates. As shown in Figure B4-10, the total transmittance of the system can be expressed as,

$$T = T_{12}T_{23}T_{31}/(1-R_{23}^2)(1-R_{31}^2) \quad \text{(B4-10)}$$

where, the reflectance between medium 2 and medium 3, $R_{23} = ((n_2 - n_3)/(n_2 + n_3))^2$, the reflectance between medium 3 and medium 1, $R_{31} = ((n_3 - n_1)/(n_3 + n_1))^2$, the transmittance between medium 2 and medium 3, $T_{23} = 4n_2n_3/(n_2 + n_3)^2$, and the transmittance between medium 3 and medium 1, $T_{31} = 4n_3n_1/(n_3 + n_1)^2$. Consequently, using known values of the transmittance, reflectance, and the refractive indices of n_1 and n_2, the refractive index n_3 can be calculated.

B4.10: Reconstructed profiles of glass spheres on P_{10} (35 µm) and P_{20} (35 µm) under water

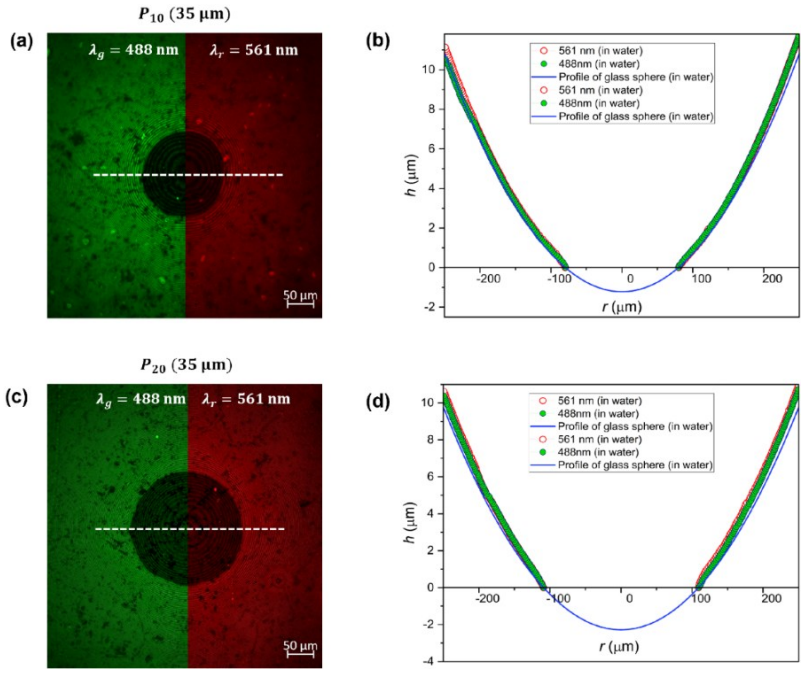


Figure B4-5 (a) and (c) Interference signatures of glass spheres on pristine, thin (35 µm) PDMS 10:1 and 20:1 substrates submerged under DI water. (b) and (d) Plots of the glass sphere profiles corresponding to the interference signatures shown in (a) and (c). The symbols represent the height extracted using $\Delta h_{g,r} = m\lambda_{g,r}/4\sqrt{n_{water}n_{PDMS}}$ and the solid lines represent the theoretical glass profile, i.e., $h = \sqrt{2600^2 - a^2} - \sqrt{2600^2 - r^2}$. Here, a is the contact radius.

B4.11: The refractive index of bare Ag

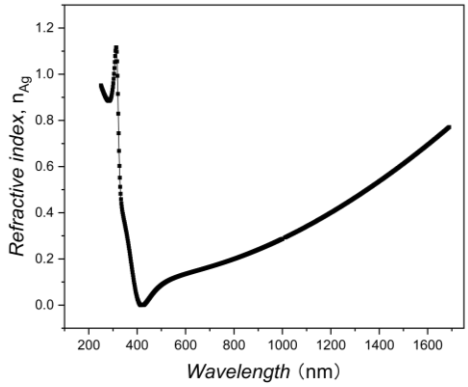


Figure B4-6 Plot of refractive index measurement of bare Ag.

B4.12: Reconstructed profiles of glass spheres on P_{10} (35 µm)-Ag(10s) and P_{10} (1 mm)-Ag(10s)

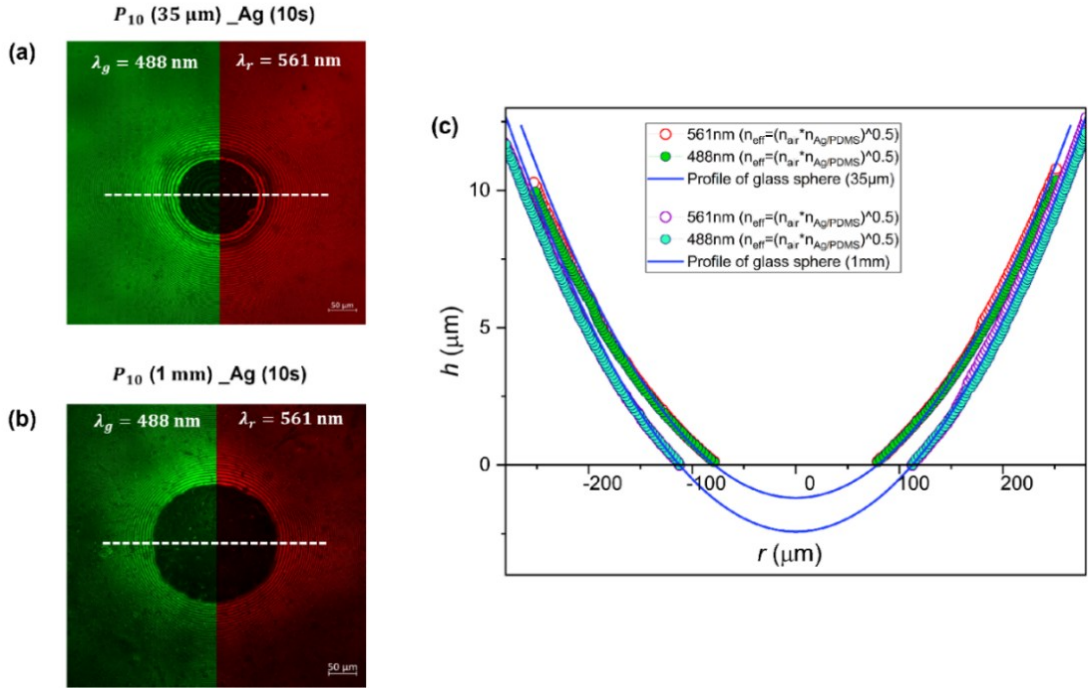


Figure B4-7 (a) and (b) Interference signatures of glass spheres on thin (35 µm) and thick (1 mm) PDMS 10:1 substrates with Ag layer of deposition time 10s. (c) Plots of the glass sphere profiles corresponding to the

interference signature shown in (a) and (b). The symbols represent the height extracted using $\Delta h_{\mathrm{g,r}} = m\lambda_{\mathrm{g,r}}/4\sqrt{n_{\mathrm{air}}n_{\mathrm{Ag/PDMS}}}$ and the solid lines represent the theoretical glass profile, i.e., $h = \sqrt{2600^2 - a^2} - \sqrt{2600^2 - r^2}$. Here, a is the contact radius.

B4.13: Reconstructed profiles of glass spheres on P_{10} (35 µm)-Ag(60s) and P_{10} (1 mm)-Ag(60s)

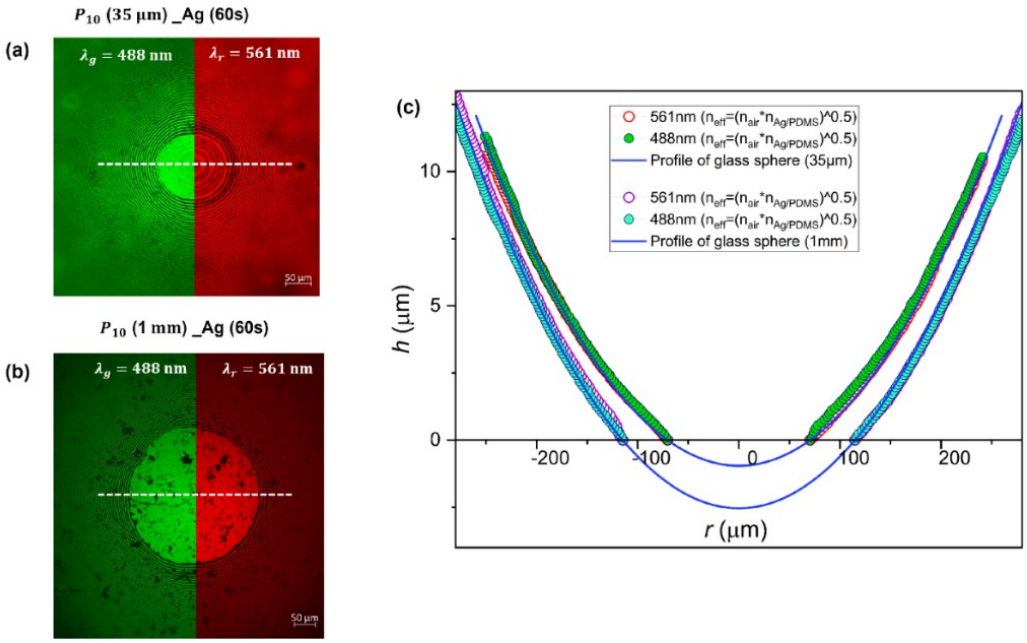


Figure B4-8 (a) and (b) Interference signatures of glass spheres on thin (35 µm) and thick (1 mm) PDMS 10:1 substrates with Ag layer of deposition time 60 s. (c) Plots of the glass sphere profiles corresponding to the interference signature shown in (a) and (b). The symbols represent the height extracted using $\Delta h_{\mathrm{g,r}} = m\lambda_{\mathrm{g,r}}/4\sqrt{n_{\mathrm{air}}n_{\mathrm{Ag/PDMS}}}$ and the solid lines represent the theoretical glass profile, i.e., $h = \sqrt{2600^2 - a^2} - \sqrt{2600^2 - r^2}$. Here, a is the contact radius.

B4.14: Reconstructed profiles of glass spheres on P_{10} (35 µm)-Ag(120s) and P_{10} (1 mm)-Ag(120s)

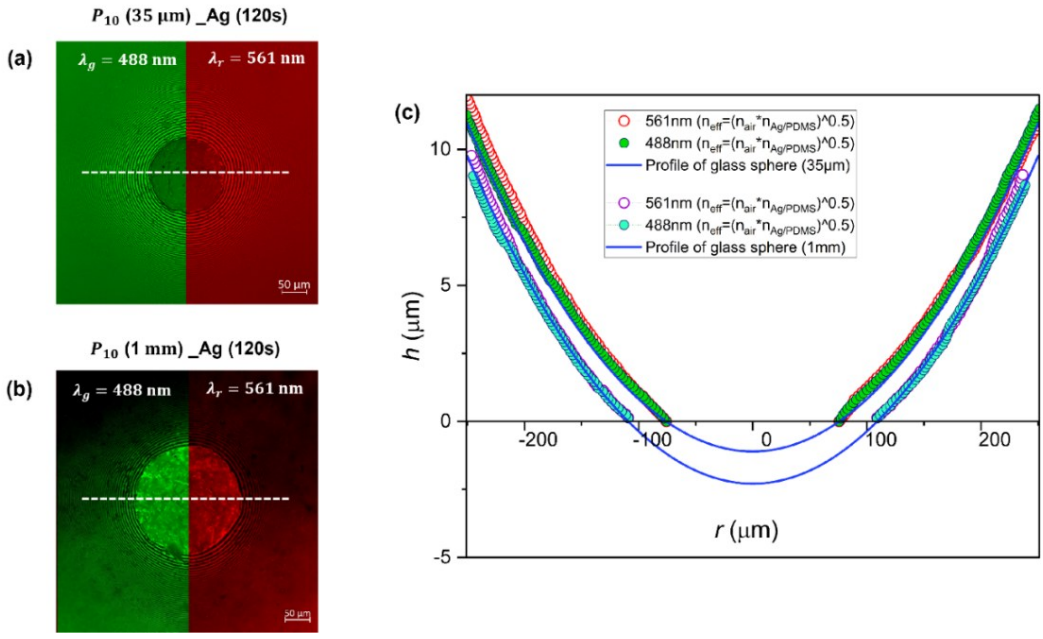


Figure B4-9 (a) and (b) Interference signatures of glass spheres on thin (35 µm) and thick (1 mm) PDMS 10:1 substrates with Ag layer of deposition time 120 s. (c) Plots of the glass sphere profiles corresponding to the interference signature shown in (a) and (b). The symbols represent the height extracted using $\Delta h_{\mathrm{g,r}} = m\lambda_{\mathrm{g,r}}/4\sqrt{n_{\mathrm{air}}n_{\mathrm{Ag/PDMS}}}$ and the solid lines represent the theoretical glass profile, i.e., $h = \sqrt{2600^2 - a^2} - \sqrt{2600^2 - r^2}$. Here, a is the contact radius.

B4.15: Reconstructed profiles of glass spheres on P_{20} (35 µm)-Ag(90s) and P_{20} (1 mm)-Ag(90s)

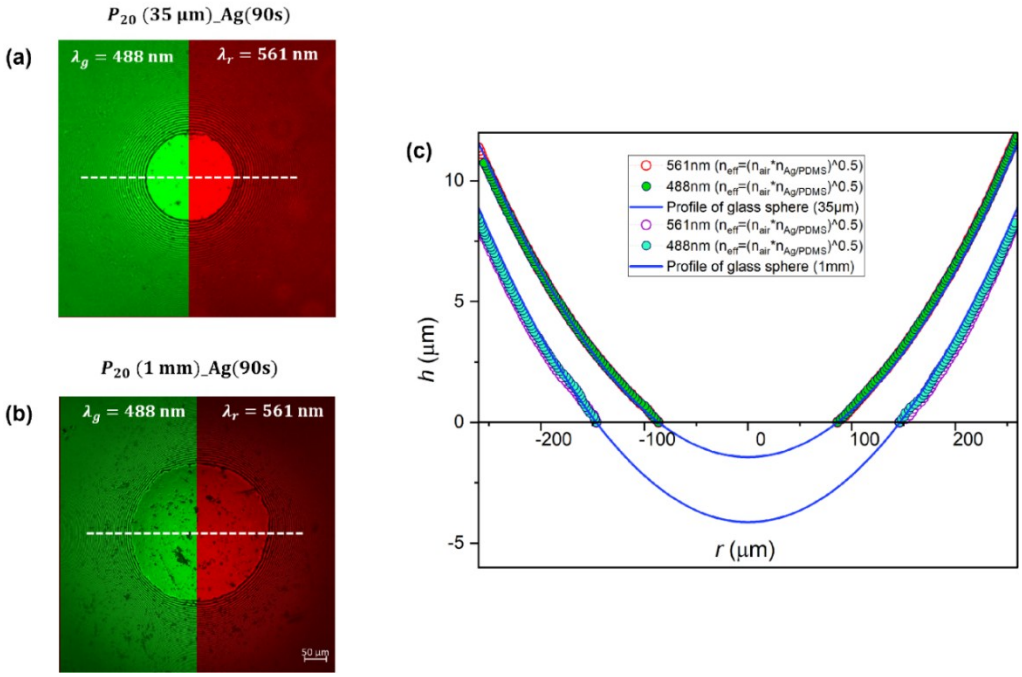


Figure B4-10 (a) and (b) Interference signatures of glass spheres on thin (35 µm) and thick (1 mm) PDMS 20:1 substrates with Ag layer of deposition time 90 s. (c) Plots of the glass sphere profiles corresponding to the interference signature shown in (a) and (b). The symbols represent the height extracted using $\Delta h_{\mathrm{g,r}} = m\lambda_{\mathrm{g,r}}/4\sqrt{n_{\mathrm{air}}n_{\mathrm{Ag/PDMS}}}$ and the solid lines represent the theoretical glass profile, i.e., $h = \sqrt{2600^2 - a^2} - \sqrt{2600^2 - r^2}$. Here, a is the contact radius.

B4.16: Reconstructed profiles of glass spheres on P_{20} (35 µm)-Ag(120s) and P_{20} (1 mm)-Ag(120s)

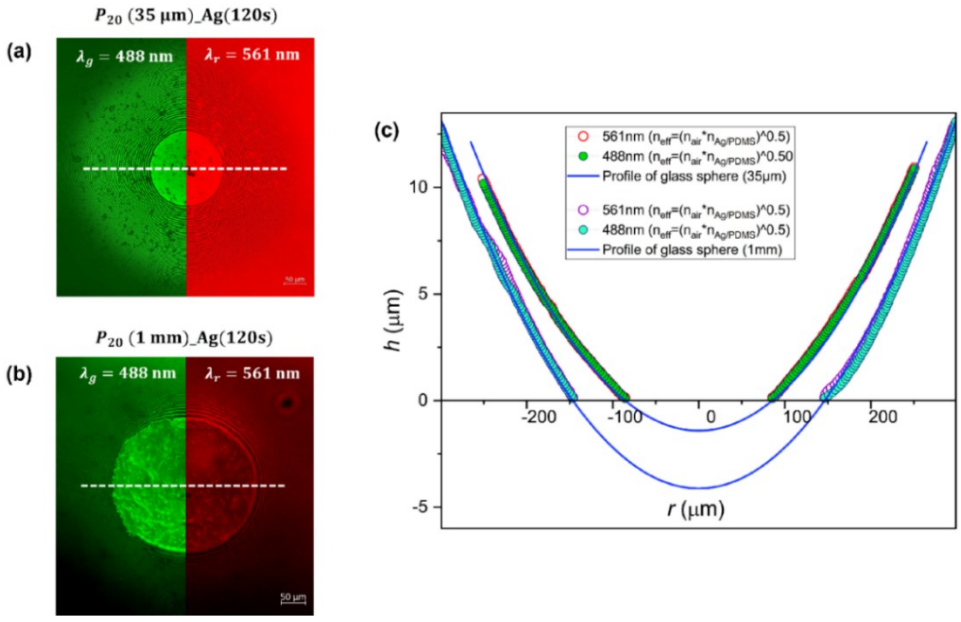


Figure B4-11 (a) and (b) Interference signatures of glass spheres on thin (35 µm) and thick (1 mm) PDMS 20:1 substrates with Ag layer of deposition time 120 s. (c) Plots of the glass sphere profiles corresponding to the interference signature shown in (a) and (b). The symbols represent the height extracted using $\Delta h_{\mathrm{g,r}} = m\lambda_{\mathrm{g,r}}/4\sqrt{n_{\mathrm{air}}n_{\mathrm{Ag/PDMS}}}$ and the solid lines represent the theoretical glass profile, i.e., $h = \sqrt{2600^2 - a^2} - \sqrt{2600^2 - r^2}$. Here, a is the contact radius.

B4.17: Comparison of predicted elastic (Young's) modulus using Hertz and JKR theories

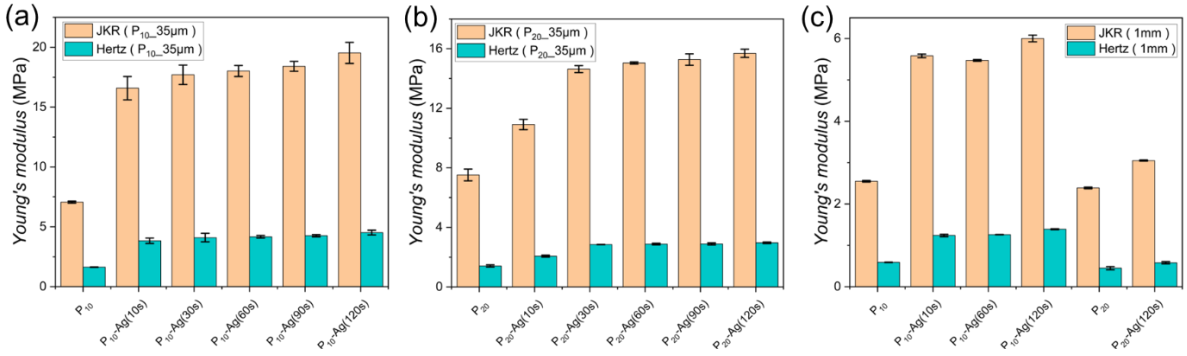


Figure B4-12 Comparison of predicted elastic (Young's) modulus values for Ag coated PDMS films using Hertz and JKR theories for (a) PDMS 20:1 substrates of film thickness 35 µm with varying Ag deposition times, (b)

PDMS 20:1 substrates of film thickness 35 µm with varying Ag deposition times, and (c) PDMS 10:1 and 20:1 substrates of film thickness 1 mm with varying Ag deposition times. Error bars represent standard deviations calculated from three independent experiments. In some cases, they are smaller than the symbol size and thus not visible.

B4.18: Schematic of Ag sputtered PDMS film adhered to glass slide

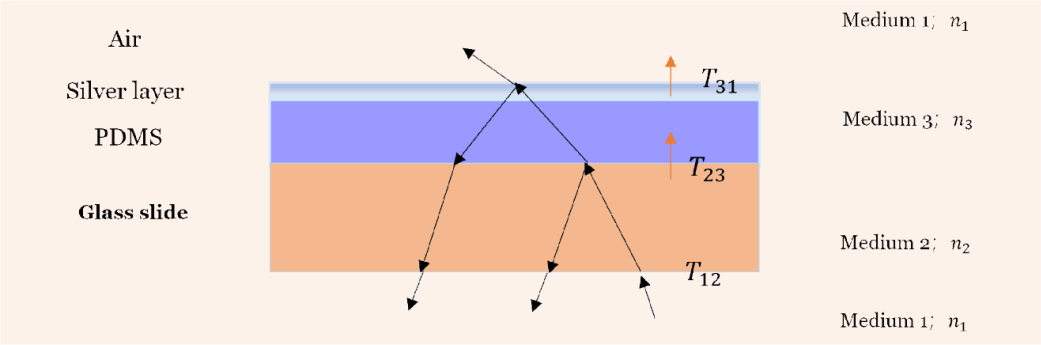


Figure B4-13 Schematic of Ag sputtered PDMS film adhered to glass slide set-up. n_1, n_2 and n_3 are the refractive indices of air, glass, and Ag coated PDMS medium, respectively.

B4.19: The transmittance and reflectance of PDMS (10:1 and 20:1) with different Ag deposition time

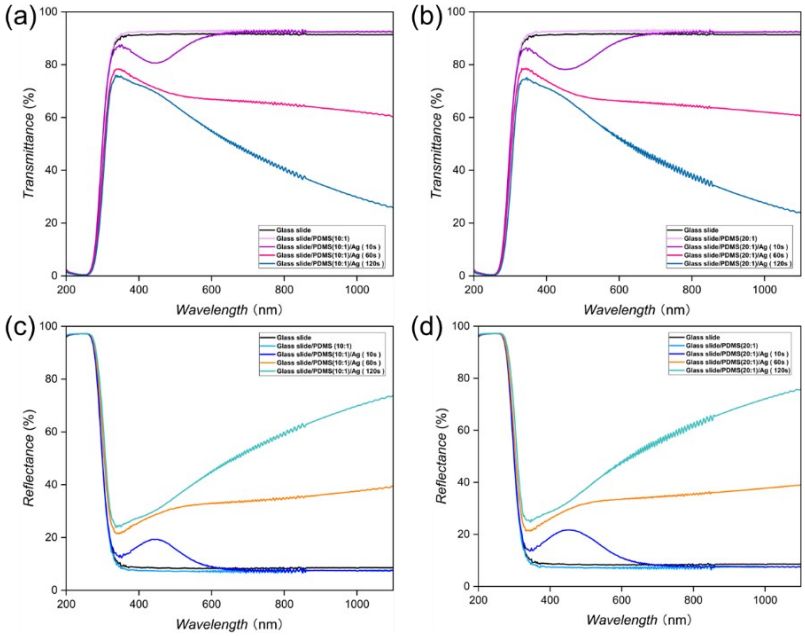


Figure B4-14 Plots of transmittance using UV/Vis spectroscopy measurements for PDMS 10:1 with Ag deposition (a) and PDMS 20:1 with Ag deposition (b). Plots of reflectance using UV/Vis spectroscopy measurements for PDMS 10:1 with Ag deposition (c) and PDMS 20:1 with Ag deposition (d).

B4.20: The transmittance and reflectance of PDMS (10:1 and 20:1) with different Au deposition time

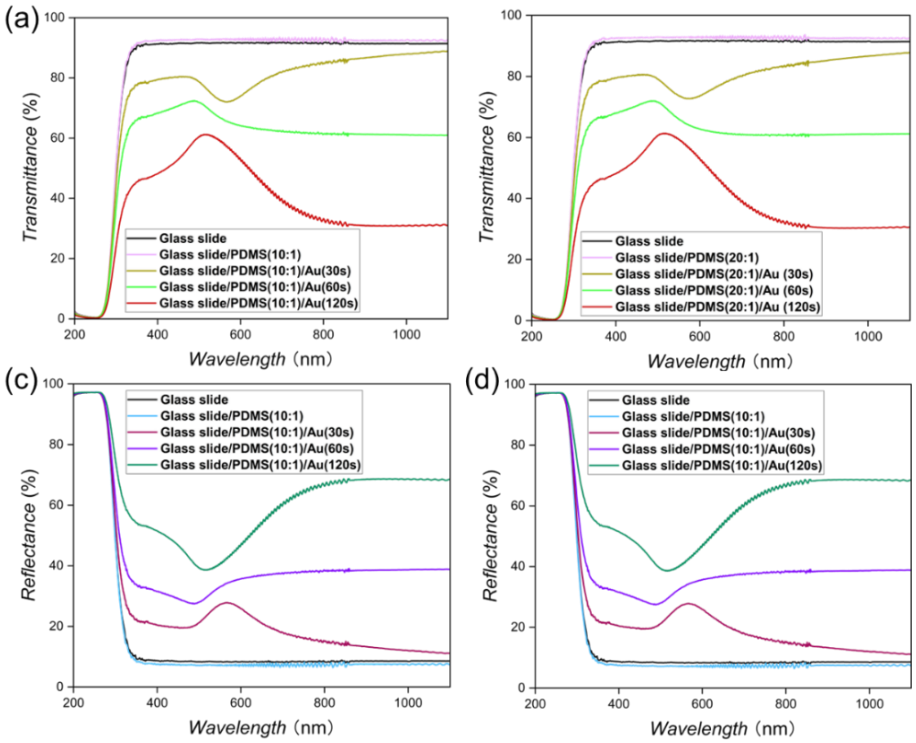


Figure B4-15 Plots of transmittance using UV/Vis spectroscopy measurements for PDMS 10:1 with Au deposition (a) and PDMS 20:1 with Au deposition (b). Plots of reflectance using UV/Vis spectroscopy measurements for PDMS 10:1 with Au deposition (c) and PDMS 20:1 with Au deposition (d).

Appendix C

Supporting Information for Chapter 5

C5.1 The principle of DW-RICM

The basic principle of dual wavelength - confocal Reflection Interference Contrast Microscopy (DW-RICM) comprises the interference of two or more electromagnetic (EM) waves [311,312]. Typically, DW-RICM set-up observations under monochromatic epi-illumination, which consists of a light source, an inverted microscope equipped with an antiflex objective and a CCD camera [201]. When the uniform monochromatic plane wave passes through the sample with multilayer, the light will reflect from different interfaces and interfere with each other, which implies that the detected intensity of interference fringes is linked to the substrate-object distance. To take the example of glass – glass contact (glass sphere contact with glass slide), the schematic and the corresponding distinctive bright and dark interference fringing are shown in Figures C5-1(a) and (b). Two interfaces can reflect the incident light: the glass slide – air interface (electric field E_1, intensity I_1) and the air – glass sphere interface (electric field E_2, intensity I_2), and create the resultant electric field E are given by [203]:

$$E = |E_1| + |E_2| \exp(i\delta) = |E_1| + |E_2|\{cos(\delta) + isin(\delta)\} \quad \text{(C5-1)}$$

where δ is the phase difference between E_1 and E_2. When the two reflected lights are superimposed, the resultant (measured) light intensity I is determined by the ensemble average of the square of the resulting electric field E [311]. Besides, since the two reflected light are in parallel oscillations, the interfered light intensity can be theoretically expressed as below [311]:

$$I \propto |E|^2 = I_1 + I_2 + 2\sqrt{I_1 I_2} cos\delta \quad \text{(C5-2)}$$

Where $\delta = 4n\pi h/\lambda$, when the refractive index of the multi-layer structure of the sample increases or decreases monotonically in sequence, which is called π-shift [79,202]. Otherwise, $\delta = 4n\pi h/\lambda + \pi$. The λ is the wavelength of monochromatic light (here, $\lambda_g = 488\ \text{nm}$ and $\lambda_r = 561\ \text{nm}$). The n is the refractive index of the corresponding medium layer. The unknown

intensities I_1 and I_2 can be expressed as, $I_{\max} = I_1 + I_2 + 2\sqrt{I_1 I_2}$ and $I_{\min} = I_1 + I_2 - 2\sqrt{I_1 I_2}$. Thus, the normalized intensity is I_0 can be expressed as:

$$I_0 = (I - I_{min})/(I_{max} - I_{min}) = (cos\delta + 1)/2 \quad \text{(C5-3)}$$

Therefore, the height profile h is as below:

$$h = \lambda arcos\left\{2\left(\frac{I - I_{min}}{I_{max} - I_{min}}\right) - 1\right\}/4\pi n \quad \text{(C5-4)}$$

Based on the simultaneous intensity information from the two wavelengths, the height information of any point in the interface can be unambiguously resolved. In the simplest case, when $4\pi nh/\lambda = m\pi$, the height difference between consecutive bright and dark fringes of the same fringe order m can be expressed as,

$$\Delta h = m\lambda/4n \quad \text{(C5-5)}$$

where m is the number of peak points. For the glass – glass contact system, the medium layer between the glass slide and glass probe is air, hence $n_{air} = 1$. The height of the glass sphere corresponding to both wavelengths can be extracted by taking $n_{air} = 1$ into the above equation, which is in excellent agreement with the theoretical profile of the glass sphere, i.e., $h(r) = R - \sqrt{R^2 - r^2}$, where $R_0 = 2600\ \mu m$ is the radius of the glass sphere (Figure C5-1(c)).

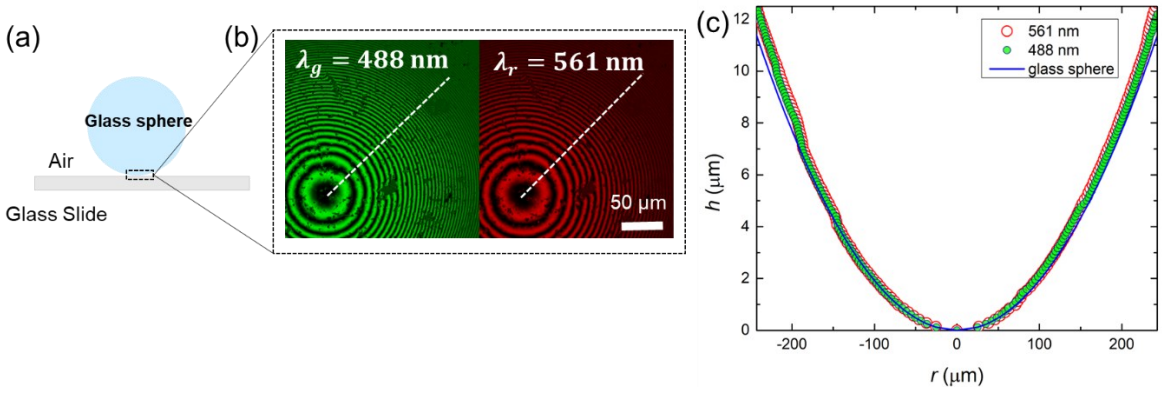


Figure C5-1 (a) Schematic of a glass sphere atop a glass slide. (b) Interference signature corresponding to green and red wavelengths for the system shown in (a). The scale bar represents 50 µm. (c) A plot of the glass sphere profile along the dashed white lines for the interference signature in (b). The symbols represent the height

extracted corresponding to the green and red wavelengths using the relation $\Delta h_{g,r} = m\lambda_{g,r}/4n_{air}$ and the solid line represents the theoretical glass profile.

C5.2 Images of black ink-coated glass probe

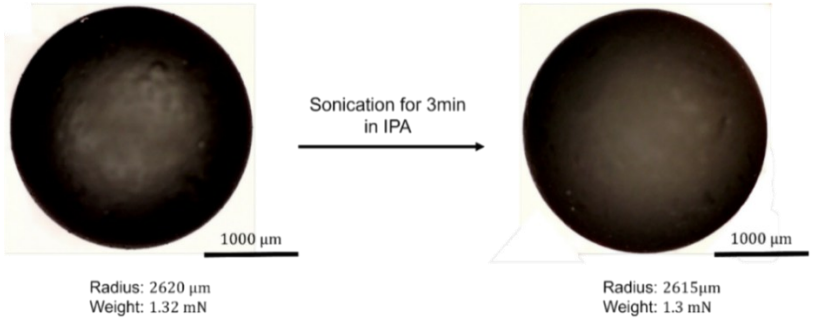


Figure C5-2 Optical images of the black ink-coated glass probe before and after sonication.

C5.3 The roughness of the mixture black ink-coated glass slides

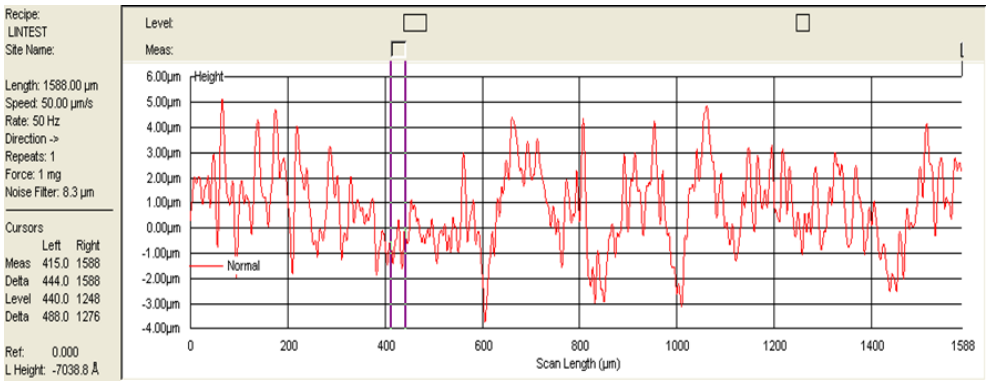


Figure C5-3 The roughness (1.29 µm) of the mixture black ink (with a thickness of 15 µm)-coated on glass slides using surface profiler measurements.

C5.4 The reflectance (R) and transmittance (T) of the black ink

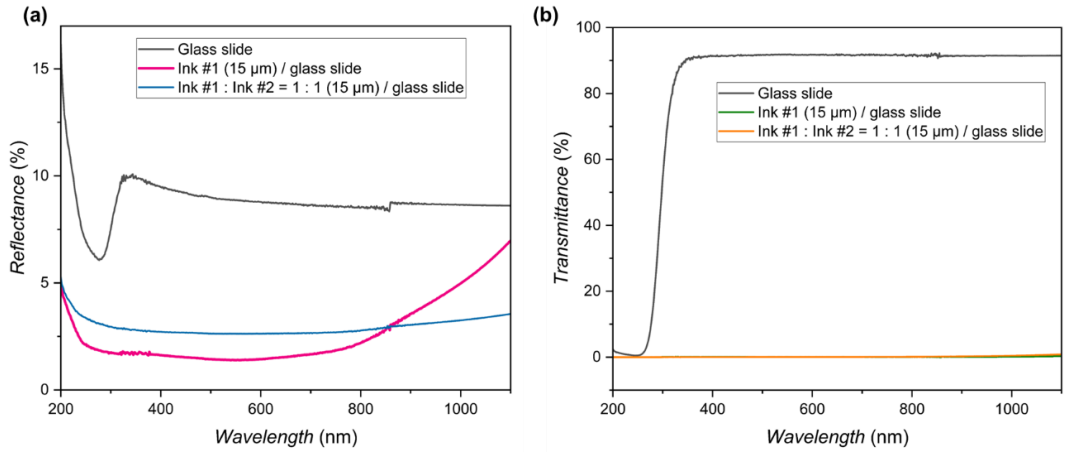


Figure C5-4 Plots of reflectance (a) and transmittance (b) using UV/VIS spectroscopy measurements for glass slide, black ink #1 (with a thickness of 15 μm) coated on a glass slide, and the mixture black ink with a weight ratio of black ink #1 and black ink #2 = 1:1 (thickness of 15 μm) coated on glass slide.

C5.5 The optical loss (L) of black ink

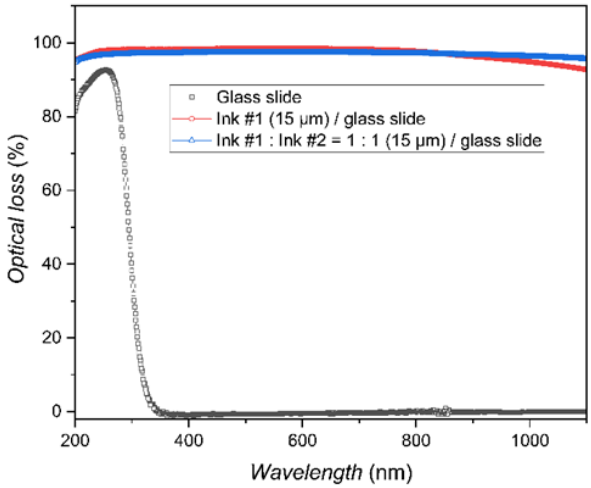


Figure C5-5 Plots of optical loss using UV/VIS spectroscopy measurements for a glass slide, black ink #1 (with a thickness of 15 μm) coated on a glass slide, and the mixture black ink with a weight ratio of black ink #1 and black ink #2 = 1:1 (thickness of 15 μm) coated on a glass slide.

C5.6 The thickness of sputter-coated gold on glass slides

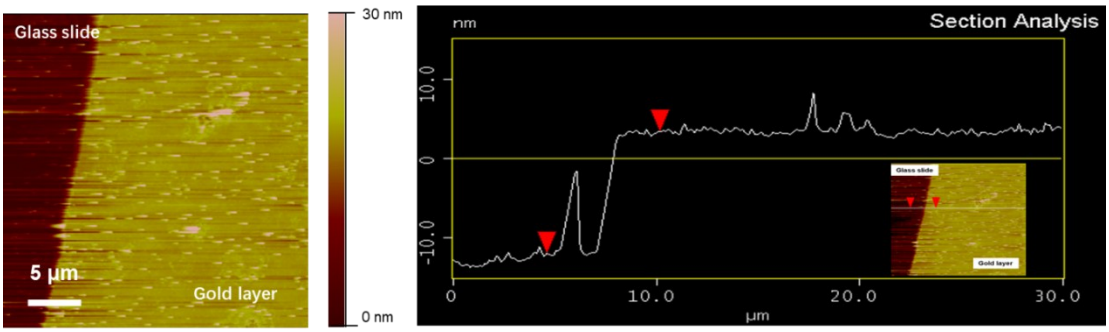


Figure C5-6 Atomic force microscopy (AFM) scans and thickness measurement of sputtered Au layer on a glass slide for 2 min.

C5.7 The image of the experimental measurement set-up using DW-RCIM

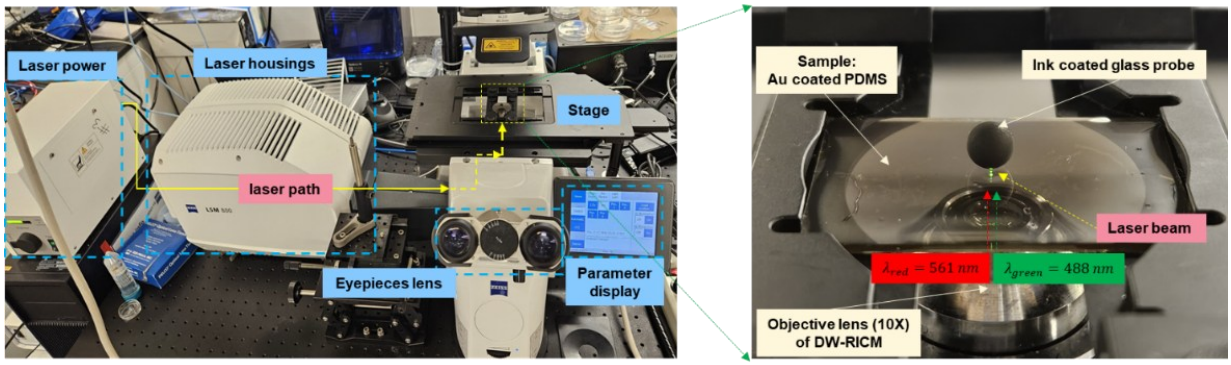


Figure C5-7 The photograph of the experimental measurement set-up using DW-RICM.

C5.8 The refractive index of P_{10} $(35\mu m)$ and P_{20} $(35\mu m)$

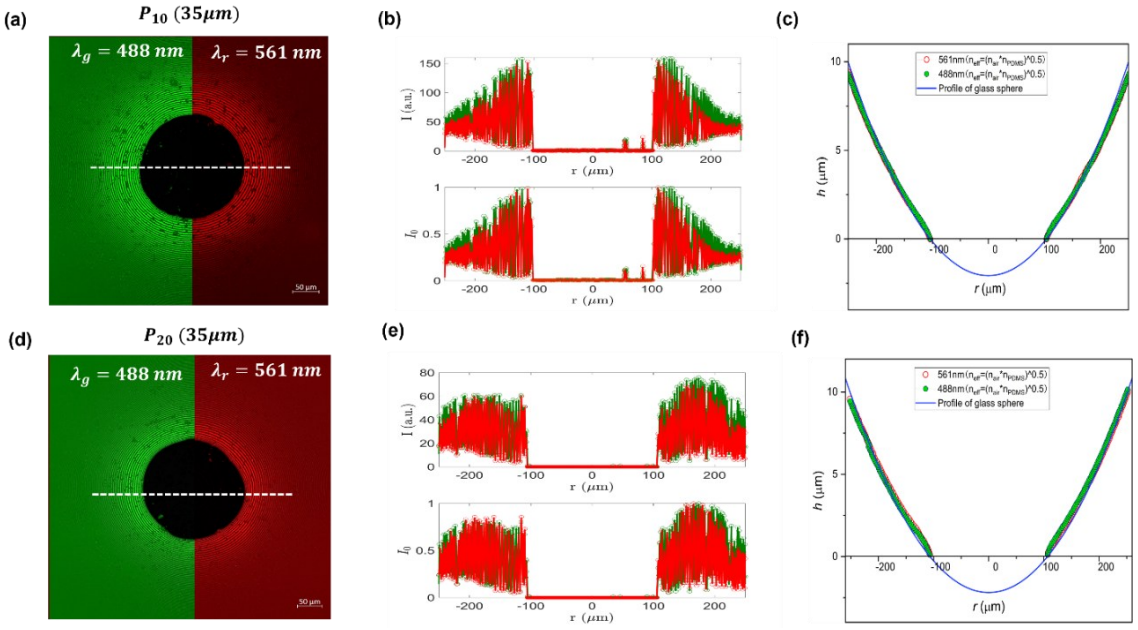


Figure C5-8 Unprocessed interference signature corresponding to the glass sphere (R_0 = 2.6 mm) on (a) PDMS 10:1 (P_{10}) and (d) PDMS 20:1 (P_{20}) coatings of finite thickness at 35 µm. (b) and (e) Plots of raw ($I(a,u)$) and normalized (I_0) intensity with radial location r for the slice shown in (a) and (d), respectively. (c) and (f) Plots of glass sphere profile for the interference signature shown in (a) and (d) along the dashed lines. The symbols represent the height extracted using $\Delta h_{g,r} = m\lambda_{g,r}/4\sqrt{n_{air}n_{PDMS}}$ and the solid lines represent the theoretical glass profile, i.e., $h = \sqrt{2600^2 - a^2} - \sqrt{2600^2 - r^2}$. Here, a is the contact radius.

C5.9 The refractive index of Au-coated PDMS

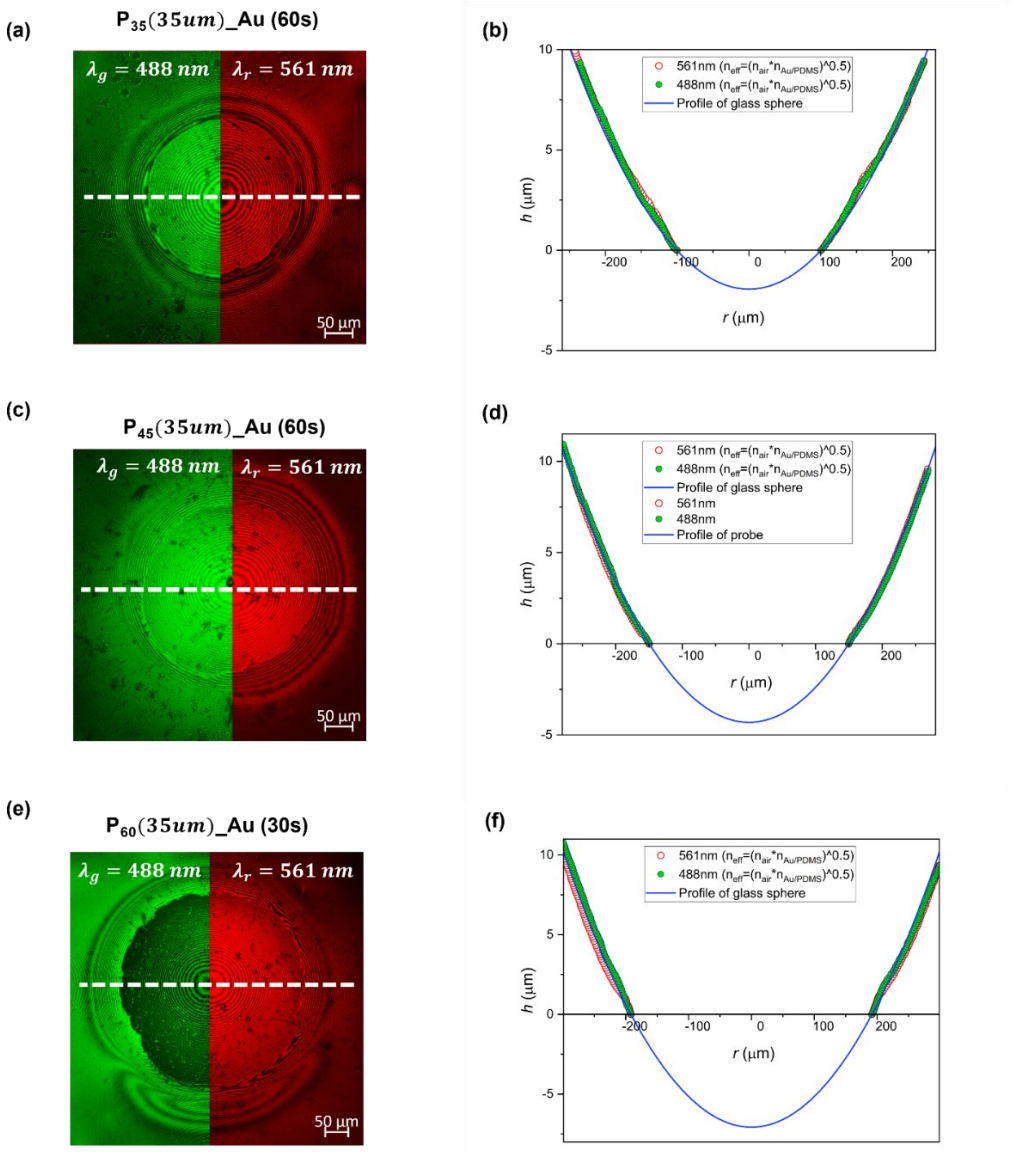


Figure C5-9 Unprocessed interference signature corresponding to the glass sphere (R_0 = 2.6 mm) on 35-μm-thickness (a) P_{35}, (c) P_{45}, and (e) P_{60} films deposited with Au for 60 s, 60 s and 30 s, respectively. (b), (d) and (f) Plots of the glass sphere profile for the interference signature shown in (a), (c), and (e) along the dashed lines. The symbols represent the height extracted using $\Delta h_{\mathrm{g,r}} = m\lambda_{\mathrm{g,r}}/4\sqrt{n_{\mathrm{air}} n_{\mathrm{Au/PDMS}}}$ and the solid lines represent the theoretical glass profile, i.e., $h = \sqrt{2600^2 - a^2} - \sqrt{2600^2 - r^2}$. Here, a is the contact radius.

C5.10 The experimental measurement set-up using Raman Microscopy

During the Raman measurements, the sample was positioned on the carrier stage with the Au/PDMS side facing upwards. A hemispherical lens was then placed on the sample's surface, ensuring direct contact. The weight of the lens exerted pressure on the sample surface, causing deformation. The laser was directed through the objective lens (50×) and the hemispherical lens, before focusing on the sample's surface (the red point in Figure C5-10). This focal point was near the center of the contact area and within the region of contact deformation.

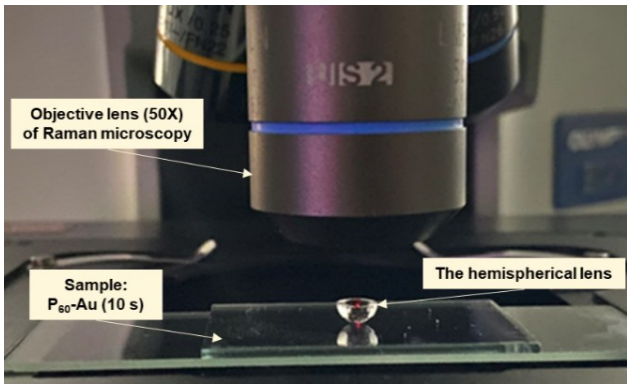


Figure C5-10 The photograph of the experimental measurement set-up using Raman Microscopy.

C5.11 Comparison of the effect of the hemispherical lens and the glass probe on Raman laser spot

Comparative measurements were performed by focusing the laser spot on the sample surface in three different cases: **(1)** The laser was focused on the sample surface without going through the hemispherical lens (Figure C5-11a left) / glass probe (Figure C5-11a right). **(2)** The laser was passed through the edge of the hemispherical lens (Figure C5-11b left) / glass probe (Figure C5-11b right) and then reached the free surface of the sample. **(3)** The laser light passed through the center region of the hemispherical lens (Figure C5-11c left) / glass probe (Figure C5-11c right) and then reached the free surface of the sample. The corresponding Raman laser spots are shown right beside each optical images. For case 1#: the laser spot is a small and bright spot (Figure C5-11b left and right). For case 2#: the laser spot was deformed due to the scattering of the hemispherical lens and glass probe edge (Figure

C5-11d left and right). For case 3#: in the case of the glass probe, the laser spot disappeared due to the scattering effect of the glass probe (Figure C5-11f right). The carrier stage was moved upward until the limiting position of the instrument of the reached (Figure C5-11g right). However, the laser still could not focus on a spot (Figure C5-11h right). This implies that the Raman laser cannot go through the glass probe and focus on the sample surface. In this way, the Raman spectrum we eventually obtain only relates to the glass probe and is not usable for the present work. Thus, the hemispherical lens provides a small, bright spot with a slight scattering.

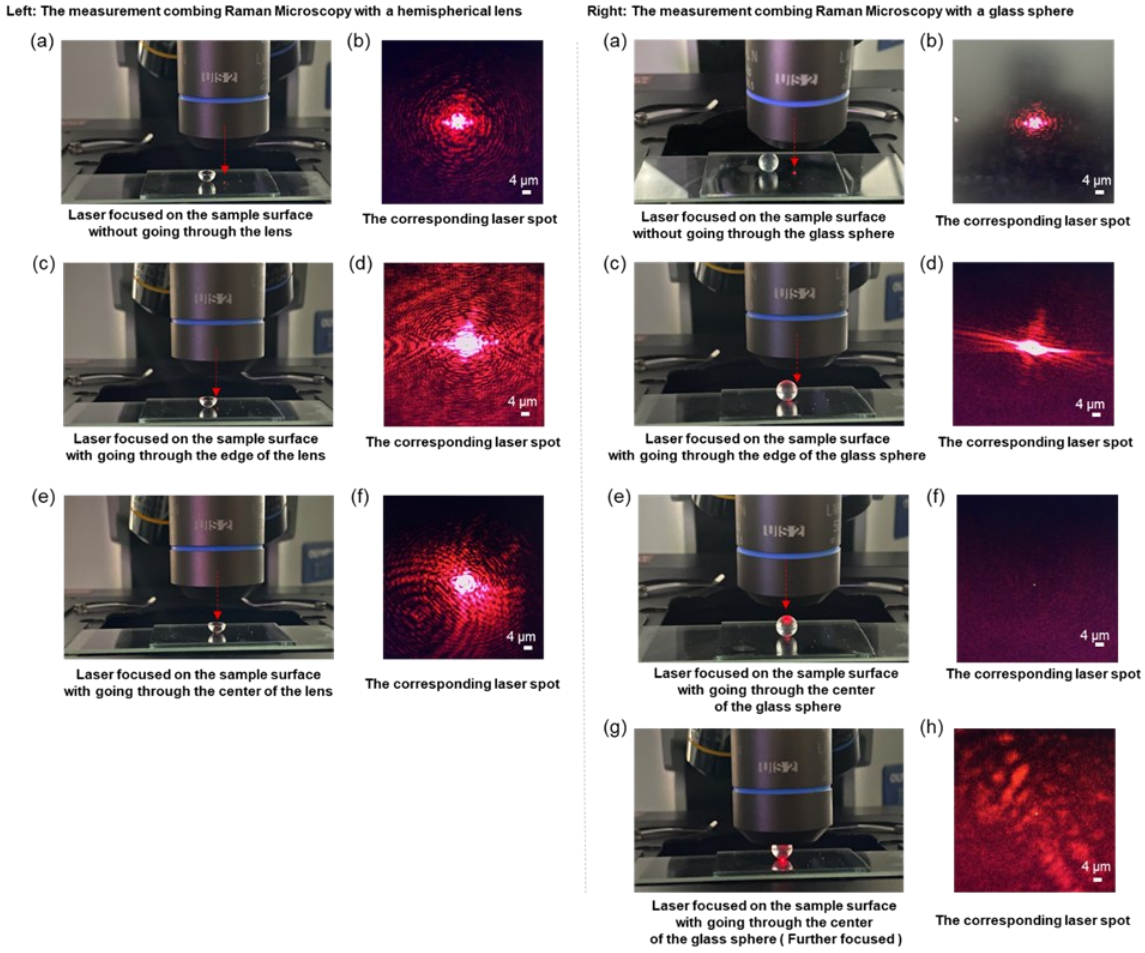


Figure C5-11 The photograph of the experimental measurement set-up of the Raman laser focused on (a) the sample surface without going through the hemispherical lens (left) and the glass probe (right); (c) the sample surface with going through the edge of the hemispherical lens (left) and the glass probe (right); (e) the sample surface with going through almost the center of the hemispherical lens (left) and the glass probe (right). The

corresponding laser spot of the Raman laser focused on (b) the sample surface without going through the hemispherical lens (left) and the glass probe (right); (d) the sample surface with going through the edge of the hemispherical lens (left) and the glass probe (right); (f) the sample surface with going through almost the center of the hemispherical lens (left) and the glass probe (right).

C5.12 The Raman spectrum of the surface and interior of P_{10} and P_{60}

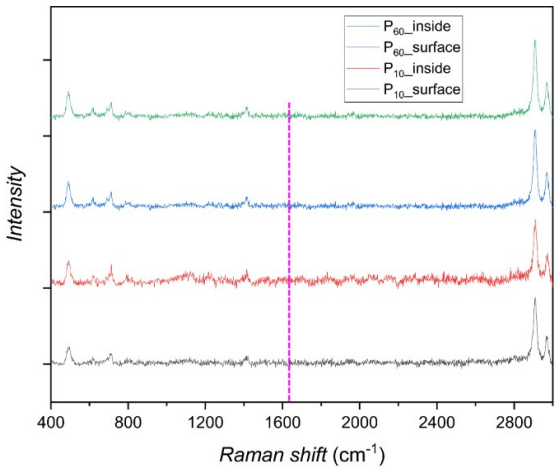


Figure C5-12 Raman spectrum of the surface and inside of P_{10} and P_{60}.

C5.13 The Raman spectrum of the surface of P_{60} - Au (10s)

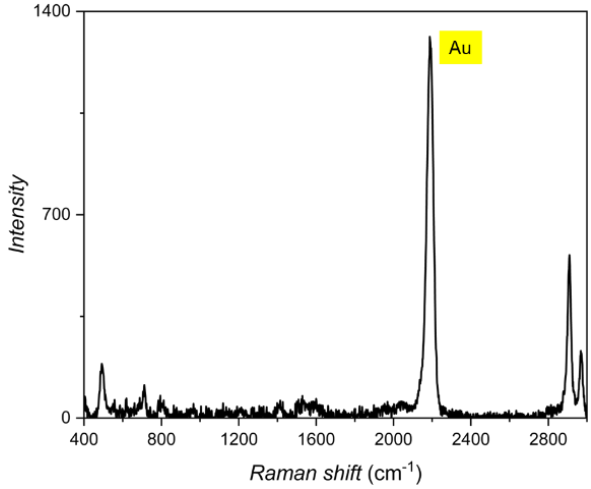


Figure C5-13 Raman spectrum of the surface of P_{60}-Au (10s) without placing the hemispherical lens.

C5.14 The reconstructed deformation profiles of P_{60}

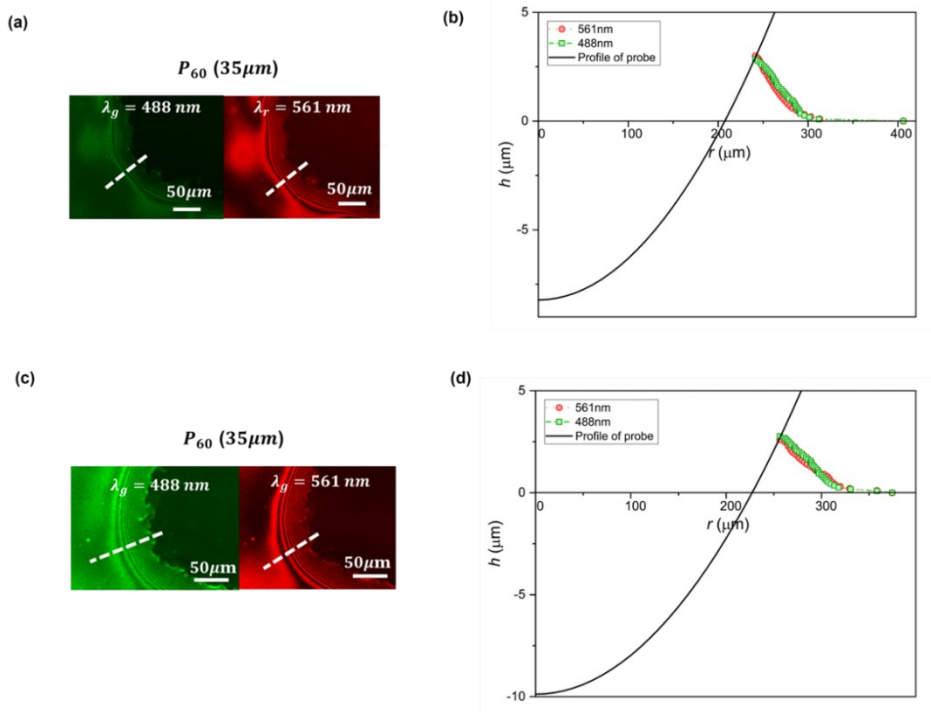


Figure C5-14 (a) and (c) Unprocessed interference signature corresponding to the black probe (R = 2.615 mm) on a 35-μm-thickness P_{60}. (b) and (d) Profiles of the probe and deformation of the soft substrate based on the interference signature shown in (a) and (c) along the marked line drawn. The green and red symbols represent the height extracted using $h_{g,r} = \mathrm{m}\lambda_{\mathrm{g,r}}/4\mathrm{n}_{\mathrm{PDMS}}$ and the dark solid line represents the theoretical profile of ink coated probe, i.e., $h = \left(\sqrt{R^2 - a^2} + h_0\right) - \sqrt{R^2 - r^2}$.

C5.15 The contact radius of ink coated probe and bare glass probe contacting with different soft substrates

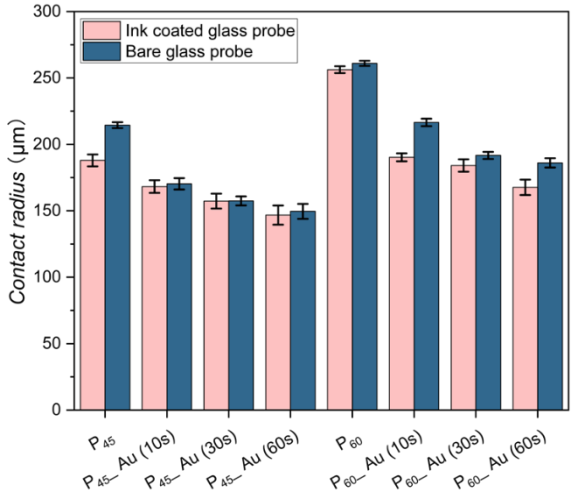


Figure C5-15 The contact radius of ink coated probe and bare glass probe contacting with different soft substrates. Error bars represent the standard deviation from three independent experiments.

C5.16 The ink-coated steel probe with a larger diameter of 19 mm contact with a soft PDMS substrate

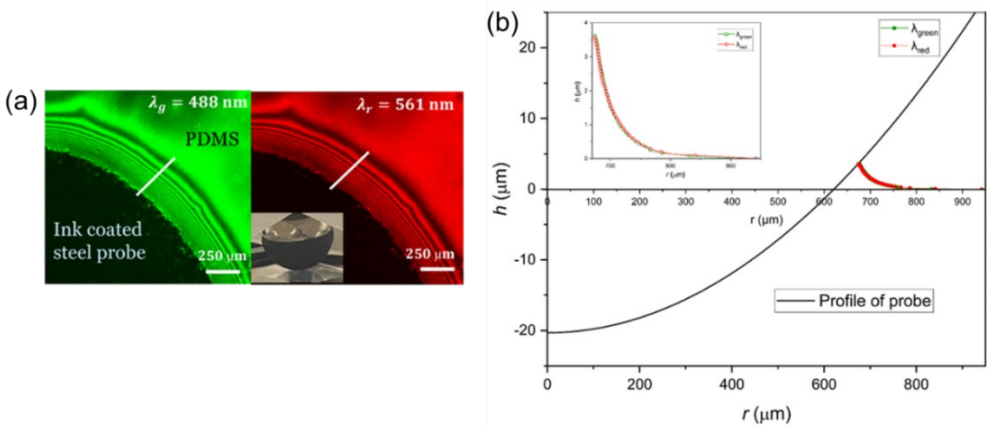


Figure C5-16 (a) Interference signature of a truncated ink-coated steel probe with a diameter of 19 mm on a 35-μm-thick soft PDMS film. The green and red interference signatures correspond to 488 nm and 561 nm wavelengths, respectively. (b) Profile of the contact ridge along the white line shown in (a). The green and red symbols represent the height extracted using $h_{g,r} = m\lambda_{g,r}/4n_{\mathrm{PDMS}}$ and the dark solid line represents the theoretical profile of the ink-coated probe, i.e., $h = \left(\sqrt{R^2 - a^2} + h_0\right) - \sqrt{R^2 - r^2}$.

Appendix D

Supporting Information for Chapter 6

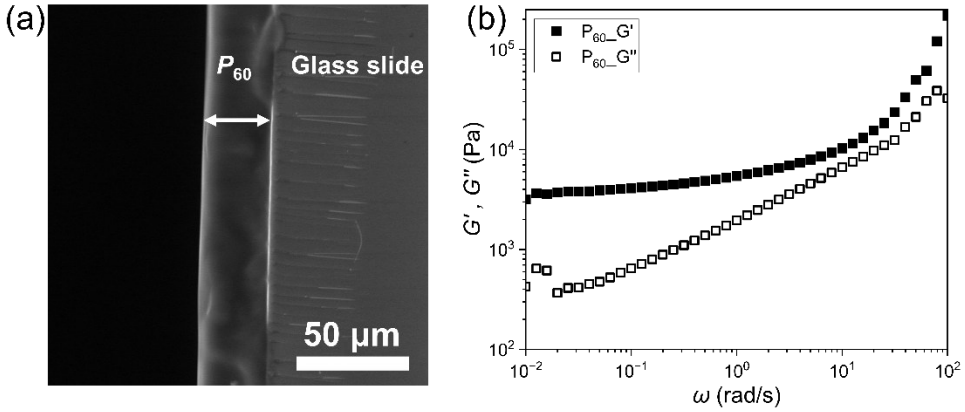


Figure D6-1 (a) The cross sectional Scanning Electron Microscopy (SEM) image of the P_{60} (PDMS base and curing agent ratio: 60:1) layer coated on a glass slide. (b) Rheology measurements showing the variation of storage modulus, G' (closed symbols) and loss modulus, G'' (open symbols) with frequency, ω for the P_{60} soft substrate.

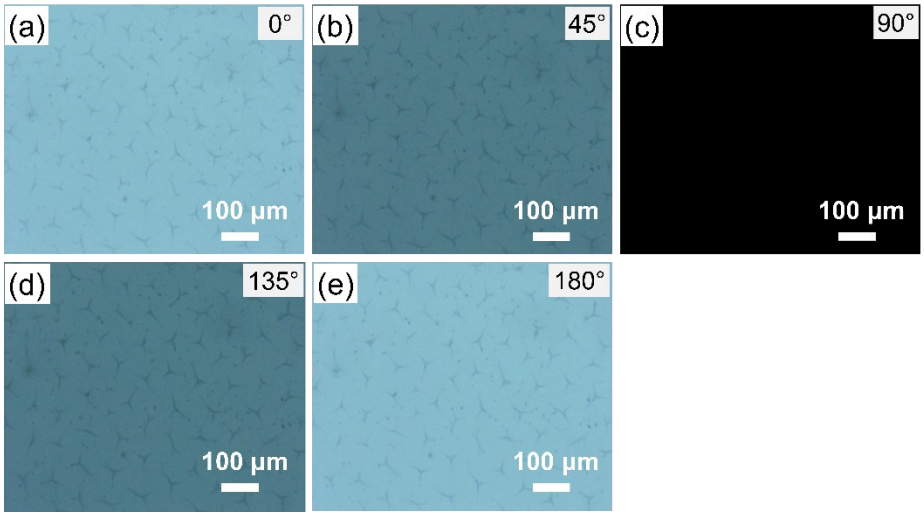


Figure D6-2 Polarized optical microscopy images of a soft PDMS P_{60} substrate after immersion in hexane for 96 hrs and drying in air.

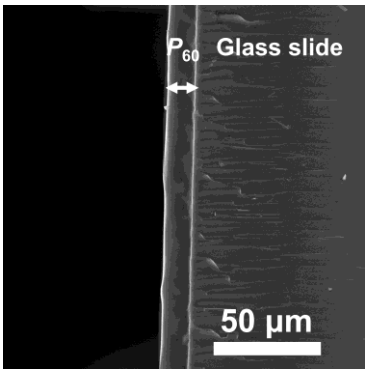


Figure D6-3 The cross sectional SEM image of a soft PDMS P_{60} substrate after immersion in hexane for 96 hrs and drying in air.

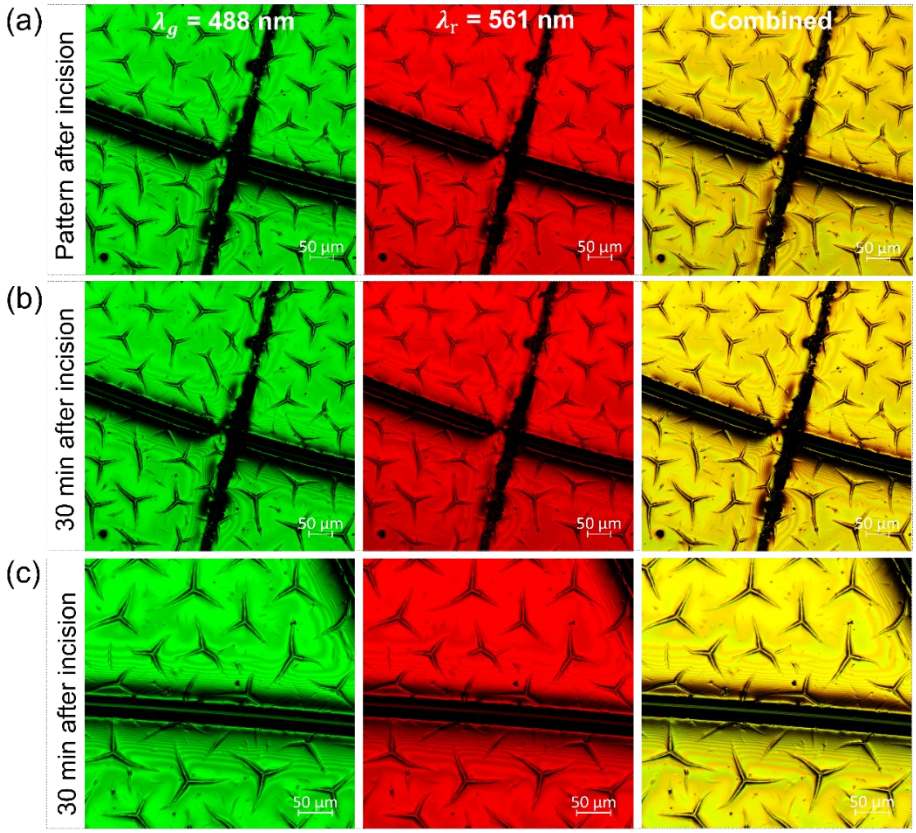


Figure D6-4 Dual-wavelength reflection interference contrast microscopy (DW-RICM) images of the soft PDMS P_{60} substrate after 96 hrs hexane extraction and 90 min air drying. The image shows the morphology of the surface pattern at a region mechanically cut by a blade to examine pattern change across the cut.

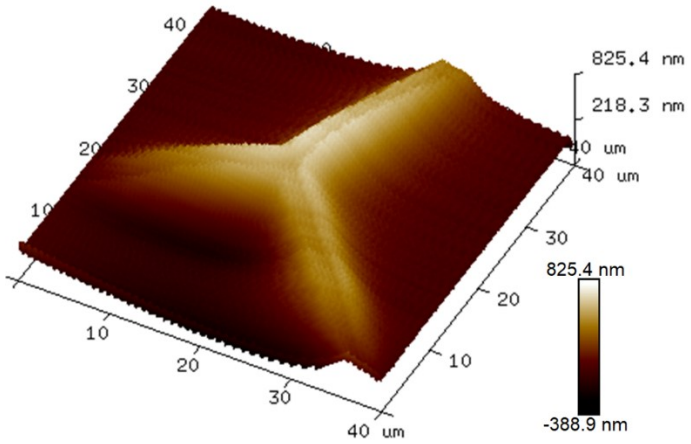


Figure D6-5 Atomic force microscopy (AFM) scan and profile of a pattern of the soft PDMS P_{60} substrate after 96 hours hexane extraction and 12 hrs fume hood drying.

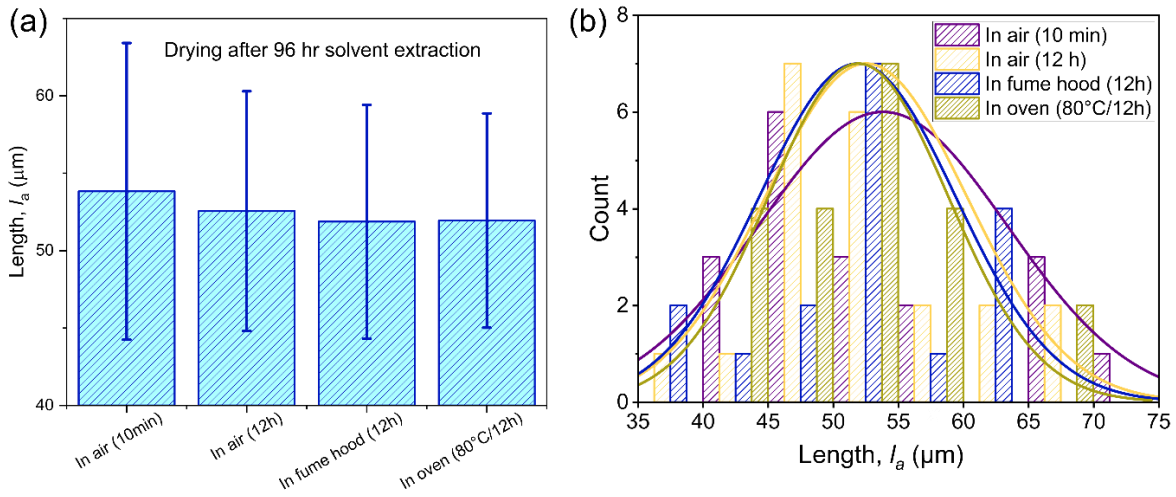


Figure D6-6 (a) Variation of pattern arm length with drying conditions for PDMS P_{60} substrate swollen in hexane for 96hrs. Error bars represent the standard deviation of the pattern lengths measured from a single sample. (b) Corresponding histograms showing the distribution of arm lengths for each drying condition, with fitted curves included to illustrate the overall spread of the data.

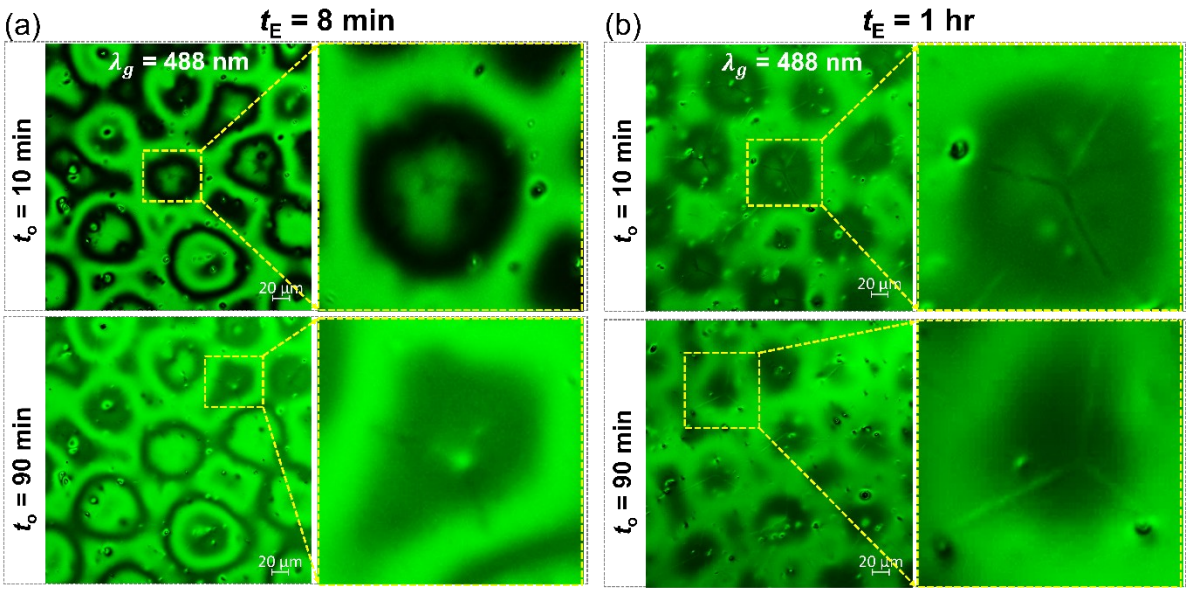


Figure D6-7 Dual-wavelength reflection interference contrasts with microscopy (DW-RICM) images and the corresponding zommed-in images of the pattern structure for soft PDMS P_{60} substrates with hexane extraction times of (a) 8 min and (b) 1 hr for air drying times of 10 min and 90 min. The green color corresponding to laser wavelength of 488 nm.

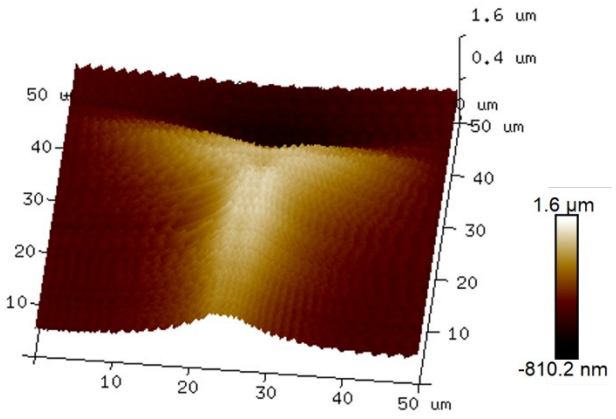


Figure D6-8 Atomic force microscopy (AFM) scan and profile of a pattern of the soft silicone gel substrate after 96 hrs hexane extraction and air drying.

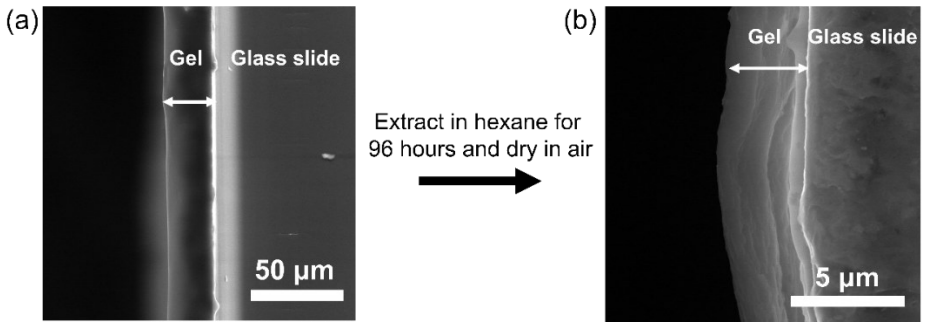


Figure D6-9 The cross sectional SEM images of a soft PDMS P_{60} substrate before (a) and after immersion in hexane for 96 hrs and drying in air (b).

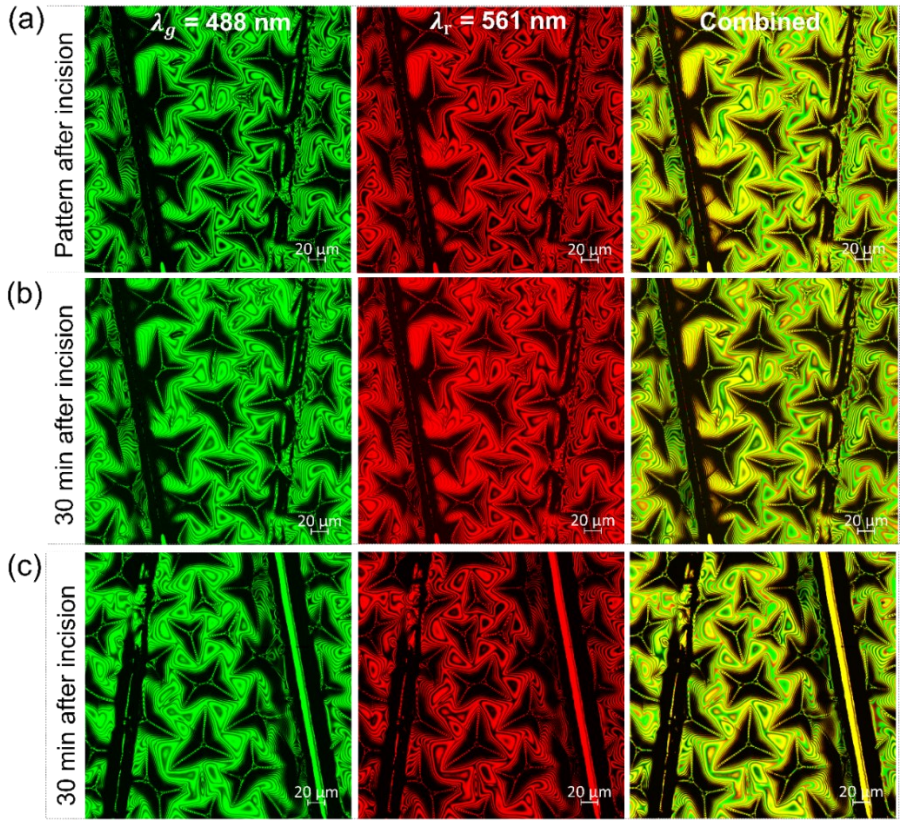


Figure D6-10 Dual-wavelength reflection interference contrast microscopy (DW-RICM) images of the soft silicone gel substrate after 96 hrs hexane extraction and 90 min air drying. The image shows the morphology of the surface pattern at a region mechanically cut by a blade to examine pattern change across the cut.

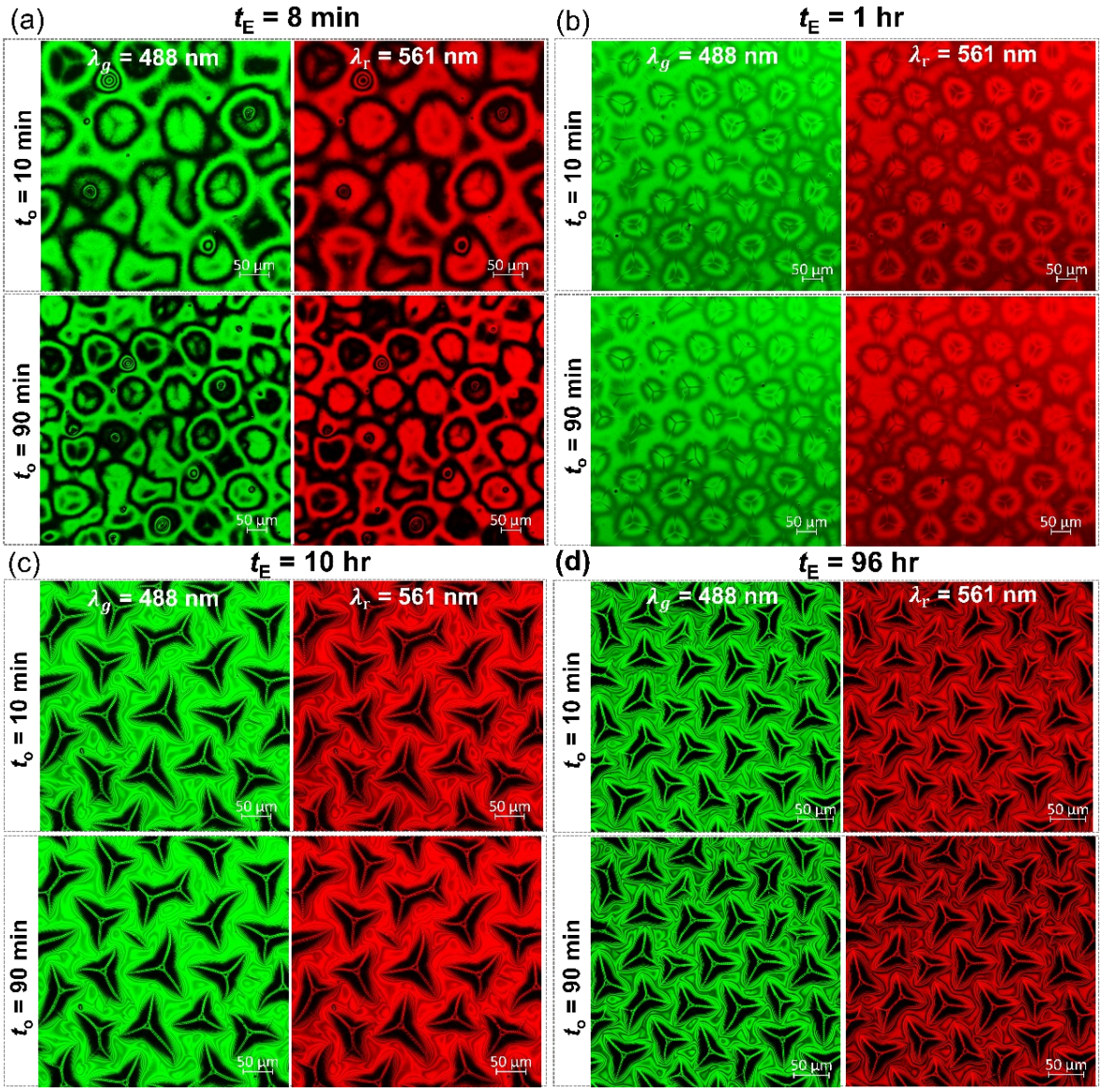


Figure D6-11 Dual-wavelength reflection interference contrast microscopy (DW-RICM) images of the silicone gel soft substrate with hexane extraction times of (a) 8 min, (b) 1 hr, (c) 10 hrs, and (d) 96 hrs for air drying times of 10 min and 90 min. The green and red color corresponding to laser wavelength of 488 nm and 561 nm, respectively.

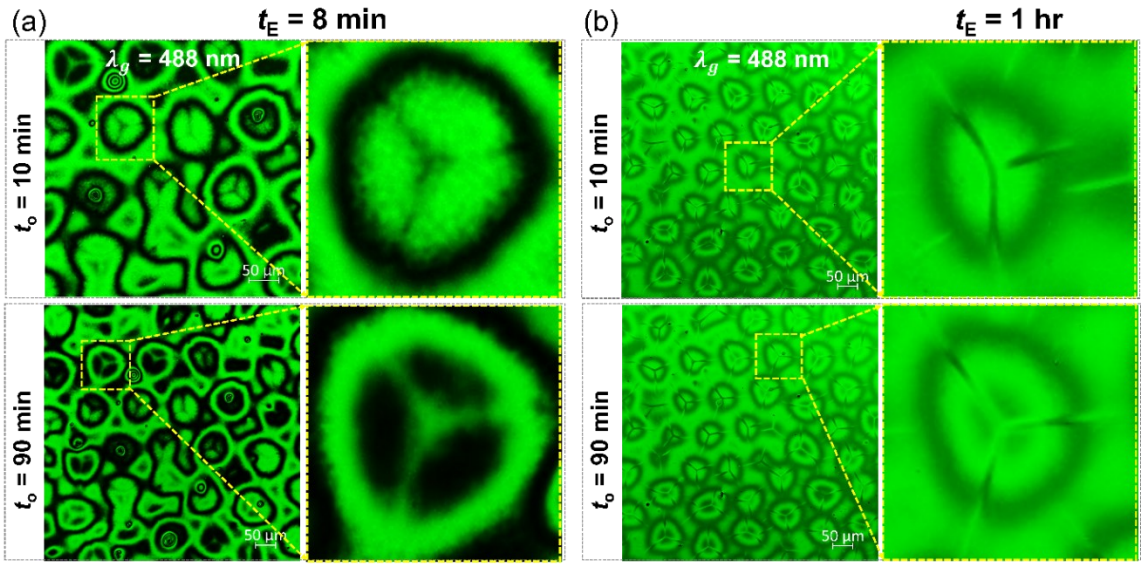


Figure D6-12 Dual-wavelength reflection interference contrast microscopy (DW-RICM) images and the corresponding zommed-in images of the pattern structure for silicone gel soft substrates with hexane extraction times of (a) 8 min and (b) 1 hr for air drying times of 10 min and 90 min. The green color corresponding to laser wavelength of 488 nm.

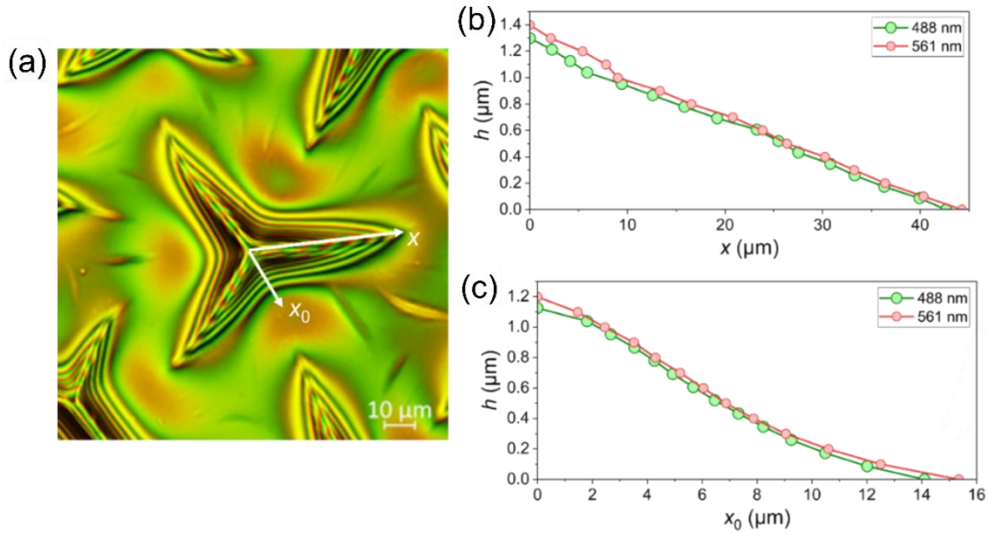


Figure D6-13 (a) Dual-wavelength reflection interference contrast microscopy (DW-RICM) image of a single pattern on soft silicone gel substrate swollen in hexane for 96 hrs and then dried in an oven for 12 hrs at 60°C. (b)

and (c) Variation of the pattern height profile along the dashed lines representing the ridge slope (x) and the ridge side (x_0).

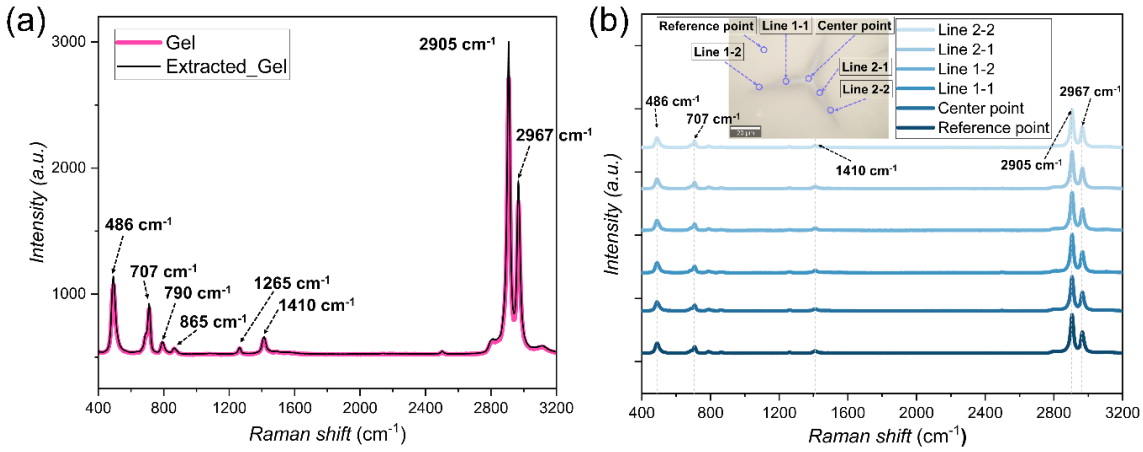


Figure D6-14 (a) Raman spectra of the gel soft substrates before and after hexane extraction of 96 hrs and drying in air more than 24 hrs. (b) Raman spectra of the pattern on the gel soft substrate surface.

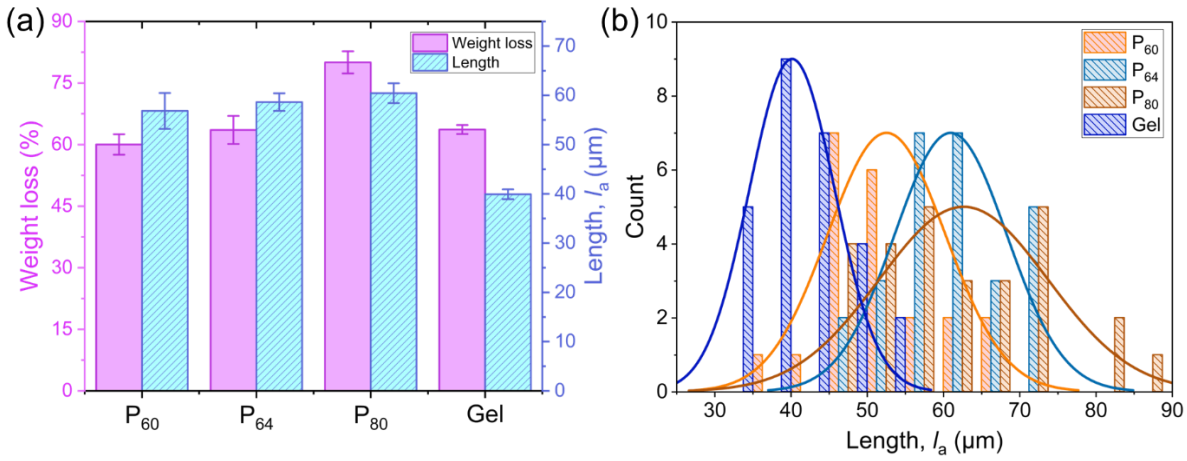


Figure D6-15 (a) Variation of post-solvent extraction weight loss % and arm length of the pattern l_a of P_{60}, P_{64}, P_{80}, and silicon gel substrates with hexane extraction time of 96 hrs followed by drying in air. Error bars for weight loss and length represent standard deviation from three independent experiments. (b) The distribution of arm lengths l_a of P_{60} (52.54 ± 7.74 μm), P_{64} (60.97 ± 7.36 μm), P_{80} (62.67 ± 11.08 μm), and silicone gel (40.14 ± 5.50 μm) under the same extraction and drying conditions.

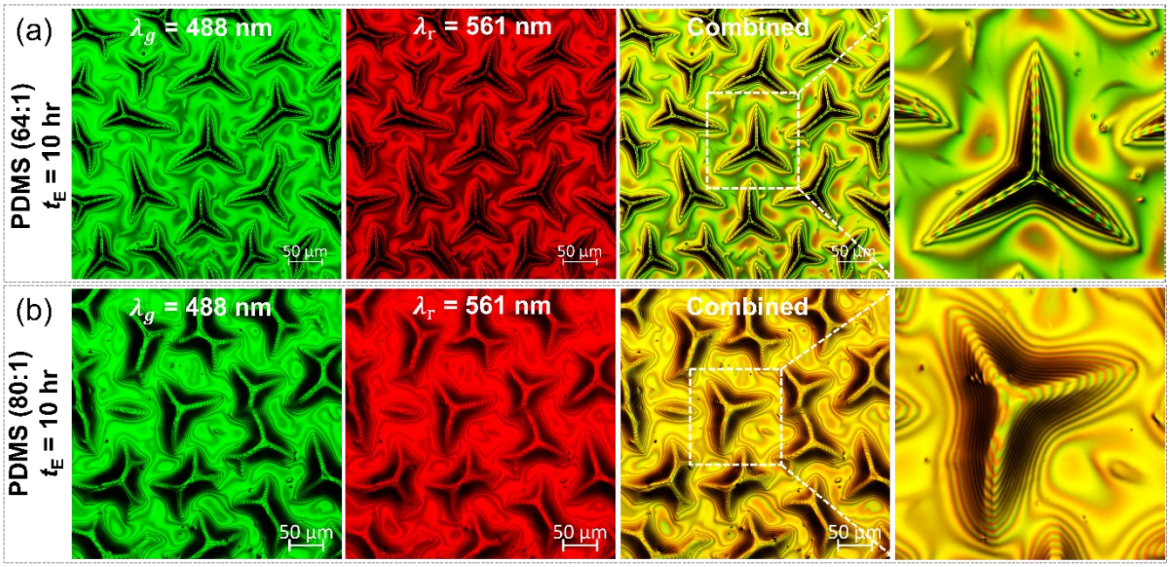


Figure D6-16 Dual-wavelength reflection interference contrast microscopy (DW-RICM) images of PDMS substrates with different base-crosslinker ratios: (a) PDMS 64:1 and (b) PDMS 80:1 with hexane extaction (t_E) for 10 hrs and then dry in air for 10 min. The green (first column) and the red channels (second column) reflect imaging using 488 nm and 561 nm wavelengths, respectively. The combined channel image (third column) is the overlay of the green and red channel images. Compared to PDMS 60:1, these surfaces have a higher fraction of free liquid chains and lower elasticity.